EFFECT OF Ti AND Zr ALLOYING ADDITIONS ON THE MICROSTRUCTURE, MECHANICAL PROPERTIES AND OXIDATION BEHAVIOUR OF Nb-18.7Si ALLOY

A dissertation work

submitted in partial fulfilment of the requirements

for the award of the degree of

DOCTOR OF PHILOSOPHY

in

METALLURGICAL AND MATERIALS ENGINEERING

by

Kommineni Geethasree
(Roll No.701628)

Under the guidance of

Dr. Brahma Raju Golla
Assistant Professor
&
Dr. V.V. Satya Prasad
Scientist 'H'

Department of Metallurgical and Materials Engineering

National Institute of Technology

Warangal-506 004, Telangana State, India

January 2021

DEPARTMENT OF METALLURGICAL AND MATERIALS ENGINEERING
NATIONAL INSTITUTE OF TECHNOLOGY
WARANGAL – 506004 (T.S) INDIA

CERTIFICATE

This is to certify that the work presented in the dissertation entitled **"Effect of Ti and Zr alloying additions on the microstructure, mechanical properties and oxidation behaviour of Nb-18.7Si alloy"** submitted to the National Institute of Technology, Warangal by **Mrs. Kommineni Geethasree** bearing **Roll No.701628**, for the award of **Doctor of Philosophy** in **Metallurgical and Materials Engineering** is a record of bonafide research work carried out by her under the supervision of Dr. Brahma Raju Golla (NIT, Warangal) and Dr. V.V. Satya Prasad (Scientist, DMRL). The results presented in this dissertation have not been submitted in either part or full elsewhere for any research degree.

Dr. Brahma Raju Golla
Assistant Professor & Thesis supervisor
Department of Metallurgical and Materials Engineering
National Institute of Technology Warangal
Warangal-506 004 (T.S) India

Dr. V. V. Satya Prasad
Scientist 'H' & Thesis Co-Supervisor
Advanced Materials Technology Group
Defence Metallurgical Research Laboratory
Hyderabad- 500 058 (T.S) India

DECLARATION

I, Kommineni Geethasree, hereby declare that this dissertation work entitled **"Effect of Ti and Zr alloying additions on the microstructure, mechanical properties and oxidation behaviour of Nb-18.7Si alloy"** submitted in partial fulfillment for the award of degree of **Doctor of Philosophy (in Metallurgical and Materials Engineering)** to the Department of Metallurgical and Materials Engineering, National Institute of Technology, Warangal is a bonafide work which was carried out by me under the supervision of **Dr. Brahma Raju Golla** and **Dr. V.V. Satya Prasad**. I also declare that the content of this thesis has not been submitted previously in part or full in any University or Institute for the award of any degree or diploma.

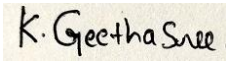

Kommineni Geethasree
Roll No. 701628
Department of Metallurgical and
Materials Engineering

Thesis Approval for Ph.D

The thesis entitled **"Effect of Ti and Zr alloying additions on the microstructure, mechanical properties and oxidation behaviour of Nb-18.7Si alloy"** Which is submitted by **Mrs. Kommineni Geethasree (Roll No.701628)** is approved for the degree of **Doctor of Philosophy** in Metallurgical and Materials Engineering.

Examiner(s)

_____

_____

Supervisors

VVS. Prasad

_____

_____

Chairman

_____ 11/01/2021

Date: 11-01-2021

DEDICATED TO

My Parents, Sister & brother for their constant love, support and encouragement

&

My Husband for his patience, advice and faith in making this achievement a reality

ACKNOWLEDGEMENTS

I express my deep sense of gratitude to my both the research supervisors and mentors **Dr. G. Brahma Raju**, Assistant Professor, Department of Metallurgical and Materials Engineering, National Institute of Technology Warangal and **Dr. V.V. Satya Prasad**, Outstanding Scientist, Defence Metallurgical Research Laboratory (DMRL) Hyderabad for their wholehearted support, encouragement, guidance and patience during the research work. Without their patient mentorship, constant inspiration, valuable discussions and suggestions, this thesis wouldn't have been possible. I appreciate them for critically going through the draft of my thesis and research papers.

I am greatly indebted to **Dr. Md Zafir Alam**, Scientist 'E' DMRL Hyderabad for mentoring, guiding and motivating me to accomplish this research work. His constant perusal for scientific excellence and perfection has helped me shape this thesis.

I gratefully acknowledge the provision of funding for the research described in this thesis by Defence Research Metallurgical Laboratory (DMRL). I express my gratitude to former directors **Dr. Amol Ghokhle, Dr. S.V. Kamat, Dr. Vikas Kumar** and present director **Dr. Madhusudan Reddy**, Outstanding Scientist, DMRL Hyderabad for giving me an opportunity to carry out research work in the organization and permitting to do PhD. I also thank **Prof. N.V. Ramana Rao**, Director, NIT Warangal, Prof. T. Srinivasa Rao, former Director, NIT Warangal for giving me an opportunity to register for PhD in the institute.

My heartfelt thanks to **Dr. M. Sankar**, Scientist 'E', DMRL Hyderabad for his help in carrying out the melting process in Vacuum arc remelting furnace (VAR) and for extending his technical support continuously in completion of this thesis. I am greatly thankful to Dr. P Sudharshan Phani, Scientist in Center for advanced coatings group, International Advanced Research Center for Powder Metallurgy and New Materials (ARCI) Hyderabad for providing me with the nanoindentation test facility and his valuable cooperation and guidance for nanoindentation test, results analysis. I profoundly thank **Dr. Rajdeep Sarkar**, Scientist 'E', DMRL Hyderabad for providing his help in carrying out TEM analysis.

I take this opportunity to thank **Dr. Asit Kumar Khanra**, Associate Professor and Head of the Department and members of Doctoral Scrutiny Committee – **Prof. G. V. S. Nageswara Rao** and

Dr. T. Mahesh Kumar, Associate Professor from the Department of Metallurgical and Materials Engineering, and **Dr. M. Joseph Davidson**, Associate Professor from Department of Mechanical Engineering, NIT Warangal for their useful suggestions and periodical review of my progress during this course of PhD work. I also would like to thank all the faculty members of MMED for their support and help during my PhD.

I take this opportunity to thank my friends and colleagues **Dr. K. Sahithya**, **Dr. S. Ranga Swamy**, **Dr. N. N. Sruthi**, **Mrs. P.S.D.R.S. Sailaja** from DMRL Hyderabad and **Dr. Md. Ali Shaik**, **T. Sravan Kumar**, **Dr. P. Prakash** from NITW for their valuable help and support on varied occasions.

I also thank technical and non-Technical staff of Advanced Materials Technology Group (AMTG), High Temperature coatings Group (HTCG), Electron Microscopy Group (EMG), Mechanical Behaviour Group (MBG) and Near net Shape Group (NNSG), DMRL Hyderabad for their help during the research work mentioned in the thesis.

Finally, I express my sincere thankfulness to my grandparents, father in-law, other family members and friends for their support and understanding all the way through this long journey.

I thank almighty God from the depth of my heart for his constant shower of blessings at all the times of my life.

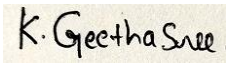

(KOMMINENI GEETHASREE)

LIST OF ABBREVIATIONS AND SYMBOLS

T_m^{Ni}	Melting temperature of Ni	**LPT**	Low pressure turbine
MPa	Megapascal	**HPT**	High pressure turbine
ρ_{Ni}	Density of Ni	**VAR**	Vacuum arc remelting
g/cm^3	gram/cubic centimeter	**XRD**	X-ray diffraction
µm	Micrometer	**SEM**	Scanning electron microscopy
°C	Degree Celsius	**EDXS**	Energy dispersive X-ray spectroscopy
RMIC	Refractory metallic intermetallic composite	**EPMA**	Electron probe micro analyzer
T_m^{Nb}	Melting temperature of Nb	**EBSD**	Electron back scattered diffraction
T_m^{Mo}	Melting temperature of Mo	**TEM**	Transmission electron microscopy
ρ_{Nb}	Density of Nb	**EDS**	Energy dispersive spectroscopy
Nb_{ss}	Nb solid solution	**SE**	Secondary electron
Å	Angstrom	**DC**	Direct current
h	hour	**A**	Ampere
AM	Arc melting	**V**	Volt
DS	Directional solidification	**mm**	Millimetre
PM	Powder metallurgy	**EDM**	Electro discharge machine
PVD	Physical vapor deposition	**PIPS**	Precision Ion polishing system
OR	Orientation relation	**KeV**	Kilo electron Volt
HT	Heat treatment	**KV**	Kilo volt
P-N	Peierls-Nabbarrow	**BCC**	Body centered cubic
CTE	Coefficient of thermal expansion	**KN**	Kilo newton
TCP	Topologically close packed	**K_Q**	Fracture toughness

B	Thickness
S	Span length
a	Crack length
kg	Kilogram
H	Hardness
E	Elastic modulus
mN	Milli Newton
WDS	Wavelength dispersive spectroscopy
SAD	Selected area diffraction
IPF	Inverse pole figure
GPa	Gigapascal
YS	Yield strength
FS	Fracture strength
$MPa.m^{1/2}$	Megapascal/sqrt (meter)
FEM	Finite element method
Kc	Fracture toughness of composite
K_b	Fracture toughness of brittle phase
K_c	Fracture toughness of ductile phase
V_b	Volume fraction of brittle phase
P_c	Plastic constraint
P_Q	Fracture load
W	Width
OL	Outer layer
IL	Intermediate layer
IDZ	Inter diffusion zone
K_p	Parabolic oxidation rate constant
$\mu m.°C^{-1}$	Micrometer/degree Celsius
ΔG_f°	Free energy of formation
Q	Activation energy
A	Pre-exponential constant
R	Universal gas constant
T	Test temperatures
kJ/mol^{-1}	Kilo joule per mole
PB	Pilling Bedworth

LIST OF FIGURES

LIST OF TABLES

Abstract

The present study investigates the effect of Ti and/or Zr alloying elements on the microstructure, phase evolution, hardness and elastic modulus of the phases, compression properties, fracture toughness and high temperature cyclic oxidation behaviour of a near eutectic Nb-18.7Si cast alloy. Both Nb-18.7Si and Nb-18.7Si-5Ti alloys displayed a two phase microstructure consisting of Nb_{ss} and Nb_3Si. The Nb_3Si is not a stable phase and require further long term heat treatments to form stable and high creep resistant α–Nb_5Si_3 phase. Interestingly, the alloys added with Zr (Nb-18.7Si-5Zr), Ti and Zr together (Nb-18.7Si-5Ti-5Zr) exhibited desirable Nb_{ss} and α–Nb_5Si_3 phases in the cast alloys. The formation of such stable phases in these alloys is beneficial in improving the properties and also cost effective. The volume fraction of the Nb_{ss} (~22-23%) is almost same in both the Nb-18.7Si and Nb-18.7Si-5Ti alloys. Whereas, the volume fraction of Nb_{ss} increased more than double (~53-55%) in Nb-18.7Si-5Zr and Nb-18.7Si-5Ti-5Zr alloys. The coarsening of the Nb_{ss} phase is also observed with alloying and is more prominant in Nb-18.7Si-5Zr and Nb-18.7Si-5Ti-5Zr alloys. The nano indentation results showed that the hardness of Nb_{ss} phase increased with Ti and decreased with Zr additions. Overall, a drastic increase in the elastic modulus of the silicide phase is evident in Nb-18.7Si-5Zr and Nb-18.7Si-5Ti-5Zr alloys as compared to other alloys (Nb-18.7Si, Nb-18.7Si-5Ti) which is due to the formation of α–Nb_5Si_3 phase in the former alloys compared to Nb_3Si phase in the later ones. The formation of equilibrium α–Nb_5Si_3 phase directly in the cast condition is a significant breakthrough since it eliminates the need for long term vacuum heat treatment at higher temperatures.

The Nb-18.7Si-5Zr and Nb-18.7Si-5Ti-5Zr alloys resulted in significant improvement in the fracture toughness (10.40±0.18 MPa. $m^{1/2}$, 10.59±0.35 MPa. $m^{1/2}$ respectively). At the same time good fracture strength of 1857±58 MPa and 2236±81 MPa is obtained in Nb-18.7Si-5Zr and Nb-18.7Si-5Ti-5Zr alloys. The formation of high strength α-Nb_5Si_3 phase is attributed to such high strength value. Whereas, the increase in the Nb_{ss} phase fraction, coarsening of Nb_{ss} phase and presence of lamellar Nb_{ss} phase morphology are the contributing factors for its enhanced fracture toughness. High strenth and fracture toughness is observed for the Nb-18.7Si-5Ti-5Zr alloy. The achievement of good combination of properties with stable microstructure without subjecting the Nb-18.7Si-5Ti-5Zr material to any additional heat treatment process is the promising outcome of

this research. Fracture in the alloys started with cracking of the silicide phase (Nb_3Si/α-Nb_5Si_3) and the crack path tortuousity increased by the crack bridging, branching and deflection mechanisms at the Nb_{ss} phase. Further, the constraint of the brittle silicide phase on the ductile Nb_{ss} phase impeded the ductility or deformation of the Nb_{ss} phase which resulted in interface debonding in the alloys. The constraint of the silicide phase on the Nb_{ss} phase is very crucial in the fracture toughness measurement of the alloy along with the phases and their microstructural features, hardness.

The uncoated samples showed extensive loose-scale formation from the initial stages of cyclic oxidation at temperatures between 800-1400°C. On the other hand, in the Fe-Cr modified silicide coated samples, the protective multi-phase oxide scale formed on the coating surface prevented dimensional degradation for at least 5-7 h at high temperatures of 1400°C. The oxide scale acted as a barrier against the inward diffusion of oxygen at both lower and higher temperatures and lowered the overall oxidation rate. The achievement of good combination of properties with stable microstructure without subjecting the Nb-Si alloys to any additional heat treatment process is the promising outcome of this research.

Keywords: Nb-Si cast alloy; Vacuum arc remelting and Casting; Microstructure; Hardness; Elastic modulus; Compression properties; Fracture toughness; Fracture mechanisms; Cyclic oxidation; Coating.

CONTENTS

(B) BULK MECHANICAL PROPERTIES

Chapter-1

Introduction

This chapter highlights the important aspects to be considered in the development of high temperature Nb-Si alloys as alternative materials for turbine engine applications in the current scenario. The necessity behind the improvement in the operating temperature in the hot section of the turbine engine materials is explained. Further, the potential of Nb-Si alloys as the hot section material for both aircraft and land based gas turbine applications is elaborated. This is followed by the problem identification, motivation, objectives of the work and organization of thesis.

1.1 Introduction

The Niobium-Silicon based alloys exhibit promising combination of properties such as high melting temperature, high stiffness, lower density, superior high temperature strength and exceptionally good creep resistance [*B.P. Bewlay, ,.R, Jackson, J.C. Zhao, P.R. Subramanian et al., 2003, P.R. Subramanian et al., 1997, T.M. Pollock et al., 2016*]. These alloys have been identified as the next generation gas turbine blade materials due to their advantageous high operating temperatures (>1750 °C) than the currently used nickel based superalloys (1150 °C) [*B.P. Bewlay,.R, Jackson, J.C. Zhao, P.R. Subramanian et al., 2003*] and owing to their best combination of properties. For instance, Nb-Si alloys exhibit better elastic modulus of 140 MPa at 1200°C compared to 75-83 MPa at 1100°C for Ni base alloys, low density of 6.6-7.2 g/cc compared to 8 g/cc for Ni-base super alloys [*B.P. Bewlay, M.R. Jackson et al., 2003*], high strength of 1700 MPa at room temperature and 310 MPa at 1350°C, compared to the 1050 MPa at room temperature and 175-200 MPa at maximum operating temperatures of 1200°C for Ni base alloys [*P.R. Subramanian et al., 1997*].

Gas turbine engines are among the most technologically complex engineering platforms and is one of the major engineering achievements of the twentieth century. These are the sole energy production systems in both the aircrafts and industrials power generation units. There is a

considerable increase in the commercial airline passenger's traffic and power generation around the world. This is expected to further increase in the coming years and can have remarkable impact on the economy and also on human lives. Therefore, there is a high demand for more gas turbine engines in the future.

The reliability and the efficiency of the engine are the important considerations while manufacturing the future gas turbine engines. The performance and efficiency of the jet engine are strongly dependent on the maximum/highest temperature in the engine. Higher operating temperatures must be realized to attain higher thrust. Therefore, the fuel consumption and the cooling air requirements in the engine can be minimized. Currently, the hot section components are being operated at temperatures of 1200°C. It is estimated that the operation at 1300°C without auxiliary cooling would increase the efficiency of the engine by 50% [*J.H. Perepezko et al., 2009*]. In addition, this wouldt simplify the manufacturing, eliminate the weight and requirement of complex auxiliary cooling equipments. Therefore, the working temperature of the hot section components is crucial. Further, the increased efficiency of the engine can reduce the CO_2 emission and thus contribute in controlling global warming. Also, the engines must be made significantly lighter to minimize the weight to thrust ratio. Therefore, the advancements in the hot section component materials can improve the working temperature and thereby the engine efficiency.

1.2 Background

Currently Ni based super alloys are being extensively used as the hot section components materials [*T. M. Pollock et al., 2006, S. J. Balsone et al., 2001*]. However, the super alloys are being used at temperature (1150°C) close to their highest application limit (almost at 85% of melting temperature of Ni, T_m^{Ni}=1453°C).

The Nb and Mo refractory metals have been considered as appropriate to use as aero-engine component materials due to the following reasons [*P. Tsakiropoulos et al., 2020*]: (a) higher melting temperatures than Ni (T_m^{Nb}= 2467°C, T_m^{Mo}= 2615°C), (b) lower densities among the refractory metals (ρ_{Nb}= 8.57g/cm^3, ρ_{Mo}=10.22g/cm^3) and (c) wide solubility for a large number of alloying additions [*R.T. Begley et al., 1961*]. Therefore, the mechanical properties and oxidation resistance can be significantly improved. Still the monolithic refractory alloys exhibit poor oxidation response. So the refractory metal-intermetallic composites (RMICs) based on Nb-Nb

silicides and Mo-Mo silicides gathered attention owing to their improved oxidation behaviour (due to formation of silica) and the creep resistance. The tetragonal 5-3 silicides of Nb and Mo (Nb_5Si_3, Mo_5Si_3) have better creep properties compared to other refractory 5-3 silicides (W_5Si_3, Ta_5Si_3) [*R. M. Nekkanti et al., 1990*]. The Nb-Nb silicide composites are of present interest due to their lower density (6.6-7.7 g/cm^3) compared to Mo-Mo silicides (8.6-9.4 g/cm^3), better fracture toughness (>20 MPa.m$^{1/2}$) compared to Mo-Mo silicides (<15 MPa. m$^{1/2}$) [*B.P. Bewlay et al., 1996*]. Further, the processability is comparatively easy for Nb alloys than Mo alloys [*J. Wadsworth et al., 1988*].

Nb-Nb silicide based RMICs consists of a ductile Nb_{ss} and brittle silicide (Nb_3Si/Nb_5Si_3) phases. The room temperature fracture toughness and high temperature creep strength of the alloy can be provided by Nb_{ss} and silicide phases, respectively. Hence, these alloys exhibit added advantage of good fracture toughness along with the creep strength. Further they are expected to show better oxidation resistance by silica formation. However, the oxidation resistance needs much more improvement for the application [*B.P. Bewlay et al., 1996*]. Nevertheless, the room temperature fracture toughness and high temperature properties should not be compromised. Therefore, alloy design and development has been indispensable to meet those requirements.

1.3 Problem identification and motivation of the work

The Nb-Nb silicide alloys composed of Nb_{ss} and Nb_3Si silicide phases in the cast stage. In particular, the high temperature creep resistant silicide (α-Nb_5Si_3) phase formation through eutectoid reaction ($Nb_3Si \rightarrow Nb_{ss} + \alpha$-$Nb_5Si_3$) necessitates the long term heat treatments (time duration of 100 h and high temperatures of 1500°C) [*M.G. Mediratta et al., 1991*]. It requires vacuum treatment to protect the alloys from environment. Heat treatment of the alloys at such higher temperatures in vacuum was really challenging and expensive. In addition to optimizing the alloy composition and the processing conditions, careful control/design of microstructure was deemed for achieving better combination of properties. Therefore, the studies on Nb-Nb silicide alloys are turned to multi-component systems to gain a balance between mechanical properties and environmental protection by attaining required microstructure and phase properties. Hence, addition of different alloying elements was being studied.

In the open literature, various alloying elements such as Ti, Hf, Zr, Mo, W, Fe, Cr, Al, Sn, Ge and Ga etc. have been used to control the microstructure and enhance the room and high

temperature properties of these alloys. Among them, alloying with Ti, Zr were noted to have beneficial effect on the eutectoid transformation kinetics, fracture toughness and oxidation resistance [*N. Sekido et al., 2004 and 2006, B.P. Bewlay et al., 1993, Miura et al., 2005 and 2009, M. Sankar et al., 2018 and 2019, P.R. Subramanian et al., 1994, B.P. Bewlay et al., 1996*].

The Zr addition (1.5 at.%) to Nb-Si alloys was reported to reduce the time and increase the kinetics of eutectoid transformation [*N. Sekido et al., 2004, S. Miura et al., 2009*]. Recent studies by Sankar et al., [*M. Sankar at al., 2018, 2019*] from our research group reported the effect of 2, 4, 6 at.% Zr on the microstructure and mechanical properties of Nb-16Si alloy. The formation of eutectic Nb_{ss}/Nb_3Si phases was reported with 2 at.%Zr addition. Interestingly, the 4 at.%Zr concentration reported to result in the microstructure with beneficial Nb_{ss}/α-Nb_5Si_3 phases and the alloy exhibited good fracture toughness and room temperature strength. Further increase in the Zr level to 6 at.% reported to form brittle γ-Nb_5Si_3 phase along with beneficial Nb_{ss}/α-Nb_5Si_3 phases. Based on our previous work, preliminary experiments and literature review, it was realized that about 5 at.% Zr concentration is beneficial in obtaining desirable microstructure with optimum properties in Nb-18.7Si alloy.

Similary, alloying with Ti, was also reported to have beneficial effect on the eutectoid transformation kinetics, fracture toughness and oxidation resistance all together [*N. Sekido et al., 2004 and 2006, B.P. Bewlay et al., 1993, Miura et al., 2005 and 2009, M. Sankar et al., 2018 and 2019, P.R. Subramanian et al., 1994, B.P. Bewlay et al., 1996*]. However, The Ti addition was reported to stabilize the unbeneficial Nb_3Si phase to lower temperatures and this decreases the melting temperature of the alloy [*B.P. Bewlay et al., 1995*]. Further, alloying with higher amount of Ti was reported to associate with compositional segregation in the alloys and stabilization of undesirable γ-Nb_5Si_3 phase [*Y.X. Tian et al., 2008, N. Sekido et al., 2004, B.P. Bewlay et al., 1995, Enyu Guo et al., 2017*]. In addition, the toughness of the α-Nb_5Si_3 phase was reported to decrease with Ti addition of beyond 12.5 at.% [*Songxin Shi et al., 2016*]. Therefore, the Ti addition should be controlled for holding the melting temperature of the alloy, to minimize the compositional segregation and to avoid γ-Nb_5Si_3 phase formation, in order to mainiain the toughness of the α-Nb_5Si_3 phase. Most of the literature reported the effect of 10 at.% Ti and above on the microstructure and mechanical properties of the alloy. Limited literature is available on the effect

of Ti (in particular, below 10 at.%) on the mechanical properties and oxidation behaviour of Nb-18.7Si alloy.

In order to understand the effect of low amount of Zr, Ti and to compare its effect on the microstructure and properties of near eutectic Nb-18.7Si, in the present work, the concentration of alloying element was limited to 5 at.%. Considering the beneficial effects of both Ti and Zr, it is of great iterest to study the combined addition which can facilitate the desirable eutectoid transformation in the alloys by minimizing the requirement for long-duration vacuum heat treatments, reduce the segregation effects, improve the fracture toughness and oxidation resistance altogether.

In view of aforementioned, the addition of Ti, Zr and both together has been explored for its beneficial effect. Particularly, in the existing literature, the effect of these alloying elements on the systematic study of microstructure, fracture toughness, compressive strength and the high temperature oxidation response of Nb-18.7Si alloy was lacking. The near eutectic composition (18.7Si) was selected because of the minimum creep rate reported for the alloy.

Further, Alloying additions of Ti, Zr, Sn, Cr, Al and Mo were reported to improve the inherent oxidation resistance of these alloys [*S. Knittel et al., 2014, K.S. Chan, 2004, K. Zelenitsas et al., 2006, N. Esparza et al., 2016, L. Su et al., 2017*], but not to significant extents [*B.P. Bewlay at al., 2003*]. Moreover, excessive alloying deteriorates the fracture toughness of the alloys. Therefore, application of protective surface coatings was an alternate approach for increasing the high-temperature oxidation resistance of the alloys, as typically done for the Ni-based superalloy turbine engine components [*W. Wand et al., 2014, W. Wang et al., 2016, S. Knittel, S. Mathieu, M. Vilasi et al., 2013, S. Knittel, S. Mathieu, L. Portebois et al., 2013*]. The silicide-based coatings provide significant oxidation resistance to the Nb-based alloys [*M.Z. Alam et al., 2010, 2016*, *M.K. Kumawat, M.Z. Alam, D.K. Das et al., 2018, M.K. Kumawat, M.Z. Alam, A. Kumar et al., 2018*]. The alloyed silicide coatings can further enhance the oxidation resistance by the formation of respective oxides along with silica [*M.D. Novak et al., 2007, S. Priceman et al., 1968, Y. Qiao et al., 2014*]. However, studies on the effectiveness of Fe and Cr-alloyed silicide coatings against oxidation of the Nb-Si alloys were limited in the open literature. Hence, in the current study, the oxidation behavior of both the uncoated and Fe, Cr modified silicide coated alloys was also studied for the above selected alloys.

1.4 Novelty of the current work

Recent studies on Nb-Si alloys have evolved into multi-component systems to make a balance between mechanical properties and environmental resistance along with the required microstructural phases. It is very crucial to know the effect of each alloying element addition to produce a multi component system for optimization of both the room and high temperature mechanical properties along with the oxidation resistance. As part of this, various alloying elements like Ti, Hf, Zr, Sn, Al, Cr, Mo, W, V, Ge, Mg and Ga additions effect on the phase stability, microstructure, mechanical properties and oxidation behaviour of the Nb-Si alloys was reported. Among the alloying elements, Ti and Zr attracted the interest due to the following reasons:

- Increase of eutectoid transformation kinetics during heat treatment [*S. Miura et al., 2005*]. Especially the transformation time reduced to below 10 h at heat treatment temperature of 1400°C with 1.5 at.% Zr addition.
- Interestingly, the 4 at.% Zr concentration reported to result in the microstructure with beneficial Nb_{ss}/α-Nb_5Si_3 phases. Further, increase of Zr to 6 at.% forms undesirable γ-Nb_5Si_3 phase along with beneficial Nb_{ss}/α-Nb_5Si_3 phases [*M. Sankar et al., 2019*]. So, it is of great importance to understand the effect of 5 at.% Zr to know the maximum amount of Zr that can be added to obtain only the beneficial phases along with good mechanical properties in the cast alloys itself.
- Improvement in the fracture toughness of the alloy with Ti and Zr [*M. Sankar et al., 2019, N. Sekido et al., 2004*].
- Enhancement in oxidation resistance of the alloy with Ti addition [*B.P. Bewlay at al., 1996*].

However, studies on the effect of low Ti (<10 at.%), Zr (5 at.%) and their combined additions on the microstructure and properties of near-eutectic Nb-Si alloys were not reported in the open literature. Further, the Fe, Cr modified silicide coatings can hold the potential application similar to Nb alloys. Such studies are vital from the point of view of processing and engineering applications

1.5 Objectives of the present study

Considering the above aspects, the current research work initiated with the main objective to study the effect of lone 5 at.%Ti, 5 at.% Zr and their combined additions (5 at.% each) on the microstructure, phase formation, room temperature mechanical properties and high temperature oxidation behaviour of near eutectic Nb-18.7Si alloy. Near eutectic composition is chosen for the study as the Nb-Si alloys reported to exhibit minimum creep rate at this composition [B.P *Bewlay, M.R. Jackson, J.C. Zhao et al., 2003, B.P. Bewlay et al., 2001*[.

The following are the major objectives of the present research work:

1. Study the effect of alloying addition of 5 at.%Ti, 5 at.% Zr, 5 at.% of Ti and Zr each on near eutectic Nb-18.7Si alloy on the microstructure, phase evolution, micromechanical properties of the phases, strength properties and fracture toughness.
2. Correlate the structure-property of the alloys by carrying out detailed microstructural characterization, mechanical properties and understanding the fracture behavior of the alloys.
3. Identify the better Nb-Si alloy that exhibit good combination of strength and fracture toughness and asserting the underlying mechanisms.
4. Understand the cyclic oxidation response and oxidation mechanisms of the alloys in uncoated and Fe-Cr modified slurry silicide coated conditions in air over the temperature range of 800°C-1400°C.

1.6 Organization of the thesis

The thesis has been divided into following seven chapters

Chapter 1: Introduction
Chapter 2: Literature review
Chapter 3: Experimental procedure
Chapter 4: Microstructure and phase evolution
Chapter 5: Structure property correlation and deformation mechanisms
Chapter 6: Cyclic oxidation behavior

Chapter 7: Conclusions and scope for future work

Brief description of these chapters is given below

Chapter 1 presents description on the requirement of new materials for the air craft engine application, background of the present work, objectives and motivation of the work followed by organization of the thesis.

Chapter 2 is devoted for the literature review on the Nb-Si alloys that includes the importance of alloying additions on the microstructure, mechanical properties and oxidation of the various alloys. It also brings out the gaps in the literature and possible suggested methods to fill these gaps.

Chapter 3 describes the material and experimental procedure such as vacuum arc re-melting (VAR) technique is used in the present study. Details of the sample preparation, equipment utilized and the analysis carried out for the microstructural characterization (such as XRD, SEM-BSE, EPMA-WDS, EBSD and TEM) and mechanical tests is presented in detail. Mechanical behavior of the alloys is carried out using compression test and three point bend test. This chapter also deals with the micro-mechanical properties of the phases using nanoindentation hardness technique. Finally, the coating procedure, details of the oxidation test and the characterization done for analyzing the oxidation behaviour is included.

Chapter 4 describes the microstructural study of the Nb-18.7Si alloy with 5 at.% Ti, 5 at.% Zr and 5 at.% of each Ti and Zr additions. It includes detailed microstructural characterization of the alloys using XRD, SEM, EBSD, EPMA and TEM techniques. Finally the schematic phase evolution sequence in the alloys is proposed.

The micro-mechanical properties of the phases such as hardness and elastic modulus using nano-indentation, mechanical properties including compression strength and fracture toughness are discussed and correlated with the microstructural observations in the *Chapter 5*. Further, the fracture mechanisms are proposed from the fractography studies and finally the importance of constraint factor on fracture toughness of the alloys is brought out from TEM analysis of the post fractured samples.

Chapter 6 discusses the comparative cyclic oxidation response of the uncoated and Fe-Cr modified slurry silicide coated alloys in air over the temperature range of 800°C to 1400°C. The detailed microstructural characterization and oxidation mechanisms of Nb-Si alloys is presented.

Finally, the *Chapter 7* brought out the conclusions drawn from the current thesis work. This chapter also list out the possible areas of research that can be taken up in future for further study. The references used in the thesis and technical outcome of the are listed at the end.

In the current work, the addition of 5 at.% Zr and both Zr+Ti of 5 at.% each resulted in the microstructure with the Nb_{ss} and α-Nb_5Si_3 silicide phases in the cast condition itself. This is a significant breakthrough for the Nb-Si alloys and is beneficial in cost and time saving during the preparation of the alloys. Besides, the fracture toughness is also improved and the use of Fe-Cr modified silicide coating enhanced the oxidation resistance.

The schematic of the work plan of the current research work is given in below **Fig. 1.1**.

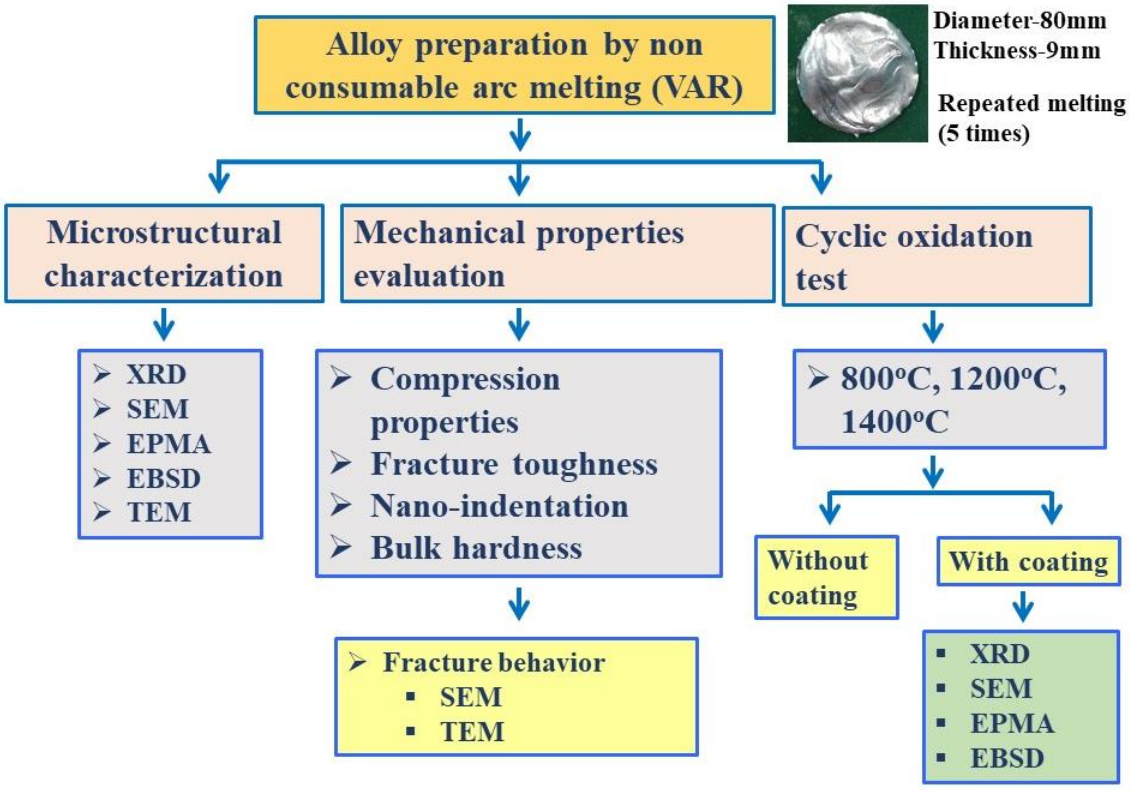

Fig. 1.1: Flow chart showing the experimental procedure followed for the current study.

Chapter-2

Literature review

The various research efforts made by the scientific community in the development of Nb-Si based alloys for the high temperature applications have been reviewed in this chapter. Initially the phase formation, microstructure and its stability in the alloys is explained briefly. The efforts made to attain the optimum balance in the room temperature and high temperature mechanical properties along with better oxidation resistance in the alloys are discussed. Influence of the various alloying elements on the phase formation, microstructure and mechanical properties (both room and high temperature) along with the oxidation behaviour is reviewed from the literature. Further, the fracture behaviour of the alloys is illustrated. The present chapter also brings out the gaps in the understanding of the development of these alloys and possible approaches to fill those gaps.

2.1 Introduction to Nb-Si system

The phase diagram of the Nb–Si binary system which is the basis for the Nb-Si based alloys is shown in **Fig. 2.1** [*T.B. Massalski et al., 1990*]. The composition of Si content from 12 to 25 at.% is of main interest because of the phase constituents present in this region. This region of the phase diagram consists of three invariant reactions as presented below.

- Eutectic reaction takes place at 1920°C at silicon content of 18.7 at.%. This region is marked as region 'B'in **Fig. 2.1**.

  $L\ (18.7\ at.\%\ Si) \rightarrow Nb_{ss}\ (3.5\ at.\%\ Si) + Nb_3Si\ (25\ at.\%\ Si)$--------- eq. 1

- Peritectic reaction takes place at 1980°C at 35.5 at.% Si.

  $L + \beta–Nb_5Si_3\ (35.5\ at.\%\ Si) \rightarrow Nb_3Si\ (25\ at.\%\ Si)$ --------- eq. 2

- Eutectoid reaction takes place at 1770°C with silicon content of 25 at.%.

Nb_3Si (25 at.% Si) $\rightarrow Nb_{ss}$ (0.5 at.% Si) + α–Nb_5Si_3 (35.5 at.% Si) ---------- eq. 3

The above mentioned composition range (12 to 25 at.%) in the Nb-Si phase diagram consists of Nb-Si solid solution (Nb_{ss}) and silicide (Nb_3Si and/or Nb_5Si_3) phases. The Nb exhibits body centered cubic structure with lattice parameter 'a' of 3.3004 Å. The solubility of Si in Nb_{ss} phase is 3.5 at.% at the eutectic temperature (1920°C) and decreases to about 0.5 at.% at eutectoid temperature (1770°C) [*T.B. Massalski et al., 1990*]. The Nb_3Si silicide phase exists in tetragonal crystal structure (a = 10.224 Å and c=5.189 Å). The Nb_5Si_3 silicide phase exists in two allotropic forms, i.e., α–Nb_5Si_3, forms at low temperature with body centered tetragonal structure (a=6.570 Å and c=11.884 Å) and the β–Nb_5Si_3, forms at high temperature with body centered tetragonal structure (a=10.026 Å, c=5.071 Å) [*M.E. Schlesinger et al., 1993*]. However, the γ–Nb_5Si_3 phase with hexagonal crystal structure with lattice parameter of a=7.536 Å and c=5.249 Å has also been reported in some of the ternary and multicomponent Nb-Si alloys [*Y.X. Tian, J.T. Guo, L.Y. Sheng et al., 2008, Y. Sainan et al., 2013*]. Among the different forms of Nb_5Si_3 phase, the enthalpy of formation is more negative for α–Nb_5Si_3 (-64.6 K J mol^{-1}) [*D. Yonghua et al., 2015*] and is less negative for γ–Nb_5Si_3 phase (-54.7 K J mol^{-1}). Therefore, α–Nb_5Si_3 phase is more stable than the other two forms and provides good high temperature creep resistance [B.P. *Bewlay et al., 2003*, *W.Y. Kim et al., 2002*]. Further, the β and γ-Nb_5Si_3 phases can be transformed to α–Nb_5Si_3 phase after high temperature heat treatment [*D. Yonghua et al., 2015, L. Zifu et al., 2010, M. Wu et al., 2010*].

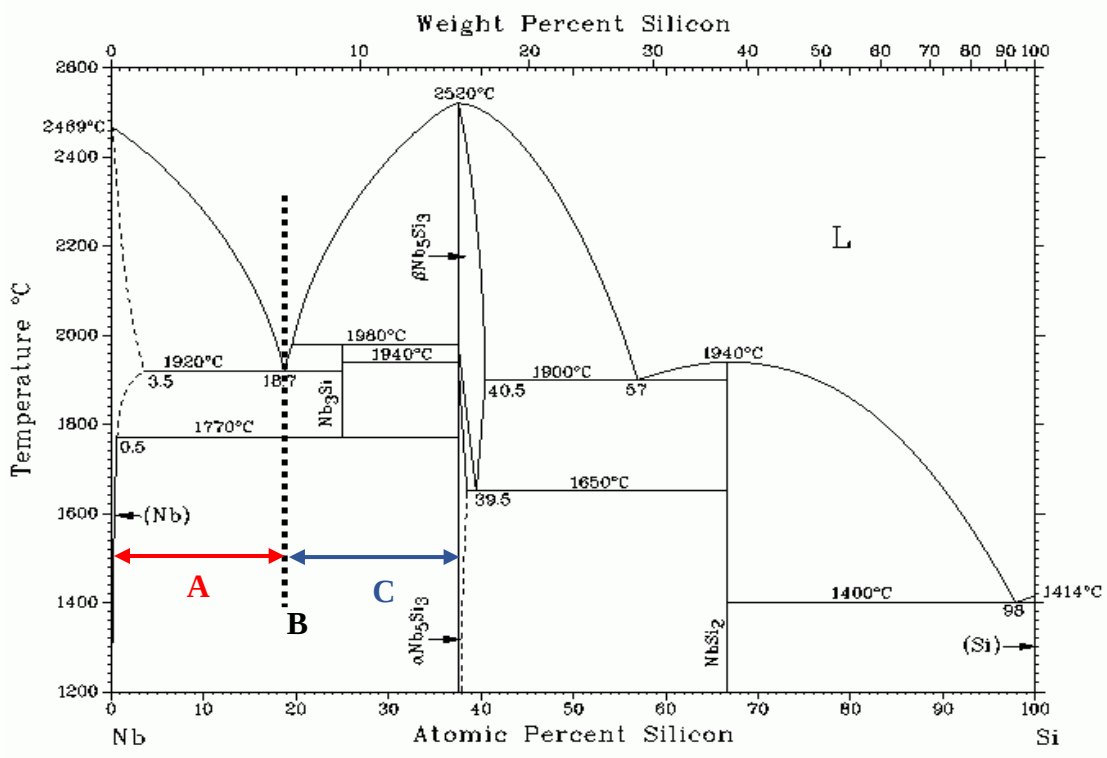

Fig. 2.1: The phase diagram of the Nb-Si binary system [*T.B. Massalski et al., 1990*]. Marked region 'A' represents the hypo-eutectic region, B: eutectic point and C: hyper-eutectic region.

Nb rich side of the Nb–Si phase diagrm is classified into three regions based on the Si content, i.e., hypo-eutectic (<18.7 at.%Si), eutectic (≈18–18.7 at.%Si) and hyper-eutectic (>18.7 at.%Si), as marked in **Fig. 2.1**. According to the phase diagram, the alloys in the mentioned range of composition consits of Nb_{ss}/α–Nb_5Si_3 phases at room temperature. The hypo-eutectic alloys consists of Nb_{ss}/α–Nb_5Si_3 phases along with primary Nb_{ss} phase. The eutectic and hyper-eutectic alloy consits of Nb_{ss}/α–Nb_5Si_3 phases along with the primary α–Nb_5Si_3 phase in the later composition. However, the high temperature silicide phase (Nb_3Si) get stabilizes to room temperature (through eq. 1) during casting of the alloys. Therefore, the eutectic alloys consist of Nb_{ss}/Nb_3Si along with primary Nb_{ss} and primary β-Nb_5Si_3 phases in the hypo-eutectic and hyper-eutectic alloys, respectively (**Fig. 2.2**).

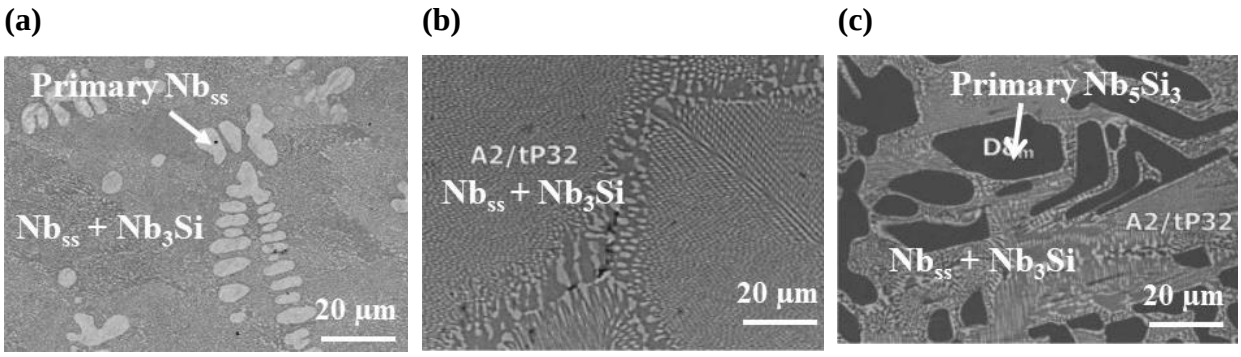

Fig. 2.2: Cast microstructures of the binary alloys. (a) Hypo-eutectic alloy (Nb-16Si) [*S. Drawin et al., 2005*], (b) Eutectic alloy (Nb-18.7Si) [*N. Sekido et al., 2004*] and (c) Hyper-eutectic alloy (Nb-25Si) [*N. Sekido et al., 2004*].

The α–Nb_5Si_3 phase provides good high temperature strength and creep resistance [B.P. *Bewlay et al., 2003*, *W. Y. Kim et al., 2002*]. Therefore, The Nb_3Si phase that forms in cast alloys needs to be converted to Nb_{ss} + α–Nb_5Si_3 through eutectoid reaction (eq. 3), which is kinetically slow/sluggish in nature. It is reported that it is required to carryout heat treatment for long durations of 100 h even at the nose of the TTT diagram (1500^{o}C) [*M.G. Mediratta. D.M. Dimiduk et al., 1991*]. The stable microstructure after the prolonged heat treatment consists of Nb_{ss}/α-Nb_5Si_3 and are given in the **Fig. 2.3**. The eutectic alloy consists of Nb_{ss} /α-Nb_5Si_3 phases while the hypo-eutectic and hyper-eutectic alloys exhibit additional primary Nb_{ss} and primary α-Nb_5Si_3 phases respectively (**Fig. 2.3**). Therefore, the desirable Nb_{ss}/α-Nb_5Si_3 phases basically form from the eutectic reaction of Nb_{ss} and Nb_3Si from the liquid phase (eq. 1) and the subsequent eutectoid reaction of Nb_3Si phase decomposing into Nb_{ss} and α-Nb_5Si_3, through eq. 3 as mentioned above.

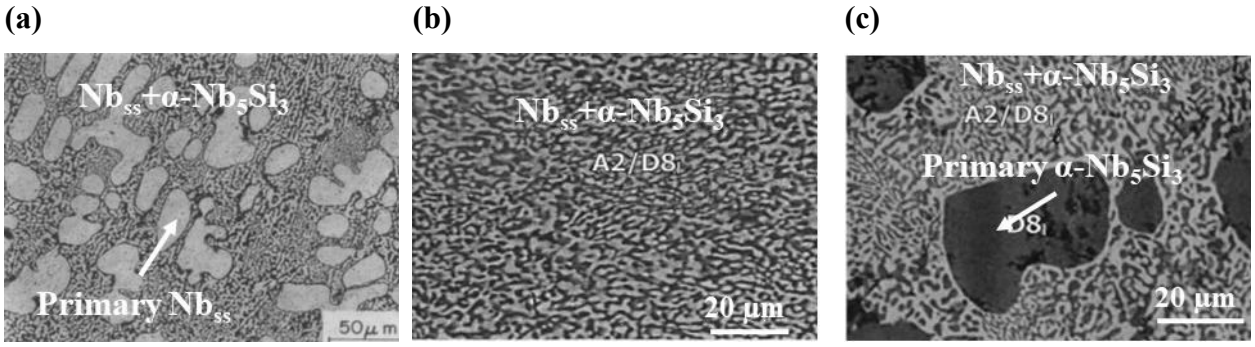

Fig. 2.3: Stable microstructures in the binary Nb–Si alloys. (a) Hypo-eutectic alloy (Nb-16Si) [*M.G. Mendiratta, J.J. Lewandowski et al., 1991*], (b) Eutectic alloy (Nb-18.7Si) [*N. Sekido et al., 2004*] and (c) Hyper-eutectic alloy (Nb-25Si) [*N. Sekido et al., 2004*] after heat treatment for 100 h at 1500°C.

2.2 Processing methods of Nb-Si alloys

The microstructure and phase morpholgies of the alloy are the major influencing parameters for obtaining the better properties. These propeties are carefully controlled by choosing proper fabrication method and corresponding parameters. Nb-Si alloys require complex shaping techniques to be used as the turbine engine blade. Several fabrication processes such as non consumable tungsten electrode arc melting (AM), ingot casting and thermomechanical processing [*M.G. Mendiratta, J.J. Lewandowski et al., 1991*], plasma arc melting, induction skull melting, directional solidification (DS) [*N. Sekido et al., 2006*], investment casting, powder metallurgy (PM) [*R.M. Nekkanti et al., 1990*] and physical vapour deposition (PVD) have been reportedly used. Each processing method provides different microstrutures with different phase chemistries.

The investment casting method is not well developed due to the reactivity of the liquid Nb-alloy which limits the use of ceramic based melting systems. The powder metallurgy route may result in higher impurities in the alloy. The good microstructural control by the cooperative growth of the phases (Nb_{ss} and silicide) reported in directionally solidified alloys are quite encouraging [*N. Sekido et al., 2006*]. The arc melting of the alloys followed by thermomechanical processing also reportedly exhibited good fracture toughness and microstructural features compared to PM and DS at room temperature [*B.P. Bewlay et al., 1995, W.Y. Kim et al., 2002*]. Further,

improvement in the mechanical properties and microstructure with stable phases can be attained with long term heat treatment of the alloys.

2.3 Microstructural phases and their contribution in the properties of the Nb-Si alloys

As mentioned in section 2.1, Nb-Si alloys comprise of Nb_{ss} and silicide (Nb_3Si and/or α-Nb_5Si_3) phases. The silicide phase is brittle and is intended to provide the high temperature strength, creep and oxidation resistance. The Nb_{ss} phase is ductile and intended for room temperature fracture toughness [*B.P. Bewlay et al., 2003*]. This approach of increasing fracture resistance in brittle material (silicide phase) by the ductile phase (Nb_{ss}) is called "Ductile phase tougheneing" [*K.S. Chan* et al.,*2002, W.Y. Kim et al., 2002 M.G. Mendiratta, J.J. Lewandowski et al., 1991*]. This improves the materials resistance against the crack extension. The ductile phase toughnening in brittle materials can be initiated by two methods. The first method is the introduction of ductile particles or layers using traditional composite fabrication procedures like vacuum hot processing. These are called ex-situ composites as obtained through phase mixing (example:WC/Co cermets, Ti_3Al/Ti). In the second method, the metallic phase forms in-situ (examples: Nb_{ss}/Nb_5Si_3, $Nb_{ss}/NbCr_2$) in the microstructure when the alloy is made. The two phase microstructure in Nb-Si alloys formed through composition control resembles microstructure of ductile phase toughnened composites obtained by phase mixing [*K.S. Chan, 2018*]. So the Nb-Si alloys are called 'Nb-silicide in-situ composites' and are termed as the same in further discussion. The metallic phase in these in-situ composites microstructure is stable even at higher temperatures as compared to ex-situ composites.

The strength of the composites increases with the volume fraction of the silicide phase [*B.P. Bewlay et al., 2003*, *W.Y. Kim et al., 2002, C. L. Ma et al., 2004*]. Whereas, the high volume fraction of the Nb_{ss} phase imparts good fracture toughness [*C. L. Ma et al., 2004*]. The coarse morphology along with the continuous Nb_{ss} phase can further enhance the fracture toughness of the composites [*C. L. Ma et al., 2004, N. Sekido et al., 2006*]. In addition, the lamellar arrangement of the Nb_{ss} phase can further improve the fracture toughness of the alloy [*N. Sekido et al., 2004*]. On the other hand, high silicide phase fraction is beneficial for high temperature strength and creep resistance. It is also to be noted that the α-Nb_5Si_3 gives good high temperature strength and creep

resistance compared to other silicides [*B.P. Bewlay et al., 2003*] and the microstructure containing Nb_{ss}/α-Nb_5Si_3 phases is reported to be stable [*B.P. Bewlay et al., 2003*, *W.Y. Kim et al., 2002*]. Further, the presence of silicide phase in coarse morphology can deteriorate the fracture toughness of the composites. According to the Nb-Si phase diagram (**Fig. 2.1**), the volume fraction of Nb_{ss} phase decreases from 70% to 22% and silicide (Nb_5Si_3) phase increases from 30% to 72%, respectively with increasing Si content from 10 to 22 at.% [*B.P. Bewlay, H.A.Lipsitt. M.R. Jackson et al., 1995*]. Therefore, the fracture toughness of the alloy decreases with increasing Si content and the strength increases as shown in the **Fig. 2.4(a)** and **Fig. 2.4(b)** respectively. Further, the intrinsic properties of the phases like hardness, elastic modulus and work of rupture also has effect on the properties of the composites. So the type of phases, volume fraction of the phases, microstructural features like morphology, size and distribution along with the intrinsic properties of the phases are needed to be controlled to obtain better combination of both room temperature fracture toughness and high temperature strength/creep resistance. This aspect is called 'microstructural design' and is shown in the **Fig. 2.5**. It is also to be noted that these parameters have interdependant effect on the mechanical properties of the composites. Alloying is an effective approach to have proper control over the phases, microstructure and properties of these alloys.

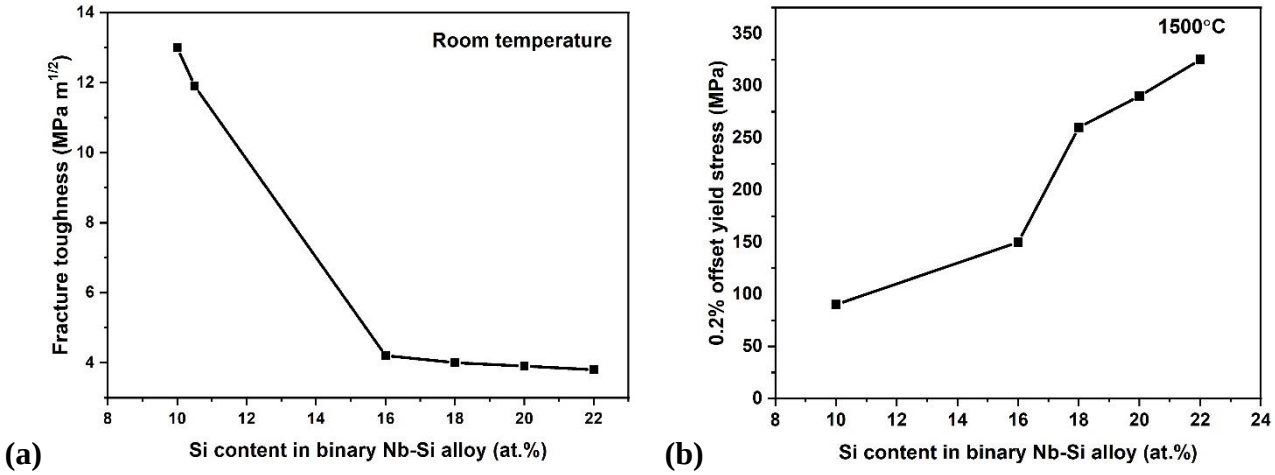

Fig. 2.4: The variation in the mechanical properties of the Nb-Si in-situ composites with Si content. (a) Room temperature fracture toughness [*W.Y. Kim et al., 2001*] and (b) High temperature yield strength [*W.Y. Kim et al., 2002*].

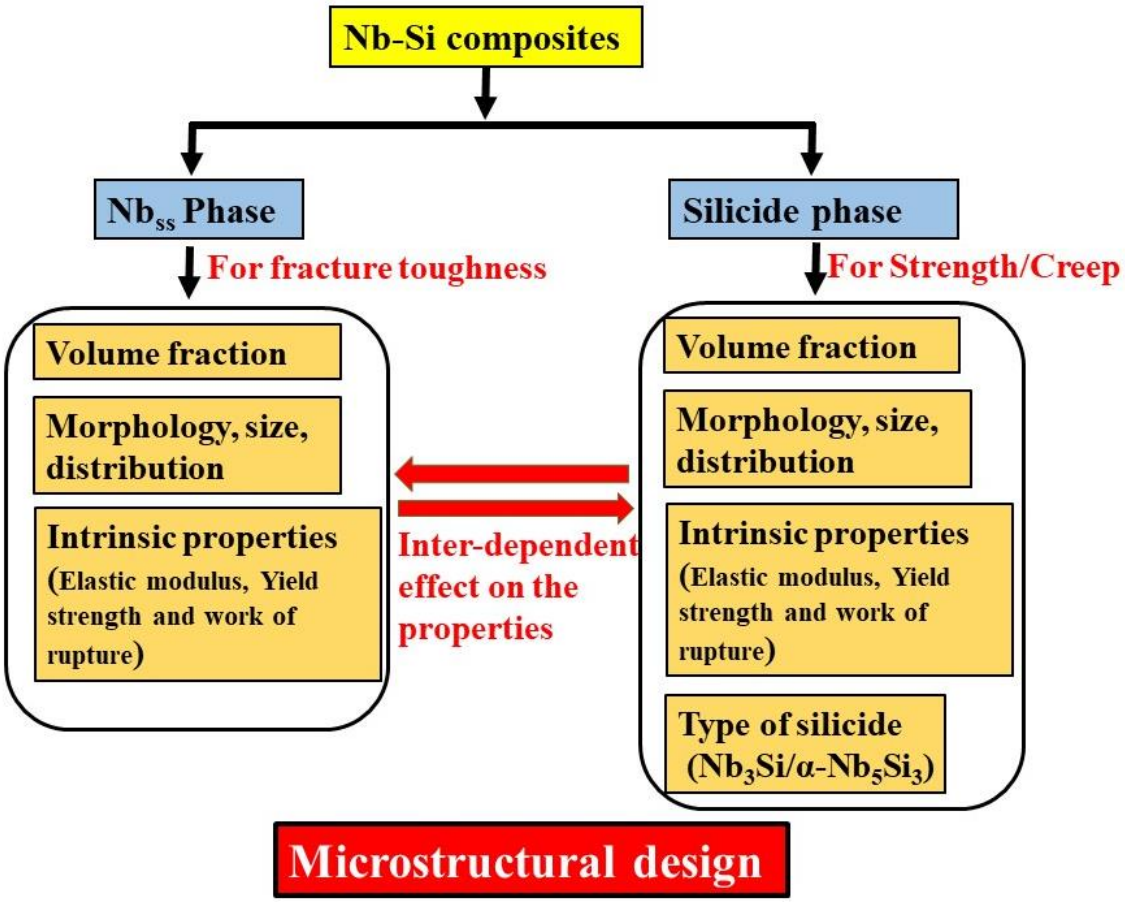

Fig. 2.5: Microstructural design for the combination of better properties in the Nb-Si alloys.

2.4 Mechanism of eutectoid transformation and importance

As mentioned in section 2.1, the Nb-Si in-situ composites exhibit Nb_{ss} and Nb_3Si phases (through eutectic reaction) in the as cast condition and stable Nb_{ss} and α-Nb_5Si_3 phases will form with further heat treatment (through eutectoid reaction). The evolution of phases and microstructure in the alloys is shown schematically in the **Fig. 2.6.** Primarily, the Nb_{ss}/Nb_3Si phases form as eutectic cells from the liquid phase of the alloys through eutectic solidification (eq. 1), as shown in the **Figs. 2.6(a, b)**. At this stage the microstructure consists of Nb_{ss} dispersoid in the matrix of Nb_3Si phase. The Nb_{ss} phase in the same eutectic cell has the same crystallographic orientation. The eutectoid transformation gets initiated at the interface of the euetctic Nb_{ss} and Nb_3Si phases during further heat treatment (**Figs. 2.6(c, d)**). First eutectoid Nb_{ss} forms at the interface of Nb_{ss}/Nb_3Si phases and the α-Nb_5Si_3 phase formation occurs in lamellar manner due to

lack of Nb at the adjacent regions (**Fig. 2.6(d)**). The formed Nb_{ss} here is termed as eutectoid Nb_{ss}. In this process, eutectoid Nb_{ss} will have same crystallographic orienation with that of the eutectic phase. Consequently, a continuous Nb_{ss} forms (**Fig. 2.6(e)**). Further the eutectoid phases grows and spheroidization of α-Nb_5Si_3 occurs, as shown in the **Figs. 2.6(e. f)**. The final microstructure consists of α-Nb_5Si_3 phase in the form of spheroids in a network of Nb_{ss} phase or vice versa.

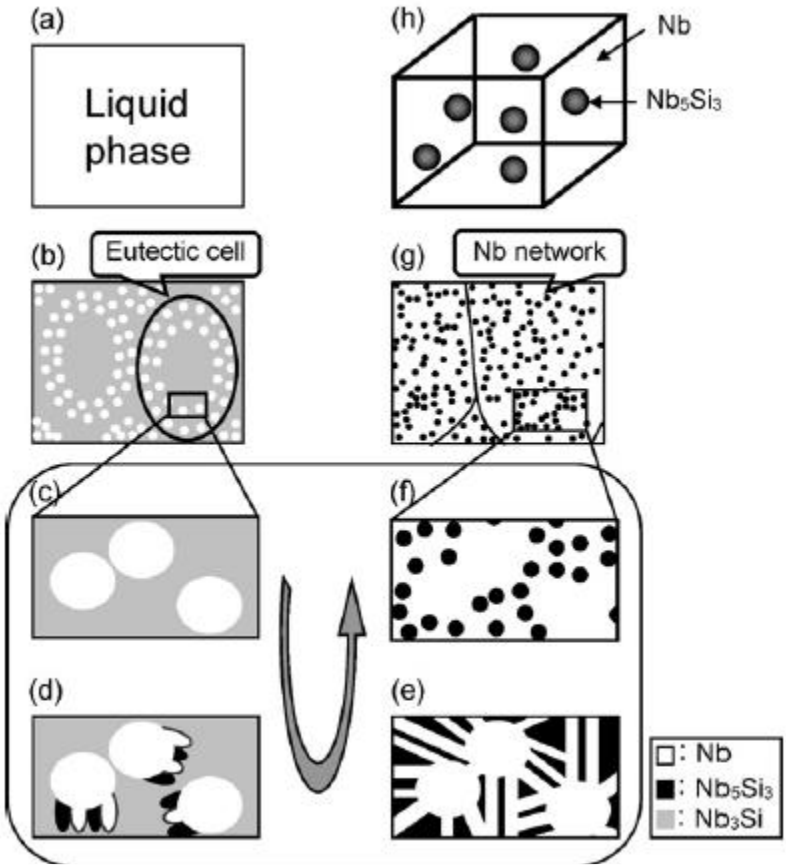

Fig. 2.6: The schematic diagram showing the microstructure evolution from liquid phase in hypoeutectic and eutectic alloys [*S. Miura et al., 2009*]. (a) liquid phase to (b) eutectic cell (Nb_{ss}/Nb_3Si) as the results of eutectic solidification followed by eutectoid reaction and spheroidization shown in (c)-(f) resulting in the Nb-network with fine Nb_5Si_3 dispersions ((g) and (f)).

The eutectoid transformation phenomena described above takes place in case of hypo eutectic and eutectic composition alloys. Whereas, in hyper eutectic composition alloys, the primary β-Nb_5Si_3 phase is expected along with the eutectic Nb_{ss}/Nb_3Si. Theerefore, primary β-Nb_5Si_3 phase can also act as the nucleation site for the eutectoid transformation in the hyper eutectic alloys along with the interface of the eutectic Nb_{ss}/Nb_3Si phases. In this case, the formed eutectoid α-Nb_5Si_3 and the primary β-Nb_5Si_3 phases have same crystallographic orientation.

If the eutectic Nb_{ss}/Nb_3Si interface acts as nucleating site for the eutectoid transformation then a particular orientation relationship (OR) is maintained between the eutectoid phases, i.e., Nb_{ss} and α–Nb_5Si_3 phases, as given below (OR1) [*S. Miura et al., 2005, S. Drawin et al., 2005*]. If the primary β-Nb_5Si_3 phase acts as the nucleating site for the eutectoid transformation then the formed eutectoid phases Nb_{ss} and α–Nb_5Si_3 have certain orientation relationship as mentioned in OR2 [*S. Muira et al., 2005*].

$<201>_{Nb}//<010>_{\alpha\text{-}Nb5Si3}$ and $(011)_{Nb}//(110)_{\alpha\text{–}Nb5Si3}$ OR1

$<201>_{Nb}//<010>_{\alpha\text{-}Nb5Si3}$ and $(001)_{Nb}//(001)_{\alpha\text{–}Nb5Si3}$ OR2

The necessary silicide phase, i.e., α-Nb_5Si_3 for good high temperature properties is achieved only after the long hours (100 h) of heat treatment at high temperatures (1500°C). As these alloys are prone to oxidation, the heat treatment can be done only in the vacuum atmosphere. The heat treatment at such a high temperatures for long duration in vacuum is really challenging for these alloys development.

2.5 Effect of alloying elements on the phase formation, microstructure and mechanical properties of the Nb-Si alloy

The recent studies on Nb-Si alloys have resulted into multi-component systems to achieve a balance between mechanical properties and environmental resistance. It is very crucial to know the effect of addition of individual alloying elements to produce a multi-component system in order to obtain better combination of properties. As part of this, effect of various alloying elements like Ti, Hf, Zr, Sn, Al, Cr, Mo, W, V, Ge, Mg and Ga on the phase stability and microstructure of the Nb-Si alloys has been reported in the literature. The summary of earlier work results on the phase

stability with addition of alloying elements is given in **Tables 2.1** to **2.4**. It has been reported that the addition of Mo, W, Mg, Al, Ge, Sn, Ga and Cr elements form β-Nb_5Si_3 and Nb_{ss} phases with or without Nb_3Si phase in cast alloys and it is irrespective of the Si content in the alloy. However, Ti, Hf, Zr and Fe additions reported to result in the Nb_3Si and Nb_{ss} phase in the cast alloys. The addition of Cr, Sn and Hf are reported to form Laves phase-$NbCr_2$, Nb_3Sn and HfO_2 phases, respectively along with the Nb_{ss} and silicide (Nb_3Si/Nb_5Si_3) phases. The addition of Fe reported to form new silicide Nb_4FeSi phase. However, the addition of more number of alloying elemets in higher fractions reported to reduced the formation of α–Nb_5Si_3 phase and instead stabilize the β and γ-Nb_5Si_3 silicide phases in the cast alloys. Further, these phases reported to remain stable even after long term heat treatments. The effect of each alloying element on the phase formation, microstructure and mechanical properties of Nb-Si alloys is discussed below in detail.

2.5.1 Effect of Ti

Ti is a more commonly used high temperature metal and has lower density (4.5 g/cm^3) compared to Nb (8.4 g/cm^3). The solubility of Ti in Nb is reported to be high [*S. Miura et al., 2009, B.P. Bewlay, M.R. Jackson et al., 1995, E. Guo et al., 2017*]. Therefore, over the years, alloys based on Nb-Si-Ti system have been widely studied. The effect of 2-40 at.% Ti addition on the microstructure and phase formation of the Nb-Si alloys of different Si contents is reported in the open literature (see **Table 2.1)**. It is reported to have no effect on the phase formation of the cast Nb-Si binary alloys, but coarsening of the ductile Nb_{ss} phase is reported. The addition of 10 at.% Ti stated to increase the eutectoid transformation kinetics during heat treatment of the Nb-18.7Si alloy [*N. Sekido et al., 2004*]. However, the higher addition (>25 at.%) is reported to stabilize the Nb_3Si phase to lower temperatures and this decreases the melting temperature of the alloy [*B.P. Bewlay et al., 1995*]. Further, alloying with higher amount of Ti (>22 at.%) addition can associate with compositional segregation, which causes stabilization of undesirable γ-Nb_5Si_3 phase in the alloys (**Table 2.1**) [*Y.X. Tian, J.T. Guo , L.Y. Sheng et al., 2008, E. Gu et al., 2017*].

The Ti addition on the fracture toughness values of the alloys is shown in the bar graph **Fig. 2.7** and also presented in **Table 2.2**. An increment in the fracture toughness value of the alloys is reported with Ti (**Table 2.2**). The addition of 10 at.%Ti to Nb-17.5Si reported to improve the toughness value from 14.5 MPa.m$^{1/2}$ to 18.7 MPa.m$^{1/2}$ in the alloy prepared through directional

solidification (**Fig. 2.7**). A drastic enhancement in the fracture toughness of the arc melted Nb-18.7Si alloy from 3.4 MPa.m$^{1/2}$ to 10.3 MPa.m$^{1/2}$ is reported with 10Ti addition [*N. Sekido et al., 2004 and 2006*]. The improvement in the fracture toughness by 50% (9.8-12.4 MPa.m$^{1/2}$) with Ti addition (21-33%Ti) to binary Nb-16Si (8 MPa.m$^{1/2}$) is also reported (**Fig. 2.7**) [*B.P. Bewlay et al., 1993*]. Nevertheless, the increase in the fracture toughness is not systematic with increase in Ti content from 21-33%Ti (**Fig. 2.7**). The addition of higher Ti of 42.5 at.%, 40 at.% to Nb-15Si and Nb-15Si-5Al has also been reported to enhance the toughness [*P.R. Subramanian et al., 1994*].

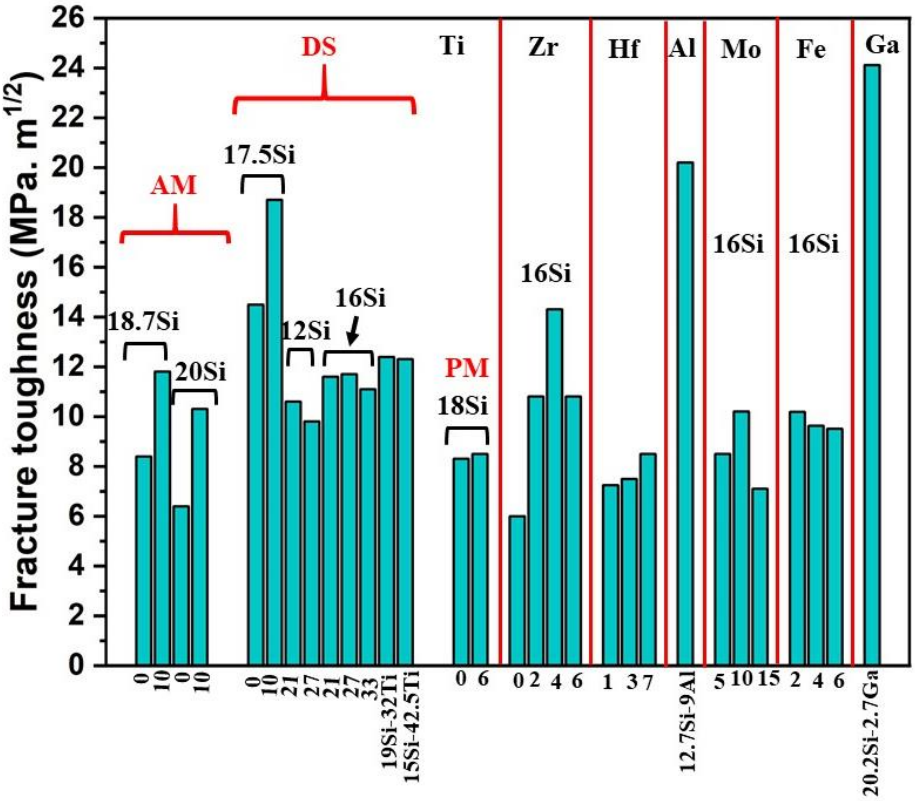

Fig. 2.7: The literature data on the fracture toughness values of the Nb-Si alloys with ternary alloying addition.

Table 2.1: The literature data on the effect of Ti additions on the phase formation of Nb-Si alloys.

S.No	Alloy composition	Alloy preperation method and heat treatment (HT)	Phases reported in the alloy		Reff
			As cast condition	**after heat treatment**	
1	Nb-XSi-YTi X= 12, 16 and Y=21,27,33	Directional Solidification	Primary Nb_{ss} and Nb_{ss}/Nb_3Si	--	*B.P. Bewlay, M.R. Jackson et al., 1995*
	Nb-XSi-YTi X=19-22,Y=21-32		Primary β-Nb_5Si_3,Nb_{ss}/Nb_3Si		
2	Nb-16Si-33Ti	Directional Solidification	Nb_{ss}/Nb_3Si	--	*B.P. Bewlay et al., 1996*
3	Nb-16Si-(3,9)Ti	Directional solidification@ HT at 1500°C for 100h	--	Primary Nb_{ss} and Nb_{ss}, Nb_3Si, α-Nb_5Si_3	*B.P. Bewlay et al., 1998*
	Nb-12Si-(21,44)Ti Nb-15Si-42.5Ti			primary Nb_{ss} and Nb_{ss}/Nb_3Si	
4	Nb-15Si-42.5Ti	Directional Solidification	Nb_{ss}/Nb_3Si		*R. J. Grylls et al., 2001*
5	Nb-18.7Si-10Ti	Arc melting@ Solution HT at 1750°C for100h +HT at 1400°C for 100h	Nb_{ss}/Nb_3Si	Nb_{ss}, α-Nb_5Si_3	*N. Sekido et al., 2004*
	Nb-20Si-10Ti		Primary β-Nb_5Si_3, Nb_{ss}/Nb_3Si	Primary α-Nb_5Si_3, Nb_{ss}, α-Nb_5Si_3	
	Nb-25Si-10Ti				
6	Nb-17.5Si-10Ti	Directional Solidification@ HT at 1400°C for 500h	Nb_{ss}/Nb_3Si	Nb_{ss},/α-Nb_5Si_3	*N. Sekido et al., 2006*
7	Nb-18Si-24Ti	VAR+ HT at 1500°C for 100h	Nb_{ss}/Nb_3Si	Nb_{ss}/Nb_3Si	*K. Zelenitsas et al., 2006*
8	Nb-17.5Si-XTi X=0, 2, 5,10	Directional solidification	Nb_{ss}/Nb_3Si	--	*N. Sekido et al., 2007*
9	Nb-XSi-6Ti (X-11,16,18)	Powder Metallurgy	Nb_{ss}/α-Nb_5Si_3	--	*Z. Li et al., 2007*
10	Nb-16Si-22Ti	Arc melting	Primary Nb_{ss} and Nb_{ss}/Nb_3Si, γ-Nb_5Si_3	--	*Y.X. Tian,J.T. Guo , L.Y. Sheng et al., 2008, E. Guo et al., 2017*
11	Nb-16Si-24Ti	Arc melting	primary Nb_{ss} and Nb_{ss}/Nb_3Si	--	*S. Qu et al., 2007, 2009*

The Ti is reported to be the solid solution softening element of the Nb_{ss} phase, i.e., the Nb_{ss} phase hardness decreases/ductility increases with increasing Ti content [*N. Sekido et.al 2004*]. It is is repoted to occupy the Nb site of both Nb_{ss} and silicide phases. The Ti element is present on the left side to the Nb position in the periodic table. So the number of d and s-shell electrons is less compared to the Nb. The replacement of the Nb sites with Ti decreases the total number of electrons. Therefore, the decrease in the electrons implies to decrease the Peierls Nobbarrow (P-N) barrier energy for the atoms movement on the slip plane. The P-N barrier energy is a direct indication of deformability of the alloy, i.e., decrease in P-N stress increases the ductility of the alloy and vice versa [*D.L. Davidson et al., 1996*]. Therefore, the P-N barrier stress decreases with Ti replacement to Nb in the Nb_{ss} phase. This behaviour of Nb_{ss} with Ti addition is also confirmed by Chan et al. due to the decrease in P-N barrier energy in the Nb_{ss} phase of Nb-Cr-Ti alloys [*K. S. Chan et al., 2002*]. Frankas et al. also reported the increase in the emmission of dislocations at the dislocation tip with Ti addition in the Nb_{ss} phase of the Nb-Ti-Al alloy [*D. Frankas et al., 1998*]. It is attributed that the lower concentration of Ti addition improves the toughness of α–Nb_5Si_3 phase, where as higher concentration (beyond 12.5 at.%) causes decrease in the toughness. This concentration sensitive effect of Ti induced by the variation of its substitutional site in α–Nb_5Si_3 phase [*S. Shi et al., 2016*].The increase in the size of the Nb_{ss} phase and ductility of both Nb_{ss} and α–Nb_5Si_3 phases with the Ti addition imparts the toughness through effective contribution in crack bridging phenomena [*N. Sekido et al., 2004 and 2006, Z. Li et al., 2007*].

The high temperature strength of the Nb-Si alloys reported to decrease with Ti addition. The strength value of 580 MPa reported to decrease to ~400 MPa at 1400˚C with 10 at.% Ti addition to Nb-17.5Si alloy. In case of Nb-18.7Si alloy, the strength decrease from 250 MPa to 100 MPa with the temperature is reported [**Table 2.3**]. This decrease in the high temperature strength of the alloys is mainly attributed to the increase in the dislocation mobility in Nb_{ss} phase [*N. Sekido et al., 2006*].

From the above discussion, the effect of Ti addition to Nb-Si alloys can be summarized as the following:

1. The addition should be limited to 25 at.% in order to avoid the stabilization of low melting point silicide phase (Nb_3Si) which exhibits poor creep properties.
2. There is no change in the phase formation of the Nb-Si alloys with Ti addition of lower concentrations, i.e., 10 at.%, whereas the formation of unstable γ-Nb_5Si_3 at higher amounts of Ti, i.e., >20 at.% (it is due to segregation).
3. The addition of Ti leads to the coarsening of the Nb_{ss} phase.
4. Addition of Ti leads to the improvement in the fracture toughness of the alloys, which is one of the major aims of the alloying additions. The increase in the size of the Nb_{ss} phase and ductility of both Nb_{ss} and α–Nb_5Si_3 phases with Ti addition causes improvement of the tougheness through effective contribution by crack bridging phenomena.
5. The high temperature strength is reported to decrease with Ti addition due to increase in the dislocation mobility in Nb_{ss} phase.

Therefore, the Ti addition should be controlled for holding the melting temperature of the alloy, to minimize the compositional segregation and to avoid γ-Nb_5Si_3 phase formation and to maintain the toughness of the α-Nb_5Si_3 phase. Most of the literature reported the effect of 10 at.% Ti and above on the microstructure and mechanical properties of the various Nb-Si alloys. Coarsening of the Nb_{ss} phase is reported with increase in Ti content from 2 to 10 at.% [*N. Sekido et al., 2004, 2006, 2007*]. However, the limited literature is available on the effect of Ti (in particular, below 10 at.%) on the mechanical properties and oxidation behaviour of the Nb-Si alloys.

Table 2.2: The literature data on the effect of alloying on the fracture toughness of the Nb-Si alloys.

Alloying	**Alloy composition**	**Processing route**	**Constituent phases**		**Method used for fracture toughness measurement**	**Fracture toughness ($MPam^{1/2}$)**		**Reff**
			Before HT	**After HT**		**Before HT**	**HT**	
Binary	**Nb-10Si**	AM+HT at 1500˚C/100h	Nb_{ss}, Nb_3Si	Nb_{ss}, α-Nb_5Si_3	Three point bend test	9.2	9.7	*M.G. Mendiratta et al., 1993*
		AM+E+HT at 1500˚C/100h	Nb_{ss}, Nb_3Si	Nb_{ss}, α-Nb_5Si_3		16.44	20.66	
	Nb-16Si	AM+HT at 1500˚C/100h	Nb_{ss}, Nb_3Si	Nb_{ss}, α-Nb_5Si_3	Three point bend test	5.40	7.35	*M.G. Mendiratta, J.J. Lewandowski et al., 1991*
		AM+E+HT at 1500˚C/100h	Nb_{ss}, Nb_3Si	Nb_{ss}, α-Nb_5Si_3		--	12.5	
		DS	Nb_{ss}+Nb_3Si	--			7.8	*B.P. Bewlay, M.R. Jackson et al.,1995*
		AM	Primary Nb_{ss}, Nb_{ss}/Nb_3Si	--	Three point bend test	5.5	--	*Y.X. Tian, J.T. Guo, L.Z. Zhouet al., 2008*
		AM	Nb_{ss}, Nb_3Si	--	Three point bend test	6.5		*Sankar et al., 2018*

	Nb-18Si	PM	Nb_{ss}, Nb_5Si_3	--	Three point bend test	8.3	--	*Z. Li et al., 2007*
	Nb-18.7Si	Arc cast+ 1400˚C/100h	Nb_{ss}, Nb_3Si	Nb_{ss}, Nb_5Si_3	Four point bend test	--	3.4	*N. Sekido et al., 2004*
	Nb-18.7Si	AM	Nb_{ss}, Nb_3Si		--	8.4	--	*N. Sekido et al., 2006*
	Nb-20Si	Arc cast+ 1400˚C/100h	Nb_{ss}, Nb_3Si, β-Nb_5Si_3	Nb_{ss}, Nb_3Si, α-Nb_5Si_3	--	--	6.4	*N. Sekido et al., 2004*
	Nb-17.5Si	DS,10mm/hr+ 1500˚C/500hr	Nb_{ss},Nb_3Si	Nb_{ss},Nb_3Si	Four point bend test	14.5	--	*N. Sekido et al., 2006*
Ti	**Nb-17.5Si-10Ti**	DS,10mm/hr+ 1400˚C/500hr	Nb_{ss},Nb_3Si	Nb_{ss}, α-Nb_5Si_3		15.4	18.7	
	Nb-18Si-6Ti	PM	Nb_{ss}, Nb_5Si_3 $(Nb,Ti)_5Si_3$,	--	Three point bend test	8.5	--	*Z. Li et al., 2007*
	Nb-18.7Si-10Ti	Arc cast+ 1400˚C/100h	Nb_{ss}, Nb_3Si	Nb_{ss}, α-Nb_5Si_3	Four point bend test	--	11.8	*N. Sekido et al., 2004*
	Nb-20Si-10Ti		Nb_{ss}, Nb_3Si	Nb_{ss}, α-Nb_5Si_3		--	10.3	
	Nb-16Si-33Ti	DS	$(Nb,Ti)_{ss}$, $(Nb,Ti)_3Si$	--	Three point bend test	11.1	--	*B.P. Bewlay, M.R. Jackson et al., 1995*
	Nb-16Si-27Ti					11.7	--	
	Nb-12Si-27Ti					9.8	--	
	Nb-16Si-21Ti					11.6	--	
	Nb-12Si-21Ti					10.6	--	
	Nb-19Si-32Ti		$(Nb,Ti)_{ss}$, $(Nb,Ti)_3Si$, $(Nb,Ti)_5Si_3$			12.4	--	

	Nb-15Si-42.5Ti		$(Nb,Ti)_{ss}$, $(Nb,Ti)_3Si$			12.3		P.R. subramanian et al., 1994
	Nb-15Si-40Ti-5Al		$(Nb,Ti)_{ss}$, $(Nb,Ti)_3Si$, $(Nb,Ti)_5Si_3$			19.5		
Zr	**Nb-16Si-2Zr**	AM	Nb_{ss}, Nb_3Si, γ-Nb_5Si_3	--	Three point bend test	10.8	--	*M. Sankar et al., 2019*
	Nb-16Si-4Zr		Nb_{ss}, α-Nb_5Si_3	--		14.3	--	
	Nb-16Si-6Zr		Nb_{ss}, α-Nb_5Si_3, γ-Nb_5Si_3	--		10.8	--	
	Nb-15Si-22Ti-5Cr-3Hf-3Al	AM	Nb_{ss}, Nb_3Si, γ-Nb_5Si_3	--	Three point bend test	11.94	--	*Y. Qiao et al., 2017*
	Nb-15Si-22Ti -5Cr-3Hf-3Al-2Zr			--		12.89	--	
	Nb-15Si-22Ti -5Cr-3Hf-3Al-4Zr			--		13.73	--	
	Nb-15Si-22Ti -5Cr-3Hf-3Al-8Zr			--		15.01	--	
Hf	**Nb-16Si-1Hf**	AM	Primary Nb_{ss}, Nb_{ss}/Nb_3Si		Three point bend test	7.25	--	*Y.X. Tian, J.T. Gio, L.Z. Zhou et al., 2008*
	Nb-16Si-3Hf					7.5	--	
	Nb-16Si-7Hf					8.5	--	

Al	**Nb-12.7Si-9Al**	Suction casting	Primary β–Nb_5Si_3, Nb_{ss}/β–Nb_5Si_3		Indentation method	20.2	--	*S. Kashyap et al., 2013*
Mo	**Nb-16Si-5Mo**	AM	Nb_{ss}, α-Nb_5Si_3		Three point bend test	8.5	--	*W.Y. Kim et al., 2001*
	Nb-16Si-15Mo		Nb_{ss}, α-Nb_5Si_3			10.2	--	
	Nb-18Si-10Mo	DS+1300˚C/100h	Nb_{ss}, Nb_5Si_3	Nb_{ss}, Nb_5Si_3	Three point bend test	7.1	7.8	*Y. Li et al., 2011*
Fe	**Nb-16Si-2Fe**	AM +HT 1350˚C/100h	Nb_{ss}, Nb_3Si, Nb_4FeSi	Nb_{ss}, Nb_3Si, Nb_4FeSi	Three point bend test	9.37	10.19	*J.R. Zhou et al., 2013*
	Nb-16Si-4Fe					9.03	9.63	
	Nb-16Si-6Fe					9.66	9.51	
	Nb-16Si-22Ti-2Hf-2Al-2Cr-1Fe	AM +HT 1350˚C/100h	Nb_{ss}, α,γ-Nb_5Si_3	Nb_{ss}, α,γ-Nb_5Si_3	Three point bend test	12.8	13.6	*S.M. Zhang et al., 2015*
	Nb-16Si-22Ti-2Hf-2Al-2Cr-2Fe		Nb_{ss}, α,γ-Nb_5Si_3	Nb_{ss}, α,γ-Nb_5Si_3, Nb_4FeSi		11.6	13.3	
	Nb-16Si-22Ti-2Hf-2Al-2Cr-4Fe		Nb_{ss}, α,γ-Nb_5Si_3, Nb_4FeSi	Nb_{ss}, α,γ-Nb_5Si_3, Nb_4FeSi		10.2	10.9	
	Nb-16Si-22Ti-2Hf-2Al-2Cr-6Fe		Nb_{ss}, Nb_4FeSi	Nb_{ss}, Nb_4FeSi		8	7.9	
Ga	**Nb-18.79Si**	Vacuum suction casting	Nb_{ss}, Nb_3Si			9.2		*S. Kashyap et al., 2011*
	Nb-20.2Si-2.7Ga		Nb_{ss}, β-Nb_5Si_3			24.11		

	Nb-18Si-10Mo-0.1Ga	DS+1300˚C/100h	Nb_{ss}, Nb_5Si_3	Nb_{ss}, Nb_5Si_3	Three point bend test	9.3	12	*Y. Li et al., 2011*
	Nb-18Si-10Mo-1Ga					6.6	10.5	
V	**Nb-15Si-24Ti-4Cr-2Al-2Hf**	DS+1450˚C/12h	Nb_{ss}, α, γ-Nb_5Si_3	Nb_{ss}, α, γ-Nb_5Si_3	Three point bend test	--	9.87	*Y.Gu et al., 2017*
	Nb-15Si-24Ti-4Cr-2Al-2Hf-1V		Nb_{ss}, α, γ-Nb_5Si_3	Nb_{ss}, α, γ-Nb_5Si_3		--	12.98	
Cr & V	**Nb-16Si-20Ti-3Al-2Hf-6Cr-4V**	AM	Nb_{ss}, β-Nb_5Si_3	--	Three point bend test	9.9		*Y. Kang et al., 2012*
	Nb-16Si-20Ti-3Al-2Hf-3Cr-4V		Nb_{ss}, β-Nb_5Si_3	--		14		
	Nb-16Si-20Ti-3Al-2Hf-6Cr-2V		Nb_{ss}, β, α-Nb_5Si_3	--		11.13		
	Nb-16Si-20Ti-3Al-2Hf-3Cr-2V		Nb_{ss}, α-Nb_5Si_3	--		14.72		

2.5.2 Effect of Zr

The Zr belongs to the same group as Ti. But the solubility of Zr is very low or almost negligible in Nb. The addition of Zr in a range of 1.5 to 6 at.% in the cast binary alloys is investigated by various authors [*S. Miura et al., 2005, 2009* and *M. Sankar et al., 2018*]. The addition of 1.5 at.% has reported to have no effect on the phase formation in Nb-25Si cast alloy. However, an increase in the eutectoid transformation kinetics is evidenced [*S. Miura et al., 2005*]. The time and temperature of the transformation got reduced significantly from 100 h duration at 1400°C for binary alloy to below 10 h with 1.5 at.% Zr. Similarly, the time has been reduced to within 4 h of heat treatment at 1700°C in Nb-18.1Si-1.5Zr alloy (**Table 2.4**) [*Miura et al., 2009*]. The very recent work reported the effect of addition of 2, 4, 6 at.% Zr on the phase formation and room temperature mechanical properties of the hypo eutectic Nb-16Si alloy [*M. Sankar et al., 2018*]. The formation of the eutectic Nb_{ss}/Nb_3Si phases is observed with 2 at.% Zr addition. Interestingly, when the Zr concentration is fixed at 4 at.%, direct formation of α-Nb_5Si_3 phase along with Nb_{ss} phase in the cast structure is noticeable. This is beneficial from processing point of view in reducing the time and cost by eliminating the need for long term vacumm heat treatment at higher temperatures. Further increase in Zr level to 6% reported with the formation of brittle γ-Nb_5Si_3 phase along with beneficial Nb_{ss}/α-Nb_5Si_3 phases. The required and stable phases formation in the cast Nb-16Si-4Zr alloy is due to the increase in the eutectoid transformation kinetics because of the change in interfacial energy (as a result of the segregation of Zr) at the interface between the Nb_3Si and Nb_{ss} phases. The addition of Zr also reported to coarsen the Nb_{ss} phase. The Zr occupies the Nb position in Nb_3Si, Nb_5Si_3 and Nb_{ss} phases. Further, the solubility of Zr is higher in Nb_5Si_3 phase compared to the Nb_{ss}, Nb_3Si phases [*M. Sankar et al., 2018*].

Table. 2.3: The literature data on the compressive strength, strain at both room temperature and high temperatures of the Nb-Si alloys.

Alloying element	**Alloy composition**	**Compressive yield strength (MPa)**		**Compressive strength (MPa)**		**Plastic strain (%)**		Reff
		RT	**High temp**	**RT**	**High temp**	**RT**	**High Temp**	
Ti	**Nb-17.5Si**	1800	580 (1400˚C) ~1350 (1200˚C)	--	--	--	--	*N. Sekido et al., 2006*
	Nb-17.5Si-10Ti	~1350	~400 (1400˚C) ~1480 (1200˚C)	--	--	--	--	
	Nb-18.7Si	~1600	~250 (1400˚C)	--	--	--	--	*N. Sekido et al., 2004*
	Nb-18.7Si-10Ti	~1400	~100 (1400˚C) 450 (1200˚C) 750 (1000˚C)	--	--	--	--	
	Nb-20Si-10Ti	~1250	~100 (1400˚C) 450 (1200˚C) 750 (1000˚C)	--	--	--	--	
	Nb-25Si-10Ti	~1350	300 (1400˚C) 500 (1200˚C) 950 (1000˚C)	--	--	--	--	
Zr	**Nb-18.1Si-1.5Zr doped with Mg**	--	--	1500	500 (1200°C)	1.5	10	*Miura et al, 2009*

	Nb-16Si-22Ti	1565	347 (1200˚C)	--	--	15.5	--	*Y.X. Tian,J.T. Guo , L.Y. Shenget al., 2008*
	Nb-16Si-22Ti-1Zr	1595	336 (1200˚C)	--	--	17.5	--	
	Nb-16Si-22Ti-2Zr	1700	305 (1200˚C)	--	--	17.8	--	
	Nb-16Si-22Ti-3Zr	1750	290 (1200˚C)	--	--	18	--	
	Nb-16Si-22Ti-4Zr	1775	305 (1200˚C)	--	--	16.5	--	
Mo	**Nb-16Si**	--	150 (1500˚C)	--	--	--	--	*W. Y. Kim et al., 2001, 2002*
	Nb-16Si-5Mo	--	250 (1500˚C)	--	--	--	--	
	Nb-16Si-15Mo	--	330 (1500˚C)	--	--	--	--	
	Nb-16Si-25Mo	--	310 (1500˚C)	--	--	--	--	
	Nb-18Si-5Mo	--	290 (1500˚C)	--	--	--	--	
	Nb-18Si-15Mo	--	390 (1500˚C)	--	--	--	--	
	Nb-22Si	--	325 (1500˚C)	--	--	--	--	
	Nb-22Si-5Mo	--	290 (1500˚C)	--	--	--	--	
	Nb-22Si-15Mo	--	375 (1500˚C)	--	--	--	--	
	Nb-22Si-25Mo	--	460 (1500˚C)	--	--	--	--	
	Nb-16Si	--	255 (1200˚C)	1850	--	--	--	*C.L. Ma et al., 2004*
	Nb-16Si-5Mo	--	140 (1227˚C)	1625	175 (1227˚C)	--	--	
	Nb-16Si-10Mo	--	210 (1227˚C)	1900	260 (1227˚C)	--	--	
	Nb-16Si-15Mo	--	310 (1227˚C)	2250	375 (1227˚C)	--	--	
	Nb-10Si-11.5Mo	1331	193 (1500°C)	--	--	--	--	
	Nb-20Si-7.8Mo	1600	265 (1500°C)	--	--	--	--	
	Nb-25Si-6Mo	1763	349 (1500°C)	--	--	--	--	

	Nb-30Si-4Mo	1895	473 (1500°C)	--	--	--	--	
W	**Nb-16Si-5W**	--	200 (1500°C)	1750	250 (1500°C)	--		*C.L. Ma et al., 2004*
	Nb-16Si-10W	--	390 (1500°C)	1850	450 (1500°C)	--		
	Nb-16Si-15W	--	520 (1500°C)	2100	610 (1500°C)	--		
	Nb-16Si-20W	--	--	2250	710 (1500°C)	--		
	Nb-10Si-11.5W	--	--	1399	270 (1500°C)	--		
	Nb-10Si-7.8W	--	--	1800	538 (1500°C)	--		
Al	**Nb-18.7Si**	--	--	550	1250 (700°C) 1200 (600˚C)	2	3 (700˚C) 4.5 (600˚C)	*S. Kashyap et al., 2013*
	Nb-12.7Si-9Al	--	--	900	1700 (700°C) 1600 (600˚C)	6	5.5 (700˚C) 5.6 (600˚C)	
	Nb-17.5So-10Mo	--	--	--	450 (1200˚C) 250 (1200˚C)	-		*Y. Li et al., 2011*
	Nb-17.5Si-10Mo-3Al	--	---	--	620 (1250˚C) 520 (1350˚C)	--		
Fe	**Nb-16Si-2Fe**	1430	479 (1250˚C) 295 (1350˚C)			--		*J.R. Zhou et al., 2013*
	Nb-16Si-4Fe	1500	425 (1250˚C) 251 (1350˚C)			--		
	Nb-16Si-6Fe	1600	385 (1250˚C) 251 (1350˚C)			--		
	Nb-18Si-5Mo-5Hf-2C			330-448	460 (1200˚C) 310 (1300˚C) 240 (1400˚C) 100 (1500˚C)	0.3	0.8 37 45 72	*J.H. Kim et al., 2003*

Table 2.4: The literature data on the effect various alloying additions on the phase formation of Nb-Si alloys.

S.No	Alloy composition	Alloy preperation method and heat treatment (HT)	Phases reported		Reff
			As cast	After heat treatment (HT)	
1	Nb-25Si-1.5Zr	VAR + 1100°C-1650°C/3-100h	primary Nb_5Si_3, Nb_{ss}/Nb_3Si	primary Nb_5Si_3, Nb_{ss}/Nb_5Si_3	*S. Miura et al., 2005*
2	Nb-18.1Si-1.5Zr	VAR + 1650-4h	Nb_{ss}/Nb_3Si	Nb_{ss}/Nb_5Si_3	*S. Miura et al., 2009*
3	Nb-16Si-2Zr	AC	Nb_{ss}, Nb_3Si, γ-Nb_5Si_3		*M. Sankar et al., 2018*
	Nb-16Si-4Zr		Nb_{ss}, α-Nb_5Si_3		
	Nb-16Si-6Zr		Nb_{ss}, α, γ-Nb_5Si_3		
4	Nb-16Si-24Ti	AM	Nb_{ss}, Nb_3Si, γ-Nb_5Si_3		*Y.X. Tian, J.T. Guo, L.Y. Sheng et al., 2008*
	Nb-16Si-24Ti-1Zr				
	Nb-16Si-24Ti-2Zr				
	Nb-16Si-24Ti-3Zr				
	Nb-16Si-24Ti-4Zr				
5	Nb-XSi-YMo (X>18), (y=5,15,20)		Primary β-Nb_5Si_3, Nb_{ss}/β-Nb_5Si_3	Primary α-Nb_5Si_3, Nb_{ss}/α-Nb_5Si_3	*W.Y Kim et al., 2001*
6	Nb-19.1Si-5.2Mo Nb-17.9Si-26.3Mo	VAR	Primary α-Nb_5Si_3, Nb_{ss}/ α-Nb_5Si_3		*K. Chattopadhyay et al., 2006*
7	Nb-12.8Si-4.1Mo Nb-12.3Si-14.8Mo		Primary Nb_{ss}, Nb_{ss}/α-Nb_5Si_3		

8	Nb-16Si-XMo (X= 5, 10,15)	VAR	Primary Nb_{ss}, Nb_{ss}/ β-Nb_5Si_3	Primary Nb_{ss}, Nb_{ss}/ α-Nb_5Si_3	*C.L. Ma et al., 2004*
9	Nb-16Si-XW (X=5,10,15)	VAR	Primary Nb_{ss}, Nb_{ss}/ β-Nb_5Si_3	Primary Nb_{ss}, Nb_{ss}/α-Nb_5Si_3	*C.L. Ma et al., 2004*
10	Nb-16Si-XHf (X=0,1,3,7)	VAR	Primary Nb_{ss}, Nb_{ss}/Nb_3Si		*Y.X. Tian, J.T. Guo, L.Z. Zhou et al., 2008*
11	Nb-16Si-2Hf	Arc melting	primary Nb_{ss}, Nb_{ss}/Nb_3Si		*S. Qu et al., 2007*
20	Nb-15.7Si-3Mg	Suction casting	Primary Nb_{ss} Nb_{ss}/ Nb_3Si, $Nb_{11}Si_4$	--	*C.S. Tiwary et al., 2013*
21	Nb-18Si-XCr (X= 15, 25, 33)	VAR	Nb_5Si_3, Nb, Cr_2Nb, $Nb_9(Cr,Si)_5$		*B.P. Bewlay et al., 2009*
22	Nb-16Si-6Cr	Arc melting	Nb_{ss}, Nb_5Si_3		*S. Qu et al., 2007*
23	Nb-18Si-XGe (X=5,10)	VAR + heat treated at 1500^{O}C-100h	β-Nb_5Si_3, Nb_{ss}/β-Nb_5Si_3	α,β- Nb_5Si_3, Nb_{ss}/ β-Nb_5Si_3	*L. Zifu et al., 2010*
24	Nb-18Si-5Sn	VAR+ heat treated at 1500°C/100h	primary α,β,γ-Nb_5Si_3, Nb_3Sn and Nb_{ss}/Nb_5Si_3	primary α,β-Nb_5Si_3, Nb_3Sn and Nb_{ss}/Nb_5Si_3	*N. Vellios et al., 2007*
25	Nb-20.2Si-2.7Ga	Suction casting	Primary β-Nb_5Si_3 , Nb_{ss}+β-Nb_5Si_3,$Nb_{11}Si_4$		*S. Kashyap et al., 2011*
26	Nb-12.3Si-9Al	Suction casting	Primary Nbss, Nb_{ss}+β-Nb_5Si_3		*S. Kashyap et al., 2013*
27	Nb-16Si-6Al	Arc melting	Nb_{ss}, Nb_5Si_3		*S. Qu et al., 2007*
28	Nb-16Si-xFe (x=2, 4, 6 at.%)	Arc melting+ HT at 1350ºC/ 100h	Nb_{ss}, Nb_3Si, Nb_4FeSi	Nb_{ss}, Nb_3Si, Nb_4FeSi	*J.R. Zhou et al., 2013*

32	Nb-18Si-24Ti	AC+HT at 1500ºC/100h	Nb_{ss}, Nb_3Si	Nb_{ss}, Nb_3Si	*K. Zelenitas et al., 2005*
33	Nb-18Si-24Ti-5Cr		Nb_{ss}, Nb_3Si, α-Nb_5Si_3, $NbCr_2$	Nb_{ss} α-Nb_5Si_3	
34	Nb-18Si-24Ti-5Al		Nb_{ss} β-Nb_5Si_3	Nb_{ss} α-Nb_5Si_3	
35	Nb-18Si-24Ti-5Cr-5Al		Nb_{ss}, β-Nb_5Si_3, Cr_2Nb,TiN	Nb_{ss}, α,β-Nb_5Si_3, Cr_2Nb,TiN	
36	Nb-18Si-24Ti-8Cr-4Al		Nb_{ss}, β-Nb_5Si_3, Cr_2Nb	Nb_{ss}, α,β-Nb_5Si_3, Cr_2Nb	
37	Nb-18Si-24Ti-5Cr-5Al-6Ta	AC+HT at 1500ºC/100h	Nb_{ss}, β-Nb_5Si_3	Nb_{ss}, α,β-Nb_5Si_3	K. Zelenitas et al., 2006
38	Nb-18Si-24Ti-8ACr-4Al-6Ta		Nb_{ss}, β-Nb_5Si_3, Cr_2Nb	Nb_{ss}, α,β-Nb_5Si_3 Cr_2Nb	
39	Nb-18Si-5Al-5Cr-5Mo	AC+HT at 1500ºC/200h	Nb_{ss},Nb_3Si, β-Nb_5Si_3, $NbCr_2$	Nb_{ss}, α-Nb_5Si_3	J. Geng et al., 2006
40	Nb-18Si-24Ti-5Al-5Cr-5Mo		Nb_{ss},Nb_3Si, β-Nb_5Si_3	Nb_{ss},α-Nb_5Si_3, β-Nb_5Si_3	
41	Nb-18Si-24Ti-5Cr-5Al-2Mo	AC+HT at 1500ºC/100h	Nb_{ss}, Nb_3Si, β-Nb_5Si_3	Nb_{ss},β-Nb_5Si_3, α-Nb_5Si_3	
42	Nb-18Si-24Ti-5Cr-5Al-2Mo-5Sn	AC+HT at 1500ºC/100h	Nb_{ss}, β-Nb_5Si_3, Cr_2Nb	Nb_{ss}, α,β,γ-Nb_5Si_3, Cr_2Nb	*J. Geng et al., 2007*
43	Nb-18Si-24Ti-5Cr-5Al-5Hf-2Mo	AC+HT at 1500ºC/100h	Nb_{ss}, β-Nb_5Si_3, γ-Nb_5Si_3, Cr_2Nb	Nb_{ss}, α,β,γ-Nb_5Si_3	*J. Geng et al., 2007*

44	Nb-18Si-24Ti-5Cr-5Al-5Hf-5Sn	AC+HT at 1500ºC/100h	Nb_{ss}, β-Nb_5Si_3, γ-Nb_5Si_3, Cr_2Nb	Nb_{ss}, β-Nb_5Si_3, γ-Nb_5Si_3, Cr_2Nb	
45	Nb-18Si-24Ti-5Al-5Cr-2Mo-5Hf-5Sn	AC+HT at 1500ºC/100h	Nb_{ss}, β,γ-Nb_5Si_3, Cr_2Nb	Nb_{ss}, β,γ-Nb_5Si_3, Cr_2Nb	*J. Geng et al., 2007 (270)*
46	Nb-18Si-24Ti-5Fe-5Sn	AC+HT/1200ºC/100h	Nb_{ss}, Nb_3Sn, Nb_3Si, α,β,γ-Nb_5Si_3, $FeNb_4Si$, Fe_2Nb_3	Nb_{ss}, Nb_3Sn, Nb_3Si, α,β,γ-Nb_5Si_3, $FeNb_4Si$, Fe_2Nb_3	*N. Vellios, P.Tsakiropoulos et al., 2007*
47	Nb-15Si-45Ti-5Fe-5Sn		Nb_{ss}, β-Nb_5Si_3, Nb_3Si, Ti_5Si_3, β-Ti_{ss}, Nb_3Sn	Nb_{ss}, Nb_3Si, α,β,γ-Nb_5Si_3 Nb_3Sn, Ti_5Si_3, Ti_3Si, β-Ti_{ss}	
48	Nb-18Si-5Sn	AC+HT 1200ºC/100h	Nb_{ss}, α,β,γ -Nb_5Si_3, Nb_3Sn	Nb_{ss}, α,β,γ -Nb_5Si_3, Nb_3Sn	*N. Vellios, P.Tsakiropoulos et al., 2007, (1518)*
49	Nb-18Si-24Ti-5Sn		Nb_{ss}, α,β,γ -Nb_5Si_3, Nb_3Sn	Nb_{ss}, α,γ -Nb_5Si_3, Nb_3Sn	
50	Nb-18Si-24Ti-5Cr-5Fe	AC+HT/1200ºC/100h	Nb_{ss}, α,β,γ -Nb_5Si_3, Nb_3Si, $FeNb_4Si$	Nb_{ss}, α,β,γ -Nb_5Si_3 $FeNb_4Si$	*N. Vellios et al., 2010*
51	Nb-18Si-24Ti-5Cr-5Sn		Nb_{ss}, α,β-Nb_5Si_3, Nb_3Si, Nb_3Sn, $FeNb_4Si$, Fe_7Nb_6	Nb_{ss}, α,β-Nb_5Si_3, Nb_3Si, Nb_3Sn, $FeNb_4Si$, β-Ti_{ss}	
52	Nb-18Si-5Hf				
53	Nb-18Si-5Hf-5Cr	AC+HT/1500ºC/100h	Nb_{ss}, Nb_3Si, α,β-Nb_5Si_3,HfO2	Nb_{ss}, Nb_3Si, α,β,γ-Nb_5Si_3,HfO_2	*I. Grammenos et al., 2010*
54	Nb-18Si-5Hf-5Al		Nb_{ss}, Nb_3Si, α,β-Nb_5Si_3,HfO2	Nb_{ss}, Nb_3Si, α,β,γ-Nb_5Si_3,HfO_2	*I. Grammenos et al., 2010*

55	Nb-18Si-5Hf-24Ti		Nb_{ss}, Nb_3Si, α,β-Nb_5Si_3	Nb_{ss}, Nb_3Si, α,β,γ-Nb_5Si_3,HfO_2, TiN	
56	Nb-18Si-5Hf-3Ta-2Mo	AC+HT/1500ºC/100h	Nb_{ss}, α,β-Nb_5Si_3, Nb_3Si,HfO_2	Nb_{ss}, α,β-Nb_5Si_3, Nb_3Si,HfO_2	*I.Grammenos et al., 2010 (1524)*
57	Nb-20Si-5Hf-5W	AC+HT/1500ºC/100h	Nb_{ss}, α,β,γ-Nb_5Si_3, Nb_3Si,HfO_2	Nb_{ss},Nb_3Si, α,β-Nb_5Si_3, Nb_3Si,HfO_2	*I.Grammenos et al., 2011*
58	Nb-20Si-5Mo-3W		Nb_{ss}, α,β-Nb_5Si_3, Nb_3Si	Nb_{ss}, α,β,γ-Nb_5Si_3, Nb_3Si	
59	Nb-20Si-5Hf-5Mo-3W		Nb_{ss}, Nb_3Si, α,β,γ-Nb_5Si_3, HfO_2	Nb_{ss}, Nb_3Si, α,β,γ-Nb_5Si_3, HfO_2	
60	Nb-18Si-24Ti-8B	AC+HT at 1500ºC/100h	Nb_{ss}, Nb_3Si, B rich Nb_3Si	Nb_{ss}, Nb_3Si , B rich Nb_3Si, TiN	*T. Thandorn et al., 2010*
61	Nb-18Si-5Ge-5Al	AC+HT at 1500ºC/100h	Nb_{ss}, β-Nb_5Si_3	Nb_{ss}, α,β-Nb_5Si_3	*L. Zifu et al., 2013*
62	Nb-18Si-5Ge-5Al-24Ti		Nb_{ss}, β-Nb_5Si_3	Nb_{ss}, α,β-Nb_5Si_3	
63	Nb-18Si-24Ti-5Ge	AC+HT at 1500ºC/100h	Nb_{ss}, Nb_3Si, β,γ-Nb_5Si_3	Nb_{ss}, Nb_3Si, α, β-Nb_5Si_3, TiO_2	*L. Zifu et al., 2011*
64	Nb-18Si-5Al-Hf		Nb_{ss}, β,γ-Nb_5Si_3	Nb_{ss}, β,γ-Nb_5Si_3	*J. Nelson et al., 2018*
65	Nb-18Si-24Ti-5Al-5Cr-5Hf		Nb_{ss}, β-Nb_5Si_3	Nb_{ss}, β-Nb_5Si_3	
66	Nb-18Si-24Ti-5Al-5Sn	AC+HT at 1500ºC/100h	Nb_{ss}, α,β-Nb_5Si_3, Nb_3Sn, $NbCr_2$	Nb_{ss}, α-Nb_5Si_3, Nb_3Sn, $NbCr_2$	*Z. Xu et al., 2020*
67	Nb-18Si-24Ti-5Cr-5Sn		Nb_{ss}, β-Nb_5Si_3, Nb_3Sn	α-Nb_5Si_3, Nb_3Sn	
78	Nb-18Si-24Ti-5Al-5Cr-5Sn		β-Nb_5Si_3, Nb_3Sn	Nb_{ss}, α-Nb_5Si_3, Nb_3Sn, $NbCr_2$	

69	Nb-18Si-24Ti-5Ge-5Al-5Cr	AC+HT at 1400ºC/100h	Nb_{ss}, β-Nb_5Si_3, $NbCr_2$	Nb_{ss}, α,β-Nb_5Si_3	*Z. Li et al., 2019*
70	Nb-18Si-24Ti-5Ge-5Al-5Cr-5Hf		Nb_{ss}, β,γ-Nb_5Si_3, HfO_2	Nb_{ss}, α,β,γ-Nb_5Si_3, $NbCr_2$	
71	Nb-18Si-12Ti-6Ta-2.5W-1Hf-2Sn-2Ge	AC+HT at 1500ºC/100h	Nb_{ss}, Nb_3Si, α,β-Nb_5Si_3, HfO_2	Nb_{ss}, α,β-Nb_5Si_3, HfO_2, TiO_2	*J. Zhao et al., 2020*
72	Nb-18Si-12Ti-6Ta-2.5W-1Hf-5Sn-5Ge		Nb_{ss}, Nb_3Si, α,β-Nb_5Si_3, Nb_3Sn, Nb_3Ge, HfO_2, TiO_2	Nb_{ss}, α,β-Nb_5Si_3, Nb_3Sn, Nb_3Ge, HfO_2	

The increase in the room temperature strength and fracture toughness of the alloy is reported with Zr addition (**Fig. 2.7, Table 2.2, 2.3**) [*Y.X. Tian, J.T. Guo, L.Y. Sheng et al., 2008, M. Sankar et al., 2019*]. Usually the mechanical properties will be measured after heat treatment of the alloys as it results in the formation of stable and required Nb_{ss}, α-Nb_5Si_3 phases. But the maximum fracture toughness value of 14.3±0.3 MPa.$m^{1/2}$ is noted in the cast Nb-16Si-4Zr alloy (**Fig. 2.7, Table 2.2**). The increase in the volume fraction and coarsesing of the Nb_{ss} phase along with the formation of α-Nb_5Si_3 phase have resulted in increase in the fracture toughness with 4Zr addition as compared to 2Zr. Further increase in the Zr content to 6% reportedly decreased the toughness (**Fig. 2.7, Table 2.2**) due to the formation of hard and brittle γ-Nb_5Si_3 phase along with decrease in the fraction of Nb_{ss} phase [*M. Sankar et al., 2019*].

The increase in the strength value to 1500 MPa with plastic strain of 1.5% is reported with 1.5Zr addition to Nb-25Si alloy [*S. Miura et al., 2009*]. Further, the high temperature strength and plastic strain of 500 MPa and 10% or more, respectively are reported at a strain rate of 1×10^{-4} s^{-1} for the Nb-18.1Si-1.5Zr alloy (**Table. 2.3**). The presence of fine α-Nb_5Si_3 particles as a result of network arrangement of Nb_{ss} phase attributed for this increase in the high temperature strength of the alloy. The room temperature strength values of 1795±67 MPa, 2159±79 MPa and 1960±50 MPa is reported with the 2, 4 and 6% Zr addition to Nb-16Si cast alloys, respectively (**Table. 2.2**) [*M. Sankar et al., 2019*]. The maximum strength is observed with the Nb-16Si-4Zr and it is due to the formation of Nb_{ss} and α–Nb_5Si_3 phases in the microstructure. Further, the 2Zr and 4Zr additions to Nb-16Si reported to decrease the the strength because of the formation of Nb_3Si phase instead of α–Nb_5Si_3 and γ–Nb_5Si_3 along with α–Nb_5Si_3 phase. The hardness of the Nb_{ss} and Nb_3Si phases in the alloy reportedly decreased with Zr concentration.

The effect of Zr on Nb-Si alloys can be summerized as below:

1. It can enhance the eutectoid transformation kinetics of the alloy by decreasing both the transformation time and temperature which results in the reduction of the duration of heat treatment for eutectoid transformation.
2. Further, appropriate amount of Zr addition can result in the formation of required silicide phase, i.e., α–Nb_5Si_3 in the cast alloys itself, thereby eliminating the need for long term heat treatments for eutectoid transformation.

3. The phase formation and mechanical properties of the Nb-Si alloys are strongly dependent on the Zr content in the alloy.
4. Addition of Zr appears to result in decrease the hardness of both the Nb_{ss} and α–Nb_5Si_3 phases. The fracture toughness of the alloys has been enhanced by decreased hardness as well as coarsening of Nb_{ss} phase.

The literature review reveals that the addition of 4 at.% Zr results in the Nb_{ss}/α–Nb_5Si_3 phases in the cast alloys with improved fracture toughness. Whereas, further increase in Zr content to 6 at.% leads to undesirable γ-Nb_5Si_3 phase along with Nb_{ss}/α–Nb_5Si_3 phases. However, no reported data is available on the effect of 5 at.% Zr addition. Hence, it is of great interest to understand the effect of 5% Zr on the microstructure and properties of the alloys.

2.5.3 Effect of combined addition of Ti and Zr

In view of the above mentioned beneficial effects of both Ti and Zr on the microstructure, fracture toughness and strength of the alloys, it is essential to know the beneficial effect Ti and Zr together.

The addition of lower Zr content (0-4 at.%) to ternary higher Ti containing alloy, i.e., Nb-16Si-22Ti alloy is reported to stabilize the γ–Nb_5Si_3 phase along with eutectic Nb_{ss}/Nb_3Si phases. This is due to the segregation of Ti and Zr in to the last liquid during solidification (**Table 2.4**) [*Y.X. Tian, J.T. Guo, L.Y. Sheng et al., 2008*]. The fraction of γ–Nb_5Si_3 phase increased with increase in the Zr content in the alloy. Further, the change in the microstructure from anomalous to lamellar morphology is also reported with increase in Zr content. The high temperature strength of the alloy has been recorded to drop from 348 to 290 MPa with increasing Zr from 0% to 3% (**Table 2.3**) due to accelerated diffusion. It is because of increasing number of interfaces as a result of the increase in the lamellar morphology in the microstructure. The low melting point of the Zr also reported to cause the reduction in the high temperature strength of the alloy. The strength further increased with 4% Zr due to coarsening in the lamellar morphology and formation of more γ–Nb_5Si_3.

Therefore, it is expected that moderate amount of Ti and Zr together may eliminate formation of undesirable γ–Nb_5Si_3 while retaining their individual beneficial effects.

2.5.4 Effect of Mo and W

Both Mo and W are same group elements in the periodic table and their addition has been reported to show similar effect on the microstructure and properties of Nb-Si alloys. Various Mo levels, i.e., nearly about 5-20 at.% addition to Nb-XSi (X=10, 16, 18, 20, 22) and W levels, i.e., 5, 10, 15, 20 at.% addition to Nb-16Si alloy is reported in the open literature (**Table 2.4)** [*W.Y. Kim et al., 2001 C.L. Ma et al.,2004*]. The Mo/W addition to Nb-Si alloys reported to favour the formation of β-Nb_5Si_3 phase and inhibits the formation of intermediate Nb_3Si phase. As a result,the eutectic Nb_{ss}/β–Nb_5Si_3 phases forms in the cast alloys (**Table. 2.4**) [*W.Y.Kim et al., 2001, K. Chattopadhyay et al.,2006, C.L. Ma et al., 2004*]. The refinement in the microstructure is also noticed with W and Mo addition [*C.L. Ma et al., 2004, K. Chattopadhyay etal., 2007*]. Both Mo and W occupy the Nb position of Nb_5Si_3 phase. The Nb_{ss} phase has reported to have higher solubility than in the Nb_5Si_3 phase [*C.L. Ma et al., 2004,K. Chattopadhyay etal., 2007*].

Low Mo containing alloys (Nb-xSi-5Mo, where x=5,10, 16, 18, 22) reported to exhibit higher fracture toughness and lower high temperature strength as compared to the high Mo containing Nb-xSi-15Mo (where x=5,10, 16, 18, 22) alloys. This is due to the solid solution strenghtening effect of Mo on the Nb_{ss} phase [*W.Y. Kim et al., 2001, C.L. Ma et al., 2004*]. The solid solution strenghtening reported to be high with W and Mo addition and it retained even at very high temperatures [*W.Y. Kim et al., 2002, C.L. Ma* et al., *2004*]. This is in contrast to the solid solution strengthening effect of Si which is effective relatively at lower temperatures [*C.L. Ma et al., 2004*]. So the increase in the Mo and W content has negative influence on the room temperature fracture toughness and benificial effect on the high temperature strength. The elastic modulus of the alloy also reported to increase with Mo addition owing to the increase in the melting point of the alloy [*K. Chattopadhyay et al., 2006*].

Among the above mentioned Mo added alloy compositions, the Nb-18Si-5Mo alloy demonstrated optimum fracture toughness at room temperature (10.5 $MPa.m^{1/2}$) together with high temperature strength (200 MPa at 1500°C) (**Fig. 2.7, Table 2.2 and 2.3**). The improvement in fracture toughness is due to the maize like arrangement of Nb_{ss} phase. Such structure makes the

crack propagation more difficult even though the strength of Nb_{ss} phase is improved when compared to the Nb_{ss} phase in the binary alloy [*W.Y. Kim et al., 2002*].

The Nb-Si alloys microstructure exhibit brittle silicide matrix and ductile Nb_{ss} phase as reinfircement. Hence, it is called as brittle-ductile type microstructure. The hypoeutectic Mo added and low W (5 at.%) added alloys are ductile-brittle (ductile matrix and brittle reinforcing phase) type instead of brittle-ductile type (brittle matrix and ductile reinforcing phase). This microstructural change from brittle-ductile to ductile-brittle type can lessen the negative effect of Mo and W on the deformability [*C.L. Ma et al., 2004*].

In summary the addition of Mo and W results in,

1. β-Nb_5Si_3 phase formation in cast alloys intead of Nb_3Si.
2. Increasing in the hardness of Nb_{ss} phase which is retained even at very high temperatures.
3. Proper amont of addition gives good combination of fracture toughness and high temperature strength.
4. Among the various compositions, i.e., Nb-XSi-YMo (where X=10, 16, 18, 20, 22, Y=5, 10, 15, 20), the near eutectic Nb-18Si-5Mo alloys are proved to give better combination of properties due to the continuous and maze like Nb_{ss} morphology in the microstructure along with ductile matrix and brittle reinforcement in the microstructure (ductile-brittle type microstructure).

2.5.5 Effect of Hf

Hf belongs to the same group as Ti in the periodic table and exhibits same crystal structure (HCP). So the effect of Hf on Nb-Si alloys is expected to be the same as that of Ti. The Hf addition of 1-7 at.% to Nb-16Si alloy is reported to have no effect on the phases formation in the cast condition [*Y.X. Tian,J.T. Guo, L.Z. Zhouet al., 2008, S. Qu et.al 2008*]. However, It is reported to increase the ductility of the Nb_{ss} phase like Ti by reducing the peierl's nabarro barrier energy (**Table. 2.2**) [*K.S. Chan et al., 2002, K.S. Chan, Mater. Sci. Eng. A 329–331 (2002) 513–522, P. Zheng et al., 2008, Y.X. Tian, J.T. Guo, L.Z. Zhou et al., 2008*]. The increase in the primary Nb_{ss} phase fraction and decrease in the fine eutectic Nb_{ss}/Nb_3Si mixture with increase in Hf addition from 0% to 7% is reported to cause the improvement in the fracture toughness (**Fig. 2.7**). However,

higher addition (when Hf>3 at.%) is reported to stabilize hafnium oxide HfO_2 phase in the cast alloys causing reduction in the fracture toughness of the alloy [*Y.X. Tian, J.T. Guo, L.Z. Zhou et al., 2008, S. Qu et al., 2007*].

2.5.6 Effect of Al and Cr

The addition of Al is reported to supress the Nb_3Si and promote the Nb_{ss}/β-Nb_5Si_3 phase formation in the cast Nb-12Si-9Al alloy (**Table 2.4**) [*S. Kashyap et al., 2013*]. It is reported to improve the strength at both room and high temperatures (up to 700°C) due to relatively coarser primary silicide phase and fine eutectic compared to the binary alloys (**Table 2.3)** [*S. Kashyap et al., 2013, Y. Li et al., 2011*].

Addition of Cr (Nb-18Si-xCr, x=15-33 at.%) is supposedly stabilize the $Nb_9(Cr,Si)_5$ silicide and brittle Laves phase ($NbCr_2$) along with the Nb_{ss} phase [*B.P. Bewlay et al., 2009, P. Maji et al., 2017*]. However, the addition of Cr is reported to have adverse effect on the fracture toughness of Nb-Si alloys due to stabilization of high brittle Laves $NbCr_2$ phase [*B.P. Bewlay et al., 2009*]. Nevertheless, the fracture toughness of the alloy has been reported to increase wih 9Al addition to Nb-12Si alloy which is due to the rapid solidification process that followed for alloy preperation (**Fig. 2.7, Table 2.2**) [*S, Kashyap et al., 2013*].

2.5.7 Effect of Fe

The addition of Fe (Nb-16Si-xFe, x=2, 4, 6 at.%) to Nb-Si alloy is reported to stabilize a new phase, i.e., Nb_4FeSi along with the Nb_{ss} and Nb_3Si phases in the cast condition (**Table 2.4**). Further the Nb_4FeSi phase is stable even after heat treatment for a duration of 100 h at 1350˚C [*J.R. Zhou et al., 2013*]. It exhibits no visible influence on the fracture toughness of cast alloys. Whereas, marginal increase in the fracture toughness is reported in the heat treated samples (**Fig. 2.7, Table 2.2**). However, the addition of 1-6 at.% Fe to multicomponent Nb-Si system deteriorated the fracture toughness of the alloy (**Table 2.2**). The increase in the strength value from 1430 to 1600 MPa with 2 to 6 at.% is reported with Fe addition (**Table 2.3**). However, the yield strength at 1250˚C reportedly decreased from 479 MPa to 385MPa with increasing Fe content from 2 to 6 at.% (**Table 2.3**). In summary, the effect of Fe addition on the properties is different in binary and multi-component systems. The addition of 5 at.% is beneficial for both fracture

toughness and high temperature strength of the binary alloy. Further increase in the Fe content exhibits adverse effect on the high temperature strength of the alloys.

2.5.8 Effect of V and Ga

Gu et al. studied the effect of V on the multicomponent Nb-15Si-24Ti-4Cr-2Al-2Hf [*Y. Gu et al., 20017*]. The phases remained unaffected (Nb_{ss}, α and γ- Nb_5Si_3) with 1 at.% V addition for above mentioned alloy (**Table 2.2**). But the fracture toughness of the alloy reported to increase from 9.87 to 12.98 $MPam^{1/2}$(**Table 2.2**). This is due to the continuity in Nb_{ss} phase, decrease in the fraction of γ- Nb_5Si_3 phase and finer size of the silicide phase in V added alloy than V free alloy.

Ga addition stabilizes the β-Nb_5Si_3 phase in the cast alloys instead of high temperature Nb_3Si phase. The fracture toughness of the binary alloy improved with 2.7 at.% of Ga addition to the binary alloy (**Fig. 2.7, Table 2.2**) [*S. Kashyap et al., 2011*]. But increasing the Ga content from 0.1 at.% to 1 at.% exhibited adverse effect on the fracture toughness in the Nb-18Si-10Mo alloy (**Table 2.2**) [*Y. Li et al., 2011*].

2.5.9 Effect of Mg and Sn

Addition of 3 at.% Mg to Nb-17.5Si binary alloy lead to formation of $Nb_{11}Si_4$ silicide phase along with Nb_{ss} and Nb_3Si phases [*C.S. Tiwary et al., 2013*]. It is reported to stabilizes the Nb_{ss} and Nb_5Si_3 phases in the binary cast alloys. It is also reported for form Nb_3Sn phase can which is beneficial for the oxidation resistance in the alloy [*B.P. Bewlay et al., 2009, N. Vellios et al., 2007*].

In summary, the addition of Ti and Zr alloying elements are reported to have beneficial effect on the eutectoid transformation kinetics, fracture toughness and high temperature strength in the Nb-Si alloys. Therefore, these elements are chosen for the current study. The near eutectic composition of Nb-18.7Si is selected because of the mimimum creep rate reported at this composition [*B.P. Bewlay et al., 2001*].

2.6. Fracture bahaviour of the Nb-Nb silicide in-situ composites

As mentioned earlier, the ductile Nb_{ss} phase contributes to the fracture toughness and brittle silicide (Nb_5Si_3) phase provides the high temperature strength/creep resistance to the Nb-Si alloys. The ductile Nb_{ss} phase can enhance the toughness of the alloy by two ways, such as intrinsic and extrinsic toughnening mechanisms. Intrinsic toughnening mechanism attributes to the initiation toughness in the alloys. The in-situ resistance of the microstructure which is the material property such as phase distribution, spacing, size and morphology of the ductile phase are the contributing factors for the intrinsic toughnening mechanism. For example, the toughness can be enhanced by changing the nature, distribution and/or interface properties of Nb_{ss} phase particles to suppress damage in the form of microcracking or microvoid formation ahead of the crack tip. Extrinsic toughening mechanism indicates the microstructure behind of the crack tip to effectively decrease the crack driving force. This improves the fracture properties by providing alternative crack propagation paths or reducing the driving force for crack propegation through various processes that shield the crack tip from applied stresses such as crack branching, deflection, and bridging phenomena.

Therefore, introducing ductile Nb_{ss} phase to impart the fracture toughness to the alloy is called ‘ductile phase toughening’. Contrarily, the hard intermetallic particles in the composite adversely influence the fracture toughness which is called ‘brittle phase embrittlement’. The ductile phase toughening effect needs to be improved and at the same time the brittle phase embrittlement effect should be controlled for achieving better toughness in the alloys. To attain this, the volume fraaction of the phases along with the microstructure should be controlled, as mentioned in the section 2.3. However, the presence of high volume fraction of the ductile Nb_{ss} phase may not always produce high fracture toughness in the Nb-Si composites. The reasons are: (i) The insufficient ductility of Nb_{ss} phase due to the reduced dislocation mobility resulting from solid solution strengthening and (ii) The high plastic constraint in the Nb_{ss} phase due to the surrounding brittle and non deformable intermetallic silicide phase (Nb_3Si/Nb_5Si_3).

The measure of the local triaxial stress state on the phase is called constraint. Therefore, the constraint forces from the surrounding brittle silicide phases results in decrease in the strain to fracture of the ductile phase. As the constraint forces increases the strain to fracture of the alloy decreases. The constraint on the Nb_{ss} phase can not be neglected and is more important because of the high brittleness of the silicide phase. The strain to fracture of the ductile phase can be increased significantly by relaxing the constraint through partial interface debonding [*M. F. Ashby et al., 1989, M. Bannister et al., 1991*]. Thus, the weak interface is beneficial in relaxing the constraint and can promote the plastic dissipation in the ductile phase.

The fracture resistance curve (R-curve) in Nb-Si in-situ composites is shown in the **Fig. 2.8(a)**. The Nb-Si alloys exhibits raising R-curve behaviour. It shows that, as the crack propagates the resistance for the further crack propagation increases. The length of the crack bridging zone is reportedly more and some amount of crack growth toughness is reported, due to the modest amount of crack bridging by Nb_{ss} phase. The raising resistance curve behaviour in Nb-Si alloys is because of the globular morphology of Nb_{ss} phase and weak interface that make the composite more conducive to crack bridging and limited inteface debonding in the Nb/Nb_5Si_3 in-situ composites [*J.D. Rigney 1996, M.G. Mediratta, J.J. Lewandowski et al., 1991*]. However, the plastic constraint of silicide phase on ductile Nb_{ss} phase is not completely avoidable due to high brittleness of the silicide phases. However, it is to be noted that the fracture toughness of the Nb-Si in-situ composites can be improved with proper control of the microstructure, intrinsic properties of the phases and the interface characterstics.

The adverse detrimental effect of high constraint is also reported in $Nb/NbCr_2$ composites. The Cr_2Nb phase fractures completely in cleavage manner in both monolithic and composite forms. Whereas, the monolithic Nb_{ss} phase is very ductile and fractures in dimple manner. In contrast Nb_{ss} fails in exclusive cleavage manner when it is in the composite form. This change in the fracture mode can be attributed to the presence of high plastic constraint in the Nb_{ss} phase as shown in the **Fig. 2.8(b)**. The $Nb/NbCr_2$ in-situ composite of Nb-36Cr-37Ti with 62 vol% Nb_{ss} and 38 vol% $NbCr_2$ phase reported to exhibit zero resistance curve/flat resistance curve. The initiation toughness of the composite is 19 $MPa.m^{1/2}$ compared to the value of 34 $MPa.m^{1/2}$ and 1.5 $MPa.m^{1/2}$ for monolithic Nb_{ss} and $NbCr_2$ phases, respectively. All of the fracture resistance in the in-situ composite comes from the initiation toughness. Fracture in the in-situ composite is almost

by cleavage, both in the Nb_{ss} and $NbCr_2$ phases. The high plastic constraint reduced the ductility and promotes fracture of ductile Nb_{ss} phase in the crack wake leading to the small bridging zone and limited fracture toughness (**Fig. 2.8(b)**). Hence, the constraint of silicide on Nb_{ss} is a major factor to be considerd while measuring the fracture toughness measuremenet of the in-situ composites.

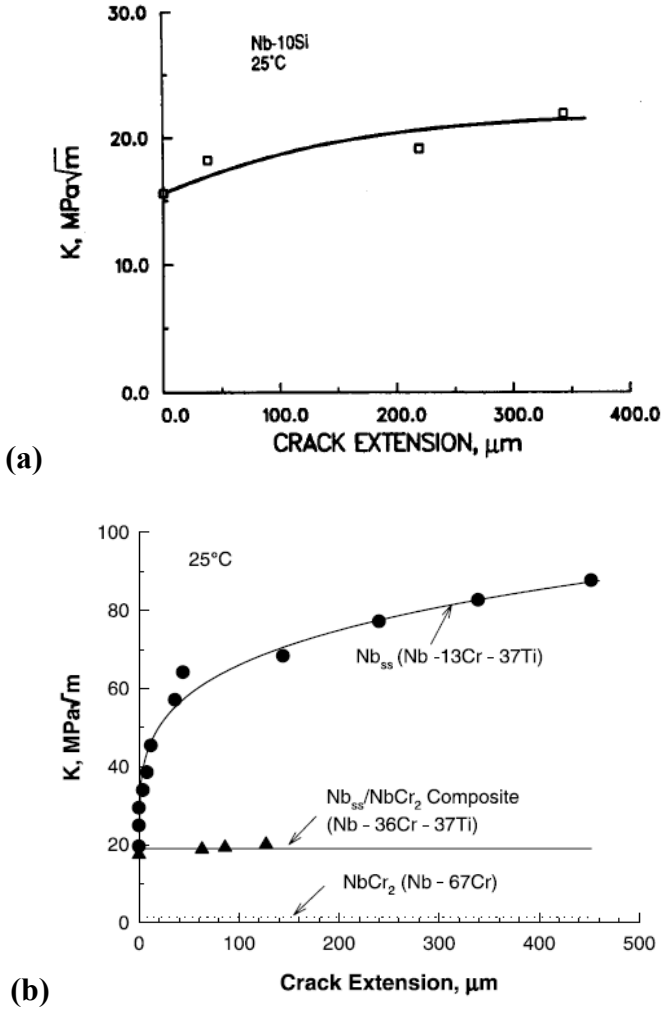

Fig. 2.8: (a) The fracture resistance curve for the Nb/Nb_5Si_3 in-situ composite, (b) Comparison of fracture resistance curve for the $Nb/NbCr_2$ in-situ composite against the Nb-solid solution alloy.

Therefore, the level of toughness enhancement is generally predicted by the amount of plastic deformation sustained in the ductile Nb_{ss} phase in the current Nb-Si alloys**.** The level of constraint in the ductile Nb_{ss} phase increases with hard intermetallic phase fraction. Therefore, delineating

the relative roles of ductile phase toughening and brittle phase embrittlement is cruicial in fracture toughness of the Nb-Si alloys. Previous studies reported that the scatter in the toughness variation with fraction of phases is substantial that it is difficult to descern the relative roles of ductile and brittle phases in fracture toughness [*K.S. Chan et al., 2001*]. The observed fracture toughness of these composites is reported to be lower than those predicted by the rule of mixtures model. This depicts the dominant role of brittle phase embrittlement compared to ductile phase toughening [*K.S. Chan et al., 2001, 2018*]. There are few proposed models for calculating the fracture toughness of the composite by considering the constraint factor of the Nb_{ss} phase and are given below.

(a). Rule of mixtures

The fracture toughness, K_C of a two phase material containing a brittle phase of toughness, K_b and a ductile phase toughness, K_d is given by

$$K_C = K_b\left[V_b + (1 - V_b)\left(\frac{K_d}{K_b}\right)^2\right]^{1/2} \text{---------} \quad \text{eq. 4}$$

(b). Constrained fracture toughness

$$K_C = K_b\left[1 + \sqrt{1 - V_b}\left(\left[\frac{K_d}{K_b}\right]^2 P_c(V_b) - 1\right)\right]^{1/2} \text{--------} \quad \text{eq. 5}$$

Where, V_b is the volume fraction of the hard phase, P_c is the plastic constraint term derived from FEM results

$$P_c(V_f) = \exp\left\{-\frac{8q'}{3}\left[\frac{V_b}{1-V_b}\right]\right\} \text{------} \quad \text{eq. 6}$$

Where q' is the indicator of the plastic constraint condition at the particle/matrix interface. The q' parameter has a value of zero when the interface is totally unbonded and has a value of unity when fully bonded and constrained plastically. $q'=1$ is assumed for Nb-silicide in-situ composites [*K.S. Chan et al., 2001, 2018]*.

So, it is of great importance to know the estimated fracture toughness calculated from the above model for comparison with the experimental values to understand the role of constraint

effect in the fracture behaviour of the Nb-Si alloys. The fracture toughness of the in-situ composites can be improved to greater values if the matrix constraint is relaxed, which in turn depends on the interface strength and the degree of debonding at the particle/matrix interface. Further understanding of the fracture behaviour and the sub-structure analysis of the fractured sample can give more insights on the constraint effect in the deformed samples.

2.7 Oxidation behaviour of the Nb-Nb silicide in-situ composites

The oxidation behaviour of the Nb-Si alloys depends on the individual oxidation response of both the Nb_{ss} and silicide (Nb_3Si/Nb_5Si_3) phases. So understanding of the oxidation behaviour of the phases is essential.

2.7.1 Oxidation of Nb and silicide phases

Oxidation of the Nb starts by dissolution of oxygen at temperature greater than 650°C and forms NbO after the maximum solubility followed by the NbO_2 formation. At this stage, the NbO_2 phase protects the nibium from oxidation. However, further exposure can leads to the formation of porus and unprotective Nb_2O_5 oxide. This transition from protective oxide to the formation of unprotective oxide at higher temperatures is called breakaway oxidation. The increase in the oxidation temperature can leads to decrease in the life of protective oxides. [*P. Kofstad, 1988*]. Further, the high residual stresses will generate at the metal-oxide interface due to the volume expansion of oxide compared to the Nb (volume of Nb-10.9 cm^3 and Nb_2O_5 is 58.3 cm^3). This leads to the spallation of the oxide layer [*O. Kubaschewski et al., 1960*]. Hence, the Nb_2O_5 oxide that forms on the surface falls off at high temperatures and no longer protects the metal [*J.T. Clenny et al.,1980*]. Thus, unlike Ni- or Fe-base alloys, the problem is not just the rapid formation of a surface oxide, but the lack of local equilibrium between the surface oxide and the substrate which is not saturate with oxygen. Even though the formation of scale may slow down the rate of internal oxidation, no real protection is afforded in the long run [*B.A. Pint et al., 2006*].

Niobium silicide (Nb_5Si_3) phase have high resistance to oxidation. However, it undergoes accelerated pest disintegration at intermediate temperatures around 700°C to 1000°C [*O. Kubaschewski et al., 1960*]. At this temperature, the exposure in air leads to the formation of niobium oxides. This causes the volume expansion. The coefficient of thermal expansion (CTE)

of Nb_2O_5 is one fourth that of Nb_5Si_3. This CTE differences between the Nb oxide and silicide phases leads to the formation of cracks in the silicide phase. The expansion of Nb phase is possible only in one direction (towards the external surface) causes shear stresses in the silicide interfaces and induces internal tensile strains in the silicide phases. The resulting tensile stresses increase up to the local critical value and pomotes the crack formation followed by propagation and finally the local rupture of the alloy. However, at higer temperatures the plastisity of the silicides allows the relaxation of stresses and prevents the cracking of silicides [*S. Mathieu et al., 2012*].

2.7.2. Oxidation of Nb-Nb silicide in-situ composites (multiphase materials)

The oxidation of the Nb-Nb silicide alloy starts with the Nb phase on the surface followed by the oxidation of silicide phase. This extends below the oxide scale and to the bulk of the alloys. Further, the alloys suffer catastrophic oxidation as explained above upon exposure to air at temperatures around 800°C [*K. Chattopadhyay et al., 2008*] and the oxides will spall off easily. The oxidation of the Nb_{ss} phase is more severe compared to the silicide phase. The increase in volume fraction of the Nb_{ss} phase increases the oxidation rate of the alloy. The oxidation resistance of the alloy can be improved by forming a long lasting protective oxide layer on the surface.

Stringer et al. reported use of alloying additions to reduce the oxidation of alloys by modifying the oxidation products. However, the formation of Nb_2O_5 a non protective oxide is too dominant to be altered by alloying additions. The subsequent studies are focused on the addition of Al to form protective alumina layer. While the formation of protective alumina layer is feasable, but the resulting alloys possess lower melting points and too brittle to be used as structural materials [*K. Zelenitsas et al., 2006, K.S. Chan et al., 2005, S. Qu et al., 2007*]. Later, the studies mostly focused on the materials that are based on niobium silicides and Laves phases ($NbCr_2$) [B.P *Bewlay, M.R. Jackson, J.C. Zhao, P.R. Subramanian et al., 2003*]. In these alloys, laves phase is intended to provide the high temperature oxidation resistance. In addition, the volume fraction of the phases, capability of the phases to form protective oxide layers play a major role in determining the oxidation resistance of the alloy. The research efforts have been directed towards the improvement of oxidation resisance of binary Nb-Si alloys by addition of different alloying elements.

2.7.3 Effect of alloying on the oxidation behaviour of Nb-Si alloys

Alloying with various elements such as Sn, Al, Cr, Ti, Hf, Ge and Ga etc. are reported to influence the oxidation beahviour of the Nb-Si alloys. The major conclusions from the literature are given below.

The addition of Sn reported to eliminate the pest phenomena by forming low melting point Sn rich compound, i.e., $NbSn_2$ at the metal-oxide interface at temperature of 815°C. However, at higher temperatures (1100°C and 1200°C) the Nb_5SiSn_2 phase formation occurs and is reported to be no longer protective. Further, the Sn addition is reported to severely impact the fracture toughness as it leads to the formation of brittle Nb_3Sn phase [*S. Knittel et al., 2014, J. Geng, P. Tsakiropoulos et al., 2007,J. Geng, P. Tsakiropoulos, G. Shao et al., 2007*].

The Nb-Si-Cr system received a considerable amount of attention due to the formation of 5-3 silicide (Nb_5Si_3) and Laves phases ($NbCr_2$) in the microstructure. The presence of Laves phase is reported to form a mixed protective and continuous oxide layer of $NbCr_2O_4$ while exposure to high temperatures. This is reported to form by the reaction between Nb_2O_5 and Cr_2O_3 phases [*K. S. Chan et al., 2004*]. Moreover, Cr is a substantial solute that interacts with oxygen more strongly than niobium, and therefore, it could act as a trap to reduce oxygen diffusivity [*K. Zelenitsas et al., 2006*] in the alloy.

The addition of Al is beneficial at high temperatures beginning at 1000°C. The Al_2O_3 particles form abundantly close to the surface of the alloy when the alloy oxidized at 1100°C. Therefore, higher content of Al is necessary to form Al_2O_3 layer which also require higher temperatures [*L. Su et al., 2017, N. Esparza et al., 2016*]. Hence, the Al addition has no beneficial effect on the oxidation below 1000°C temperatures. Both the Cr and Al additions to alloy reported to improve the oxidation resistance at low and high temperatures, respectively. However, the additions of Al and Cr should be limited to balance the negative impact on the fracture toughness of the alloy [*K. Zelenitsas et al., 2006, K.S. Chan et al., 2005, S. Qu et al., 2007, S. Zhang et al., 2015]*.

The Ti addition is reported to reduce the oxygen diffusivity in Nb. It results in the selective oxidation of Ti and formation of TiO_2 scale on the surface [*S.Y Liu et al., 2015*]. Further, it is

reportedly improved the oxidation resistance of both Nb_{ss} and silicide phases and hence the metal recession rate can be reduced [*P.R. Subramanian et al., 1994, B.P. Bewlay et al., 1996*].

Further, additions of Hf, Mo also reported to improve the oxidation behaviour to some extent. However, the improvement in the oxidation resistance of the Nb-Si alloys through alloying is not sufficient to meet the requirement for their practical application. It is imposible to achieve continuous scale of SiO_2 which could provide protection against high temperature oxidation resistance. Moreover, addition of alloying elements have deleterious effect on the mechanical properties of the alloys and also the improvement in the oxidation behaviour is not sufficient for the need of actual high temperature materials [*P. R. Subramanian et al., 1994, 1997, B. P. Bewlay et al., 1995*]. Therefore, the reqirement of high-temperature oxidation resistance of the Nb-Si alloys demanded the application of protective surface coatings, as typically done for the Ni-based superalloy turbine engine components [*S.J. Balsone et al., 2001, W. Wand et al., 2014, W.Wang et al., 2016,S. Knittel, S. Mathieu, M. Vilasi 2013, S. Knittel, S. Mathieu, L. Portebois et al., 2013*].

The protective coating should succeed to form a slow growing SiO_2 or Al_2O_3 scale to serve as a barrier against oxygen penetration and it should also be tightly adherent to the substrate. The deposition of coatings that can be dense, adherent and slow growing oxide scale offer promising approach to improve the long term environmental stability at higher temperatures. Many studies have focused on the silicon as the coating material for these alloys by various methods like hot dipping, slurry method, pack cementation etc. [*M. Z. Alam et al., 2010, L.X. Zao et al., 2007*]. Knittel et al. demonstrated the effective oxidation resistance provided by $Nb_4Fe_4Si_7$ pack silicide coatings applied on Nb and Nb-Si composites during oxidation in air at 1100°C [*S. Knittel, S. Mathieu, M. Vilasi 2013, S. Knittel, S. Mathieu, L. Portebois et al., 2013]*. The susceptability of Nb-silicides to catastropic oxidation (pesting) at moderate temperatures require carefull selection of the silicides to be deposited. This becomes a serious hinderance for practical application of the alloys. Several studies revealed that the complex type of silicides can eliminate this kind of oxidation behaviour [*S. Priceman et al., 1968, Y. Qiao et al., 2014, M.D. Novak et al., 2007, M.Z. Alam et al., 2016*]. Therefore, it is essential to develop modified silicide coatings with less micro cracks and excellent high temperature protection to the alloy [*Y.Q. Qiao et al., 2010*].

Additions of Fe and Cr to silicide coating further enhance the oxidation resistance of coatings by the formation of Fe- and Cr-oxides along with silica [*S. Priceman et al., 1968, Y. Qiao*

et al., 2014 M.D. Novak et al., 2007, M.Z. Alam et al., 2016]. Besides, the chemical compatibity of the silicide coatings with that of the substrate Nb-Si alloys is good. This can be beneficial in preventing interdiffusion of Nb and Si across the coating/substrate interface. This avoids the associated microstructural instability as well as the formation of deleterious topolologically close packed (TCP) phases during thermal exposure. Therefore, the silicide coatings can hold the potential for application on Nb-Si alloys [*S. Knittel, S. Mathieu, M. Vilasi 2013, S. Knittel, S. Mathieu, L. Portebois et al., 2013*]. The Fe-Cr modified silicide coatings are shown to provide good resistance to the Nb-based C103 (Nb-10Hf-1Ti) alloy during cyclic oxidation in air at temperatures until 1500°C [*M.Z. Alam et al., 2016*]. However, studies on the effectiveness of alloyed silicide coatings against oxidation of the Nb-Si alloys are limited in the open literature.

So, the present study is carried out to examine the cyclic oxidation behavior of uncoated and the Fe-Cr-modified slurry coated Nb-18.7Si, Nb-18.7Si-5Ti, Nb-18.7Si-5Zr and Nb-18.7Si-5Ti-5Zr alloys in air over the temperature range of 800°C-1400°C. This is to understand the effect of alloying addition and also the coating on the oxidation response of the Nb-Si alloys.

2.8 Applications of the Nb-Si alloys

The Nb-Si in-situ composites are being developed as possible hot section material in the turbine engines for application in the temperature range of 1200°C-1400°C. Both the aerospace vehicles and fossil energy power generation units works with turbine engines. The **Fig. 2.9** shows the schematic of the GE 90-115B turbine engine where the engine sucks the air from front and releases the hot air at the back [*J.-C. Zhao et al., 2003*]. This gives thrust to the engine and vehicle moves in forward direction. It consists of stationary cylindrical case (**Fig. 2.9**). Initially, the air is sucked by the rotating fan at the front and is compressed by the compressor. The pressure and temperature of the gas raises in the compressor. The compressed gas mixes with the fuel in the combustion chamber and the combustion takes place therby, the temperature and pressure of the gas raises. The high temperature, high pressure gas coming out of the combustion chamber enters to the high pressure turbine followed by low pressure turbine (LPT). Both the compressor and turbine section consists of alternating rows of vanes and blades. The vanes duct the air into appropriated directions to propell the blades. The performance and efficiency of the jet engine depends on the highest temperature in the hot section. As the gas with high temperature and high pressure enters to the high pressure turbine (HPT), the temperature of it is cruicial. Nb-Si alloys

have the potential to be used as HPT blade material in the jet engine (shown in **Fig. 2.9)**. Similarly, the Nb-Si alloys can be applied to hot section turbine blade material in the fossil energy power generation units.

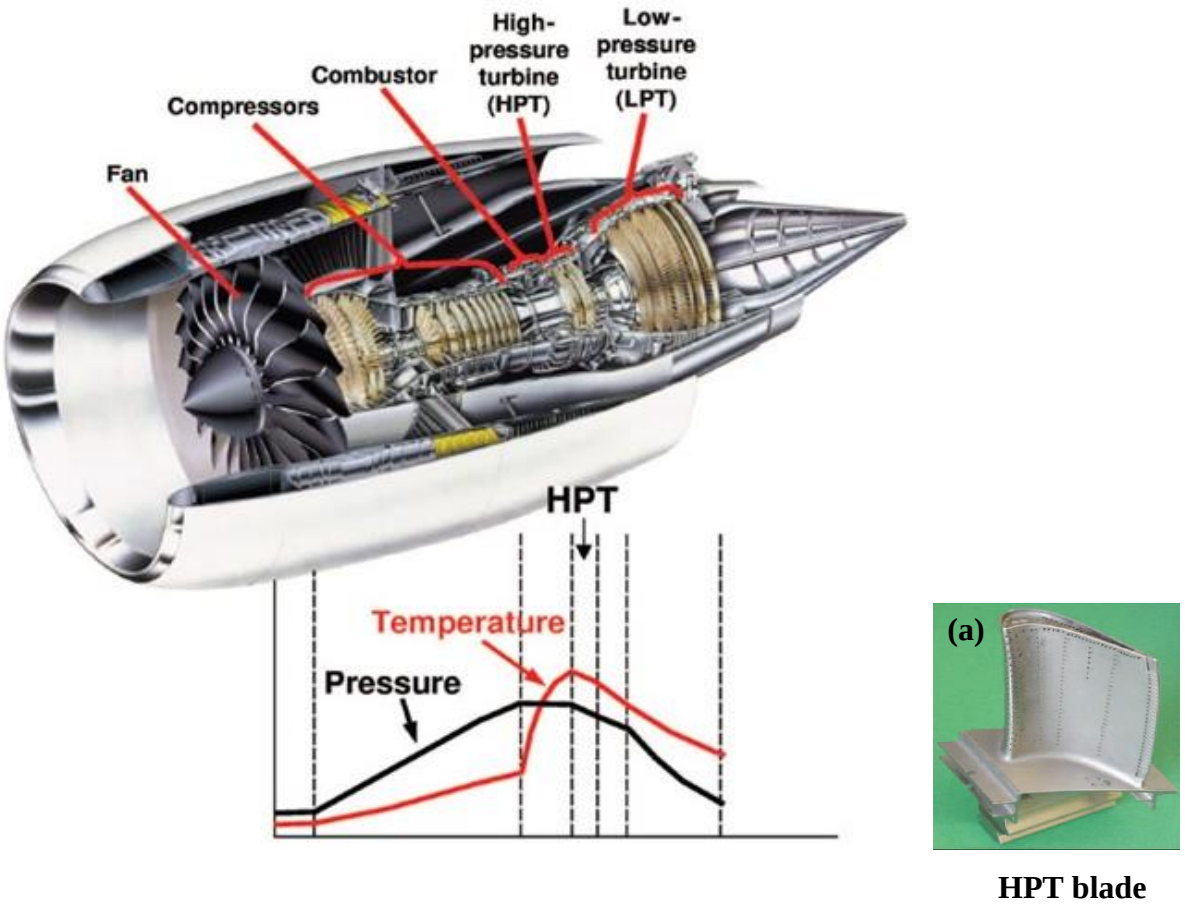

HPT blade

Fig. 2.9: The schematic of the Jet engine and the temperature, pressure profile from the front to the back of the engine and inset (a) shows the HPT blade.

Chapter-3

Experimental procedure

In this chaper, the experimental procedure and various techniques used for the microstructural characterization, mechanical properties evaluation and the high temperature cyclic oxidation tests have been discussed. The experimental procedure includes the preperation of alloy pancakes using non consumable vacuume arc remelting (VAR) followed by the microstructural characterization, room temperature mechanical properties and high temperature oxidation measurements.

The microstructural characterization of the alloys were carried out using X-Ray diffraction (XRD), scanning electron microscope (SEM) equipped with energy dispersive X-ray spectroscopy (EDXS), Electron probe microanalyzer (EPMA), Electron back scattered diffraction (EBSD) and Transmission electron microscopy (TEM) attached with energy dispersive spectroscopy (EDS) techniques. The mechanical properties were evaluated using compression test, three point bend test and nano indentation tests. Bulk indentation was also carriedout at higher loads for generating cracks inorder to understand the crack phenomena in the alloys. The failed samples in compression and three point bend tests were observed in SEM-secondary electron (SE) mode for fractography studies and also the substructure was analysed in TEM. The cyclic oxidation test for the uncoated and Fe-Cr modified slurry silicide coated samples was performed at three different temperatures, i.e., 800°C, 1200°C, 1400°C followed by the oxidation behaviour analysis through XRD, SEM, EPMA and EBSD techniques. The flow chart showing the experimental procedure was given in **Fig 1.1** and the detailed information will be presented in the following sections.

3.1 Alloy preperation by vacuum arc remelting (VAR)

High purity Nb (99.9 wt.%) peaces, Si chunks (99.999 wt.%), Ti sponge (99.99 wt.%) and Zr (99.8 wt.%) were used as raw materials and alloys were prepared using non-consumable electrode arc melting furnace (Hind High Vacuum, Banglore, **Fig. 3.1(a)**). The schematic of non consumable arc melting furnace was given in the **Fig. 3.1(b)**. The melt chamber was evacuated

twice to vacuum level of 10^{-4} mbar and refilled with 600 mbar argon gas prior to the start of the melting process. The raw materials were premixed based on the target composition and directly placed in a water cooled copper crucible cavity. The raw materials were melted by DC arc in argon atmosphere. Argon gas at 600 mbar pressure was maintained throughout the melting process.

(a)

(b)

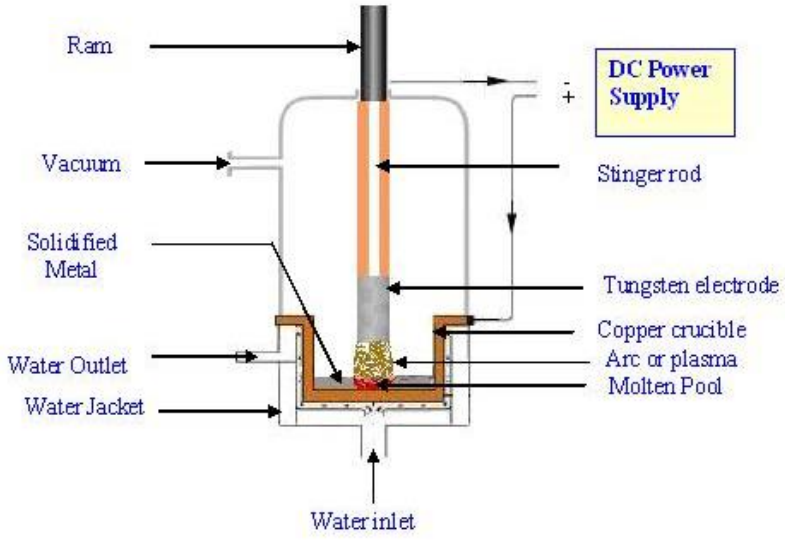

Fig. 3.1: (a) Photograph of the Vacuum arc remelting furnace and (b) Schematic diagram of the non-consumable vacuum arc melting process.

A high frequency ignition system was used to initiate the DC arc between the thoriated tungsten electrode and the charge material without any physical contact. This was done to prevent the contamination of charge material due to pick up of impurities from the electrode material. The current and voltage associated with the melting of the charge was in the range of 800-1000A and 28-32V, respectively. The liquid melt pool was stirred using a magneto stirrer for homogenization and the molten metal was allowed to solidify in a water cooled copper crucible. The solidified alloy pancake was broken into pieces and re-melted by placing in reverse direction. These steps were repeated five times to achieve compositional homogeneity. The photograph of the alloy pancakes prepared are shown in the **Fig. 3.2**. The pancakes typically measured of 80 mm in diameter and 9 mm in thickness, and each alloy pancake weighed around 320 grams. The overall weight loss of the alloys was marginal (less than 0.5 wt.%), which indicated that the composition of the solidified alloys was similar to that of the theoretical stoichiometry.

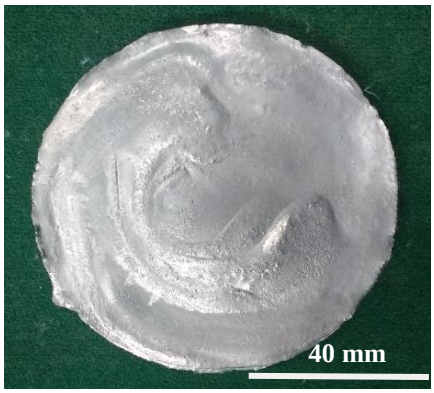

Fig. 3.2: Photograph of the pancake prepared.

3.2 Samples extraction

The samples from the pancake were extracted using wire electro-discharge machine (wire EDM). The centre portion of the pancake was chosen for the study. The schematic showing the pancake and areas selected for samples extraction is given in **Fig. 3.3**. Two sets of samples with dimension of 10×10×5 in mm were extracted. One set of samples were manually polished till fine finish on 600, 800 followed by 1000 grit paper for XRD analysis. The other set of samples were mounted with bakelite powder and metallographically polished on 600, 800, 1000 and 1200 grit papers followed by cloth polishing using 9, 3 and 1 µm diamond grit and vibratory polishing in a liquid suspension containing 50 nm colloidal silica particles for SEM and EPMA analysis. The

samples were cleaned manually with acetone after each step of polishing. Finally, ultrasonic cleaning was done for five minutes in acetone prior to the characterization to remove any foreign particles embedded on the surface while polishing. The polished samples were further vibro-met polished for 12 h for EBSD analysis.

A thin sample of length: 5 mm, width: 5 mm, thickness: 2 mm was extracted from the pancake for TEM studies using wire–EDM. Subsequently, the sample was mechanically polished till 100 µm thickness on 800 and 1000 grit papers. Followed by, a 3 mm diameter sample was extracted from the centre by punching, subsequently, ion milling was carried out for further thinning. Ion milling (Precision Ion Polishing System (PIPS), GATAN-691) was done at beam energy of 4 KeV with gun angle +4 and -4 degrees for 7 h to make samples electron transparent. Then, the transparent foils after ion milling were analyzed in TEM at 200 KV and equipped with EDAX energy dispersive X-ray spectroscopy. All the microstructural studies were carried out on the surface corresponding to solidification direction of the pancake.

Cylindrical compression samples, having dimensions of 5 mm diameter and 7.5 mm length were excised from the cast alloys such that the long axis of the samples was along the solidification direction of the disks (**Fig. 3.3**). The samples were manually polished using 600 grit abrasive papers to make the surface scratch free before testing. Cuboidal samples with dimensions: length = 30, width = 6 and thickness = 3 (mm) (**Fig. 3.3**) were extracted for three point bend fracture toughness test. Subsequently, a notch of depth 3 mm and width 0.15 mm was machined by EDM such that the length of the notch was along the solidification direction (**Fig. 3.3**). The samples were polished using 600 grit abrasive papers prior to the test for smooth surface finish. Cuboidal coupons having dimensions of 12×10×2 (in mm) were excised from the alloy pancakes for the oxidation tests (**Fig. 3.3**). The samples were acid pickled prior the test to remove the surface oxides generated while EDM cutting.

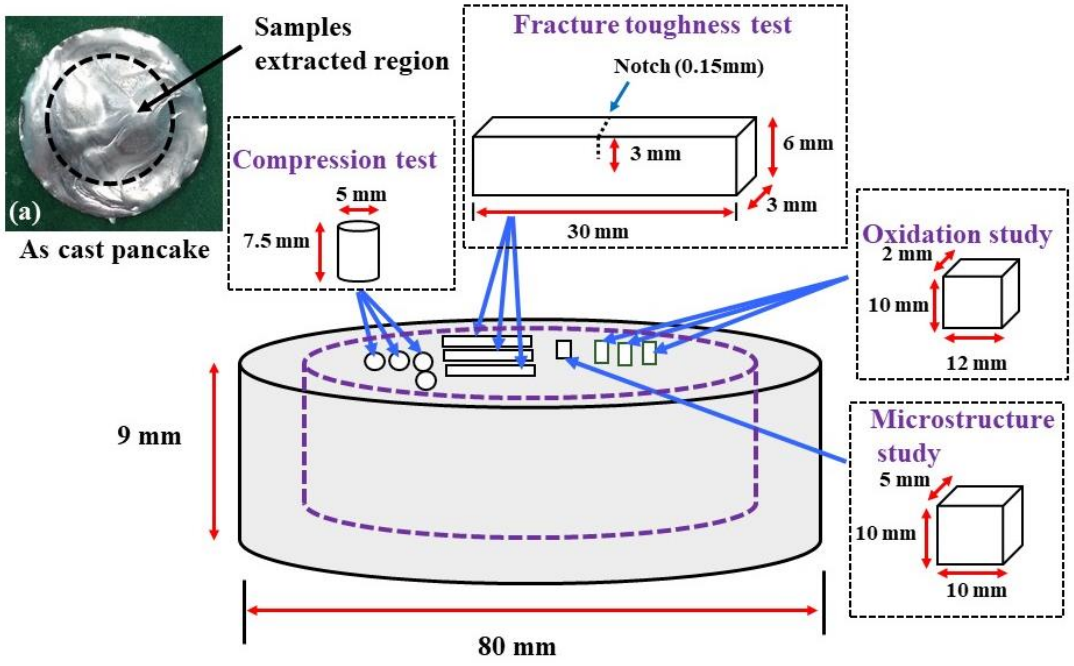

Fig. 3.3: The schematic showing the pancake and dimensions of the samples extracted for various studies and inset (a) shows the pancake with highlighted region chosen for samples extraction.

3.3 Microstructural characterization

3.3.1 X-ray diffraction (XRD)

The phases present in the alloys were analyzed using X-ray diffraction (XRD, Philips PW3020) with monochromatic Cu–Kα radiation of wave length 1.540562Å. The phases were identified by matching the characteristic XRD peaks against standard JCPDS (Joint Committee on Powder Diffraction Standards) data. Lattice parameter of the phases in the alloys were also determined. Lattice parameter of the BCC crystal structure and Nb phase was calculated using the following equation [*William D. Callister, 1940*].

$$a = d\sqrt{h^2 + k^2 + l^2} \quad --- \text{eq. } 7$$

Lattice parameters a and c of the tetragonal Nb_3Si and α–Nb_5Si_3 were also measured using the following equation [*William D. Callister, 1940*].

$$\frac{1}{d^2} = \frac{h^2 + k^2}{a^2} + \frac{l^2}{c^2} - - - \text{eq. } 8$$

where d is the interplanar spacing and h, k, l are the miller indices corresponding to the peak position. Data corresponding to high angle peaks was used for the calculation to minimize the error in the lattice parameter value.

3.3.2 Scanning electron microscopy (SEM)

The scanning electron microscope (SEM) equipped with energy dispersive X-ray spectroscopy (EDXS) was used for the microstructural and composition analysis (Zeiss Supra 55, **Fig. 3.4**). The volume fraction of the phases present in the microstructure was calculated from the occupied area of the phases using image analysis software 'Image J'. For the analysis, the microstructural images were taken in SEM–BSE mode from minimum of 8 to 10 locations at same magnification and the average value was taken. Samples were carefully polished metallographycally to avoid scratches and images were taken at a slow scan rate to get sharp contrast in the microstructure for obtaining accurate values.

Fig. 3.4: Photograph of the Scanning electron microscope (SEM).

3.3.3 Electron probe micro analyzer (EPMA)

The composition/elemental concentration of the phases present in the alloys were analyzed using wavelength dispersive X-ray spectroscopy (WDS) in a Cameca SX-100, electron probe micro-analyzer (EPMA, **Fig. 3.5**). The distribution of the elements that were present in the phases were also observed using the X-Ray mapping of the perticular microstructural area in the EPMA.

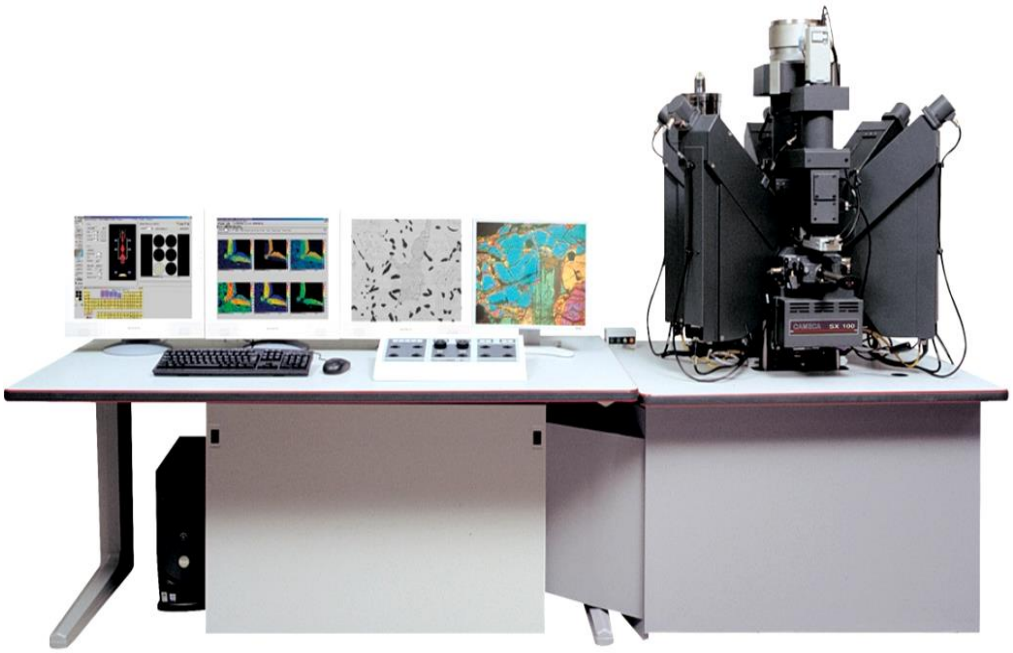

Fig. 3.5: Photograph of electron probe micro analyzer (EPMA).

3.3.4 Electron backscattered diffraction (EBSD)

Electron back scattered diffraction (EBSD, XL30 FEG) was used for analyzing the microstructure, phases and microtexture of the alloys. Measurements were made with a voltage of 20 kV and with a working distance of 15.8 mm. The Crystal structure, lattice parameter and space group employed for the identification of the phases in the EBSD analysis were mentioned in the **Table 3.1**. The microtexture data was processed using the commercially available HKL-Channel 5 software.

Table 3.1. Crystal structure, lattice parameter and space group employed for the identification of phases in the alloys through EBSD analysis [*W.B. Pearson, 1967*]

Phase type	Structure Pearson symbol	Structure/ space group	Lattice parameter (˚A)
Nb	CI2	Cubic Im-3m	a=3.306
Nb_3Si	tP32	Tetragonal P42/n	a=10.224, c=5.189
α-Nb_5Si_3, low temperature	tI32	Tetragonal I4/mcm	a=6.570, c=11.884
β-Nb_5Si_3, high temperature	tI32	Tetragonal I4/mcm	a=10.026, c=5.071
γ-Nb_5Si_3	hP16	Hexagonal P63/mcm	a=7.536, c=5.249

3.3.5 Transmission electron microscopy (TEM)

The phases and the microstructure of the alloys were analyzed in high resolution TEM (Philips model EM 430T, **Fig. 3.6**). The bright field images were collected and the selected area diffraction (SAD) patterns corresponding to the phases were also indexed. The composition of the each phase was also analyzed with the attached EDS to it.

Fig. 3.6: Photograph of the Transmission electron microscopy (TEM).

3.4 Mechanical properties

3.4.1 Compression test

Room temperature (RT) compression test was carried out at a strain rate of 1×10^{-3} s^{-1} (200 kN servo-hydraulic testing machine custom built by M/s BISS, Bangalore). The snap shots of the samples before and after the test was shown in the **Fig. 3.7**. The loading direction was parallel to the long axis, i.e., the solidification direction of the alloys. Atleast three samples were tested to check the repeatability in the values. The 0.2% yield strength (compressive strength) and fracture strength (corresponds to the value at maximum stress) was calculated from the stress strain data generated from the compression test. Further the elastic strain and total strain values were also calculated.

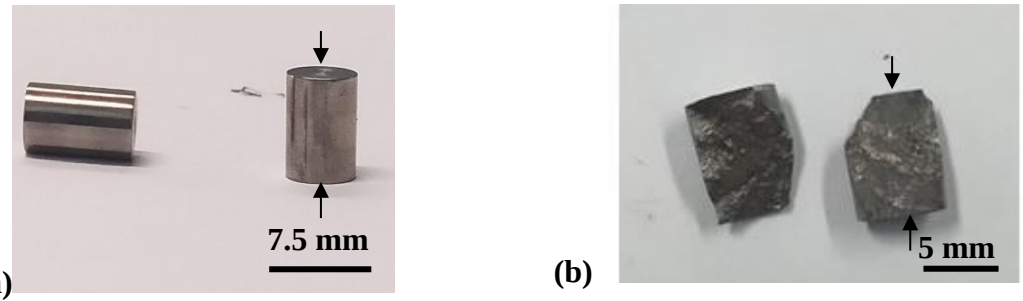

Fig. 3.7: The compression test sample. (a) before and (b) after the test (arrows indicate the loading direction)

The fractured surfaces shown in **Fig. 3.7(b)** were observed in SEM-SE mode for the fractography studies. These surfaces were also mounted in bakelite and fine polished to observe the microcracking behaviour in SEM-BSE. Further, the deformation substructure was examined in TEM.

3.4.2 Three point bend test

The fracture toughness of the alloy was measured by conducting three point bend test using an Instron 5500 R universal testing machine with a cross head speed of 0.1 mm/min and spam length of 20 mm. The Fracture toughness (K_Q) measurement is performed according to ASTM E399 [*ASTM E399–12 International, 2012*]. The photographs of the samples before and after the fracture toughness test with loading direction was shown in the **Fig. 3.8**. Three samples were tested for the repeatability in the values.

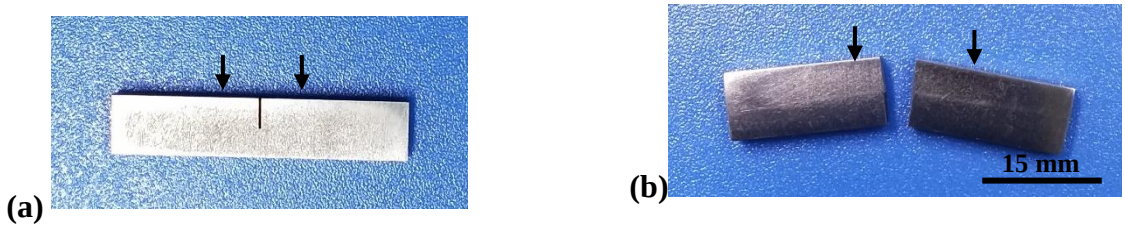

Fig. 3.8: Three point bend test smaple (a) before and (b) after the test. The arrows indicate the loading direction.

The value of fracture toughness (K_Q) was calculated using the following equation

$$KQ = \left(\frac{P_Q . S}{BW^{3/2}}\right) . f(a/w) \quad --- \text{eq. 9}$$

The parameters‘P_Q’, ‘B’, ‘S’, ‘W’ and ‘a’ denote the fracture load, specimen thickness, span length, specimen width, and crack length, respectively. The fractured surfaces were observed in SEM for the fractography studies.

Further, indentations on the samples were taken at 30 kg load using bulk vickers hardness tester (Chennai Metco, Ecomet VH 50MD), such that the cracks generated at the indent corners and observed the crack propegation behaviour. The microstructure of the bulk hardness tested samples was also observed in SEM-BSE.

3.4.3. Nano hardness test

The nano indentation experiments were carried out to know the hardness (H) and elastic modulus (E) of the individual phases present in the alloy. Indentation experiments were carried out using an iNano® nanoindenter with an InForce 50 electromagnetic actuator (Nanomechanics Inc., now KLA Corporation, Oak Ridge, USA, **Fig. 3.9**) that has a maximum load capability of 50 mN. The displacement sensor has a time constant of 20 ms and the maximum data acquisition rate is 100 kHz. A sharp diamond Berkovich indenter was used for all the measurements. Constant Strain Rate Indentation experiments with Continuous Stiffness Measurement (CSM) was used to perform the indentation tests to the prescribed load. A fixed 2 nm displacement oscillation at 100 Hz and indentation start rate of 0.2 s^{-1} was used for the CSM based experiments. Load frame stiffness and area function calibration was performed as per standard procedures [*W.C. Oliveer et al., 2004*] on fused silica standard specimen.

CSM based measurements were done to measure the H and E with respect to the indentation depth. The indentation load was chosen accordingly to confirm a minimum indent spacing to indent depth ratio of 10 for preventing the interaction between the strain fields of the adjacent indents [P. Sudharshan Phani et al., 2019]. The optimal maximum depth to measure the intrinsic properties was decided from the load versus depth plots generated from CSM data. Thus all the maps for hardness (H) and modulus (E) were generated at a load 2.5 mN with 1μm spacing between the indents. The H, E corresponding to each indent location was measured from the load-depth data using the standard Oliver and Pharr method [*W.C. Oliveer et al., 1992, 2004*]. The H, E maps were generated using the data of 2,500 indents collected over microstrucural length scales of 50×50 μm. The statistical analysis of the data is done at micrometer length scale. Further, the

SEM-BSE images were collected from the mapped regions and compared the microstructure with the properties.

(a)

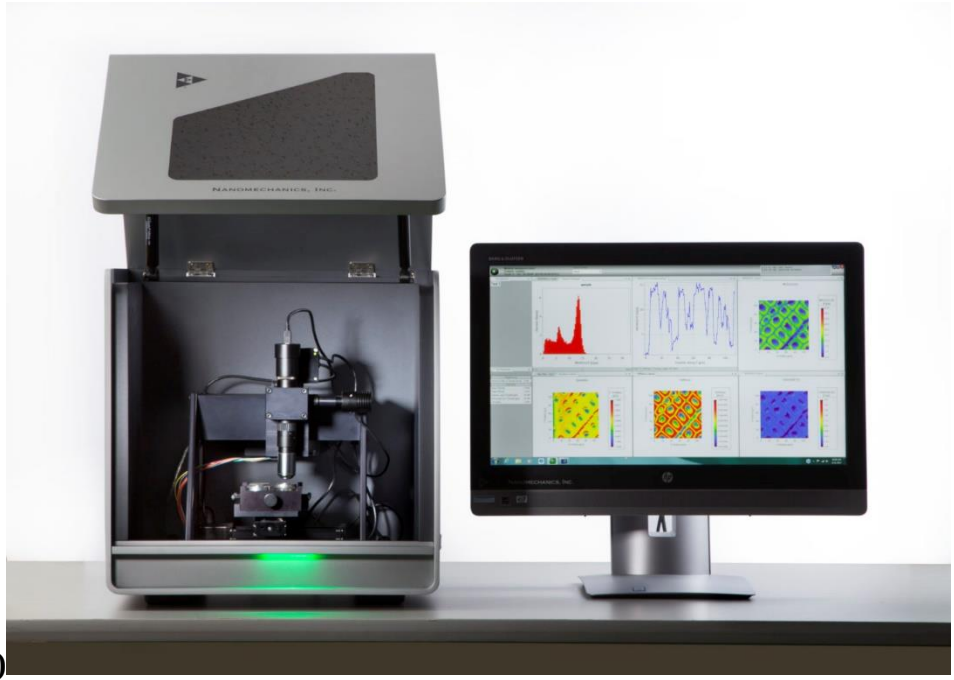

(b)

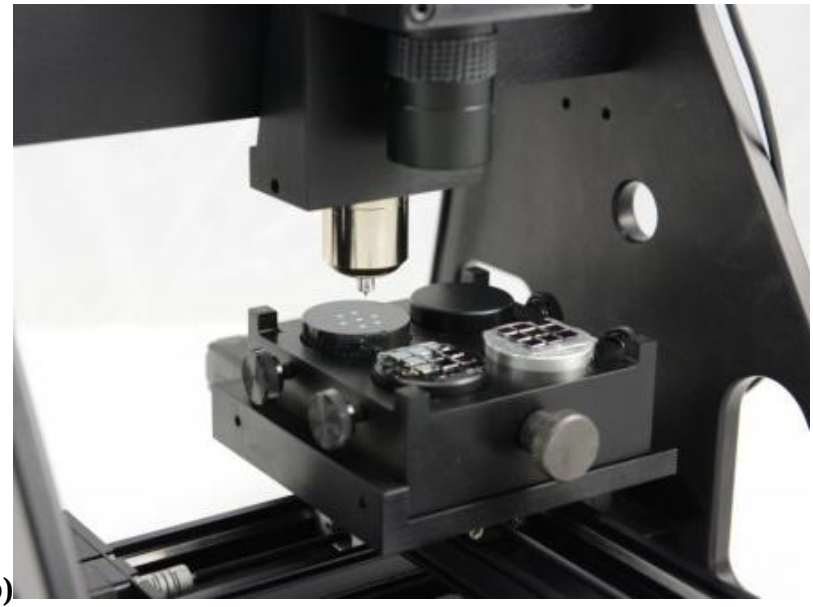

Fig. 3.9: (a) Photograph of Nano indentation equipment and (b) close view of the sample holder and indenter.

3.5 Oxidation test

3.5.1 Coating process

In this process, high purity (99.99%) elemental powders of Si, Fe and Cr were mixed in the ratio of 60:20:20 (wt.%). These powders were mixed in attritor mill for about 1 h. Subsequently, the powders were added to suitable liquid binder to form a slurry. The powders were blended with the liquid medium by mechanical stirring for 15 min. The coupons were dipped in the slurry with a controlled rate of 1 mm s^{-1} and held in the slurry for about 30 seconds. Subsequently, the samples were taken out from the slurry at a controlled rate of 1 mm s^{-1}. The above dipping process was repeated three times to ensure a proper build-up of the green coating on the sample surface. The drying time of five minutes was allowed between the two consecutive dips for proper drying of the green coating. The green coated samples were diffusion heat treated in vacuum at 1400°C for 2 h for removal of binder and to effect interdiffusion between the Fe, Cr and Si contained in the slurry and Nb from the substrate, which was essential for the formation of the diffusion silicide coating. The photographs of the uncoated and as coated samples were shown in the **Fig. 3.10**.

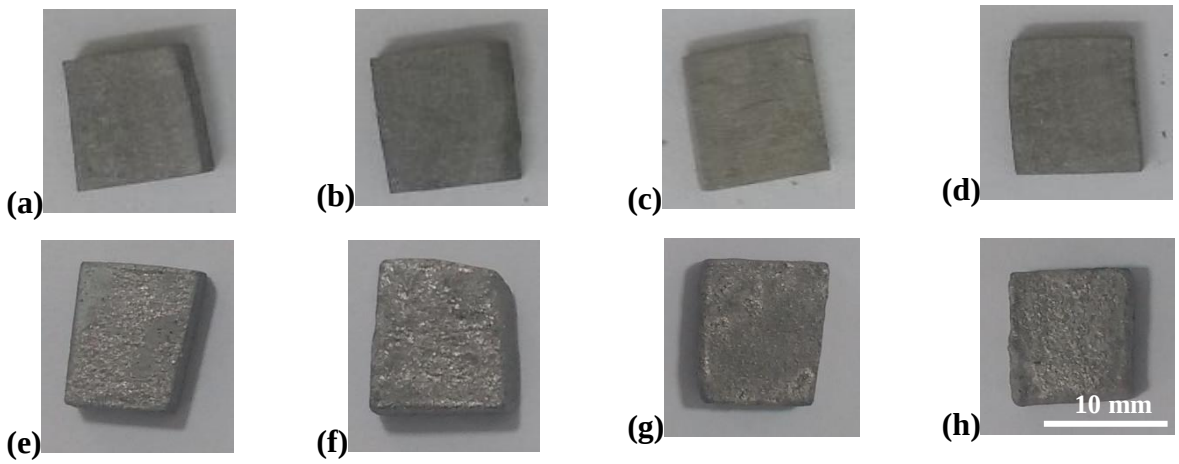

Fig. 3.10: Photographs of the samples used for cyclic oxidation test. (a-d) corresponds to uncoated samples and (e-h) corresponds to coated samples, where (a, e) Nb-18.7Si, (b, f) Nb-18.7Si-5Ti, (c, g) Nb-18.7Si-5Zr and (d, h) Nb-18.7Si-5Ti-5Zr.

3.5.2 Cyclic oxidation test

Both the coated and un coated samples were subjected to cyclic oxidation in air at 800°C, 1200°C and 1400°C in an automated thermal cycling furnace. Each sample was placed into a seperate alumina cruicible and placed inside automated thermal cycling furnace. Each cycle comprised of soaking the samples at the test temperature for 15 min and cooling outside of the furnace for 15 min. The soaking time was counted only after the samples attained the oxidation test temperature, which was monitored using a thermocouple placed in proximity to the samples on the sample loading stage. The typical temperature profile of the samples during one cycle of oxidation was shown in **Fig. 3.11**. The automated thermal cycling furnace enabled the hot stage movement inside and out of the heating zone after temperature reached the test temperature and exactly after 15 min of heating. The weight of the samples after each cycle of oxidation was recorded manually using precision analytical balance with accuracy of 0.00001 g. The weight of any loose scales/oxide powders which got detached from the sample surface was not considered, and only the weight of the net intact sample was measured. The specific change in the nett weight, i.e., the change in weight per unit initial surface area of the samples, was calculated after each cycle. For assessing the oxidation behavior, thermo-gravimetric plots, i.e., the change in specific weight of the samples with respect to the duration of oxidation was generated. The phases present in the as coated and oxidation tested samples were analyzed using XRD. The surface morpholoy and cross section microstructure of the as deposited and oxidized coatings were examined using SEM coupled with EDS, EPMA and EBSD techniques.

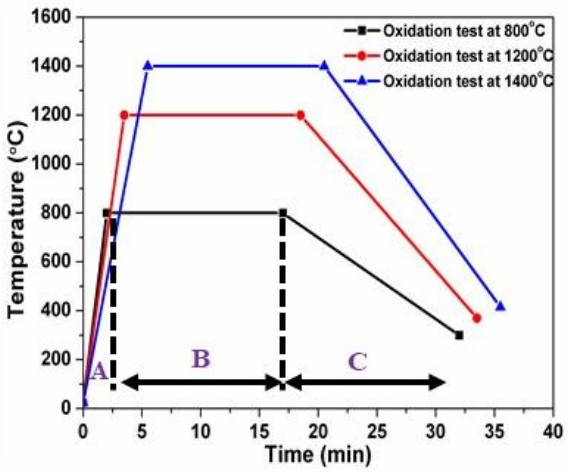

Fig. 3.11: Temperature profile of the sample during a cycle, where regions A, B and C corresponds to the heating, soaking and air cooling respectively.

Chapter- 4

Microstructure and phase evolution

4.0 Introduction

The present chapter covers the microstructural characterization of the selected alloys, i.e., Nb-18.7Si, Nb-18.7Si-5Ti, Nb-18.7Si-5Zr and Nb-18.7Si-5Ti-5Zr. It includes the preparation of the alloy pancakes in vacuum arc remelting (VAR) furnace followed by analysis of the microstructural behaviour using XRD, SEM, EBSD, EPMA and TEM techniques. The experimental results depicted that the 5Ti addition does not have influence on the phase formation of the Nb-18.7Si alloy, since, both the Nb-18.7Si and Nb-18.7Si-5Ti alloys exhibited two phase microstructure consisting of Nb_{ss} and Nb_3Si. Whereas, the addition of 5Zr alone, and 5Ti and 5Zr together formed stable and high creep resistant α-Nb_5Si_3 phase along with Nb_{ss} in the cast condition itself. The formation of α-Nb_5Si_3 phase in the cast alloys is advantageous as this eliminated the requirement of long term vacuum heat treatment which is generally required after casting. Further, the orientation relation between the phases is also studied using EBSD. Finally, the phase evolution sequence in the alloys is proposed.

4.1 Results

4.1.1 Pancake behaviour

Photographs of the pancakes of all the four alloys are shown in **Fig. 4.1**. The radiography of all the pancakes has indicated that they are sound and free from internal defects such as cracks and porosity. However, the surface of the pancakes is observed to be uneven (**Fig. 4.1**). The overall weight loss of the alloys is marginal (less than 0.5 wt.%), which indicated that the composition of the solidified alloys is similar to that of the theoretical stoichiometry.

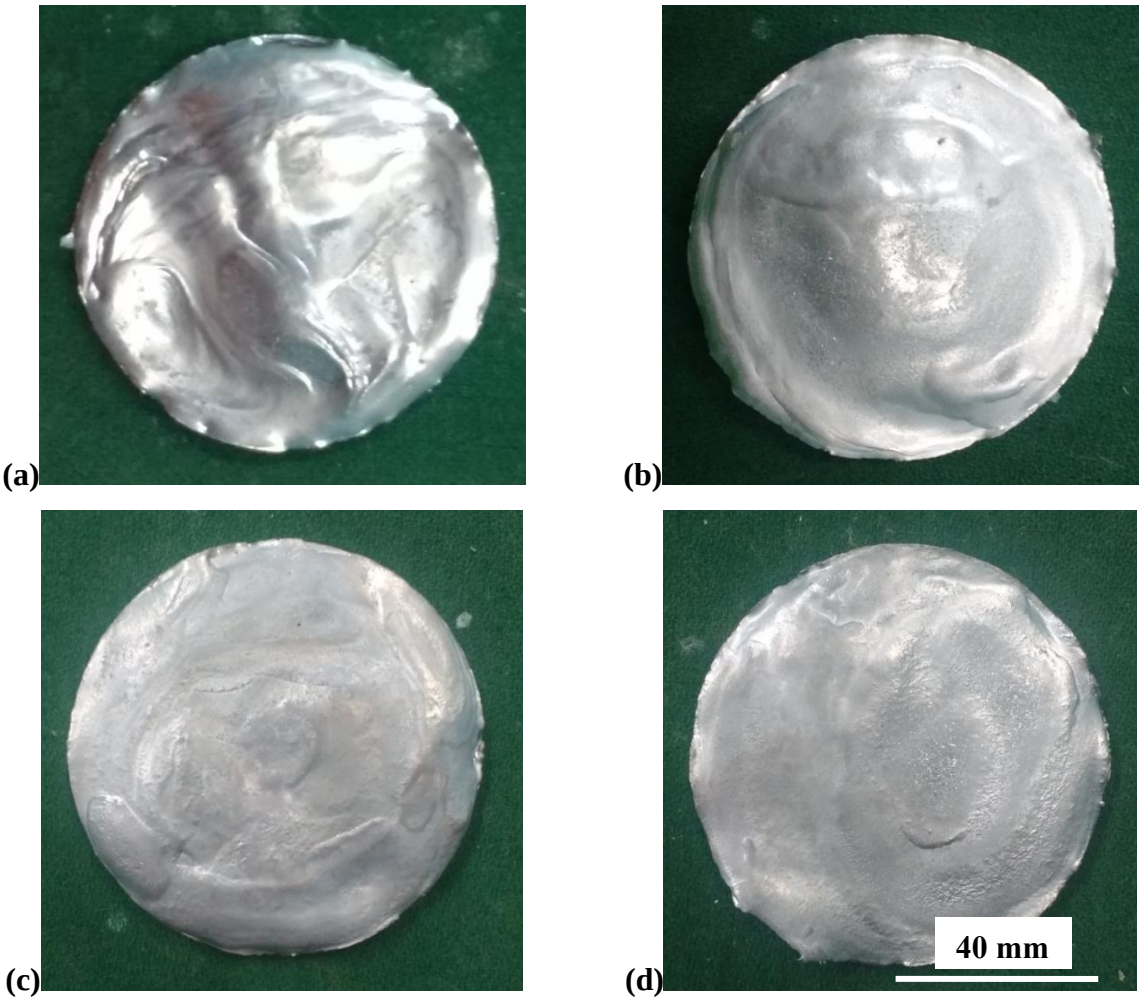

Fig. 4.1: Photographs of the alloy pancakes prepared through non consumable Vacuum arc remelting (VAR). (a) Nb-18.7Si, (b) Nb-18.7Si-5Ti, (c) Nb-18.7Si-5Zr and (d) Nb-18.7Si-5Ti-5Zr.

4.1.2 Microstructure and phase analysis

4.1.2.1 Nb-18.7Si Alloy

The microstructure of the Nb-18.7Si alloy consists of two phases, i.e., Nb_{ss} and Nb_3Si, which appear bright and grey in contrast, respectively (**Fig. 4.2**). The Nb_{ss} phase is present in the form of dispersions in the matrix of Nb_3Si phase. Minor amount of Si (1.70 at.%) is present in solid solution of the Nb_{ss} phase (**Table 4.1**). The Nb_3Si phase is confirmed from the presence of ~75 at.% of Nb and 25 at.% of Si, i.e., the 3:1 atomic ratio of Nb:Si (**Table 4.1**). The Nb_3Si phase has been found to present in two forms, i.e., primary Nb_3Si which is in the elongated faceted

morphology which is devoid of Nb_{ss} phase and eutectic Nb_3Si which contained dispersions of fine Nb_{ss} phase, typical of eutectic phase transformation (**Figs. 4.2(a, b)**) [*S. Kashyap et al., 2013, B.P. Bewlay et al.,2004*]. The overall volume fraction of the Nb_{ss} and Nb_3Si phases measured as 22.00±1.52% and 78.00±1.52%, respectively (**Table 4.2**). The above phase constituents in the alloy, i.e., Nb (JCPDS NO:89-5291) and Nb_3Si (JCPDS NO: 71-0372), are also confirmed from the XRD analyses (**Fig. 4.3**).

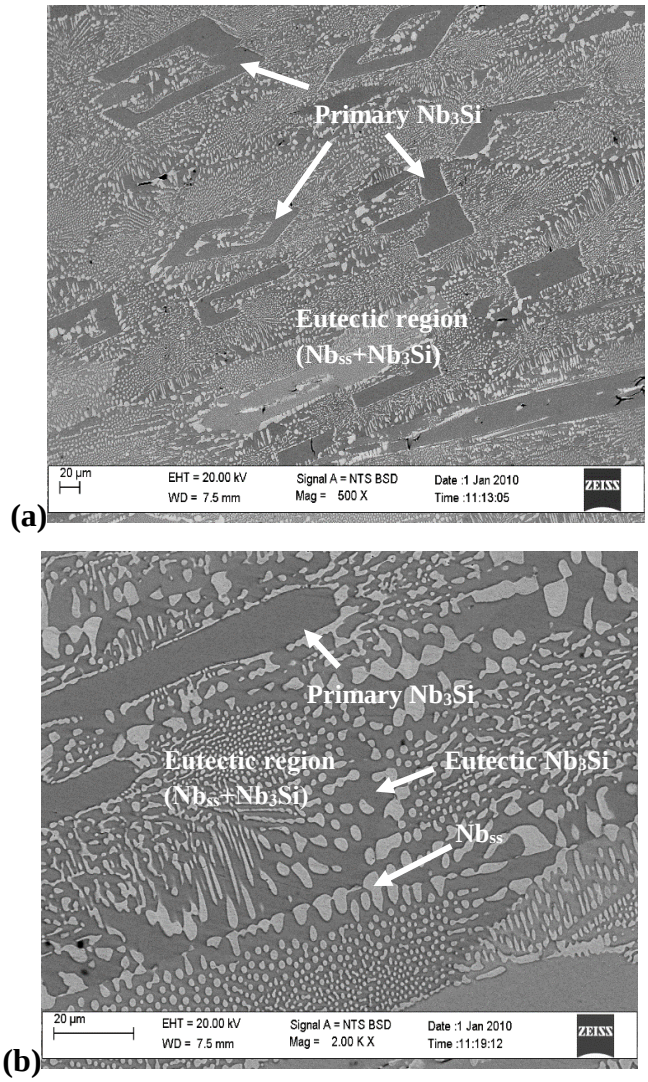

Fig. 4.2: Microstructure of the cast Nb-18.7Si alloy. (a) shows the elongated faceted primary Nb_3Si phase and the eutectic region consists of Nb_{ss}, Nb_3Si phases, (b) Magnified view of the (a), shows the eutectic Nb_3Si and Nb_{ss} phases in the eutectic region along with the primary Nb_3Si phase.

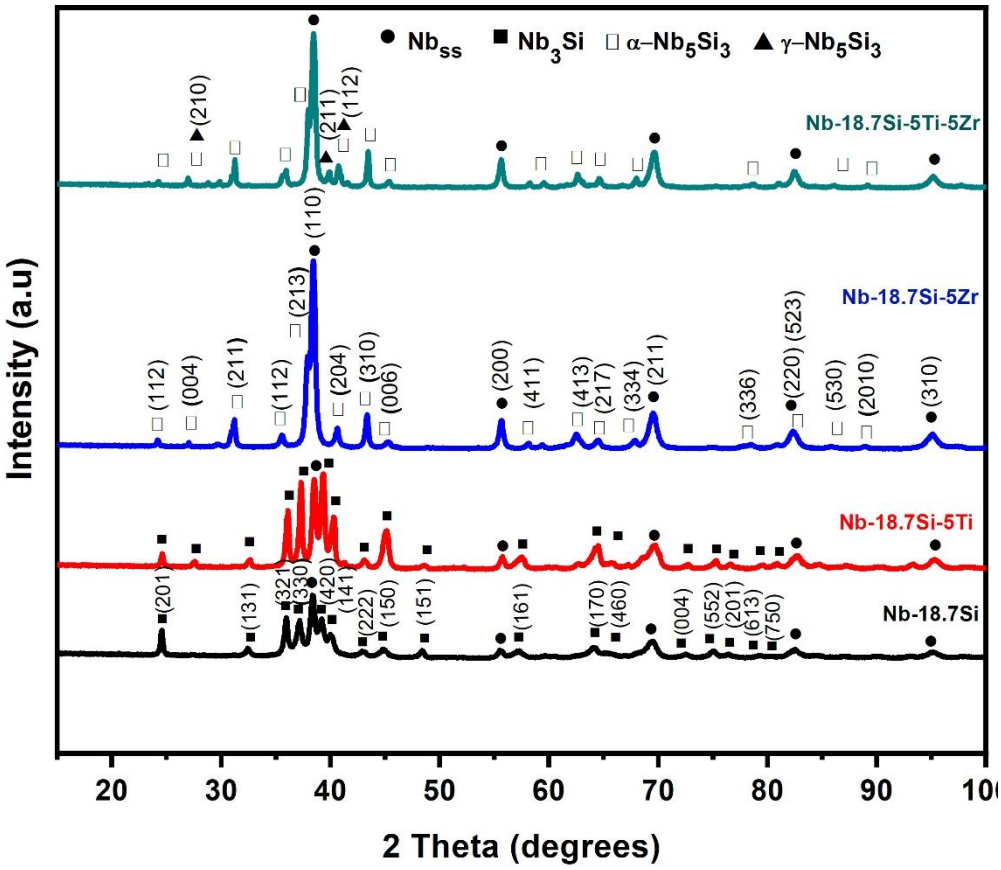

Fig. 4.3: X-ray diffraction pattern for the cast alloys. Nb-18.7Si and Nb-18.7Si-5Ti alloys showed Nb_{ss}, Nb_3Si phases, in contrast Nb-18.7Si-5Zr, Nb-18.7Si-5Ti-5Zr alloys showed Nb_{ss} and α–Nb_5Si_3 phases along with γ–Nb_5Si_3 phase in the later alloy.

Table 4.1: Compositional analysis of the phases present in the alloys by EPMA-WDS analysis.

Alloy	Phases	Nb (at.%)	Si (at.%)	Ti (at.%)	Zr (at.%)
Nb-18.7Si	Nb_{ss}	98.30 ±0.14	1.70±0.14	--	--
	Nb_3Si	75.30 ±0.17	24.70±0.17	--	--
Nb-18.7Si-5Ti	Nb_{ss}	91.07 ±0.60	2.98±0.16	5.94 ±0.63	--
	Primary Nb_3Si	71.70±0.26	24.92 ±0.15	3.33±0.14	--
	Eutectic Nb_3Si	69.73±0.34	24.90±0.10	4.36±0.29	--
Nb-18.7Si-5Zr	Nb_{ss}	96.30±0.40	1.82±0.20	--	1.88±0.40
	Primary α–Nb_5Si_3	57.60±0.13	37.70±0.10	--	4.70±0.10
	Eutectoid α–Nb_5Si_3	55.10±1.14	37.50±0.17	--	7.30±1.12
Nb-18.7Si-5Ti-5Zr	Nb_{ss}	90.50±1.10	2.20±0.05	5.10±0.76	2.13±0.40
	Primary α–Nb_5Si_3	54.30±0.40	38.20±0.20	2.79±0.06	4.71±0.62
	Eutectoid α–Nb_5Si_3	52.20±1.10	36.90±1.50	3.80±0.40	7.00±0.70
	Eutectoid α–Nb_5Si_3 phase rich in Ti, Zr	37.70±1.90	36.70±0.47	9.97±0.70	15.50±1.80

Table 4.2: Volume fraction (%) of the constituent phases present in the alloys.

Alloy composition	**Volume fraction of phases (%)**			
	Nb_{ss}	**Nb_3Si**	**α-Nb_5Si_3**	**γ-Nb_5Si_3**
Nb-18.7Si	22.00±1.52	78.00±1.52	--	--
Nb-18.7Si-5Ti	23.10±2.00	77.10± 2.00	--	--
Nb-18.7Si-5Zr	53.20±0.51	--	47.20±0.51	--
Nb-18.7Si-5Ti-5Zr	55.00±0.30	--	38.00±0.30	7.00±0.30

The lattice parameter of the Nb_{ss} phase calculated using eq. 7 (mentioned in chapter 3) is 3.312 Å (**Fig. 4.4(a)**), which is higher than the standard value of 3.300Å for pure Nb. The 'c' and 'a' values of the tetragonal Nb_3Si phase in the Nb-18.7Si alloy, calculated from eq. 8 (mentioned in chapter 3), are 5.209Å and 10.240Å, respectively (**Fig. 4.4(b)**).

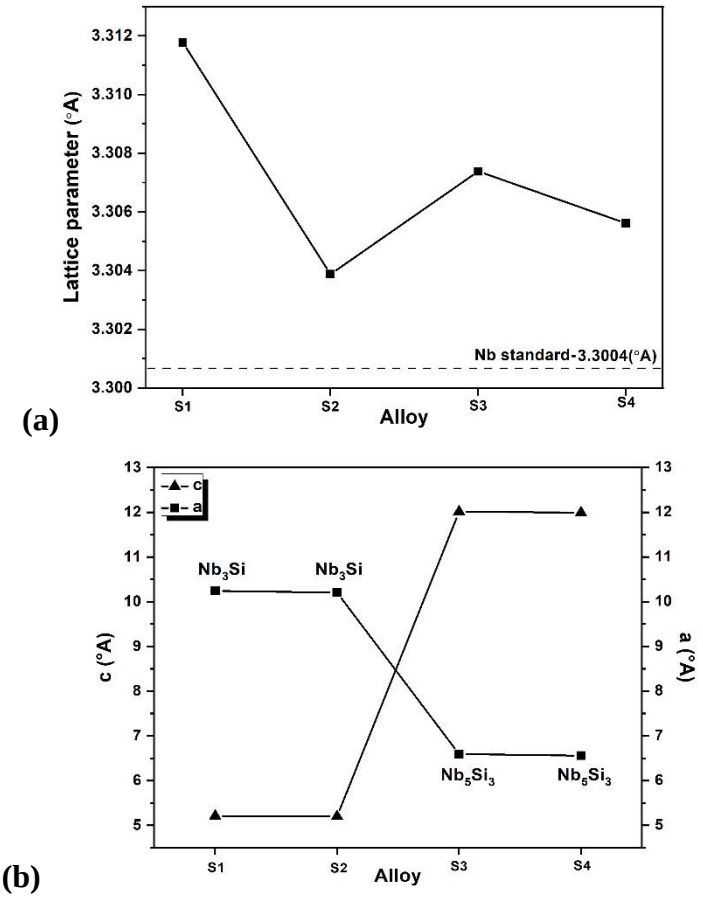

Fig. 4.4: Lattice parameter variation of the phases in the alloys with alloying additions. (a) Nb_{ss} and (b) silicide (Nb_3Si/α-Nb_5Si_3) phase. Where, S1, S2, S3 and S4 labelling in the figures corresponds to the Nb-18.7Si, Nb-18.7Si-5Ti, Nb-18.7Si-5Zr and Nb-18.7Si-5Ti-5Zr alloy, respectively.

4.1.2.2 Nb-18.7Si-5Ti Alloy

The microstructure of the Nb-18.7Si-5Ti alloy also consists of two phases, i.e., Nb_{ss} (bright in contrast) and Nb_3Si (grey in contrast), as evident from **Fig. 4.3** and **Fig. 4.5**. The Nb_{ss} phase is present as dispersions in the Nb_3Si matrix phase. The Nb_3Si can be classified into primary Nb_3Si and eutectic Nb_3Si forms, as similar to the Nb-18.7Si alloy (**Figs. 4.5(a, b)**). From the **Table 4.1**, it is noted that the Nb_{ss} phase contained 3.33 at.% of Si. Both the primary and eutectic Nb_3Si phases contained ~25 at.%Si. The amount of Ti present in Nb_{ss}, primary Nb_3Si and eutectic Nb_3Si phases is noted as 5.94 ±0.63, 3.33±0.14 and 4.36±0.29 (at.%), respectively. The solubility of Ti in the primary Nb_3Si phase is noticeably less compared to the eutectic Nb_3Si (**Table 4.1**). The entire Ti

is partitioned in both the Nb_{ss} and Nb_3Si phases, and formed the substitutional solid solution in the phases. This is also evident from the absence of Ti-silicide phases in the XRD analysis (**Fig. 4.3**). The Si content (~25 at.%) is similar in the Nb_3Si phase for both the Nb-18.7Si and Nb-18.7Si-5Ti alloys, whereas the corresponding Nb content is lower in the Nb-18.7Si-5Ti alloy (**Table 4.1**). This indicates that the Ti replaced the Nb atoms in the Nb_3Si phase. Therefore, the Nb_{ss} and Nb_3Si phases in the Nb-18.7Si-5Ti alloy can be represented as $(Nb,Ti)_{ss}$ and $(Nb,Ti)_3Si$, respectively [*S. Miura et al., 2009, B.P. Bewlay, M.R. Jackson et al., 1995, E. Guo et al., 2017*]. The relative amount of $(Nb,Ti)_{ss}$ and $(Nb,Ti)_3Si$ phases are measured as 23±2% and 77±2%, respectively (**Table 4.2**).

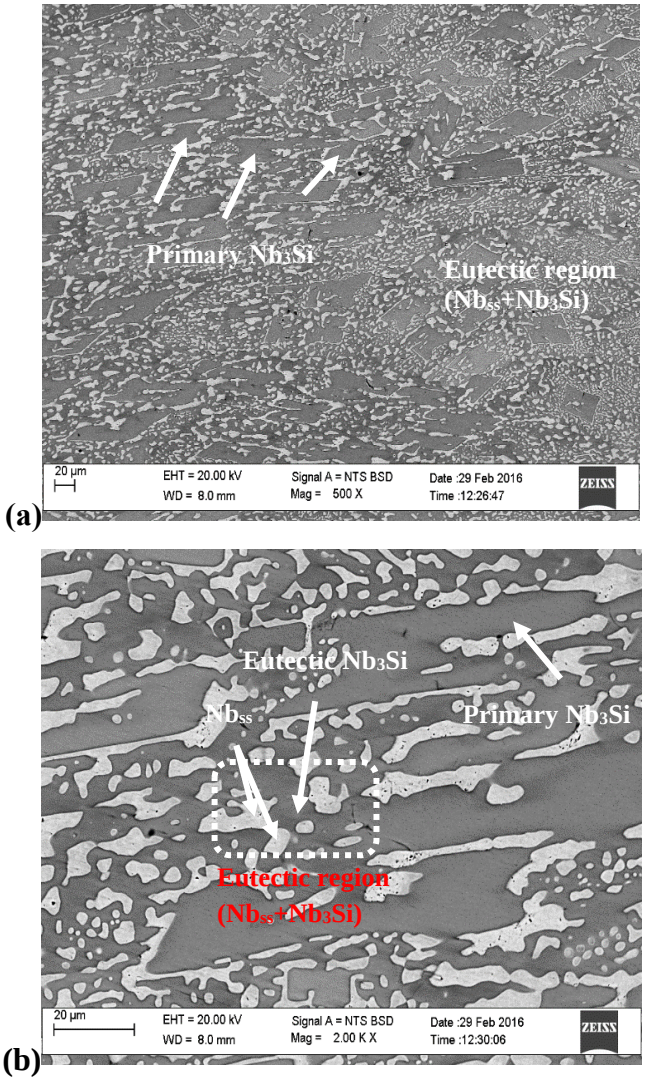

Fig. 4.5: Microstructure of the cast Nb-18.7Si-5Ti alloy. (a) shows the faceted primary Nb_3Si phase and the eutectic region consists of Nb_{ss}, Nb_3Si phases, (b) magnified view of the (a) showing

the presence of Nb_{ss} and Nb_3Si phases in the eutectic region along with the primary Nb_3Si phase in the microstructure.

Coarsening in the Nb_{ss} phase is observed as compared to the Nb_{ss} phase in the Nb-18.7Si alloy (**Figs. 4.2(b), 4.5(b)**). The lattice parameter of the Nb_{ss} phase (3.304 Å) is higher than the lattice parameter of Nb_{ss} phase in the binary alloy (Nb-18.7Si) (**Fig. 4.4(a)**). The 'c' and 'a' values of the tetragonal Nb_3Si phase are calculated as 5.198 Å and 10.204 Å, respectively (**Fig. 4.4(b)**). Both the c and a values of the Nb_3Si phase are decreased with Ti addition compared to the Nb_3Si phase in Nb-18.7Si alloy.

4.1.2.3 Nb-18.7Si-5Zr Alloy

The microstructure of the Nb-18.7Si-5Zr alloy exhibited bright Nb_{ss} phase as dispersion in a grey Nb_5Si_3 matrix (**Fig. 4.6**). The presence of Nb_5Si_3 phase is confirmed from the 5:3 atomic ratio of Nb:Si from the EPMA-WDS analysis (**Table 4.1**). The XRD analyses (**Fig. 4.3**) and EBSD phase maps (**Fig. 4.7**) confirm that the silicide phase corresponds to that of α–Nb_5Si_3. The α–Nb_5Si_3 phase at some places is big in size, faceted morphology and devoid of Nb_{ss} phase (**Fig. 4.6(b)**). This is termed as primary α–Nb_5Si_3 [*X. Zhang et al., 2015*]. Whereas, the α–Nb_5Si_3 phase present along with Nb_{ss} phase in eutectoid region is termed as eutectoid α–Nb_5Si_3 (**Fig. 4.6(a)**). The eutectoid region is present in lamellar morphology at some places, as indicated by arrow in red color in the **Fig. 4.6(b)**.

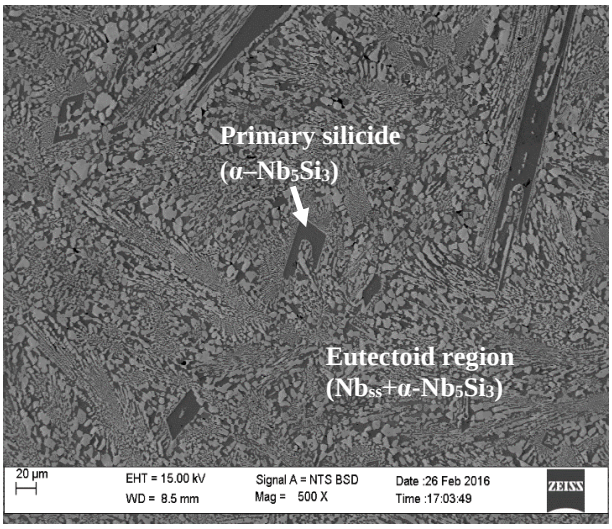

(a)

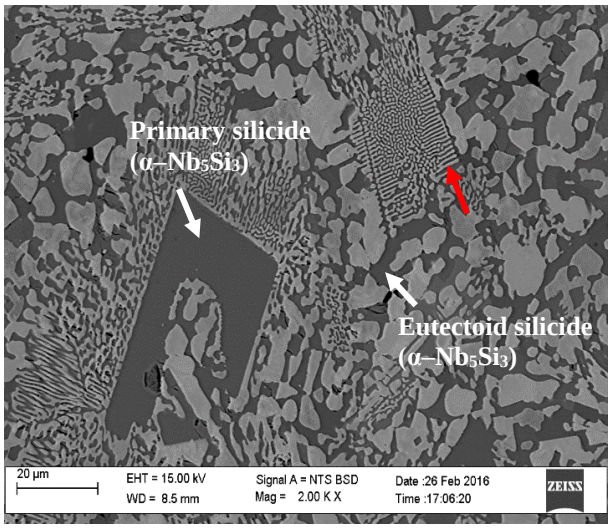

(b)

Fig.4.6: As cast microstructure of the Nb-18.7Si-5Zr alloy. (a) showing the faceted primary α–Nb_5Si_3 phase and eutectoid region consists of Nb_{ss}, α–Nb_5Si_3 phases, (b) magnified view of (a) shows the primary α–Nb_5Si_3 along with eutectoid α–Nb_5Si_3 and Nb_{ss} phases.

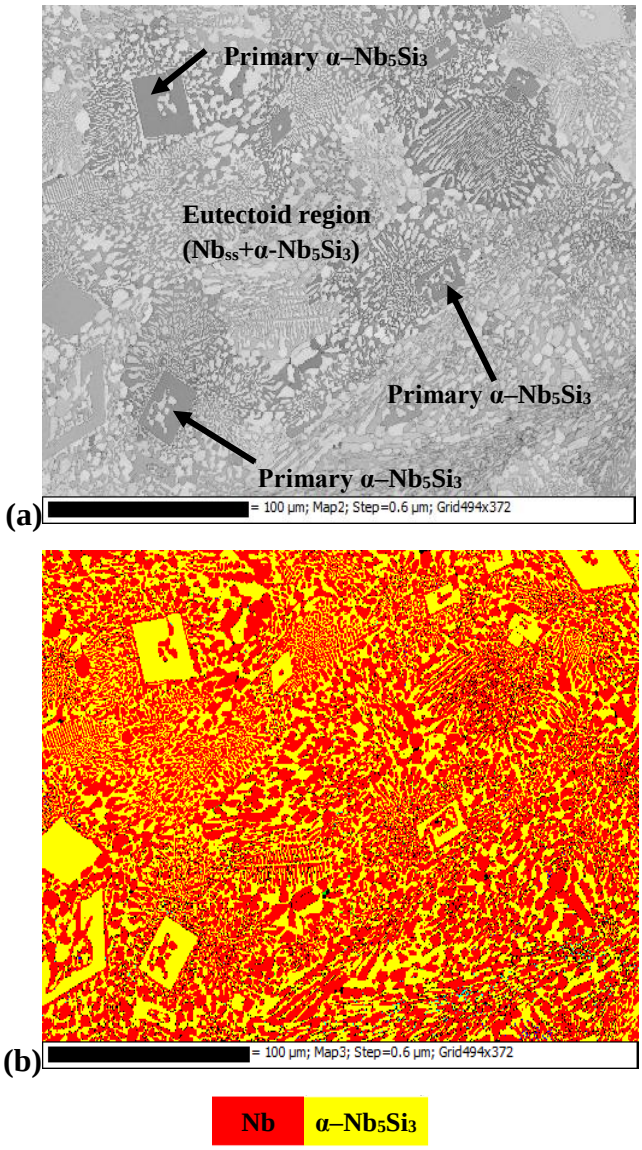

Fig. 4.7: EBSD results of Nb-18.7Si-5Zr alloy. (a) Image quality map, (b) EBSD phase map showing the Nb_{ss}, α–Nb_5Si_3 phases.

The dissolution of Si in Nb_{ss} phase is about 1.82±0.20 at.% and it is high in primary and eutectoid α–Nb_5Si_3 phases (37.70±0.10 at.%, 37.50±0.17 at.%, respectively) (**Table 4.1**). This indicates that the Si is primarily present in the silicide phase. The Zr content in Nb_{ss}, primary α-Nb_5Si_3 and eutectoid α-Nb_5Si_3 phases is estimated as 1.88±0.40, 4.70±0.10 and 7.30±1.12 at.%, respectively (**Table 4.1**). Concomitantly, no Zr-Si phases are detected in the XRD as well as the EBSD results. There is a large difference in the solubility of Zr in the primary α–Nb_5Si_3 and eutectoid α–Nb_5Si_3 phases. As evident from **Table 4.1**, the primary α–Nb_5Si_3 contains less Zr than that of the eutectoid α–Nb_5Si_3 phase. The low Nb content in α–Nb_5Si_3 (55.10-57.60 at.%) than that

of the expected stoichiometric content (62.50 at.%) and corresponding presence of Zr (**Table 4.1**) suggests that Zr substitutes for Nb in the α–Nb_5Si_3 phase. Therefore, the Nb_{ss} and α–Nb_5Si_3 phases in the Nb-18.7Si-5Zr alloy can be represented as $(Nb,Zr)_{ss}$ and α–$(Nb,Zr)_5Si_3$. The volume fraction of the Nb and α–Nb_5Si_3 phases are measured as 53.20±0.51% and 47.20±0.51%, respectively (**Table 4.2**).

The Nb_{ss} phase is coarsened and more of spherical form compared to the Nb_{ss} phase in Nb-18.7Si and Nb-18.7Si-5Ti alloys (**Figs. 4.2(b) and 4.6(b)**). The lattice parameter of the Nb_{ss} phase measured as 3.307 Å and this is lower than the lattice parameter of the Nb_{ss} phase in the Nb-18.7Si alloy (**Fig. 4.4(a)**). The measured lattice parameters a, c of tetragonal α–Nb_5Si_3 phase are of 6.590Å and 12.010Å, respectively (**Fig. 4.4(b)**).

4.1.2.4 Nb-18.7Si-5Ti-5Zr Alloy

The Nb-18.7Si-5Ti-5Zr alloy exhibits the Nb_{ss} (bright contrast) and α–Nb_5Si_3 (grey contrast) phases, as shown in **Figs. 4.8(a, b)**. The presence of α–Nb_5Si_3 phase is confirmed from the 5:3 atomic ratio of Nb:Si from EPMA-WDS analysis (**Table 4.1**). Further, presence of another non equilibrium phase γ–Nb_5Si_3 is also detected in the EBSD phase map (**Figs. 4.9(a. b)**). The presence of the above phases is also confirmed from the XRD analysis (**Fig. 4.3**). The α-Nb_5Si_3 and γ–Nb_5Si_3 phases could not be differentiated clearly in the SEM-BSE image (**Figs. 4.8(a. b)**). The α–Nb_5Si_3 phase is categerized into primary α–Nb_5Si_3 and eutectoid α–Nb_5Si_3 (**Figs. 4.8(b)**). The primary α–Nb_5Si_3 phase is present in faceted morphology and devoid of Nb_{ss} phase [*X. Zhang et al., 2015*]. The eutectoid α–Nb_5Si_3 phase is present along with dispersions of Nb_{ss} phase (**Figs. 4.8(b)**). The eutectoid region is present in lamellar morphology at some places, as shown with red color arrow in **Figs. 4.8(b)**. From the EBSD phase map, it is observed that the γ–Nb_5Si_3 phase is present along with the Nb_{ss} phase in fine morphology (**Figs. 4.9(a. b)**).

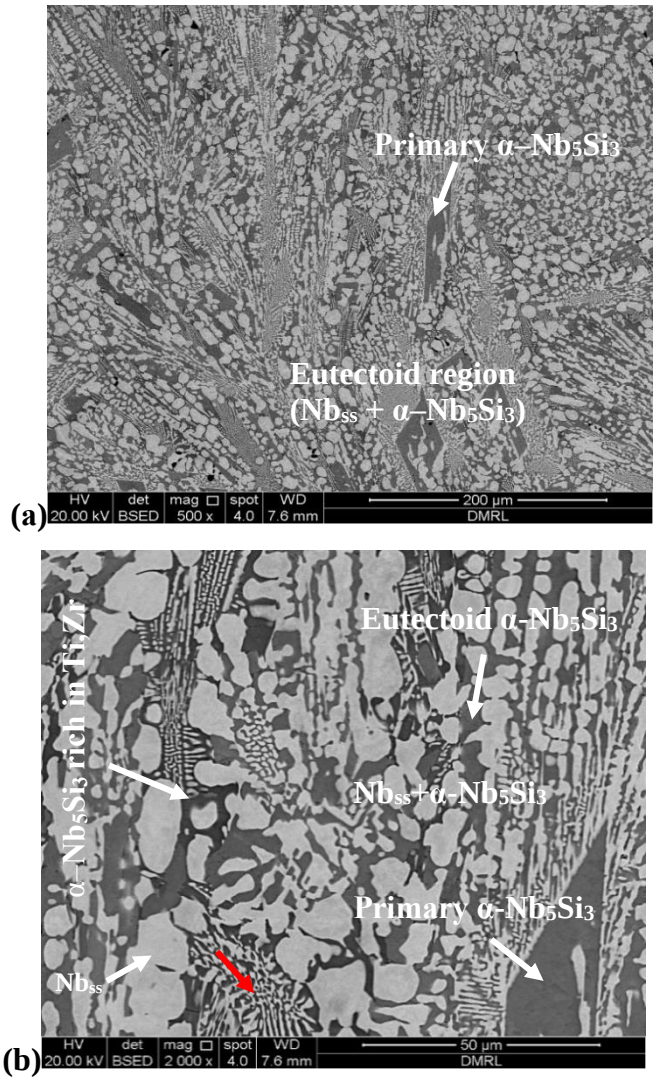

Figs. 4.8: As cast microstructure of the Nb-18.7Si-5Ti-5Zr alloy, (a) shows the primary α–Nb_5Si_3 phase and eutectoid region consists of Nb_{ss}, α–Nb_5Si_3 phases, (b) magnified view of (a) shows the eutectoid α–Nb_5Si_3 and Nb_{ss} phase in the eutectoid region along with primary α–Nb_5Si_3 phase.

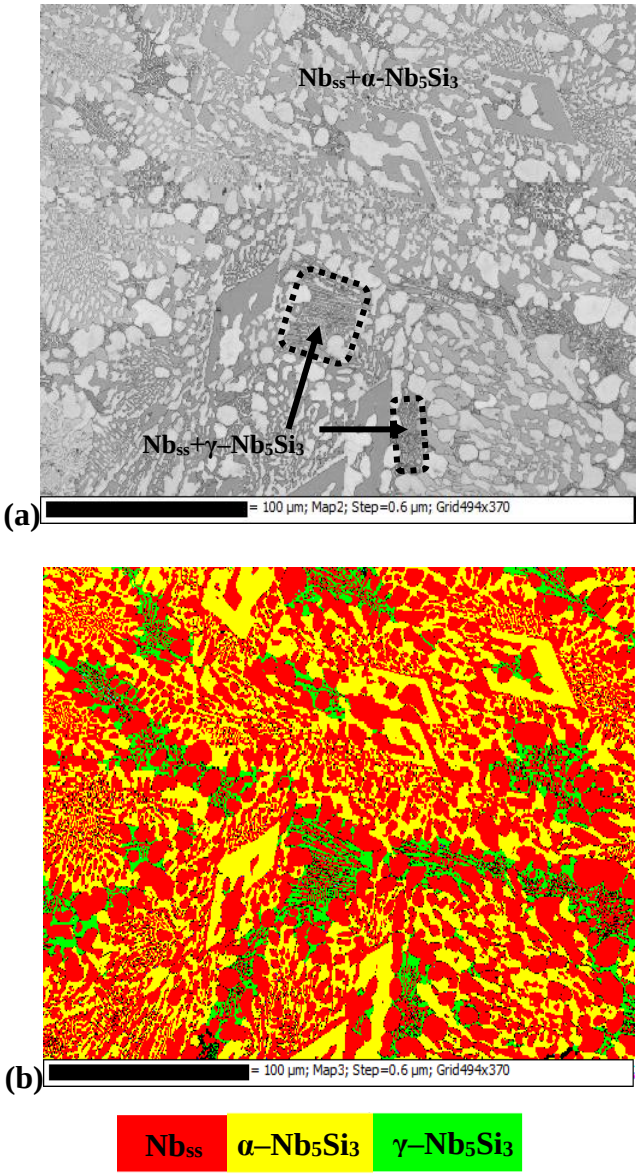

Figs. 4.9: EBSD results of the Nb-18.7Si-5Ti-5Zr alloy. (a) Image quality map, (b) EBSD phase map shows the Nb_{ss}, α–Nb_5Si_3 and γ-Nb_5Si_3 phases.

The Nb_{ss} phase consist of 2.20±0.05 at.% Si, 5.10±0.76 at.% Ti and 2.13±0.40 at.% Zr, respectively (**Table 4.1**). Therefore, Nb_{ss} phase can be represented as $(Nb,Ti,Zr)_{ss}$. The dissolved contents of Si, Ti and Zr in the primary α–Nb_5Si_3 are 38.20±0.20, 2.79±0.06 and 4.71±0.62, respectively (in at. %). Their contents in the eutectoid α–Nb_5Si_3 are 36.9±1.5, 3.8±0.4 and 7.0±0.7, respectively (in at.%). The primary α–Nb_5Si_3 contains less Ti and Zr than that of the eutectoid α–Nb_5Si_3 phase. Further, at some places the Ti and Zr contents within the eutectoid α–Nb_5Si_3 phase are found to be higher, i.e., 9.97±0.70 and 15.50±1.80 (at.%), respectively and the regions are as

shown in the **Fig.4.8(b)**. The composition of the γ–Nb_5Si_3 could not be measured due to its fine morphology. The X-ray mapping of this alloy is shown in the **Fig.4.10**. It shows the presence of high Ti and Zr content in the fine mixture of Nb_{ss} and γ–Nb_5Si_3 phase region. The regions of Ti and Zr rich eutectoid α–Nb_5Si_3 phase is also identified (**Fig.4.10 (a, d, e)**). From **Table 4.1**, it is observed that the α-Nb_5Si_3 phase contains low Nb content than the stoichiometric ratio along with the presence of Ti and Zr. From this it is noted that the Ti and Zr occupied the Nb positions of the α–Nb_5Si_3 phase. Therefore, the phases can be represented as α–$(Nb,Ti,Zr)_5Si_3$ and γ–$(Nb,Ti,Zr)_5Si_3$. The relative amounts of Nb_{ss}, α–Nb_5Si_3 and γ–Nb_5Si_3 phases are of 55.00±0.30, 38.00±0.30 and 7.00±0.30%, respectively (**Table 4.2**).

Bright field TEM images of the Nb-18.7Si-5Ti-5Zr alloy is shown in **Fig. 4.11(a)** revealed a two phase microstructure. The selected area diffraction (SAD) pattern obtained from phase 1 region is indexed in terms of [001] zone axis of cubic Nb phase (**Fig. 4.11(b)**). The SAD pattern obtained from the phase 2 region is indexed in terms of [001] zone axis of tetragonal α–Nb_5Si_3 (**Fig. 4.11(c)**). No additional spot could be observed in the electron diffraction patterns obtained from Nb_{ss} and silicide phases (**Fig. 4.11(a)**). This confirms that no Ti or Zr silicide precipitates are formed in the alloy. The EDAX results of these phases are presented in **Figs. 4.11(d, e)**. The composition of the Nb_{ss} phase analyzed from EDAX is 1.70 at.% Si, 3.00 at.%Ti, 3.00 at.% Zr and 92.20 at.% of Nb (**Fig. 4.11(d)**). The composition of the silicide phase is 36.00 at.% Si, 2.50 at.% Ti, 6.50 at.% Zr and 59.00 at.% Nb (**Fig. 4.11(e)**).

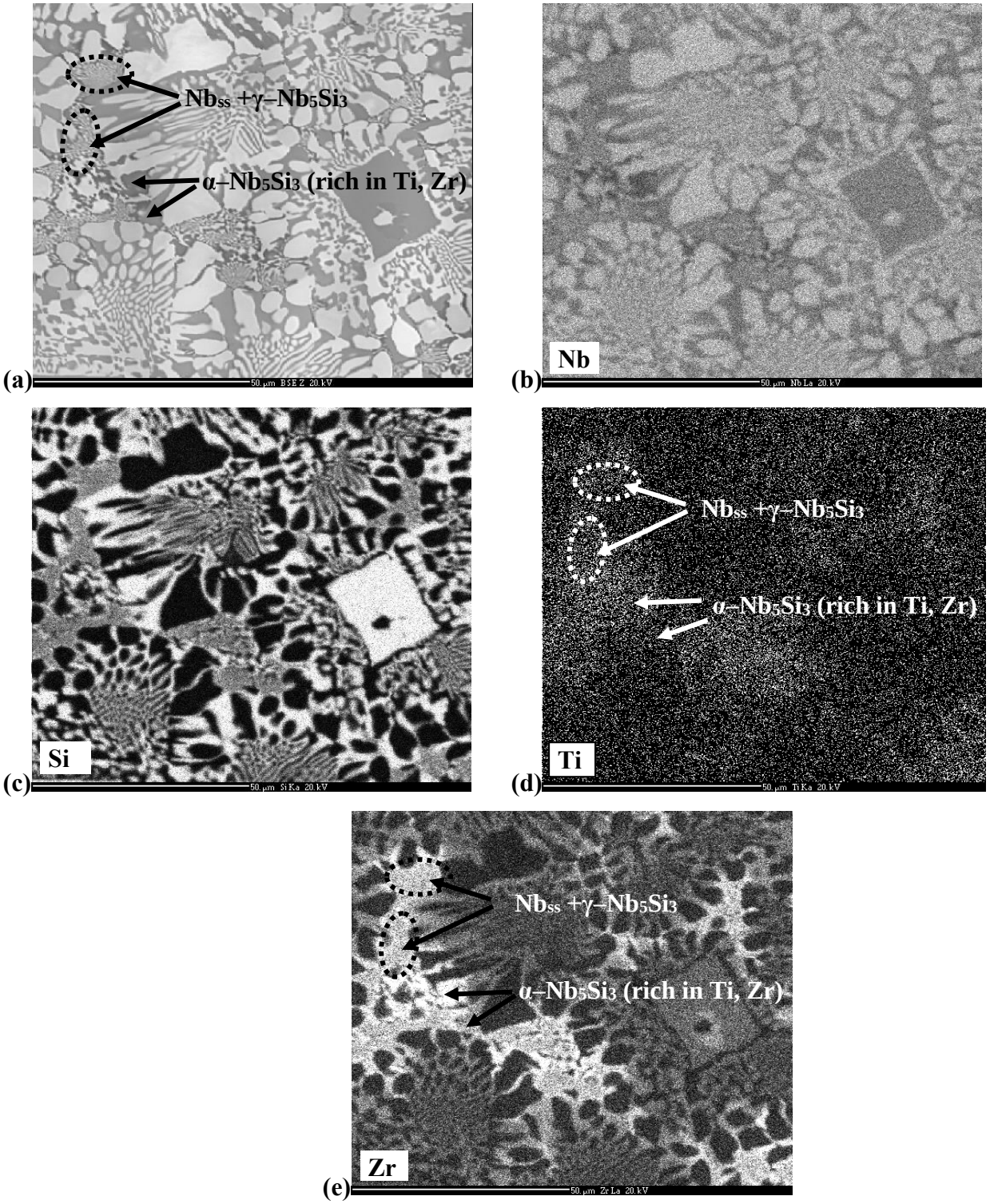

Fig. 4.10: (a) BSE image and corresponding X-ray elemental mapping for Nb-18.7Si-5Ti-5Zr alloy showing the elemental distribution for (b) Nb, (c) Si, (d) Ti and (e) Zr.

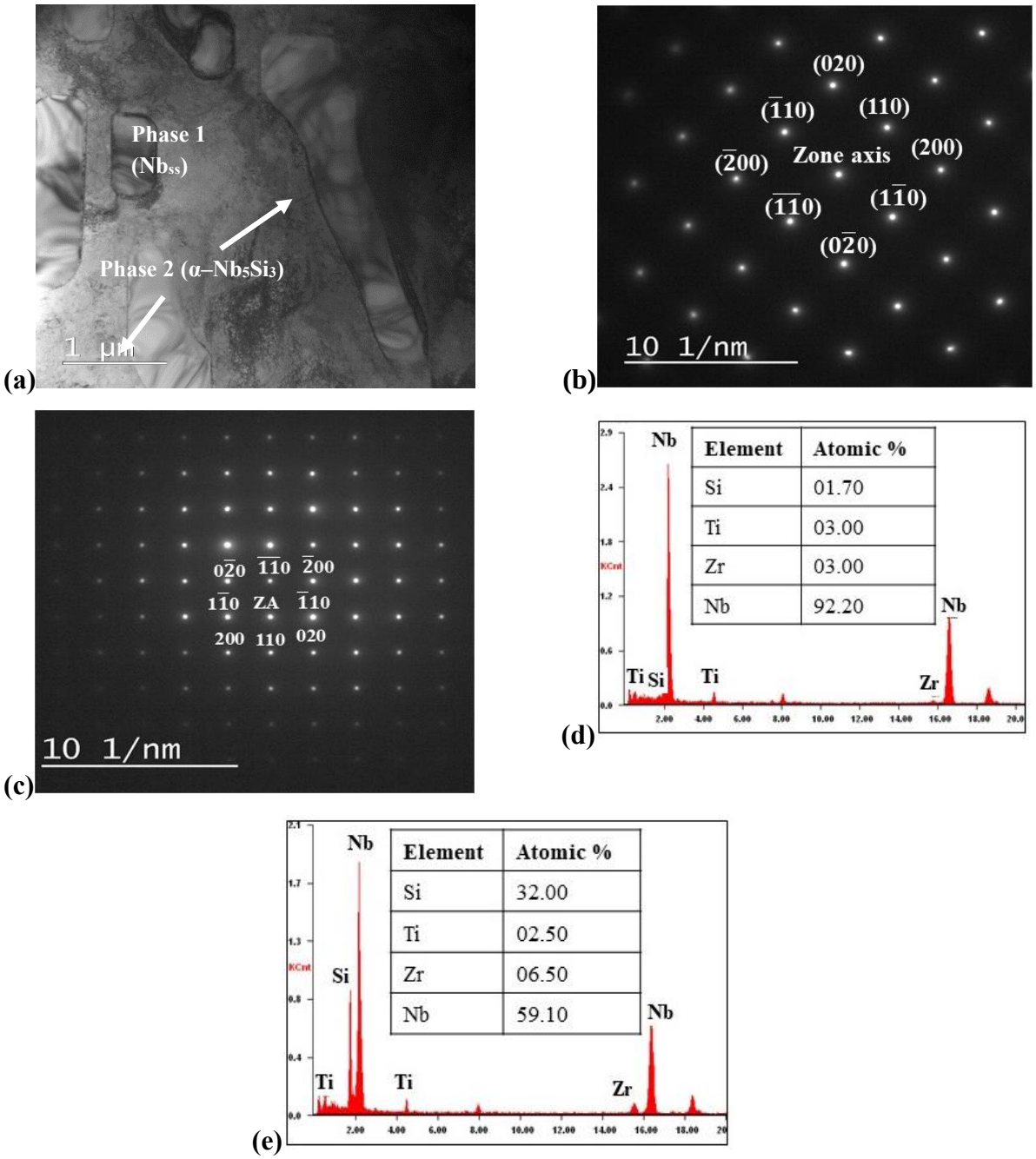

Fig. 4.11: TEM results of Nb-18.7Si-5Ti-5Zr alloy. (a) Bright field image showing the Nb_{ss} and α–Nb_5Si_3 phases, (b,c) SAD pattern for phase 1 (Nb_{ss}) and phase 2 (α–Nb_5Si_3), (d,e) EDAX results of Nb_{ss} and α–Nb_5Si_3 phases, respectively.

The lattice parameter of the Nb_{ss} phase in the alloy is 3.306 Å (**Fig. 4.4(a)**). The a and c of tetragonal α–Nb_5Si_3 phase is observed as 6.56, 11.99, respectively (**Fig. 4.4(b)**). The 'a' values of α–Nb_5Si_3 phase remained almost same whereas 'c' value increased with Ti and Zr additions compared the α–Nb_5Si_3 phase in the Nb-18.7Si-5Zr alloy.

4.1.3 Orientation relationship (OR) in Nb-18.7Si-5Zr and Nb-18.7Si-5Ti-5Zr alloys

The orientation relationship present between the Nb_{ss} and α–Nb_5Si_3 phases in the Nb-18.7Si-5Zr and Nb-18.7Si-5Ti-5Zr alloys is analyzed. Various orientation relationships (OR) between Nb_{ss} and α–Nb_5Si_3 phases reported in the literature are mentioned in the **Table 4.3**. All these orientation relationships are given as input in the HKL channel 5 software and the phase boundaries having these OR is highlighted in the microstructures captured using EBSD (**Figs. 4.12(a,c), 4.13(a,c)**). The phase boundaries with two orientation relationshops (OR1 and OR2 mentioned in **Table 4.3**) reported by Miura et al. [*S. Miura et al., 2005*] are observed to present in the current Nb-18.7Si-5Zr and Nb-18.7Si-5Ti-5Zr alloys. In the present analysis, the OR1 (**Figs. 4.12(a), 4.13(a)**) is observed between Nb_{ss} and α–Nb_5Si_3 phases in the eutectoid region that is mostly present around the primary α–Nb_5Si_3 phase. Similarly, the OR2 (**Figs. 4.12(c), 4.13(c)**) is mostly seen in the eutectoid region which is away from primary α–Nb_5Si_3. **Figs. 4.12(b), Fig. 4.13(d)** shows the angle of deviation between the phase boundaries in the **Figs. 4.12(a), 4.13(c)** from the OR1 ad OR2, respectively in the Nb-18.7Si-5Zr alloy. Similarly, in the Nb-18.7Si-5Ti-5Zr alloy, **Figs. 4.13(b), Fig. 4.13(d)** show the angle of deviation between the phase boundaries in the **Figs. 4.13(a), Fig. 4.13(c)** from the reported OR1 and OR2, respectively. The phase boundaries with OR1 and OR2 with less than 20 degrees deviation is considered. It is also noted from the IPF (Inverse pole figure) orientation map that the Nb_{ss} phase within the domain of eutectoid cell has same crystallographic orientations (**Figs. 4.12(e), Fig. 4.13(e)**).

Table 4.3: Literature data on the orientation relationship between Nb_{ss} and α-Nb_5Si phases in the Nb-Si alloys.

Alloy composition	**Alloy preparation method and heat treatment (HT)**	**Orientation relation (OR)**	**Characterization tool used**	**Reference**
Nb-22Si	Non-consumable arc melting+ HT at 1500 °C for 75 h	(011)α−Nb_5Si_3//(011)Nb (100) α−Nb_5Si_3//(111)Nb	EBSD	*S. Drawin et al., 2005*
Nb-25Si-1.5Zr	Arc melting HT at 1100 °C to 1650 °C for 3 to 100 h	(001)Nb_5Si_3//(001)Nb –when Nb_{ss} acts as nucleating site for eutectoid transformation (OR1)	EBSD	*S. Miura et al., 2005*
		((110)Nb_5Si_3//011)Nb- when primary Nb_5Si_3 acts as nucleating site for eutectoid transformation (OR2)		
Nb-16Si-4Zr	Non consumable arc melting	(011)α−Nb_5Si_3//(011)Nb (100) α−Nb_5Si_3 //(111)Nb	EBSD	*M. Sankar et al., 2018*
Nb-18.7Si-5Zr and Nb-18.7Si-5Ti-5Zr	Non consumable arc melting	(001)Nb_5Si_3//(001)Nb ((110)Nb_5Si_3//011)Nb	EBSD	*Current study*

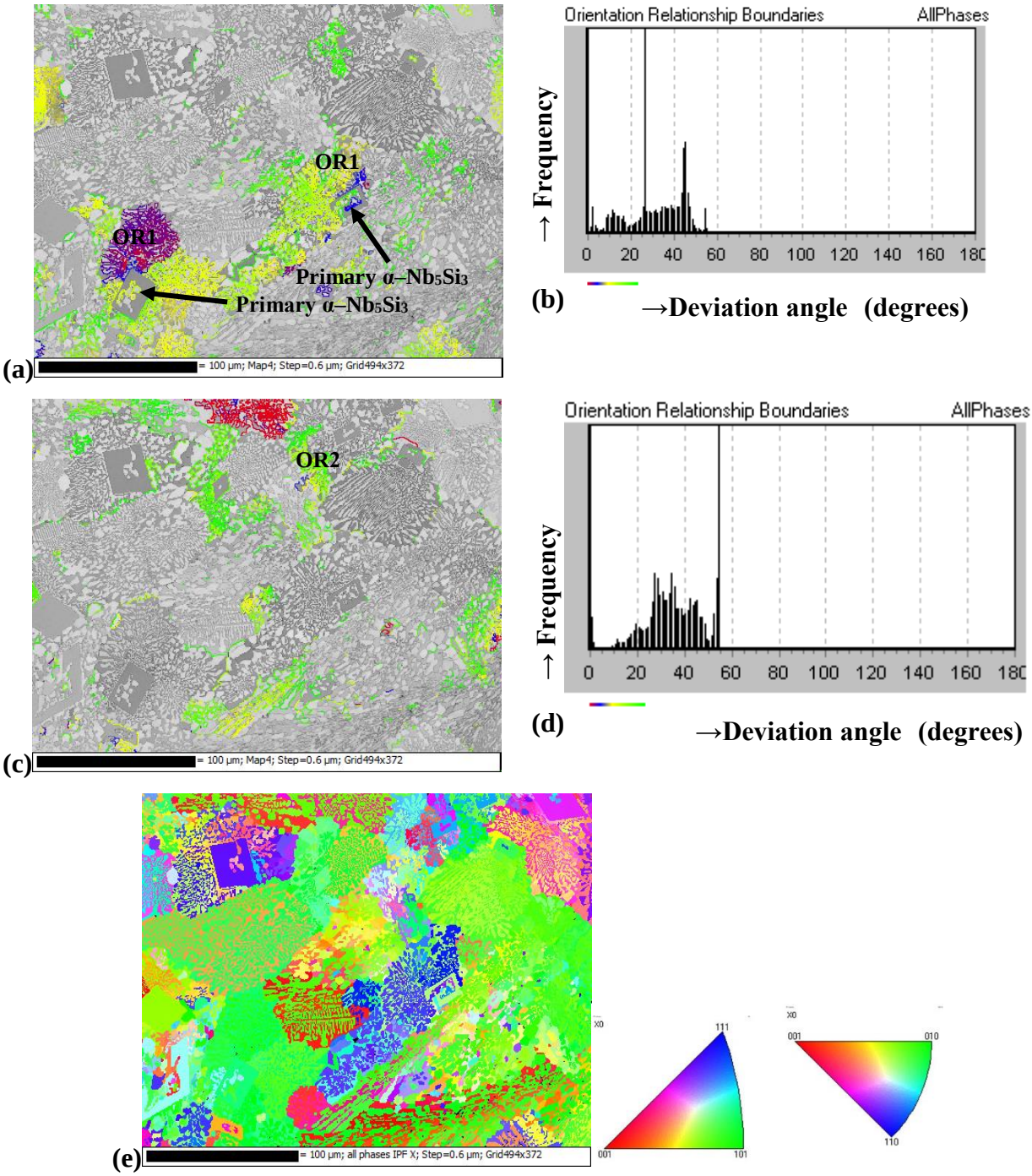

Figs. 4.12: EBSD results of Nb-18.7Si-5Zr alloy. (a) and (c) represent the image quality maps highlighted with OR1 and OR2 adjacent to primary α–Nb_5Si_3 and away from α–Nb_5Si_3 phase, respectively, (b) and (d) shows the deviation angle between the phase boundaries in (a), (c) from the OR1 and OR2, respectively, (e) representation of inverse pole figure (IPF) orientation map. The reader may please refer to the web version of this article for the colored image.

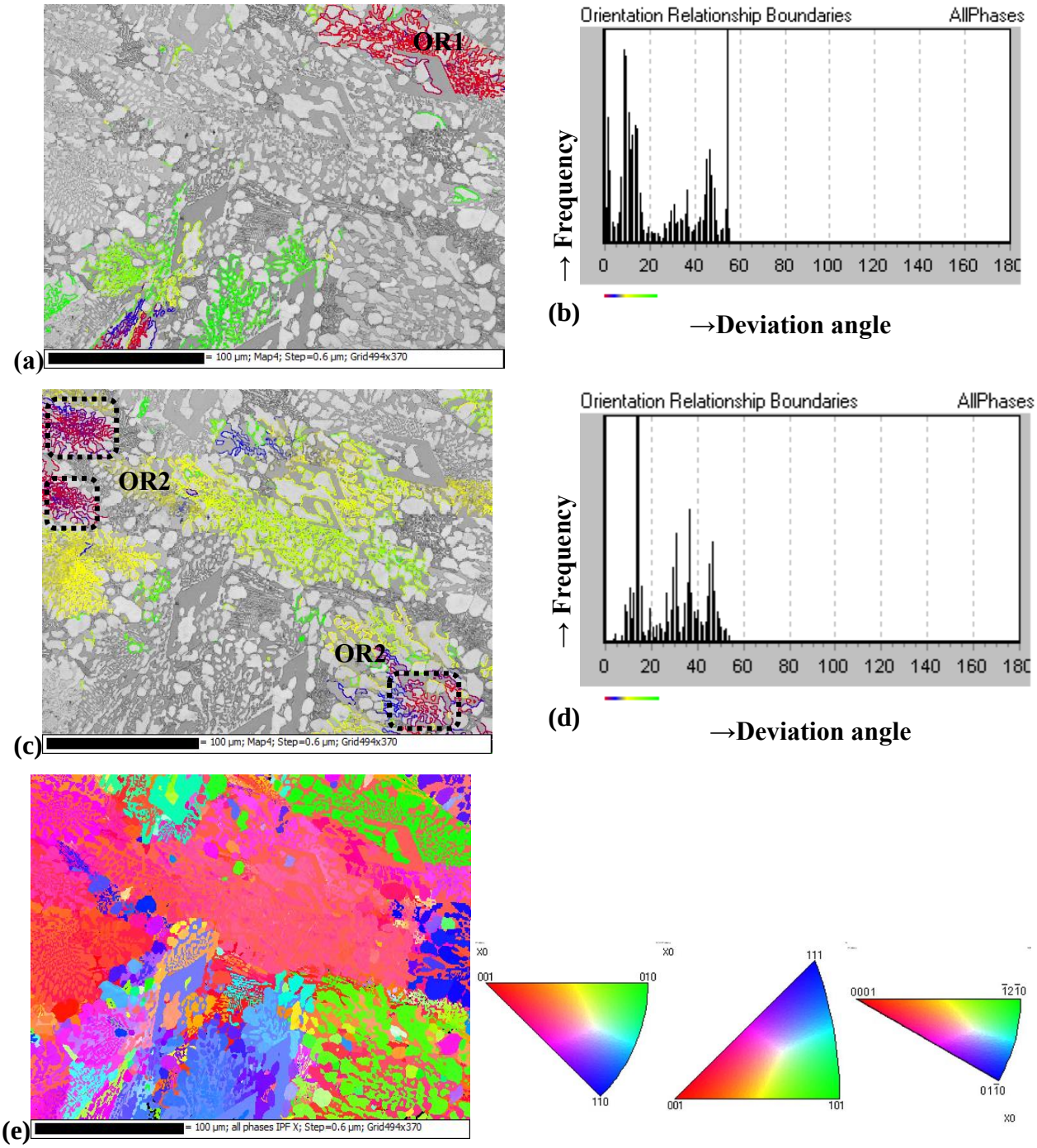

Figs. 4.13: EBSD results of the Nb-18.7Si-5Ti-5Zr alloy. (a), (c) shows the image quality maps highlighted with OR1 and OR2 present adjacent to primary α–Nb_5Si_3 and away from primary α–Nb_5Si_3 phase, respectively, (b), (d) shows the deviation angle between the phase boundaries in (a), (c) from the OR1 and OR2, respectively, (e) representation of IPF orientation map.

The formed eutectoid α–Nb_5Si_3 in OR1 region and primary α–Nb_5Si_3 phases are oriented in same direction (**Figs. 4.12(e), 4.13(e)**) [*S. Miura et al., 2005*]. The Nb_{ss} phase in the formed eutectoid region with OR2 and the eutectic Nb_{ss} phase are oriented in same diection **Figs. 4.12(e), 4.13(e)**) [*L.I. Zifu et al., 2010*].The OR2 is also reported in hypoeutectic Nb-16Si-XZr (X=2,4,6) alloys [*M. Sankar et al., 2018*].

4.2 Discussion

4.2.1 Pancake behavior

The unevenness observed on the surface of the pancakes may be attributed to the localized melting of the alloy (**Fig. 4.1**). The melting occurs in small puddles which solidify quickly due to higher melting temperature of the alloy when the arc zone is moved to other places. The pancake is continuous as a whole although the individual puddles can be distinguished.

4.2.2 Microstructural phase evolution

4.2.2.1 Nb-18.7Si and Nb-18.7Si-5Ti alloys

The Nb-18.7Si and Nb-18.7Si-5Ti alloys have shown the presence of Nb_{ss} and Nb_3Si phase constituents (**Figs. 4.2, 4.5**). The phase constituents remained same in both the alloys in contrast to the presence of 5Ti in alloy Nb-18.7Si-5Ti. It can be understood that the addition of 5Ti did not effect the phase constituents of the near eutectic Nb-18.7Si alloy. It was demonstrated that the higher Ti contents result in the formation of **γ**-Nb_5Si_3 along with Nb_{ss} and Nb_3Si phases [*Y.X. Tian,J.T. Guo, L.Y. Sheng et al., 2008*]. However, such **γ**-Nb_5Si_3 phase is not observed in the current Nb-18.7Si-5Ti alloy due to lower Ti content. Further, coarsening in the Nb_{ss} phase is noticed in Nb-18.7Si-5Ti alloy when compared to Nb-18.7Si alloy (**Figs. 4.2(b) and 4.5(b)**). Similar effect is also reported by Sekido et al. [*N. Sekido et al., 2004, 2006*] in near eutectic alloy with 10Ti addition. Further, in the present alloys, the Nb_3Si phase is also present in the primary form along with the eutectic Nb_3Si. In the exact eutectic composition of Nb-Si alloy, the primary silicide phase formation is not expected. Whereas, in the current study it is observed. So, it appears that the 18.7 at.% of Si concentration is slightly higher side of the eutectic composition [*T.B. Massalski, 1990, Schlesinger et al., 1993, B.P.Bewlay, H.A.Lipsitt et al., 1995*]. Hence, the primary

Nb_3Si phase is expected to form during solidification (**Figs. 4.2 and 4.5**) [*T.B. Massalski, 1990, B.P.Bewlay, H.A.Lipsitt et al., 1995, S. Kashyap et al., 2013*].

Variation of Ti in the silicide phases (primary and eutectic Nb_3Si) in alloy Nb-18.7Si-5Ti has been noted (**Table 4.1**). The Ti content in the primary Nb_3Si is found to be lower than the eutectic Nb_3Si (**Table 4.1**). This is attributed to the solidification phenomena of the alloy. The schematic of phase evolution sequence in the alloys is given in **Fig. 4.14**. The primary Nb_3Si phase is expected to form initially from the liquid phase (**Figs. 4.14(a, b)**). During its formation stage, the Ti segregates or diffuses to the remaining liquid due to its lower melting point [*https://www.americanelements.com/meltingpoint.html*]. Further, at the eutectic temperature, the remaining liquid undergoes eutectic transformation (**Figs. 4.14(b, c)**). Since the liquid is rich in Ti, the corresponding eutectic Nb_3Si is found to be rich in Ti (**Table 4.1**) as compared to primary Nb_3Si phase. The final microstructure consist of primary Nb_3Si along with the eutectic region with eutectic Nb_{ss} and eutectic Nb_3Si phases (**Figs. 4.14(c), 4.2, 4.5**). Therefore, the phase evolution sequence in Nb-18.7Si and Nb-18.7Si-5Ti alloys is written as

$$L \rightarrow \text{Primary } Nb_3Si + L$$
$$\rightarrow \text{Primary } Nb_3Si + (Nb_{ss} + Nb_3Si)_{\text{Eutectic}}$$

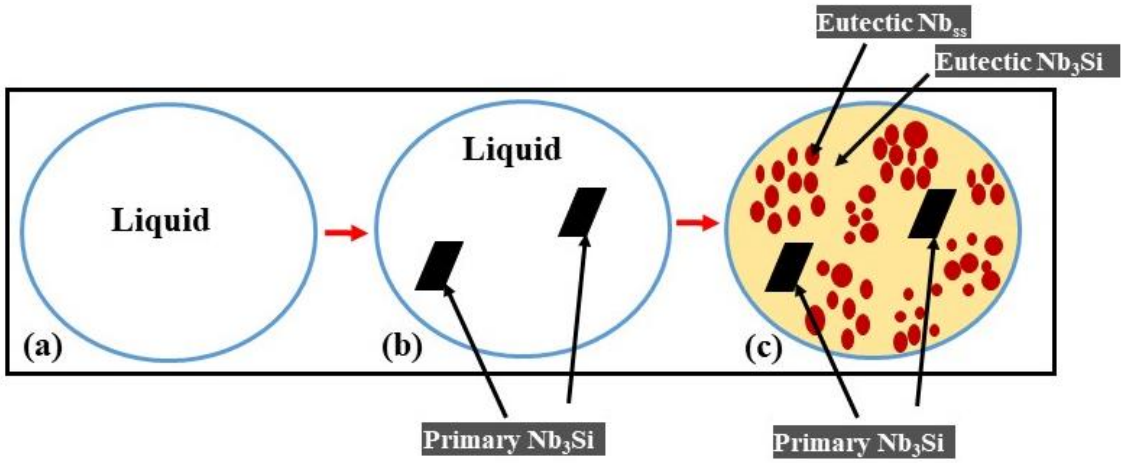

Fig. 4.14: The schematic illustration of the phase evolution in the Nb-18.7Si and Nb-18.7Si-5Ti alloys.

4.2.2.2 Nb-18.7Si-5Zr and Nb-18.7Si-5Ti-5Zr alloys

The formation of Nb_{ss} and α–Nb_5Si_3 silicide phases is observed in Nb-18.7Si-5Zr and Nb-18.7Si-5Ti-5Zr alloys (**Figs. 4.6(a,b), 4.8(a,b)**), in contrast to the Nb_3Si silicide phase in Nb-18.7Si and Nb-18.7Si-5Ti alloys (**Figs. 4.2, 4.5**).

According to the Nb-Si phase diagram, the Nb_{ss} and Nb_3Si phases are expected to form in Nb-Si alloys. There is no possibility to form α–Nb_5Si_3 phase directly from the liquid phase and high temperature Nb_3Si phase retains to room temperature in the microstructure. This is clearly noticed in case of Nb-18.7Si and Nb-18.7Si-5Ti alloys. However, the Nb-18.7Si-5Zr and Nb-18.7Si-5Ti-5Zr alloys exhibited the formation of Nb_{ss} and α–Nb_5Si_3 phases. It has been reported that the α–Nb_5Si_3 phase is expected to form through eutectoid reaction/decomposition of Nb_3Si phase and is reported to be very sluggish even at higher temperatures [*M.G. Mediratta and D.M. Dimiduk et al., 1991*]. The usual practice is to subject these alloys for long hours of vacuum heat treatment to obtain desirable α–Nb_5Si_3 phase through eutectoid reaction ($Nb_3Si \rightarrow Nb_{ss}$+ α–$Nb_5Si_3$). The eutectoid transformation has been reportedly require 100 h of heat treatment at 1500°C in vacuum [*M.G. Mediratta and D.M. Dimiduk et al., 1991, K.S. Chan 2002, B.P. Bewlay et al., 2004*].

In the present work, in Nb-18.7Si-5Zr and Nb-18.7Si-5Ti-5Zr alloys, the cast microstructure exhibited Nb_{ss} and α–Nb_5Si_3 phases. It appears that the Nb_3Si must have formed at the eutectic temperature which might have got transformed to Nb_{ss} and α–Nb_5Si_3 phases during cooling. Further, identification of the orientation relationship between the phases confirms this phase transformation phenomenon. The orientation relationships of (001)Nb_5Si_3 // (001)Nb (OR1) and (110)Nb_5Si_3 // (011)Nb (OR2) are observed between the Nb_{ss} and α–Nb_5Si_3 phases in the Nb-18.7Si-5Zr, Nb-18.7Si-5Ti-5Zr alloys in the present study (**Figs. 4.12(a,c), 4.13(a,c)**) are same as the orientation relationship reported between the Nb_{ss} and α–Nb_5Si_3 phases for the Nb-25Si-1.5Zr alloy after the heat treatment [*S. Miura et al., 2005*]. Hence, it was confirmed that the formation of Nb_{ss} and α–Nb_5Si_3 phases in the current work was mainly due to the eutectoid transformation which occurred during the solidification of the alloy itself.

The recent work by Sankar et al. [*M. Sankar et al., 2018*] observed the formation of α–Nb_5Si_3 phase in cast hypoeutectic Nb-16Si alloy with 4Zr addition. However, for eutectic

composition formation of α–Nb_5Si_3 in the cast condition has never been reported. It is to be noted that 5Zr and combined 5Ti and 5Zr addition to Nb-18.7Si alloy resulted in the eutectoid transformation/decomposition during casting of the alloy. The formation of α–Nb_5Si_3 phase in the cast condition is beneficial as it avoids heat treatment and saves the cost during the preperation of these alloys. The possible reasons for the reduction in time and temperature of eutectoid decompostion of Nb_3Si phase is related to the reduction in the interfacial energy of Nb_{ss}/α–Nb_5Si_3 phases in the presence of Zr [*S. Miura et al., 2008, M. Sankar et al., 2018*].

According to the literature reports, the eutectoid transformation of Nb_3Si leads to the formation of α–Nb_5Si_3 and Nb_{ss} phases in the eutectoid region [*M.G. Mediratta and D.M. Dimiduk et al., 1991, N. Sekido et al., 2004*]. However, the primary α–Nb_5Si_3 phase that is observed in the present work, in case of Nb-18.7Si-5Zr and Nb-18.7Si-5Ti-5Zr alloys found to be faceted, continuous and free from Nb_{ss} phase. This indicates that the primary α–Nb_5Si_3 phase observed in the present work might not have formed through eutectoid reaction. The primary α –Nb_5Si_3 phase formation in the cast alloys is also reported in the hyper eutectic Nb-20Si and Nb-25Si alloys and also in ternary eutectic Nb-18Si-(5,10)Ge alloy [*S. Miura et al., 2008, N. Sekido et al., 2004, L .Zifu et al., 2010*]. The cast microstructures of these alloysreported to form primary β–Nb_5Si_3. Further, the allotropic transformation of primary β–Nb_5Si_3 to primary α–Nb_5Si_3 phase is reported after the vacuum heat treatment at 1400°C for 100 h as well [*S. Miura et al., 2008, N. Sekido et al., 2004, L .Zifu et al., 2010*]. The chosen compositions of Si (Nb-18.7Si-5Zr and Nb-18.7Si-5Ti-5Zr alloys) in the present work might be corresponding to similar type of above hyper eutectic compositions. In such a case, β-Nb_5Si_3 could have formed from the liquid phase which might have subsequently got transformed into primary α–Nb_5Si_3. Hence, it can be attributed that similar allotropic transformation of β–Nb_5Si_3 to α–Nb_5Si_3 phase might have taken place during solidification of the Nb-18.7Si-5Zr and Nb-18.7Si-5Ti-5Zr alloys.

Therefore, The schematic illustration of the phase evolution in Nb-18.7Si-5Zr alloys is given in the **Fig. 4.15**. The solidification of the alloy started by forming primary β–Nb_5Si_3 phase from the liquid (**Fig. 4.15(a, b)**). The remaining liquid transformed to Nb_{ss} and Nb_3Si phases through eutectic rection (**Fig. 4.15(c)**). The product phases from eutectic reaction is termed as eutectic Nb_{ss} and eutectic Nb_3Si. At this stage the microstructure consisted of primary β–Nb_5Si_3, eutectic region with Nb_{ss} and Nb_3Si phases (**Fig. 4.15(c)**). Now the eutectoid products, i.e., Nb_{ss}+

α-Nb_5Si_3 formed from Nb_3Si phase through eutectoid reaction (**Fig. 4.15(d)**). These phases are termed as eutectoid Nb_{ss} and eutecoid α-Nb_5Si_3. Further, the allotropic transformation of primary β-Nb_5Si_3 to α-Nb_5Si_3 phase also took place as shown in the **Fig. 4.15(d)**. The final microstructure consisted of primary α–Nb_5Si_3 phase, eutectic Nb_{ss}, eutectoid Nb_{ss} and eutectoid α–Nb_5Si_3 phases (**Figs. 4.15(d), 4.6**). Finally, the phase evolution sequence in Nb-18.7Si-5Zr alloy can be given as the following:

$$L \rightarrow \text{Primary } \beta\text{–}Nb_5Si_3 + L$$
$$\rightarrow \text{Primary } \alpha\text{–}Nb_5Si_3 + (Nb_{ss}+Nb_3Si)_{\text{Eutectic}}$$
$$\rightarrow \text{Primary } \alpha\text{–}Nb_5Si_3 + \text{Eutectic } Nb_{ss} + (Nb_{ss}+\alpha\text{–}Nb_5Si_3)_{\text{Eutectoid}}$$

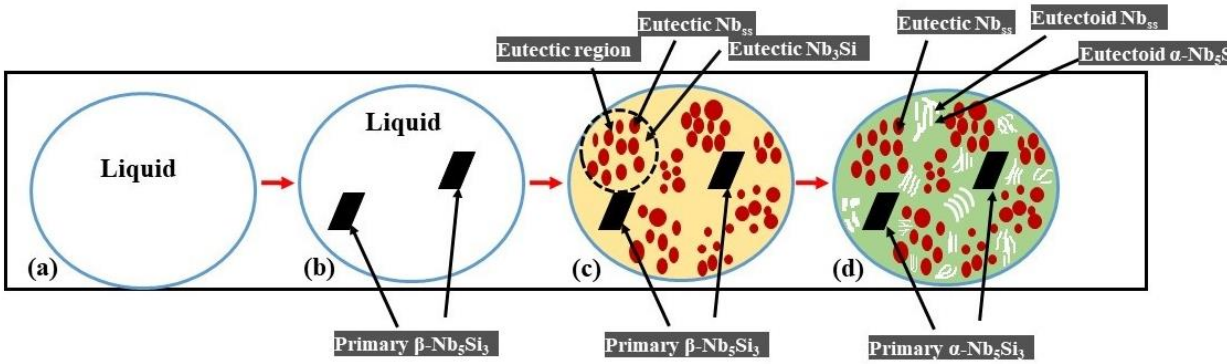

Fig. 4.15: Schematic illustration of the phase evolution in the Nb-18.7Si-5Zr alloy.

The Zr concentration in the primary/faceted morphology α–Nb_5Si_3 phase is lower as compared to the eutectoid α–Nb_5Si_3 (**Table 4.1**). As mentioned in the solidification sequence, the primary α–Nb_5Si_3 phase is expected to form first. During the phase formation stage the Zr diffuses to the liquid phase due to low melting point of Zr [*https://www.americanelements.com/meltingpoint.html*]. The eutectoid α–Nb_5Si_3 phase formation takes place during final stages of the solidification and it results with higher Zr content.

The phase constituents in alloy Nb-18.7Si-5Ti-5Zr are similar to the Nb-18.7Si-5Zr alloy (**Figs. 4.6, 4.8**). However, in addition another phase has been identified in the microstructure is and identified as γ–Nb_5Si_3 on the basis of its hexagonal structure (**Figs. 4.9(a, b)**). The fraction of γ–Nb_5Si_3 phase analyzed is 7%. In the current study, individual addition of Zr or Ti to Nb–18.7Si alloy did not result in the formation of γ–Nb_5Si_3. Whereas, the combined addition formed γ–Nb_5Si_3

in the alloy Nb-18.7Si-5Ti-5Zr. The silicide phase remained as α–Nb_5Si_3 till the concentration of Ti and Zr is 3.80±0.40 and 7.00±0.70 at.%, respectively (named as eutectoid α–Nb_5Si_3 rich in Ti and Zr) (**Fig. 4.8(b), Table 4.1**). The γ–Nb_5Si_3 along with Nb_{ss} phase is observed in very fine morphologies (**Figs. 4.9(a, b)**). The Zr_5Si_3 and Ti_5Si_3 ᵗ are isomorphous with γ–Nb_5Si_3 phase and has hexagonal crystal structure [*Y. Qiao et al., 2017*]. In this alloy, the segregation of low melting point elements Ti and Zr to the last liquid to solidify tend to form the eutectic mixture of $(Nb,Ti,Zr)_5Si_3$ (γ–Nb_5Si_3) and $(Nb,Ti,Zr)_{ss}$ as a direct solidification product (**Figs. 4.9(b), 4.10**). Hence, this Nb_{ss} and γ–Nb_5Si_3 is termed as eutectic product. The presence of γ–Nb_5Si_3 phase has been reported in the high Ti containing alloy with Zr addition, i.e., Nb–24Ti–16Si–(1 to 4) Zr alloy [*Y. X. Tian, J.T. Guo, L.Y. Sheng et al., 2008, Y. Qiao et al., 2017*]. It has been mentioned in the literature that γ–Nb_5Si_3 phase can be formed in the presence of higher concentration of Zr and/or Ti [*Y. X. Tian, J.T. Guo, L.Y. Sheng et al., 2008, M. Sankar et al., 2018, Y. Qiao et al., 2017*]. However, in the current study, it is observed that the combined addition of Ti and Zr in low fraction can even stabilize the γ–Nb_5Si_3 phase.

Therefore, the schematic of the phase evolution sequence in Nb-18.7Si-5Ti-5Zr alloy is shown in **Fig. 4.16** and can be written as the following:

$$L \rightarrow \text{Primary } \beta\text{–}Nb_5Si_3 + L$$
$$\rightarrow \text{Primary } \alpha\text{–}Nb_5Si_3 + (Nb_{ss}+Nb_3Si)_{\text{Eutectic}} + L$$
$$\rightarrow \text{Primary } \alpha\text{–}Nb_5Si_3 + \text{Eutectic } Nb_{ss} + (Nb_{ss}+\alpha\text{–}Nb_5Si_3)_{\text{Eutectoid}} + L$$
$$\rightarrow \text{Primary } \alpha\text{–}Nb_5Si_3 + \text{Eutectic } Nb_{ss} + (Nb_{ss}+\alpha\text{–}Nb_5Si_3)_{\text{Eutectoid}} + (Nb_{ss}+\gamma\text{–}Nb_5Si_3)_{\text{Eutectic}}$$

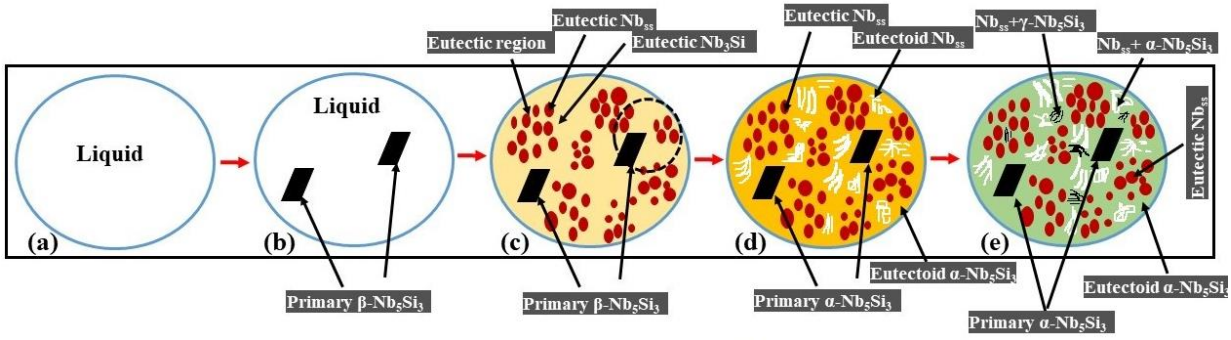

Fig. 4.16: Schematic illustration of the solidification sequence in the Nb-18.7Si-5Ti-5Zr alloy.

From the orientation relationship analysis mentioned in the section 4.1.3, the OR1 in the microstructure (**Figs. 4.12(a), 4.13(a)**) is observed between Nb_{ss} and α–Nb_5Si_3 phases in the eutectoid region that is mostly present around the primary α–Nb_5Si_3 phase. Similarly, the OR2 (**Figs. 4.12(c), 4.13(c)**) is mostly seen in the eutectoid region which is away from primary α–Nb_5Si_3. The OR1 is reported to present between Nb_{ss} and α–Nb_5Si_3 phases if the eutectoid transformation proceeded from primary Nb_5Si_3 phase. This phenomena is generally observed in the hyper eutectic alloys where the primary Nb_5Si_3 phase is expected to form [*S. Miura et al., 2005*]. Similarly, OR2 is reported for the eutectoid region that proceed from Nb_{ss} phase. The presence of both OR1 and OR2 between the eutectoid phases (Nb_{ss} and α–Nb_5Si_3)in the Nb-18.7Si-5Zr, Nb-18.7Si-5Ti-5Zr alloys microstructure shows that the eutectoid transformation in these alloys proceeded from both primary α–Nb_5Si_3 and eutectic Nb_{ss} phases. This shows that the chances of the nucleating sites for the eutectoid transformation increased and hence the transformation kinetics. It can be said that the addition of Zr lone and combined Ti and Zr contibuted in: (1) Primary β–Nb_5Si_3 formation instead of Nb_3Si phase, followed by the allotropic transformation to α–Nb_5Si_3 phase and (2) enhanced the kinetics of the eutectoid transformation of Nb_3Si phase to Nb_{ss} and α–Nb_5Si_3 phases during solidification of the alloy itself.

The Nb_{ss} phase is relatively coarse and distribution is more anomalous (**Fig. 4.15(a)**) in alloy Nb-18.7Si-5Ti as compared to the Nb_{ss} phase in the Nb-18.7Si alloy (**Fig. 4.6(a)**). Similar phase constituents and microstructural observations have been reported for Nb-18.7Si alloy with 10 at.% Ti addition [*N. Sekido et al., 2004, 2006*] and also with 20 at.%Ti addition to Nb-20Si-6Mo alloy [*F. Wang et al., 2017*]. It is noted that the size of Nb_{ss} phase in Nb-18.7Si-5Zr (**Fig. 4.6(a)**) is more coarse and spherical compared to the Nb_{ss} phases in the both the Nb-18.7Si and Nb-18.7Si-5Ti alloys (**Figs. 4.2(a), 4.5(a)**). The Nb_{ss} phase in Nb-18.7Si-5Ti-5Zr alloy is even more coarse and present as continuous at some places compared to Nb-18.7Si, Nb-18.7Si-5Ti and Nb-18.7Si-5Zr alloys (**Fig. 4.8**). The coarsening in the Nb_{ss} phase is observed in the alloys is in the order of Nb-18.7Si<Nb-18.7Si-5Ti<Nb-18.7Si-5Zr<Nb-18.7Si-5Ti-5Zr. In addition, coarsening of the Nb_{ss} lead to it's continuity in the same order. It can be observed that the volume fraction of the Nb_{ss} phase in Nb-18.7Si and Nb-18.7Si-5Ti alloys is almost same (22%). This fraction is more than two times in Nb-18.7Si-5Zr (53%) and Nb-18.7Si-5Ti-5Zr (55%) alloys due to additional eutectoid transformation and resulted in the continuity of the phase compared to Nb-18.7Si and Nb-18.7Si-5Ti alloys. Further, the eutectoid region at some places is present in lamellar

morphology in Nb-18.7Si-5Zr and Nb-18.7Si-5Ti-5Zr alloys (**Figs. 4.6(b), 4.8(b)**) which is reported to be beneficial for the mechanical properties [*N. Sekido et al., 2000*].

The solubility of Si in the Nb_{ss} phase is less in alloy Nb-18.7Si (1.70 at.%) compared to the Nb_{ss} phase in alloy Nb-18.7Si-5Ti (2.98 at.%), given in **Table 4.1**. This increase in the Si content with Ti addition has also been reported in the literature [*N. Villios et al., 2007*]. The presence of higher concentration of lower atomic radius element (Si) might have attributed the decrease in the lattice parameter of Nb_{ss} phase in Nb-18.7Si-5Ti alloy (**Fig. 4.4(a)**) even after presence of Ti which is of higher radius than Nb. The partition of Si is not much changed with Zr addition in alloy Nb-18.7Si-5Zr (1.82 at.%.). Further, the lattice parameter of the Nb_{ss} phase is increased, due to the higher atomic radius of Zr (**Fig. 4.4(a)**). The Si dissolution in Nb_{ss} phase is increased with combined Ti and Zr addition compared to binary alloy and the corresponding lattice parameter value is decreased in Nb-18.7Si-5Ti-5Zr alloy but still the value is lower than the Nb_{ss} phase in Nb-18.7Si alloy (**Fig. 4.4(a)**). The Nb_{ss} phase of Nb-18.7Si-5Ti-5Zr alloy consisted of Ti, Si of low atomic radius and Zr of high atomic radius than the Nb. Presence of lower atomic radius elements (Ti, Si) in higher concentration than the high atomic radius element (Zr) might have played dominant role in the lattice parameter value of the Nb_{ss} phase (**Table 4.1**).

As mentioned in **Fig. 4.4(b)**, there is a slight decrease in both a and c of the Nb_3Si phase with Ti addition resulting in reduction in c/a ratio. This indicates that the Ti occupied both a and c axis of the tetragonal Nb_3Si. The a and c of tetragonal α–Nb_5Si_3 phase in Nb-18.7Si-5Zr alloy is 6.59Å and 12.01Å, respectively. The c/a ratio is 1.8224, which is slightly higher than the c/a ratio of standard tetragonal α–Nb_5Si_3 phase (1.8107). This idicates that the Zr occupied c axis of the tetragonal α–Nb_5Si_3 phase. The ‘a’ values of tetragonal α–Nb_5Si_3 phase decreased to 6.56 and ‘c’ value increased to 11.99 in Nb-18.7Si-5Ti-5Zr alloy. Therfore, a slight increase in the c/a value to 1.822 is noticed. The effect of Ti and Zr on the a and c values needs further analysis.

4.3 Summary

The current chapter included the understanding of the microstructure and phase evolution in the near eutectic Nb-18.7Si with lone 5Ti, 5Zr and their combined addition. The major findings are as the following:

1. The microstructure of cast Nb-18.7Si and Nb-18.7Si-5Ti alloys exhibited Nb_{ss} and Nb_3Si phases.
2. Addition of 5 at.% Zr (Nb-18.7Si-5Zr) and combined addition of 5 at.% Ti and 5 at.% Zr to the Nb-18.7Si alloy (Nb-18.7Si-5Ti-5Zr) resulted in Nb_{ss} and α–Nb_5Si_3 phases in the cast alloys. This is ascribed to the increase in the eutectoid transformation during casting. Such phase transformation is beneficial in the time and cost saving during the preparation of the alloys.
3. In particular, coarsening and increase in the volume fraction of the Nb_{ss} phase is observed in the order of Nb-18.7Si < Nb-18.7Si-5Ti < Nb-18.7Si-5Zr < Nb-18.7Si-5Ti-5Zr alloys.
4. The alloying addition effected the dissolution of Si content in the Nb_{ss} phase.

Chapter- 5

Structure-property correlation and deformation mechanisms

5.0 Introduction

This chapter is devoted to the mechanical behaviour of the selected alloys i.e., Nb-18.7Si, Nb-18.7Si-5Ti, Nb-18.7Si-5Zr and Nb-18.7Si-5Ti-5Zr. The chapter is divided into two sections. In the first section, the micro-mechanical properties (hardness, elastic modulus) of the phases are discussed in the first section. The room temperature bulk mechanical properties such as compression strength and fracture toughness are presented in the second section. Further, the fracture behaviour of the alloys is discussed from the surface morphology and microstructural characterization of the failed samples using SEM and TEM analysis.

(A) Micro mechanical properties of the phases

5.1 Results

The micromechanical properties such as hardness (H) and elastic modulus (E) of the individual phases play a major role in the bulk mechanical properties of the alloys. Therefore, the H and E values of the phases are measured in all the alloys using nano indentation method.

5.1.1 Statistical analysis of the indentation data

In this section, the results of the large number of indentation tests and the representative statistical analysis results are discussed. Maps for the hardness and modulus are generated over the microstructural area of 10×10 μm with 2.5 mN load. **Fig. 5.1(a)** shows the hardness histograms for all the samples collected from 2,500 indentation data from the selected microstructural area of each sample. The histogram corresponding to each alloy exhibited multiple peaks. It can be noted

that the Nb-18.7Si and Nb-18.7Si-5Ti alloys consists of two peaks. The Nb-18.7Si alloy showed peaks centered at around the hardness value of 4.57 GPa and 12.88 GPa, likewise at the hardness value of around 5.15 GPa and 13.41 GPa for Nb-18.7Si-5Ti alloy. Whereas, the histogram corresponding to the Nb-18.7Si-5Zr and Nb-18.7Si-5Ti-5Zr alloys revealed three peaks. The peaks in the Nb-18.7Si-5Zr alloy are located at the hardness value of around 4.41 GPa, 26.50 GPa and 16.74 GPa. Similarly, at 5.39 GPa, 25.17 GPa and 15.67 GPa for the Nb-18.7Si-5Ti-5Zr alloy. The counts on the Y-axis represents the fraction of the phases present in the microstructural area considered for maps generation. The counts for the Nb_{ss} phase are more for Nb-18.7Si-5Zr and Nb-18.7Si-5Ti-5Zr alloys due to high volume fraction of the phase compare to the Nb-18.7Si and Nb-18.7Si-5Ti alloys. This is in line with the observed phase fractions in the alloys, as given in **Table 4.2** of Chapter-4.

Similarly, **Fig. 5.1(b)** shows the histogram for elastic modulus data collected from 2,500 indentations data. The peaks in the curves are not as sharp as in the hardness histogram (**Fig. 5.1(a)**). The Nb-18.7Si and Nb-18.7Si-5Ti alloys exhibited two peaks centered at around the value of 175 GPa, 210 GPa and 140 GPa, 225 GPa, respectively. Whereas, only one peak is distinguishable clearly in Nb-18.7Si-5Zr and Nb-18.7Si-5Ti-5Zr alloys which are present at around 150 GPa.

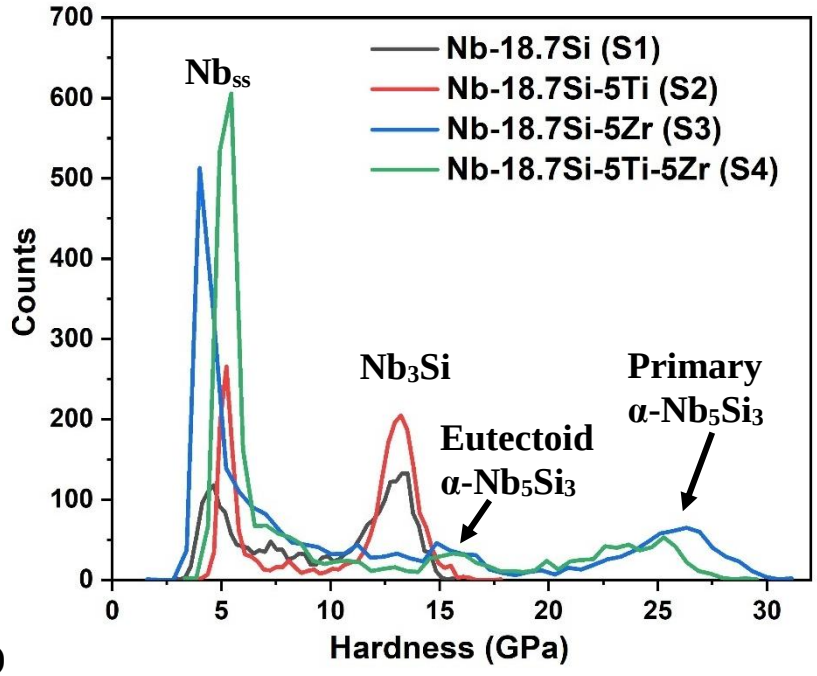

(a)

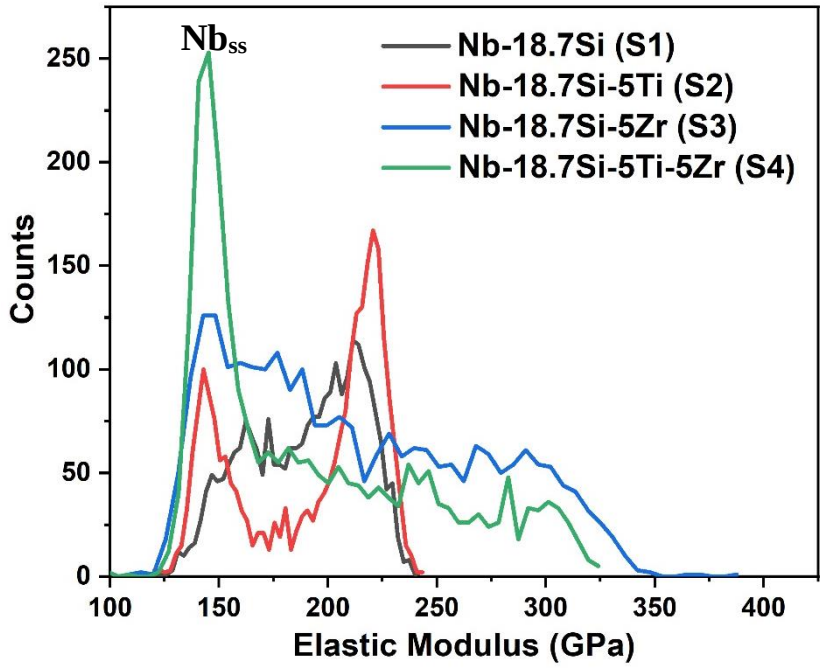

(b)

Fig. 5.1: Histograms showing the hardness (a) and elastic modulus variation in the phases of the alloys determined from 2,500 indents done at a load of 2.5 mN.

Fig. 5.2(a) and **5.2(b)** shows the cumulative distribution of the hardness and elastic modulus respectively, in the microstructural area considered in the alloys. The hardness values of the H_{30}, H_{50} and H_{90} corresponds to the 30^{th}, 50^{th} and 90^{th} percentile, respectively are given in **Table 5.1**. Similarly, the elastic modulus values of the E_{30}, E_{50} and E_{90} are also given. There is a change in the cumulative hardness behaviour for the alloys at around H_{40} (40^{th} percentile). Till this point the Nb-18.7Si and Nb-18.7Si-5Ti alloys has higher hardness and lower cumulative probability than for the Nb-18.7Si-5Zr and Nb-18.7Si-5Ti-5Zr alloys (**Fig. 5.2(a)**). After H_{40} the distribution of Nb-18.7Si and Nb-18.7Si-5Ti alloys shifted to lower hardness values and the cumulative probability is more compared to the Nb-18.7Si-5Zr and Nb-18.7Si-5Ti-5Zr alloys. This gives the comparative data of the phase fractions present in the particular microstructural area of the alloys. Cumulative probability is a direct indicative of the volume fraction of the phases in the present case. The less cumulative probability for Nb-18.7Si and Nb-18.7Si-5Ti alloys till H_{40} represents low volume fraction of the low hardness phase compared to Nb-18.7Si-5Zr and Nb-18.7Si-5Ti-5Zr alloys. Similarly, the cumulative distribution of the high hardness phase is less in Nb-18.7Si-5Zr and Nb-18.7Si-5Ti-5Zr alloys compared to Nb-18.7Si and Nb-18.7Si-5Ti alloys. This represents the low volume fraction of the high hardness phase in Nb-18.7Si-5Zr and Nb-

18.7Si-5Ti-5Zr alloys compared to Nb-18.7Si and Nb-18.7Si-5Ti alloys. This trend in the volume fraction of the phases is in line with the measured volume fraction of the phases given in the **Table 4.2** of Chapter-4. Similar kind of results can be understood from the elastic modulus cumulative distribution profiles (**Fig. 5.2(b)**).

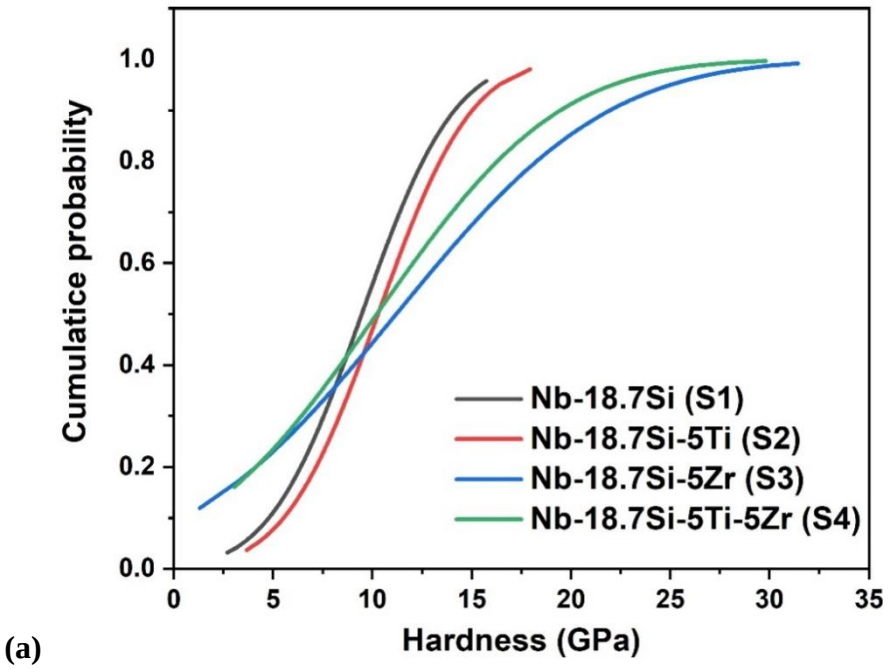

(a)

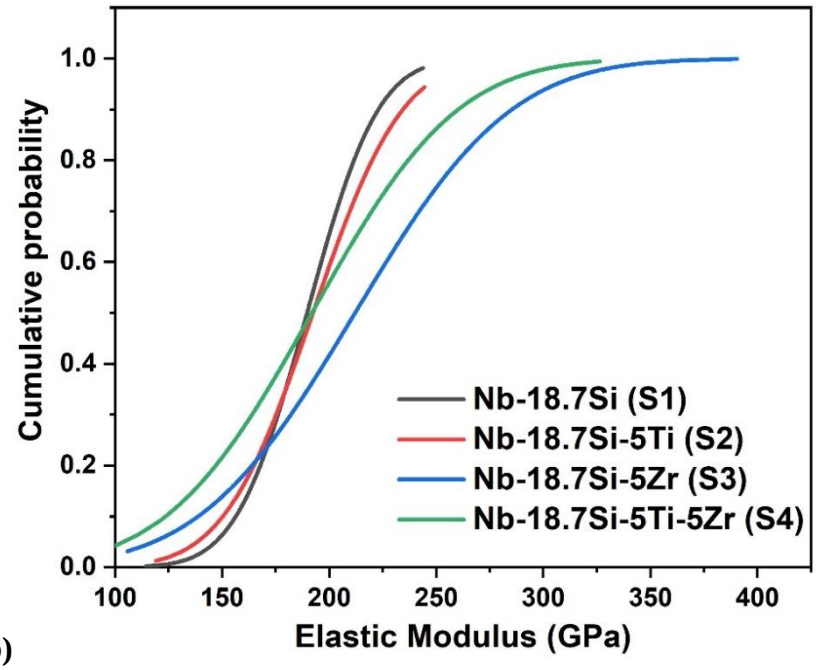

(b)

Fig. 5.2: Cumulative distribution profiles corresponding to the hardness (a) and elastic modulus (b) which are determined from 2,500 indents done at a load of 2.5 mN.

Table 5.1: Nano indentation hardness and elastic modulus values of the alloys obtained from the Cummulative distribution function (in GPa)

Alloy	H_{30}	E_{30}	H_{50}	E_{50}	H_{90}	E_{90}
Nb-18.7Si	7.5	175	9	185	14	225
Nb-18.7Si-5Ti	8.5	175	10	185	15	230
Nb-18.7Su-5Zr	6.0	185	10	217	20	280
Nb-18.7Si-5Ti-5Zr	6	165	12.5	190	22.5	260

5.1.2 Mechanical property mapping

Hardness (H) and modulus (E) maps are discussed in this section for better understanding of the histograms given in section 5.1.1. The H and E maps performed for the various alloys are shown in the **Fig. 5.3-5.6**. The correlation with the local SEM-BSE images (**Figs. 5.3(a), 5.4(a), 5.5(a), 5.6(a)**) allows for the direct evaluation of the representative properties of the phases. A large variation in the hardness and modulus values among the phases present in the alloys is noticed from the color contrast in the maps (**Figs. 5.3(b, c), 5.4(b, c), 5.5(b, c), 5.6(b, c)**).

The microstructure of the Nb-18.7Si and Nb-18.7Si-5Ti alloys exhibited two phase region corresponding to Nb_{ss} and Nb_3Si, as discussed in the previous chapter and also shown in **Figs. 5.3(a), 5.4(a)**. In contrast, the Nb-18.7Si-5Zr and Nb-18.7Si-5Ti-5Zr alloys exhibited Nb_{ss} and α-Nb_5Si_3 phases. Further, the presence of elemental rich (Ti and/or Zr) α-Nb_5Si_3 phase is also identified as discussed in the previous chapter-4 and also shown in **Figs. 5.5(a), 5.6(a)**. All these phase regions are clearly seen and distinguishable in the hardness and modulus maps (**Figs. 5.3-5.6**).

The hardness and modulus values of the phases are mentioned in the **Table 5.2**. The H values for the Nb_{ss} and Nb_3Si phases in Nb-18.7Si alloy are of 4.57±0.68 GPa and 12.83±0.39 GPa (**Fig. 5.3 (b), Table 5.2**) and their corresponding E values are of 136.4± 8.70 GPa and 212.2± 9.37 GPa, respectively (**Fig. 5.3 (c), Table 5.2**). The primary and eutectic variants of Nb_3Si phase exhibited same H value and also the E values (**Table 5.2**).

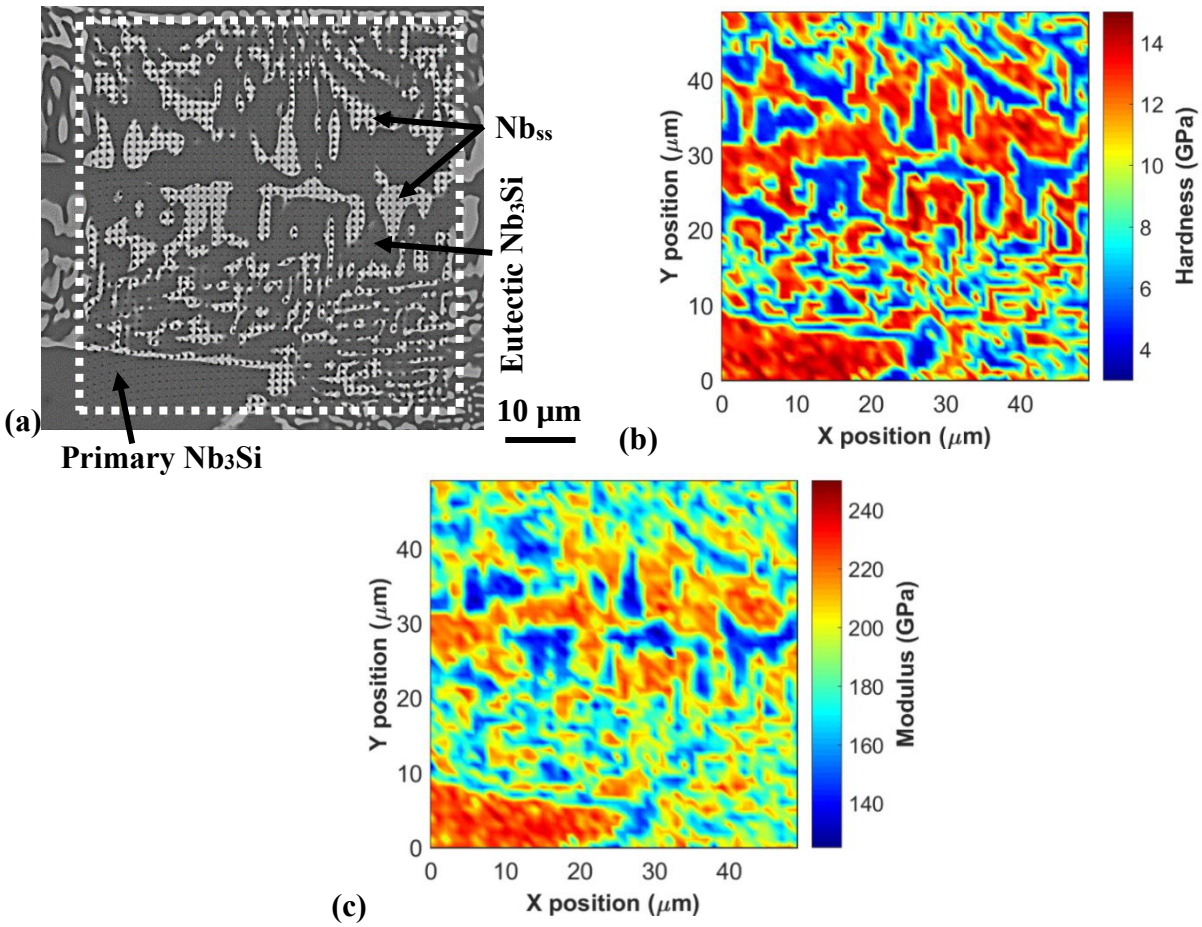

Fig. 5.3: Nb-18.7Si alloy. (a) SEM-BSE image with marked region shows the microstructural area considered for maps with the indentation array, (b) Hardness and (c) Elastic modulus maps.

The H value for the Nb_{ss} and Nb_3Si phases in Nb-18.7Si-5Ti alloy are of 5.15±0.24 GPa and 13.41±0.83 GPa, respectively and the corresponding E values are 144.69±5.06 GPa and 219.20±9.88 GPa (**Fig. 5.4 (b, c), Table 5.2**). The primary and eutectic variants of Nb_3Si phase did not exhibit significant differences in the respective H and E values.

The Nb_{ss} phase in Nb-18.7Si-5Zr alloy exhibited the H value of 4.41±0.25 GPa. The H value of primary α–Nb_5Si_3 is of 26.50±1.40 GPa (**Fig. 5.5(b)**) and eutectoid α–Nb_5Si_3 phase (**Fig. 5.5(a, b)**) measured with 16.74±1.26 GPa. The Nb_{ss} phase has E of 140.23±8.53 GPa (**Fig. 5.5(c)**). The E of the primary α–Nb_5Si_3 and eutectoid α–Nb_5Si_3 is 303.4±10.80 GPa and 265.02±7.93 respectively (**Fig. 5.5(c), Table 5.2**).

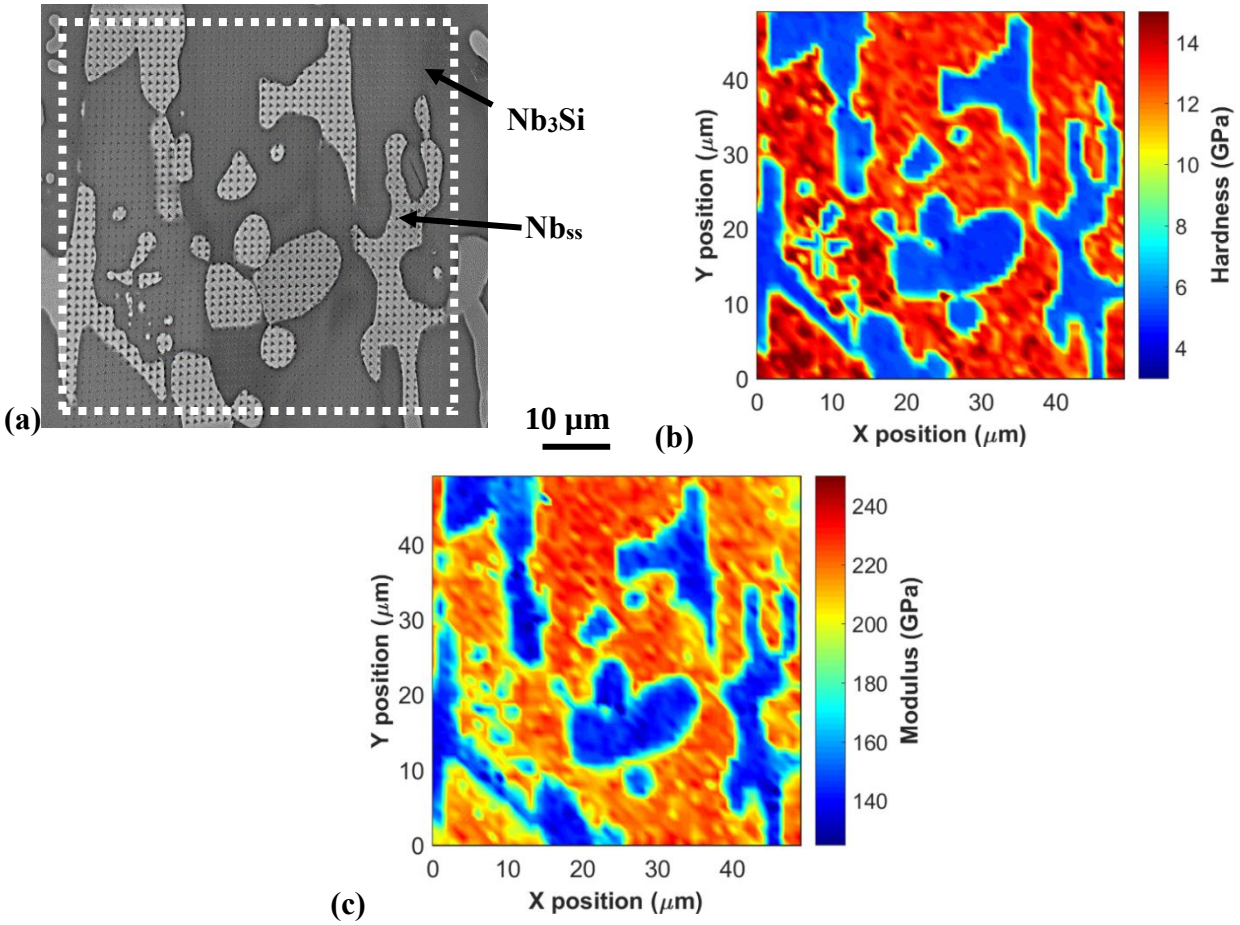

Fig. 5.4: Nb-18.7Si-5Ti alloy, (a) SEM-BSE image with marked region shows the microstructural area considered for maps with the indentation array, (b) hardness and (c) elastic modulus maps.

The H value of 5.39±0.22 GPa is recorded with the Nb_{ss} phase in Nb-18.7Si-5Ti-5Zr alloy. The hardness of primary α–Nb_5Si_3 and eutectoid α–Nb_5Si_3 phase has almost same value of 25.17±1.26 GPa (**Fig. 5.6(a, b), Table 5.2**). The hardness of eutectoid α–Nb_5Si_3 phase in the Ti and Zr rich region (can be seen in **Fig. 4.8 (b). 5.6(a)**) is of 15.67±1.39 GPa. The hardness of the γ–Nb_5Si_3 could not be evaluated as it is present in fine morphology (**Figs. 4.9** and **5.6(a)**). The modulus of the Nb_{ss} phase (140.25±5.34 GPa) is significantly lower than primary α–Nb_5Si_3 and eutectoid α–Nb_5Si_3 phase (290.00±8.92 GPa) (**Fig. 5.6(c), Table 5.2**). The modulus of the eutectoid α–Nb_5Si_3 which is rich in Ti and Zr is of 247.82±9.69 GPa.

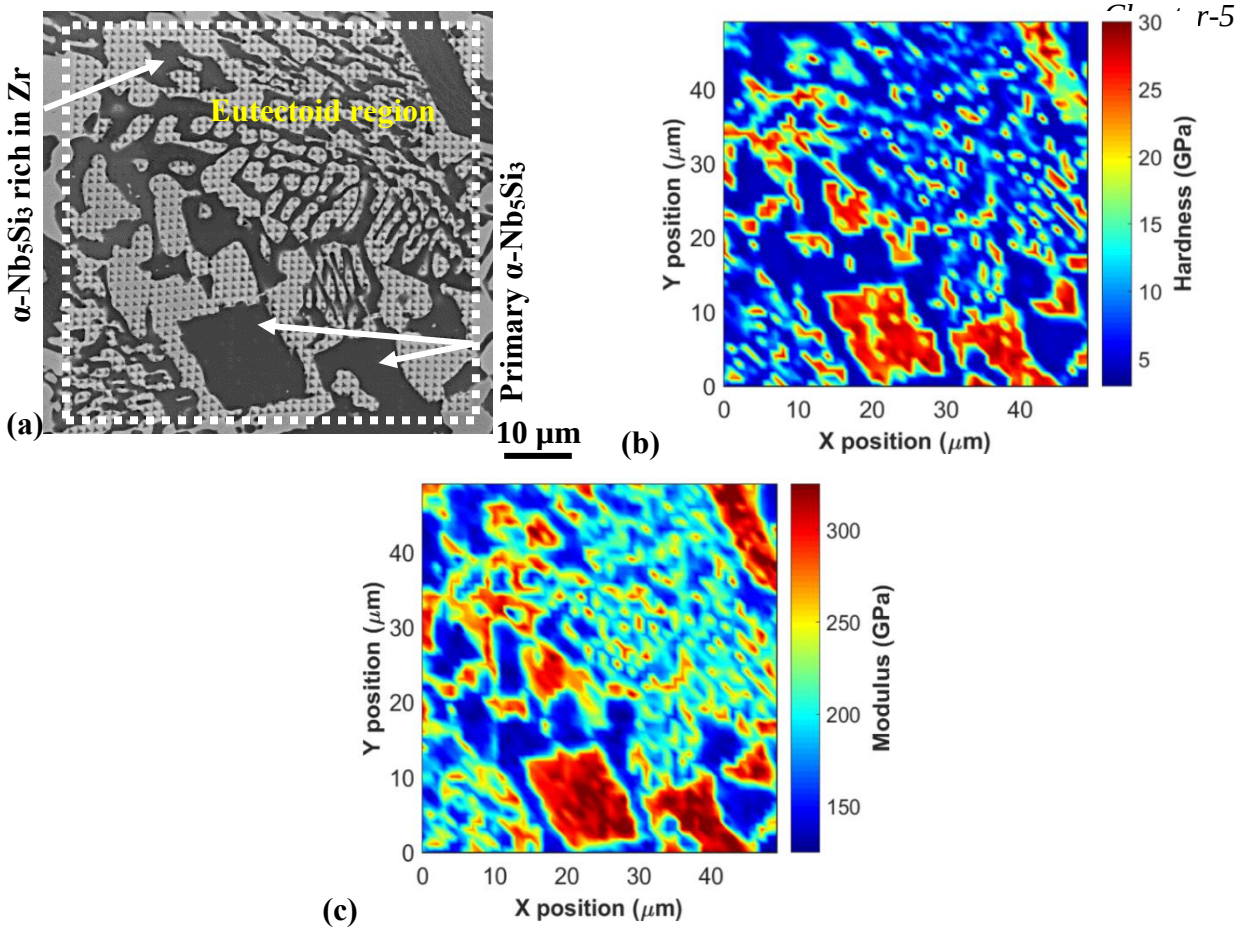

Fig. 5.5: Nb-18.7Si-5Zr alloy. (a) SEM-BSE image with marked region shows the microstructural area considered for maps with the indentation array, (b) and (c) hardness and modulus maps, respectively corresponding to the microstructure in (a).

Table 5.2: Phases present in the alloys with volume fraction and corresponding hardness, modulus values.

Alloy composition	**Phases observed**	**Volume fraction (%)**	**Hardness (GPa)**	**Modulus (GPa)**
Nb-18.7Si	Nb_{ss}	22±1.52	4.57±0.68	136.4± 8.70
	Primary & eutectic Nb_3Si	78±1.52	12.83±0.99	212.2± 9.37
Nb-18.7Si-5Ti	Nb_{ss}	23±2	5.15±0.24	144.69±5.06
	Primary & eutectic Nb_3Si	77±2	13.41±0.83	219.20±9.88
Nb-18.7Si-5Zr	Nb_{ss}	53±0.51	4.41±0.25	140.23±8.53
	Primary α–Nb_5Si_3	47±0.51	26.50±1.40	303.4±14.80
	Eutectoid α–Nb_5Si_3		16.74±1.26	265.02±7.93
Nb-18.7Si-5Ti-5Zr	Nb_{ss}	55±2	5.39±0.22	140.25±5.34
	Primary α–Nb_5Si_3 and eutectoid α–Nb_5Si_3	38±2	25.17±1.26	290.00±8.92
	Eutectoid α–Nb_5Si_3 rich in Ti, Zr		15.67±1.39	247.82±9.69
	γ–Nb_5Si_3	7±2	--	--

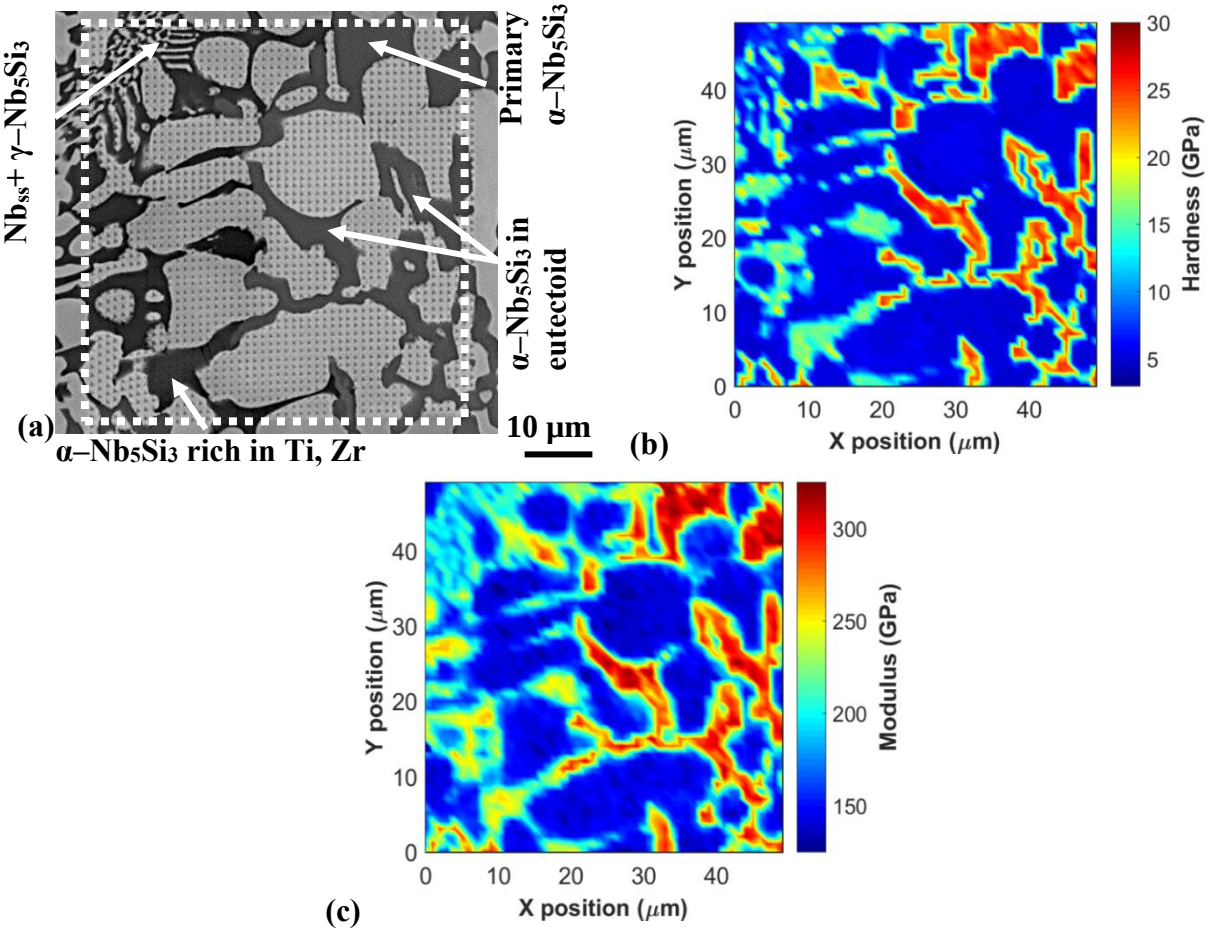

Fig. 5.6: Nb-18.7Si-5Ti-5Zr alloy. (a) SEM-BSE image with marked region shows the microstructural area considered for maps with the indentation array, (b) and (c) hardness and modulus maps corresponding to the microstrucutre in (a).

The variation in the hardness and modulus values of the phases are compared and presented in the bar graph in **Fig. 5.7**. The hardness of the Nb_{ss} phase is increased by 12.6% with Ti addition in Nb-18.7Si-5Ti alloy (**Fig. 5.7(a)**). The hardness value is slightly decreased with Zr addition in Nb-18.7Si-5Zr alloy (**Fig. 5.7(a), Table 5.2**). This value is again increased by 17.9% with combined addition of Ti and Zr in Nb-18.7Si-5Ti-5Zr. A minor increase in the hardness of the silicide (Nb_3Si) phase by 4.3% is observed in Nb-18.7Si-5Ti alloy compared to Nb-18.7Si-5Ti alloy. The hardness of the silicide phase (α–Nb_5Si_3) in Nb-18.7Si-5Zr and Nb-18.7Si-5Ti-5Zr alloys is almost doubled compared to the silicide phase (Nb_3Si) in Nb-18.7Si and Nb-18.7Si-5Ti alloys. The hardness of the α–Nb_5Si_3 phase, i.e., both primary and eutectoid variants is decreased

by 5% and 6.4%, respectively with combined addition of Ti and Zr in Nb-18.7Si-5Ti-5Zr alloy compared to Nb-18.7Si-5Zr alloy in which Zr alone is added (**Fig. 5.7(a), Table 5.2**).

The modulus of the Nb_{ss} phase increased in the alloy Nb-18.7Si-5Ti by 6.10% compared to the alloy Nb-18.7Si. This modulus value of Nb_{ss} phase almost same in Nb-18.7Si-5Zr and Nb-18.7Si-5Ti-5Zr alloys (**Fig. 5.7(b), Table 5.2**) and the value increased by 2.8% compared to Nb_{ss} phase in the Nb-18.7Si alloy. The modulus value of the Nb_3Si phase is increased by 4.5% with Ti addition in Nb-18.7Si-5Ti compared to binary Nb-18.7Si alloy (**Fig. 5.7(b), Table 5.2**). The silicide phase (α–Nb_5Si_3) modulus in the Nb-18.7Si-5Zr and Nb-18.7Si-5Ti-5Zr alloys is increased by 30% than the silicide phase (Nb_3Si) in Nb-18.7Si and Nb-18.7Si-5Ti alloys. Both the primary and eutectoid variants of α–Nb_5Si_3 phase is decreased by 4.3% and 18.3% with combined addition of Ti and Zr in Nb-18.7Si-5Ti-5Zr alloy compared to Nb-18.7Si-5Zr alloy in which Zr alone is added (**Fig. 5.7(b), Table 5.2**).

5.2 Discussion

5.2.1 Alloying effect on the micro-mechanical properties of the phases

The silicide phase (Nb_3Si) is three times harder than the Nb_{ss} phase in both the Nb-18.7Si and Nb-18.7Si-5Ti alloys. The silicide phase (α–Nb_5Si_3) in Nb-18.7Si-5Zr and Nb-18.7Si-5Ti-5Zr alloys is almost five times harder than the Nb_{ss} phase. Both the intermetallic silicide phases have complex tetragonal crystal structures compared to the simple body centered cubic structure of the Nb_{ss} phase. This attributed to the higher hardness of silicide phases compared to the Nb_{ss} phase. Further, the α–Nb_5Si_3 phase exhibited even higher hardness due to its more complex tetragonal structure compared to the Nb_3Si tetragonal phase.

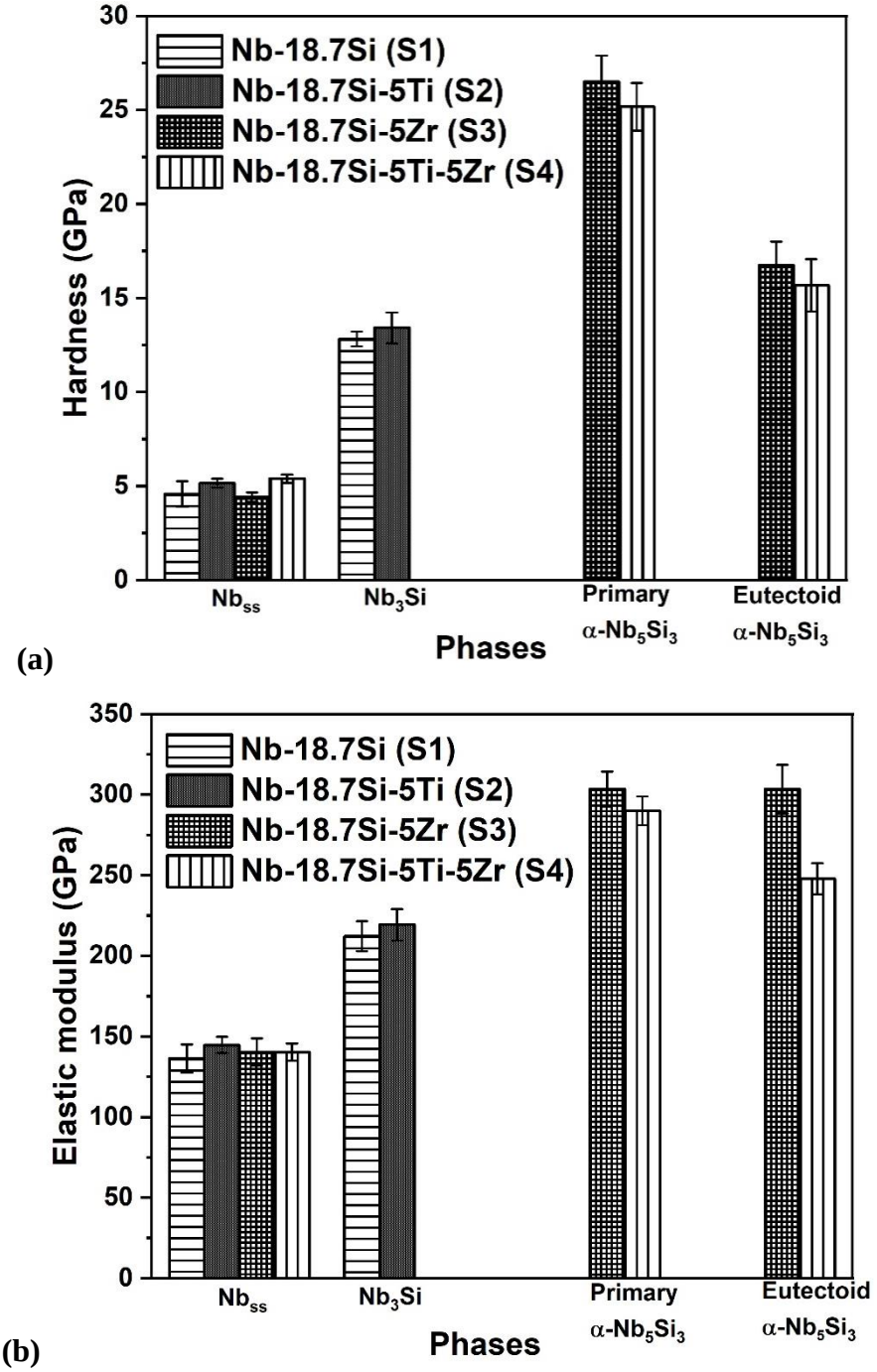

Fig. 5.7: Bar chart showing the variation in the mechanical properties of the phases. (a) Hardness and (b) Elastic modulus.

The H and E of the Nb_{ss} phase is higher in alloy Nb-18.7Si-5Ti (5.15±0.22 GPa) compared to the Nb_{ss} phase (4.57±0.28 GPa) in the Nb-18.7Si alloy. This can be attributed to the the higher Si distribution and presence of Ti in the Nb-18.7Si-5Ti alloy (**Table 4.1**). Ti is known to be a softening element to Nb phase. A decrease in the H of Nb_{ss} phase is reported with Ti addition in Nb-xTi-1Si and Nb-xTi-4Si (where x = 0-10 at.%) alloys [*N. Sekido et al., 2004*]. The solid solution softening of Nb_{ss} phase with Ti addition is also reported in the Nb-Cr-Ti system [*K.S. Chan et al., 1997*]. However, in the present case though Ti is present in Nb_{ss} phase in the Nb-18.7Si-5Ti alloy, the relative contribution of higher Si content increased the hardness significantly. On the other hand, a slight decrease in the hardness value is observed (4.41±0.25 GPa) with Zr addition in Nb-18.7Si-5Zr alloy (**Fig. 5.7(a)**). This decrease in the hardness of the Nb_{ss} phase is also reported in Nb-16Si-6 Zr alloy [*M. Sankar et al., 2018*]. The combined addition of Ti and Zr in Nb-18.7Si-5Ti-5Zr again increased the H value to 5.39±0.22 GPa. This shows the solid solution strengthening of Nb_{ss} phase with combined Ti and Zr addition. The Si content in the Nb_{ss} phase of Nb-18.7Si-5Ti-5Zr is higher than the Nb_{ss} phase of Nb-18.7Si-5Zr alloy (**Table 4.1**).

As mentioned earlier (in chapter-4), the addition of Ti or Zr effects the solubility of Si in the Nb_{ss} phase. The presence of Ti increased the solubility of Si in Nb_{ss} phase while the solubility remains alomost the same with Zr addition. The Si content in the Nb_{ss} phase of Nb-18.7Si-5Ti-5Zr is higher than the Nb_{ss} phase of the Nb-18.7Si-5Zr alloy (**Table 4.1**). In the present study, Ti contained alloys exhibited high hardness than Ti free alloys for the Nbss phase due to increase in the solubility of Si in the phase in presence of Ti. Thereby, resulting in the higher hardness in Nb-18.7Si-5Ti and Nb-18.7Si-5Ti-5Zr alloys compared to Nb-18.7Si and Nb-18.7Si-5Zr alloys. It appears from the hardness values that the dissolved Si content in the Nb_{ss} phase is playing a dominant role in deciding the hardness value of the phase.

A minor increase in the H and E value of the Nb_3Si phase in alloy Nb-18.7Si-5Ti (219.20±9.88 GPa) compared to alloy Nb-18.7Si (212.2± 9.37 GPa) is noticeable (**Fig. 5.7, Table 5.2**). This shows the solid solution strengthening of Nb_3Si phase with Ti addition. The hardness of the primary and eutectic Nb_3Si phases is same in the Nb-18.7Si alloy as the composition remained same (**Table 4.1**). There is no change in the H and E of the primary and eutectic Nb_3Si phase in the Nb-18.7Si-5Ti alloy irrespective of the difference in Ti content (**Table 4.1**). This Ti variation in the phases might not have affected the H and E properties of the silicide phase significantly.

The primary α–Nb_5Si_3 phase exhibited higher hardness of 26.50±1.40 GPa than the eutectoid α–Nb_5Si_3 phase (16.74±1.26 GPa) in the Nb-18.7Si-5Zr alloy. This may be due to the softeninig effect of the silicide phase with higher content of Zr in the eutectoid α–Nb_5Si_3 phase than in the primary α–Nb_5Si_3 phase. This solid solution softening of α–Nb_5Si_3 by Zr addition is in line with the literature reports [*M. Sankar et al., 2019*]. Similarly, the E of the primary and eutectoid α–Nb_5Si_3 phases is 303.4±14.80 GPa and 265.02±7.93 GPa respectively. In Nb-18.7Si-5Ti-5Zr alloy, The primary α–Nb_5Si_3 which is lean in Ti and Zr contents exhibited higher H and E values compared to the Ti and Zr rich eutectoid α–Nb_5Si_3 phase (**Fig. 5.6(a), Table 5.2**). The solid solution softening of the α–Nb_5Si_3 phase with Ti and Zr additions might have caused this variation. The lower H and E of eutectoid α–Nb_5Si_3 phase in Nb-18.7Si-5Ti-5Zr alloy than in Nb-18.7Si-5Zr alloy shows the dominance of solid solution softening effect of the silicide phase with combined addition of Ti and Zr compared to Zr addition alone (**Fig. 5.6(a), Table 5.2**).

(B) Bulk mechanical properties

5.3 Results

5.3.1 Compression properties and Fracture behavior of the alloys

The compression properties evaluated for the alloys are given in the **Fig. 5.8** and **Table 5.3**. The Nb-18.7Si alloy exhibited the yield strength (YS) and fracture strength (FS) of 727±145 MPa and 735±140 MPa, respectively (**Fig. 5.8(a)**). Similarly, the Nb-18.7Si-5Ti alloy showed YS and FS values of 958±147 MPa and 961±149 MPa, respectively. In contrast, the alloys Nb-18.7Si-5Zr and Nb-18.7Si-5Ti-5Zr exhibited a drastic increase in both the YS and FS values. The Nb-18.7Si-5Zr alloy displayed the YS and FS values of 1639±28 MPa and 1857±58 MPa, respectively. Further the Nb-18.7Si-5Ti-5Zr alloy exhibited the values of 1589±59 MPa and 2236±81 MPa for YS and CS, respectively (**Fig. 5.8(a)**). The change in the strain values are also presented in **Fig. 5.8(b)** and **Table 5.3**. The total fracture strain of 2.67±0.25%, 2.43±0.50% is noted for Nb-18.7Si and Nb-18.7Si-5Ti alloys, respectively (**Fig. 5.8(b)**, **Table 5.3**). Relatively high fracture strain was observed for Nb-18.7Si-5Zr and Nb-18.7Si-5Ti-5Zr alloys and measured as 6.23±0.66% and 10.16±0.59%, respectively. The plastic strain of 0.47±0.03%, 0.33±0.05%, 1.31±0.30% and 2.67±0.33% was evidenced for Nb-18.7Si, Nb-18.7Si-5Ti, Nb-18.7Si-5Zr and Nb-18.7Si-5Ti-5Zr

alloys, respectively. In summary, the following points can be drwan from the compression properties of the alloys: (i) The YS and FS in the Nb-18.7Si alloys is almost the same, similarly for the Nb-18.7Si-5Ti alloy, (ii) The YS of the Nb-18.7Si-5Ti alloy increased by 24% compared to the Nb-18.7Si alloy, (iii) Nb-18.7Si-5Zr and Nb-18.7Si-5Ti-5Zr alloys exhibited a drastic increase in the YS to almost double the value compared to Nb-18.7Si alloy, Further (iv) The FS is higher than the YS in both Nb-18.7Si-5Zr and Nb-18.7Si-5Ti-5Zr alloys and also (v) the plastic strain is increased in both Nb-18.7Si-5Zr, Nb-18.7Si-5Ti-5Zr alloys compared to Nb-18.7Si and Nb-18.7Si-5Ti alloys, which indicates good amount of deformation prior to fracture in the former alloys.

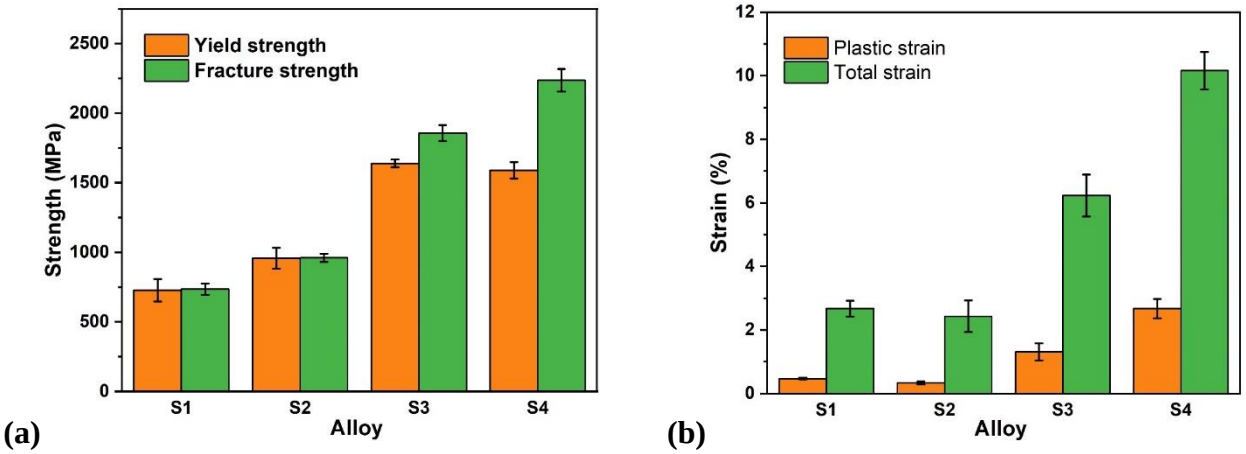

Fig. 5.8: Bar graph showing the variation in the room temperature compression properties of the alloys, (a) Yield and compressive strength (b) total and plastic strain. The S1, S2, S3 and S4 in the figures corresponds to the Nb-18.7Si, Nb-18.7Si-5Ti, Nb-18.7Si-5Zr and Nb-18.7Si-5Ti-5Zr alloys respectively.

Table 5.3: Room temperature compression and fracture toughness properties of the alloys.

Alloy	**yield strength (YS in MPa)**	**Fracture strength (FS in MPa)**	**Plastic strain (%)**	**Total fracture strain (%)**	**Fracture toughness (MPa.m$^{1/2}$)**
Nb-18.7Si	727±145	735±140	0.47±0.03	2.67±0.25	5.84±0.38
Nb-18.7Si-5Ti	958±147	961±149	0.33±0.05	2.43±0.50	6.69±0.15
Nb-18.7Si-5Zr	1639±28	1857±58	1.31±0.30	6.23±0.66	10.40±0.18
Nb-18.7Si-5Ti-5Zr	1589±59	2236±81	2.67±0.33	10.16±0.59	10.59±0.35

The fracture surfaces of the compression tested samples are shown in the **Fig. 5.9**. The surface of both the primary and eutectic/eutectoid constituents of the silicide phase (Nb_3Si/α-Nb_5Si_3) is smooth and faceted features are observed (**Figs. 5.9 (a-d, h)**). Further cracks are observed in the silicide phase (**Figs. 5.9 (d, h)**). This depicts the brittle nature of fracture of the silicide phase (Nb_3Si/ α-Nb_5Si_3 phase) (**Figs. 5.9 (a-d, h)**). The bright contrast of the fractured surface indicates a slight amount of plastic deformation in the Nb_{ss} phase [**Figs. 5.9 (b, e-h)**]. Further, interface seperation at the Nb_{ss} and silicide (Nb_3Si/α-Nb_5Si_3) phases in the eutectic/eutectoid regions (**Figs. 5.9 (b, e)**) and also between primary silicide to eutectoid region is noticed **Fig. 5.9 (h)**. This indicates the interface debonding/decohesion in the alloys. Pull out of the Nb_{ss} phase is also noticed in the Nb-18.7Si-5Zr alloy **Fig. 5.9 (e)**. Further, non linear growth of the crack by formation of steps in the lamellar eutectoid region is observed (**Fig. 5.9 (g, i)**).

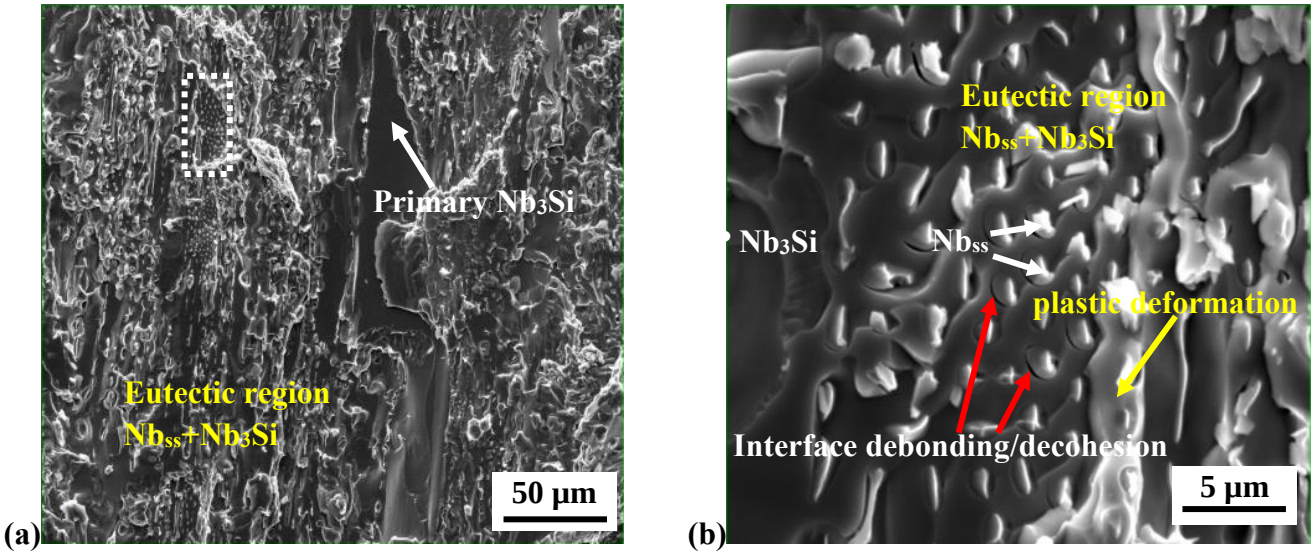

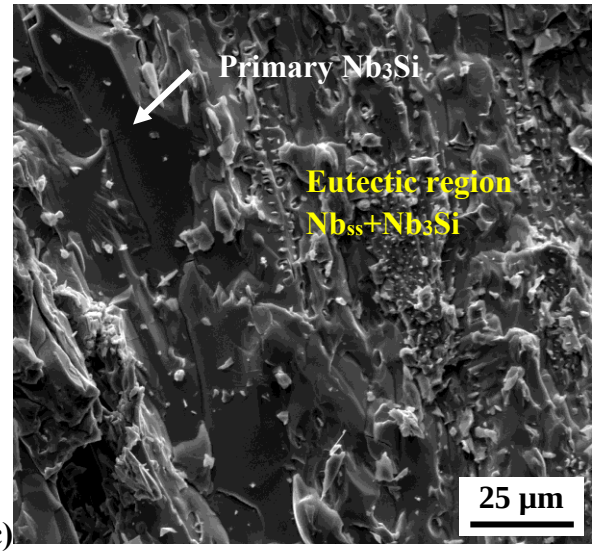
Primary Nb_3Si
Eutectic region
Nb_{ss}+Nb_3Si
25 µm

(c)

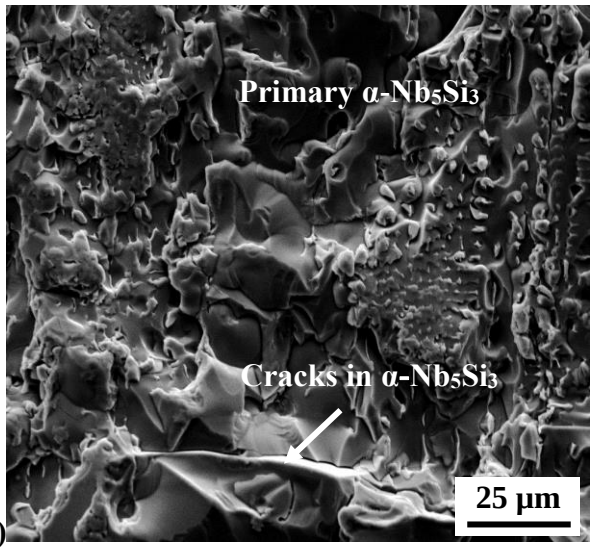
Primary α-Nb_5Si_3
Cracks in α-Nb_5Si_3
25 µm

(d)

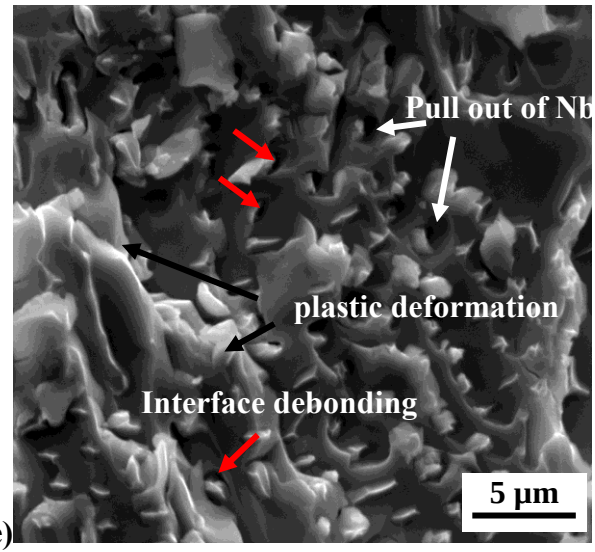
Pull out of Nb
plastic deformation
Interface debonding
5 µm

(e)

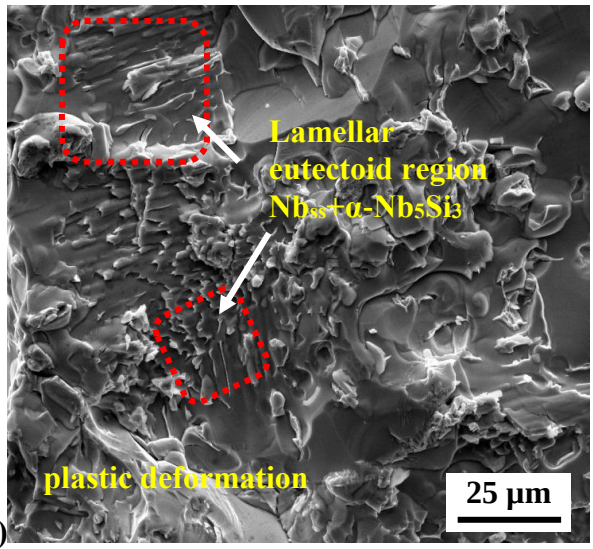
Lamellar
eutectoid region
Nb_{ss}+α-Nb_5Si_3
plastic deformation
25 µm

(f)

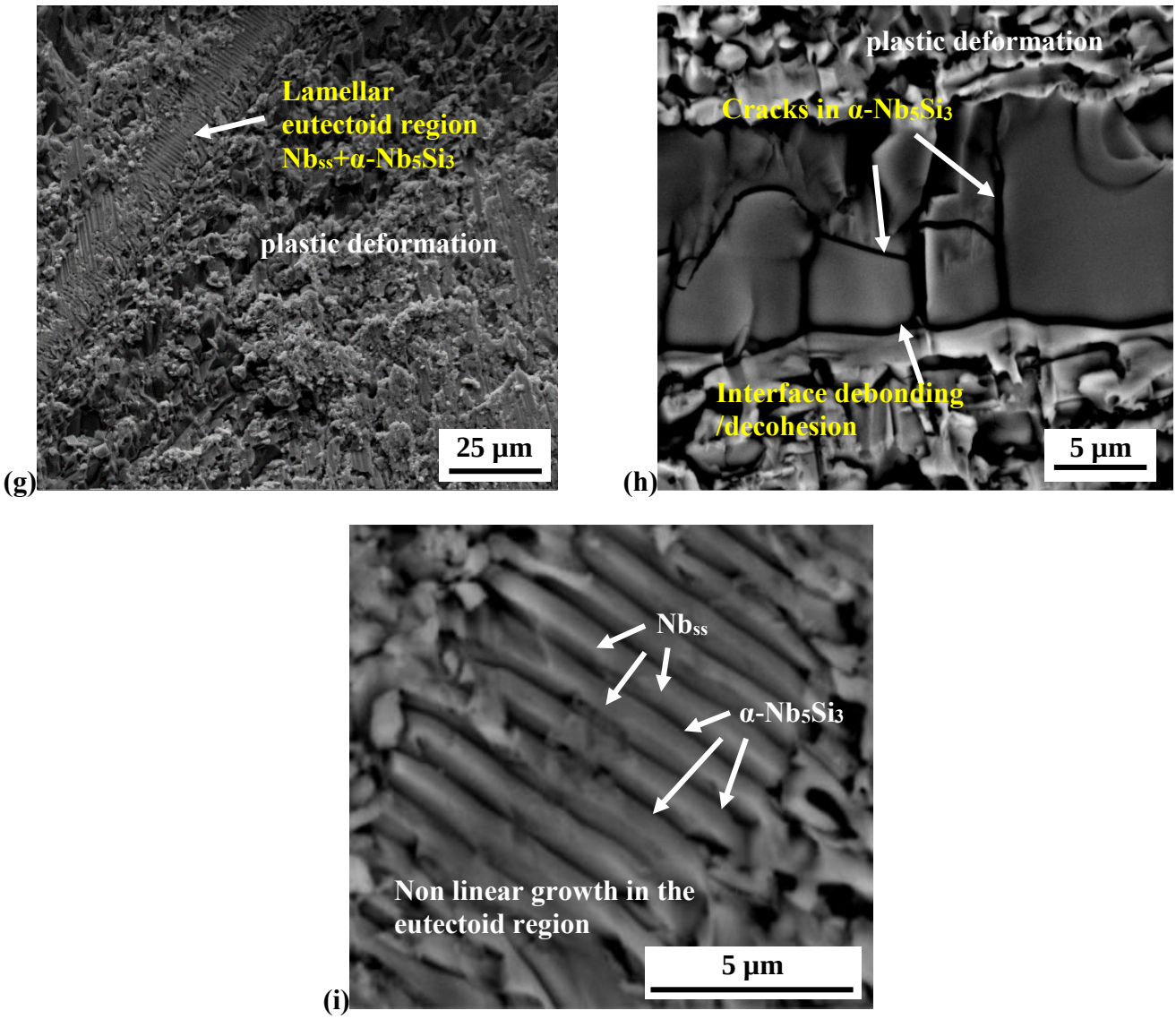

Fig. 5.9: Fracture surfaces of the compression tested samples where, (a,b) Nb-18.7Si, (c) Nb-18.7Si-5Ti, (d-f) Nb-18.7Si-5Zr, (g-i) Nb-18.7Si-5Ti-5Zr alloys.

The crack initiation and propagation behaviour in the alloy is further understood from the analysis of SEM-BSE images taken from the crack initiation region (indent corners) of the bulk indents and also from the polished samples of the post fractured surfaces (**Fig. 5.10**). It is noticed that the cracks initiated in the silicide phase (Nb_3Si/α-Nb_5Si_3) and propagated in tortuous manner by leaving the ductile Nb_{ss} phase. The crack propagation energy was reduced by crack bridging (**Fig. 5.10(a)**), crack branching and deflection (**Fig. 5.10(b)**) phenomena in the Nb-18.7Si alloy. On the other hand, crack deflection and bridging phenomena is seen in the alloy Nb-18.7Si-5Ti

(**Figs. 5.10(c, d)**). Further, crack deflection phenomena and severe fracture in the primary α-Nb_5Si_3 phase can be seen in Nb-18.7Si-5Zr and Nb-18.7Si-5Ti-5Zr alloys (**Figs. 5.10(e, f)**). In addition, the crack propagation path is more crooked in the eutectoid region with coarse Nb_{ss} phase absorbing more energy compared to the propagation path in the eutectic/eutectoid region with fine Nb_{ss} phase (**Fig. 5.10(f)**).

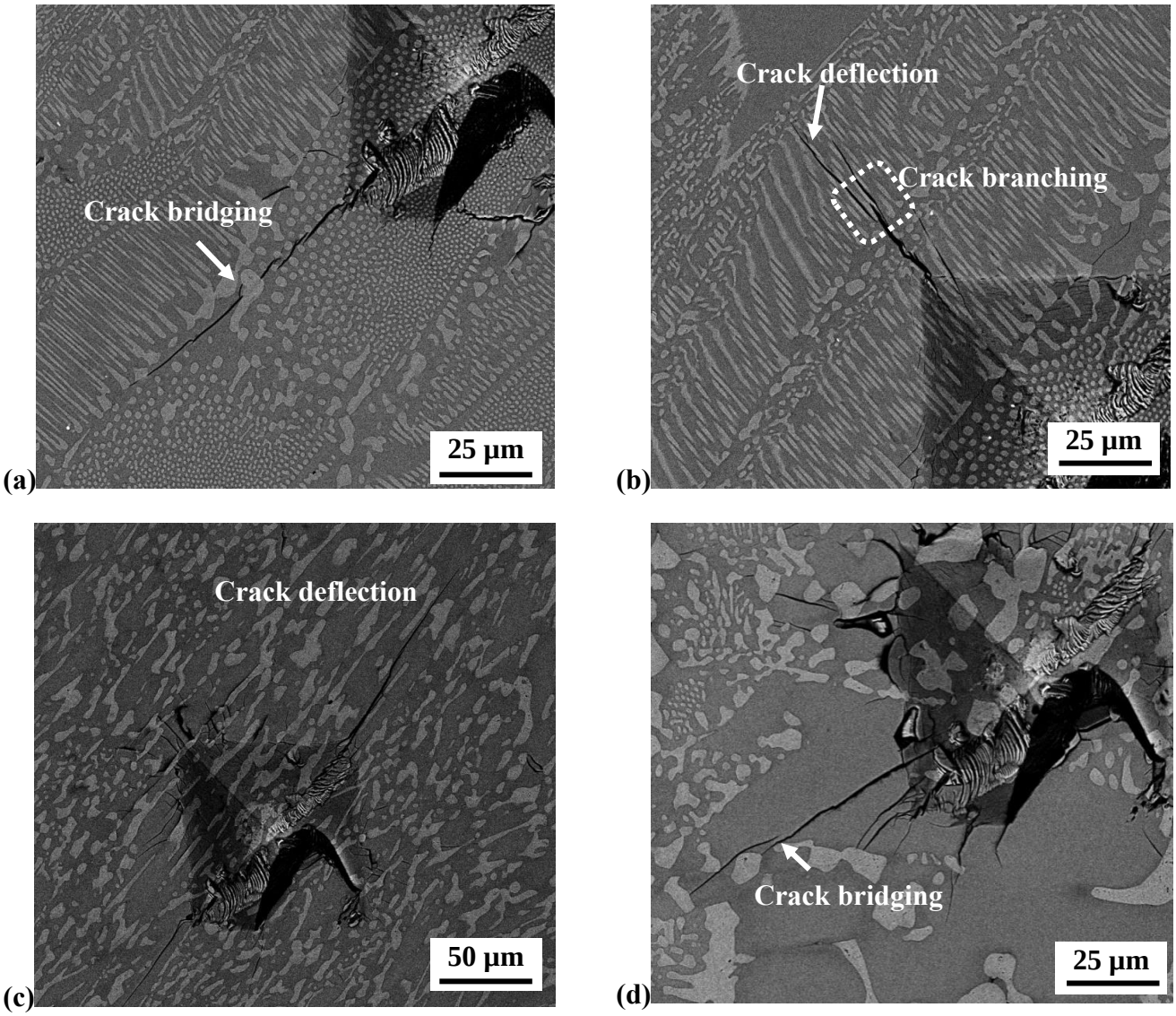

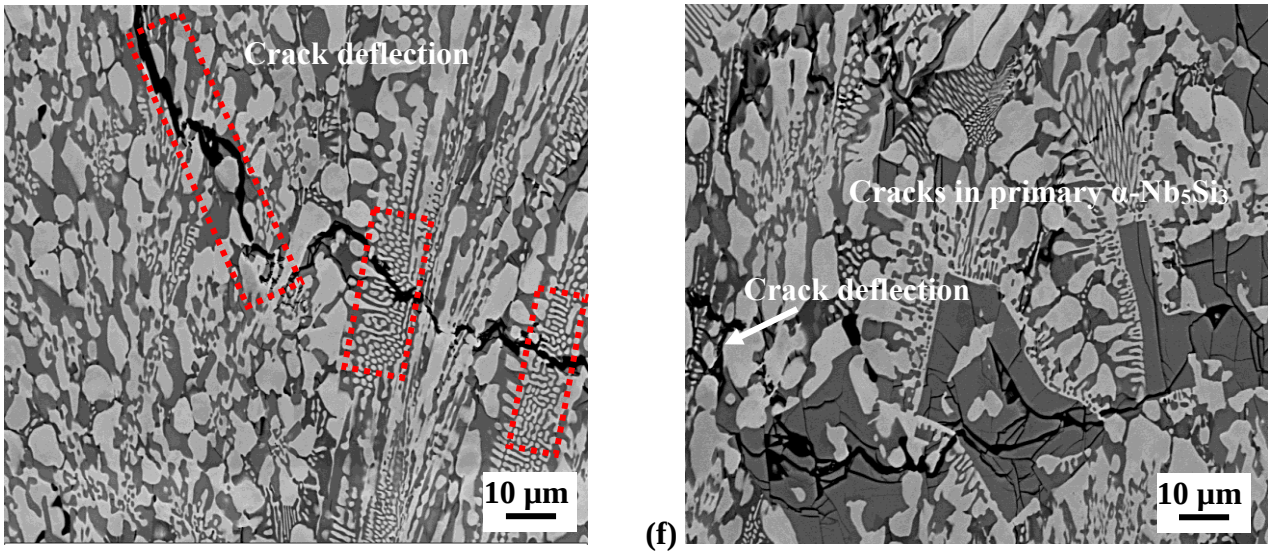

Fig. 5.10: SEM-BSE images taken at the bulk indent corners and polished fractured samples in compression test in order to understand the crack behaviour, (a,b) Nb-18.7Si alloy, (c,d) Nb-18.7Si-5Ti alloy, (e) Nb-18.7Si-5Zr and (f) Nb-18.7Si-5Ti-5Zr alloys.

In summary, the silicide phase (Nb_3Si/α–Nb_5Si_3) in the alloys is fractured in cleavage/brittle manner, irrespective of the alloying addition. Little plastic stretching is observed in the Nb_{ss} phase of Nb-18.7Si and Nb-18.7Si-5Ti alloys and is comparatively more in Nb-18.7Si-5Zr and Nb-18.7Si-5Ti-5Zr alloys (more bright regions in the fracture surfaces **Figs. 5.9(f-h)**. The cracks propagated selectively in silicide phase with crack bridging, crack deflection and crack branching as operative mechanisms at the Nb_{ss} phase. In addition, interface debonding/decohesion is also seen in the alloys.

5.3.2 Fracture toughness

The load (P) versus displacement (δ) plots from 3-point bend test results of the alloys are shown in the **Fig. 5.11(a)**. The onset of crack propagation can be ascertained from the pop-in load drop in the P-δ plot, as indicated with arrows (**Fig. 5.11(a)**). The detectable pop-in is observed at a strain of ~0.1% for Nb-18.7Si alloy and the maximum load for the failure is 142 N. There is no detectable pop-in is evident in the Nb-18.7Si-5Ti alloy before failure. The maximum load at the failure was 170 N. The detectable pop-in is noticed at a strain of ~0.18% and ~0.22% for the Nb-18.7Si-5Zr and Nb-18.7Si-5Ti-5Zr alloys, respectively. The maximum load of 271 N and 276 N at the failure is noticed for Nb-18.7Si-5Zr and Nb-18.7Si-5Ti-5Zr alloys, respectively. The

calculated fracture toughness (K_Q) values for the alloys using eq. 9 (mentioned in the chapter-3)is given in the **Table 5.3** & **Fig. 5.11(b)**. The alloy Nb-18.7Si exhibited the fracture toughness values of 5.84±0.38 MPa.m$^{1/2}$. The value increased to 6.69±0.15 MPa.m$^{1/2}$ with Ti addition in Nb-18.7Si-5Ti alloy. The Nb-18.7Si-5Zr and Nb-18.7Si-5Ti-5Zr alloys showed high fracture toughness value of 10.40±0.18 MPa.m$^{1/2}$ and 10.59±0.35 MPa.m$^{1/2}$, respectively.

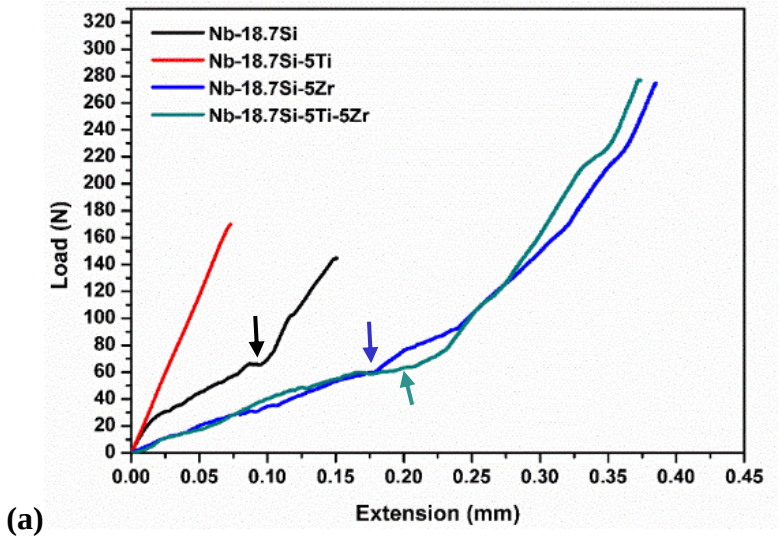

(a)

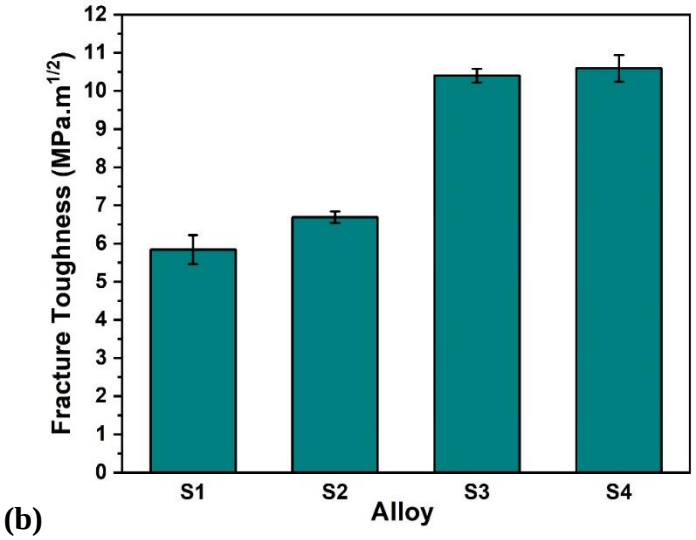

(b)

Fig. 5.11: Three point bend test data, (a) load versus extension plots, arrows indicate the onset of detectable load drop/pop-ins and (c) bar chart depicting the variation of fracture toughness values in the alloys. The S1, S2, S3 and S4 in the figure (b) corresponds to the Nb-18.7Si, Nb-18.7Si-5Ti, Nb-18.7Si-5Zr and Nb-18.7Si-5Ti-5Zr alloys respectively.

Fracture surface of the 3-point bend tested samples is shown in the **Fig. 5.12**. The silicide phase, i.e., Nb_3Si/α–Nb_5Si_3 (both primary and eutectic/eutectoid varients) appeared as facets which is the characteristic of the brittle cleavage fracture behaviour (**Figs. 5.12(a-d, g, h)**). The ductile Nb_{ss} phase also fractured in brittle manner with river pattern and ductile tearing ridges are observed at some places which are more prominent in Nb-18.7Si-5Zr and Nb-18.7Si-5Ti-5Zr alloys (**Figs. 5.12(f, g)**). The fracture surface of the Nb-18.7Si and Nb-18.7Si-5Ti alloys is more of flat type (**Figs. 5.12(a, c)**), whereas severer uneven and more fracture steps are observed in Nb-18.7Si-5Zr and Nb-18.7Si-5Ti-5Zr alloys (**Figs. 5.12(e, g, h)**). The fracture steps are clearly seen and are more in eutectoid region with fine lamellar type morphology of Nb_{ss} phase which can be seen in **Figs. 5.12(e, h)**. Interface debonding/decohesion at the interphase and interface of Nb_{ss} and Nb_3Si in eutectoid regions and also at the primary silicide, eutectoid region is noted (**Figs. 5.12(b-d)**)). In addition, pull out of the Nb_{ss} phase is also happened due to complete interphase debonding (**Fig. 5.12(b)**).

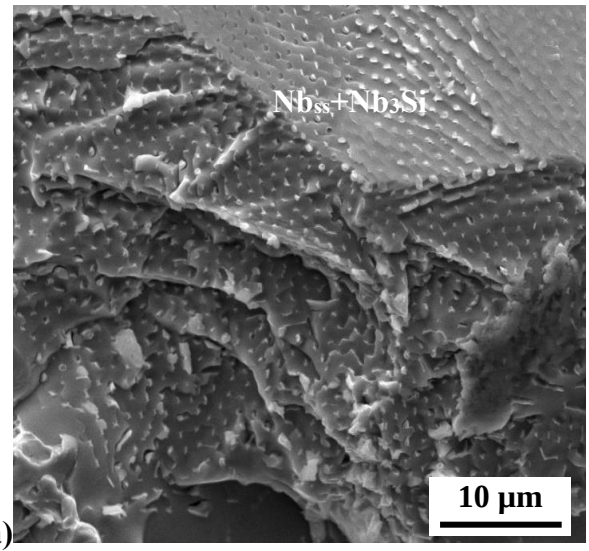

(a)

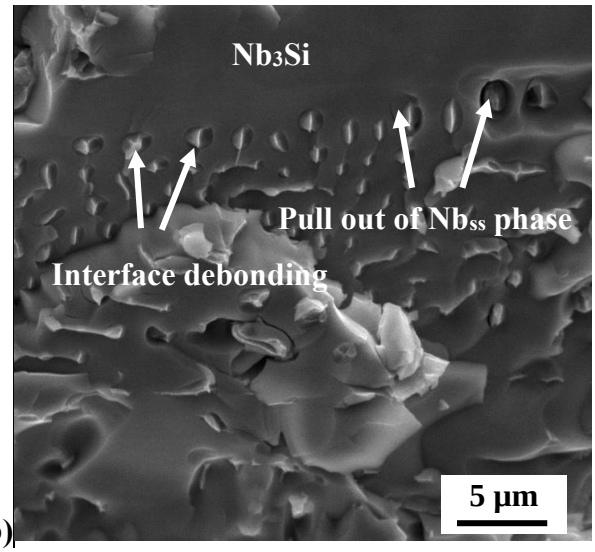

(b)

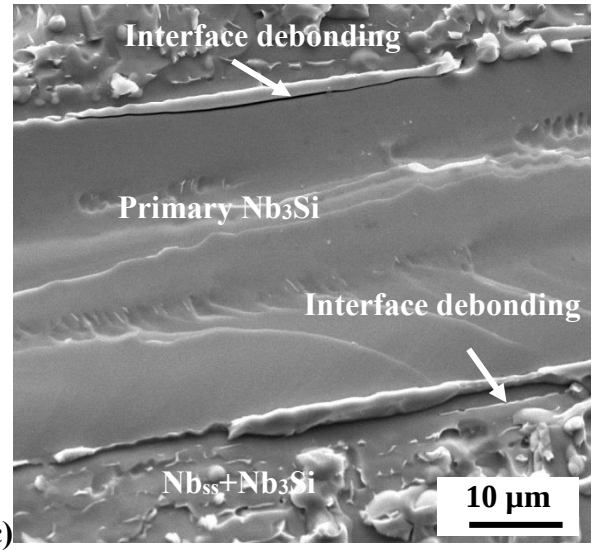
Interface debonding
Primary Nb3Si
Interface debonding
Nbss+Nb3Si
10 µm

(c)

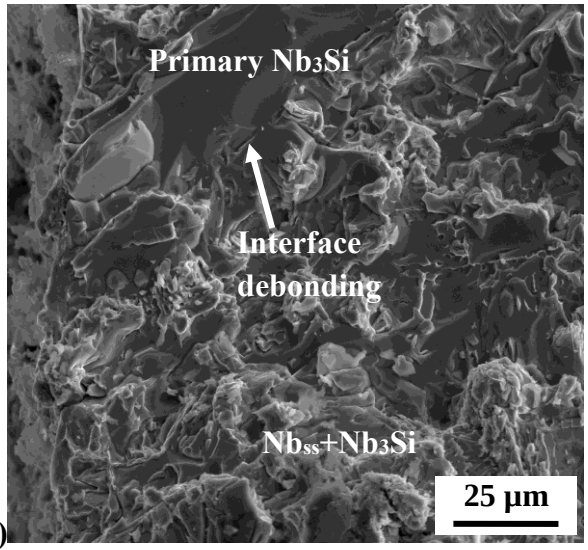
Primary Nb3Si
Interface debonding
Nbss+Nb3Si
25 µm

(d)

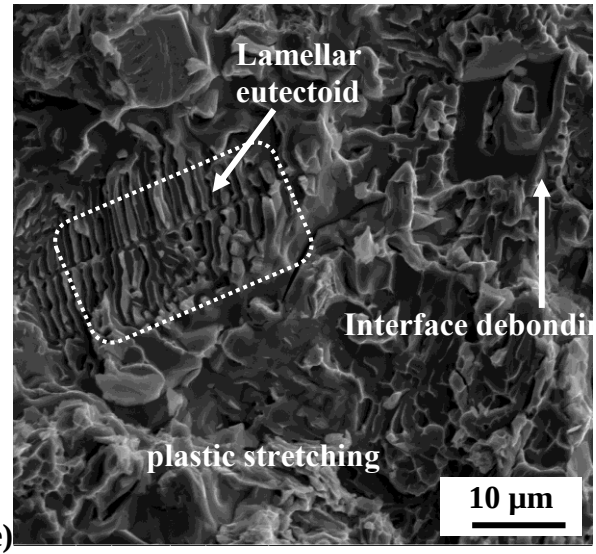
Lamellar eutectoid
Interface debondi
plastic stretching
10 µm

(e)

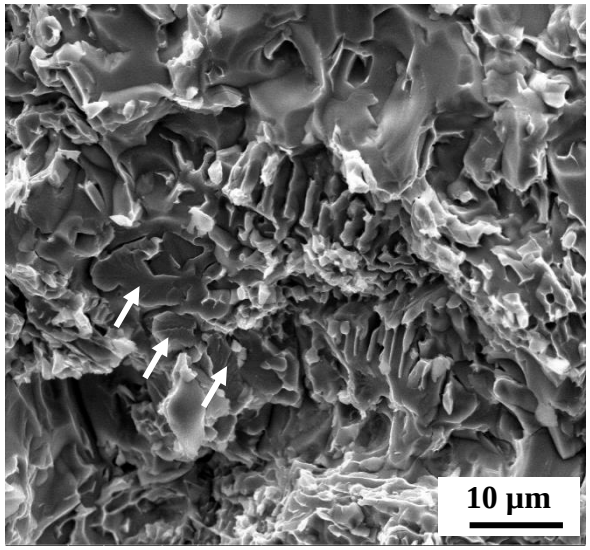
10 µm

(f)

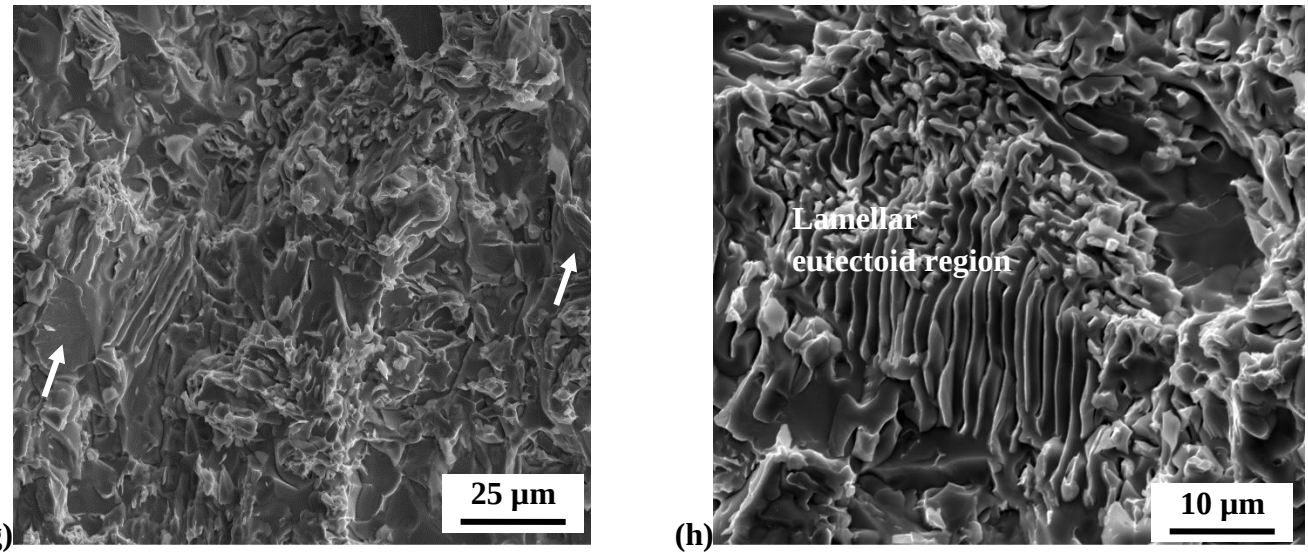

Fig. 5.12: Fracture surface of the 3-point bend tested samples. (a, b, c) corresponding to Nb-18.7Si (d) Nb-18.7Si-5Ti, (e,f) Nb-18.7Si-5Zr and (g, h) Nb-18.7Si-5Ti-5Zr. (a-d) The brittle fracture of the silicide Nb-18.7Si & Nb-18.7Si-5Ti alloys, respectively, (b) The pull out of Nb_{ss} phase in Nb-18.7Si alloy, (b, c, d, e) interface debonding between silicide and Nb_{ss} phases indicated with arrow symbol in all the alloys and (f, g) ductile tearing ridges in Nb_{ss} phase in Nb-18.7Si-5Zr and Nb-18.7Si-5Ti-5Zr alloys, indicated with arrow marks.

5.3.3 Sub-structure analysis of the fractured sample: Nb-18.7Si-5Ti-5Zr

The compression tested Nb-18.7Si-5Ti-5Zr alloy is analyzed in TEM in order to further understand the deformation substructure (**Fig. 5.13**). The bright field images exhibited two phase region (**Fig. 5.13(a)**). The selected area electron diffraction (SAED) patterns collected from these phase regions are given in the **Fig. 5.13(b, c)**. The SAED pattern of the bright contrast region corresponds to α–Nb_5Si_3 (**Fig. 5.13(b)**) and dark contrast region corresponds to the Nb phase (**Fig. 5.13(c)**). Presence of the dislocations are noticed in the Nb_{ss} phase. Whereas, the α–Nb_5Si_3 phase is doslocations free (**Fig. 5.13(a, d, e)**). Further, pile up of the dislocations can be seen at the interface of Nb_{ss} and α–Nb_5Si_3 phases (**Fig. 5.13(d, e)**). In addition, cracks are present in the α–Nb_5Si_3 phase (**Fig. 5.13(f)**). The dislocation free nature, smooth surface and presence of cracks indicates the brittle fracture behaviour of the α–Nb_5Si_3 phase. Further, from the pile-up of dislocations, it can be inferred that the dislocation movement in the Nb_{ss} phase is hindered at the interface of the α–Nb_5Si_3 due to its brittle nature. Consequently, greater amount of stress field

generates at the interface and is called plastic constraint. This caused the cracking at the interface of Nb_{ss} and α–Nb_5Si_3 phases (**Fig. 5.13(f)**).

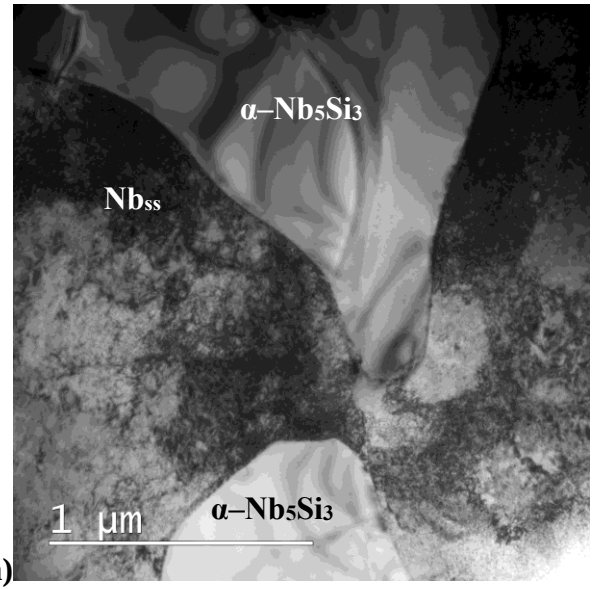

(a)

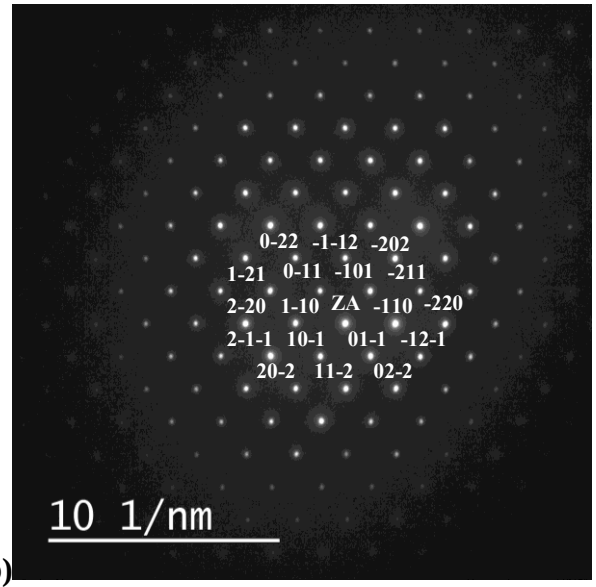

(b)

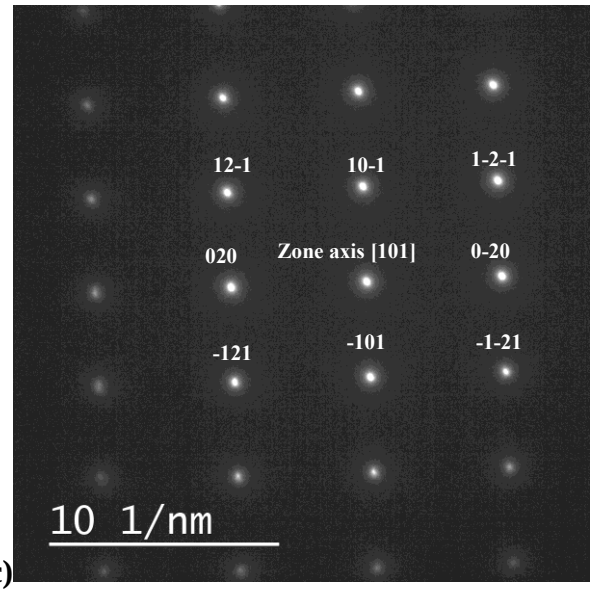

(c)

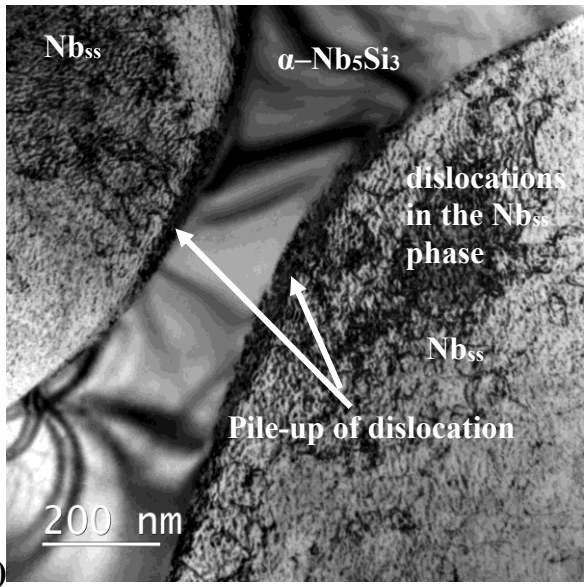

(d)

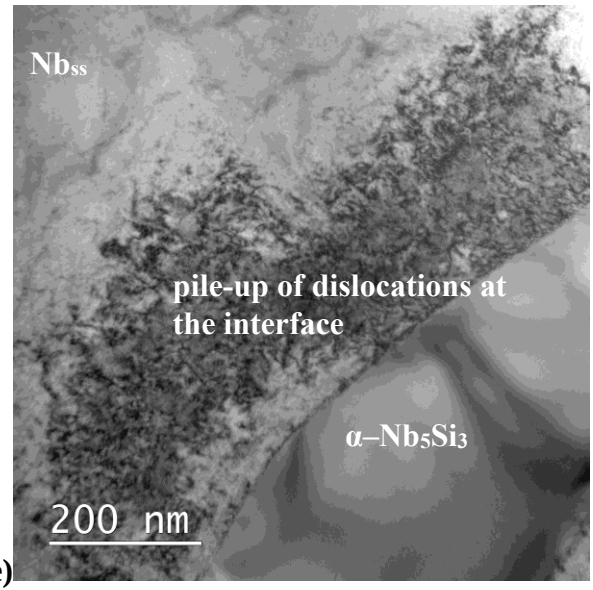

(e)

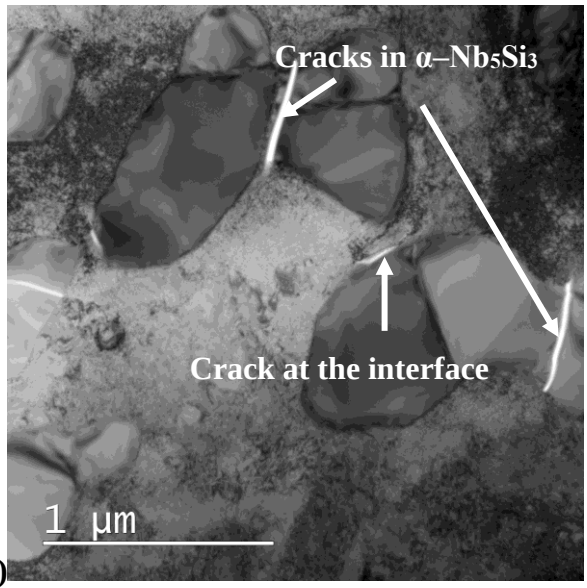

(f)

Fig. 5.13: TEM substructure of the compression tested Nb-18.7Si-5Ti-5Zr alloy, (a) Bright field image showing Nb_{ss} and α–Nb_5Si_3 phases, (b) and (c) shows the indexed SAED patterns corresponding to α–Nb_5Si_3 and Nb_{ss} phases, respectively, (d,e) Shows the pile up of dislocations at the Nb_{ss}, α–Nb_5Si_3 interface and huge amount of dislocations in the Nb_{ss} phase, (f) The cracking in α–Nb_5Si_3 phase and at the interface of Nb_{ss} and α–Nb_5Si_3 phases.

5.4 Discussion

5.4.1 Structure property correlation in the alloys

The variation in the compression properties and fracture toughness of alloys in the present study indicates the mechanical properties are directly influenced by the composition, volume fraction and morphology of the constituent phases.

The YS and FS values of the Nb-18.7Si alloy are the same and is similarly for the Nb-18.7Si-5Ti alloy (**Fig. 5.8(a)** and **Table 5.3**). In addition, the plastic strain in both the Nb-18.7Si and Nb-18.7Si-5Ti alloys is very low (**Fig. 5.8(b)**). This can be concured to the minimum or no deformation in the Nb-18.7Si and Nb-18.7Si-5Ti alloys prior to the fracture. However, both the YS and FS values of the alloy Nb-18.7Si-5Ti (958±147 MPa and 961±149 MPa, respectively) are higher than for the alloy Nb-18.7Si (727±145 MPa and 735±140 MPa) (**Fig. 5.8(a)**). It is attributed to the solid solution strengthening of the Nb_{ss} and silicide (Nb_3Si) phases with 5 at.%Ti addition

in Nb-18.7Si-5Ti alloy compared to the Nb-18.7Si alloy (**Table 5.2**). A drastic increase in both the YS (1639±28 MPa) and FS (1857±58 MPa) is noted for Nb-18.7Si-5Zr alloy (**Fig. 5.8(a)**). Further, the total and plastic strain values are also increased (**Fig. 5.8(b), Table 5.3**). The increase in the FS and plastic strain indicates considerable amount of plastic deformation in Nb-18.7Si-5Zr alloy prior to the fracture. The YS in Nb-18.7Si-5Ti-5Zr alloy is decreased slightly to 1589±59 MPa compared to the Nb-18.7Si-5Zr alloy. Further, the FS is increased to 2236±81 MPa and the plastic strain also increased. This indicates good amount of plastic deformation before fracture in the in Nb-18.7Si-5Ti-5Zr alloy compared to in Nb-18.7Si-5Zr alloy. The increase in the YS in the alloys Nb-18.7Si-5Zr and Nb-18.7Si-5Ti-5Zr is primarily attributed to the presence of hard α–Nb_5Si_3 phase compared to lower hardness phase Nb_3Si in the binary and Nb-18.7Si-5Ti alloys (**Fig. 5.8(a), Table 5.2**). The increase in the FS and plastic strain in the alloys can be attributed to the increase in the volume fraction and coarsening of the Nb_{ss} phase (**Figs. 4.2, 4.5, 4.6, 4.8** and **Table 5.2**). In addition, the lamellar microstructure consisting of Nb_{ss} and α–Nb_5Si_3 phases reported to exhibit better combination of mechanical properties [*N. Sekido et al., 2000*]. Therefore, the presence of lamellar Nb_{ss} phase in alternative layers of the eutectoid region (Nb_{ss}+ α–Nb_5Si_3) might have also caused this increment in the strength values of Nb-18.7Si-5Zr and Nb-18.7Si-5Ti-5Zr alloys (**Figs. 4.6, 4.8**). Further, solid solution softening of the Nb_{ss} phase in Nb-18.7Si-5Zr alloy also influenced this increment in the plastic strain (**Table 5.2**).

In summary, the modulus of the silicide phase in the alloys increased in the order of Nb-18.7Si, Nb-18.7Si-5Ti, Nb-18.7Si-5Zr and further decreased for Nb-18.7Si-5Ti-5Zr (**Table 5.2**). Therefore, the alloys exhibited the same trend for the yield strength values according to Griffith Theory [*George E. Dieter, 1986*] (**Fig. 5.8(a)**). The increase in the plastic strain in Nb-18.7Si-5Zr and Nb-18.7Si-5Ti-5Zr alloys is attributed to the increase in the volume fraction, coarsening of Nb_{ss} phase along with the presence of lamellar eutectoid regions in the microstructure (**Table 5.2**). Additionally, the constraint effect at the interface of Nb_{ss} and α-Nb_5Si_3 phases also might have increased the resistance for the deformation which might have also attributed to the compressive strength of the Nb-18.7Si-5Zr and Nb-18.7Si-5Ti-5Zr alloys (**Figs. 5.13(d, e)**).

It is well known that the Nb_{ss} phase imparts the toughness in the niobium-niobium silicide in-situ composites. It can increase the fracture resistance by effecting both the initiation and the propagation behaviour of the crack. The crack propagation is affected by extrinsic toughening mechanisms such as crack branching, deflection, bridging and interface delamination which are

directly related to the fraction, morphology and distribution of soft Nb_{ss} phase [*W.Y. Kim et al., 2001, K.S. Chan et al., 2005*]. The increase in the volume fraction and coarsening of Nb_{ss} phase can resist the crack propegation more effectively. In addition, soft Nb_{ss} phase will further oppose the crack from propagation [*K.S. Chan et al., 2005*]. On the other hand, brittle intermetallic phases affects the fracture toughness adversely [*W.Y. Kim et al., 2001*]. The increase in the fraction of intermetallic phase simply leads to particle fracture.

The fracture toughness value of 5.84±0.38 MPa.$m^{1/2}$ is measured for the alloy Nb-18.7Si and is well matching with the literature reports [*W.Y. Kim et al., 2001*]. This value increased to 6.69±0.15 MPa.$m^{1/2}$ in Nb-18.7Si-5Ti alloy (**Fig. 5.11(b)**), regardless of the same volume fraction of the phases in both the alloys (**Table 4.2**). Chan et al., also reported the fracture toughness improvement in Nb-Si alloys with the Ti addition and is due to solid solution softening of Nb_{ss} phase [*K.S. Chan et al., 2005*]. However, in the present work, hardening of the Nb_{ss} phase is noted with 5 at.%Ti addition in alloy Nb-18.7Si-5Ti compared to Nb-18.7Si. Even after the solid solution hardening of the Nb_{ss} phase, higher fracture toughness value is noted in Nb-18.7Si-5Ti alloy. It could be due to the coarsening of the Nb_{ss} phase that might have lead to the improved fracture toughness value (**Figs. 4.2, 4.5**). Therefore, it can be explicable that the coarsening of Nb_{ss} phase contributed greately in improving the fracture toughness of the Nb-18.7Si-5Ti alloy [*N. Sekido et al., 2004*]. In case of alloys Nb-18.7Si and Nb-18.7Si-5Ti, the phase fraction of Nb_3Si is about three times higher than the Nb_{ss}. Therefore, the brittle manner of fracture in these alloys observed and the fracture surface appeared to be even when compared to Nb-18.7Si-5Zr and Nb-18.7Si-5Ti-5Zr alloys (**Figs. 5.9(a-c), 5.12(a-d)**).

The fracture toughness values of the Nb-18.7Si-5Zr and Nb-18.7Si-5Ti-5Zr alloys are increased to 10.40±0.18 MPa.$m^{1/2}$ and 10.59±0.35 MPa.$m^{1/2}$, respectively. The following reasons might have contributed to the improvement in the fracture toughness: (i) The increase in the Nb_{ss} phase fraction, (ii) decrease in the silicide phase volume fraction and (iii) Coarsening of the Nb_{ss} phase compared to the Nb-18.7Si and Nb-18.7Si-5Ti alloys. The volume fraction of the Nb_{ss} phase increased to more than double and the hard phase (α-Nb_5Si_3) fraction decreased by 40% compared to alloys Nb-18.7Si and Nb-18.7Si-5Ti (**Table 4.2**). Therefore, presence of higher volume fraction and coarsening of the ductile Nb_{ss} phase offered more hinderance for the crack growth through crack deflection, bridging and branching phenomena (**Figs. 5.9(e-h), 5.10(e, f)**) and improved the fracture toughness. Further, the Nb-Si alloys with lamellar morphology of the Nb_{ss} and α–Nb_5Si_3

phases reported to exhibit better fracture toughness [*N. Sekido et al., 2000*]. Therefore, the presence of lamellar Nb_{ss} and α–Nb_5Si_3 phases might have also attributed to the enhancement in the fracture toughness of alloys Nb-18.7Si-5Zr and Nb-18.7Si-5Ti-5Zr compared to Nb-18.7Si, Nb-18.7Si-5Ti alloys. This can be attributed to increase in the crack propagation energy. Hence, non linear growth of crack through silicide phase by formation of steps is observed in the lamellar eutectoid regions (**Figs. 5.9(g, i), 5.12(e, f, h)**). Therefore, the crack deflection is more in alloys Nb-18.7Si-5Zr and Nb-18.7Si-5Ti-5Zr alloys. However, the crack path is more tortuous in the eutectoid region consistiing of coarse Nb_{ss} phase region compared to fine lamellar region (**Figs. 5.10(e)**). In addition, the large difference in elastic modulus values of Nb_{ss} and α–Nb_5Si_3 phases might have increased the crack deflection in the Nb-18.7Si-5Zr and Nb-18.7Si-5Ti-5Zr alloys. The solid solution softening of Nb_{ss} phase in Nb-18.7Si-5Zr alloy might have further enhanced the fracture toughness of the alloy (**Table 5.2**). However, the fracture toughness of the Nb-18.7Si-5Ti-5Zr alloy remained almost same irrespective of the solid solution strengthening of Nb_{ss} phase and presence γ–Nb_5Si_3 (a small fraction) which is a harder phase than α–Nb_5Si_3 [*K.S. Chan et al., 2005*]. Coarsening of the Nb_{ss} phase is observed in Nb-18.7Si-5Ti-5Zr alloy compared to the Nb_{ss} phase in Nb-18.7Si-5Zr alloy. It may be inferred that the coarsening of the Nb_{ss} phase might have caused predominant increase in the fracture toughness compared to the solid solution strengthening effect.

Pile-up of the dislocations observed at the interface of the Nb_{ss} and α–Nb_5Si_3 phases in the sub-structure of the post fractured samples depicts the accumulation of high stress fields (**Figs. 5.13(d, e)**). High stress fileds might have promoted the interface debonding/interface decohesion in the alloys. The seperation at the interface of the Nb_{ss} and α–Nb_5Si_3 phases is considered as the primary failure mode in the Nb-Si alloys.

It can be concluded that the crack bridging, crack branching and deflection are the major contributing mechanisms for the fracture toughness of these alloys. The weak interface promoted plastic dissipation by interface debonding/interface decohesion which also played a major role in the fracture toughness enhancement.

5.4.2 Importance of constraint effect on the fracture toughness of the Nb-Si alloys

Various fracture toughness models were reported in the open literature for estimating the fracture toughness of the Nb-Si alloys using the volume fraction and fracture toughness of the constituent phases (mentioned in the section 2.6 of chapter-2). The theoretical fracture toughness values using rule of mixture model (eq. 4) and constrained fracture toughnes model (eq. 5) [*K.S. Chan et al., 2018*] are calculated for the present alloys and compared with the experimental fracture toughness values measured from three point bend test (**Fig. 5.14**). The K_b, K_d in the eq. 4 corresponds to the fracture toughness values of the silicide and ductile Nb phases considered as 3 $MPa.m^{1/2}$ [*N. Sekido et al., 2000*] and 32 $MPa.m^{1/2}$ [*K.S. Chan et al., 2018*] respectively.

The ductile Nb_{ss} phase enhances the fracture toughness of the Nb-Si alloys through ductile phase toughening. On the other hand, hard silicide phases in the composite adversely influences the fracture toughness through brittle phase embrittlement. However, the presence of ductile Nb_{ss} phase does not always produce high fracture toughness. The brittle silicide phase is non deformable and induces high plastic constraint on the ductile Nb_{ss} phase (**Figs. 5.13(d, e)**). Therefore, the dislocation movement is hindered by the silicide phase. Hence, pile-up of the dislocations at the Nb_{ss} and silicide interface is noticed in the deformation substructure due to discontinuity of defromation or the incompatability in strain between the phases, as shown in the **Figs. 5.13(d, e)**. The theoretical fracture toughness values calculated using basic rule of mixtures model are over predicted than the experimental values (**Fig. 5.14**). The theoretical fracture toughness values calculated using the constrained model are near to the experimental values. However, the experimental values are still lower. The presence of primary silicide phase in faceted morphology, might have increased the constraint effect on the Nb_{ss} phase resulting lower experimental fracture toughness values even after considering the constraint effect. Further, the sharp edges of primary silicide phase might have acted as crack nucleating sites even at the lower loads and decreased the fracture toughness of the alloys. Therefore, the morphology and size of the constituent phases can also plays a major role along with the volume fraction on fracture toughness in the theretical fracture toughness calculation of the alloys.

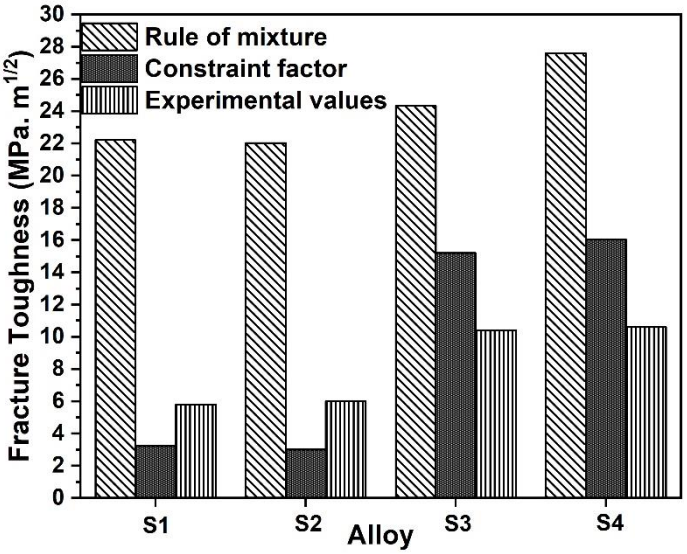

Fig. 5.14: Bar chart comparing the experimental and theoretical fracture toughness values of the alloys calculated using various models.

5.5 Summary

The current chapter covered the mechanical properties and fracture behaviour of the alloys. The major findings are as following:

1. The dissolved Si content in the Nb_{ss} phase is playing a dominant role in deciding the hardness value of the in the alloys.
2. Solid solution strengthening and solid solution softening of the alloy is observed with Ti and Zr additions, respectively. The combined addition of Ti and Zr resulted in the solid solution strengthening of Nb_{ss} phase.
3. The strength value of the Nb-18.7Si-5Ti alloy increased to 961±149 MPa compared to the 735±140 MPa value of the binary Nb-18.7Si alloy. This is attributed to the solid solution strengthening of the Nb_{ss} phase with Ti addition.
4. A drastic increase in the strength value to 1857±58 MPa and 2236±81 MPa and plastic strain to 6.23±0.66% and 10.16±0.59% is noted for Nb-18.7Si-5Zr and Nb-18.7Si-5Ti-5Zr alloys. This is attributed to the formation of hard and highly brittle α-Nb_5Si_3 compared to the Nb_3Si phase in the Nb-18.7Si and Nb-18.7Si-5Ti alloys. In addition, the Nb_{ss} and α-Nb_5Si_3 phases in lamellar morphology also aided in the enhancement of strength.

5. The fracture toughness value of 5.84±0.38 MPa.m$^{1/2}$, 6.69±0.15 MPa.m$^{1/2}$, 10.40±0.18 MPa.m$^{1/2}$ and 10.59±0.35 MPa.m$^{1/2}$ for the Nb-18.7Si, Nb-18.7Si-5Ti, Nb-18.7Si-5Zr and Nb-18.7Si-5Ti-5Zr alloys is noted. The increase in the fracture toughness of the Nb-18.7Si-5Ti is ascribed to the coarsening of the Nb_{ss} phase compared to Nb-18.7Si alloy.
6. The microstructure consisting of high volume fraction and coarse Nb_{ss} phase increased the crack path tortuousity by crack bridging, branching and deflection mechanisms in the Nb-18.7Si-5Zr and Nb-18.7Si-5Ti-5Zr alloys and resulted with high fracture toughness. Further, decrease in the silicide phase fraction also contributed to the toughness enhancement.
7. Among the alloys, Nb-18.7Si-5Ti-5Zr (combined addition of Ti and Zr) exhibited maximum compressive strength (2236±81 MPa) along with the good fracture toughness (10.59±0.35 MPa.m$^{1/2}$) value.
8. Fracture in the alloys started with microcrack in the silicide phase and the Nb_{ss} phase acted as the barrier for the crack propagation by crack bridging, branching and deflection mechanisms and increased the crack path tortuousity. Further, the constraint of the brittle silicide phase on the Nb_{ss} phase obstructed the deformation of the Nb_{ss} phase and resulted in interface debonding in the alloys.

Chapter-6

Cyclic oxidation behaviour

6.0 Introduction

In this chapter, the cyclic oxidation test results of the alloys is discussed. It consisted of the oxidation response of the uncoated and Fe-Cr modified slurry silicide coated alloys over the temperature range of 800°C-1400°C in air. The oxidation behaviour is assessed from the weight change with respect to duration of oxidation test data. Further, the microstructure analysis of the oxidized samples is carried out to understand the oxidation protection mechanism.

6.1. Results

6.1.1. Oxidation behaviour of the uncoated alloys

The photographs of the oxidation tested samples at 800°C and 1400°C is given in **Fig. 6.1(a)**. All the uncoated samples (irrespective of addition of Ti and/or Zr), exhibited rapid formation of loose oxide scales and dimensional degradation from the initial stages, i.e., within 15min/1 cycle of oxidation at all the test temperatures, as shown in the **Fig. 6.1(a)**. The oxide scales detached from the sample surfaces and are non-protective in nature. Higher oxidation temperature caused greater scale formation and catastrophic dimensional degradation in the uncoated samples. The oxides reacted and got stuck with the crucibles during oxidation at temperatures of 1400°C. Therefore, the weight change of the uncoated samples could not be measured without ambuguity. However, the formation of the loose oxide scales and their detachment from the surface (**Fig. 6.1(a)**) are indicative of loss in the nett weight of the samples.

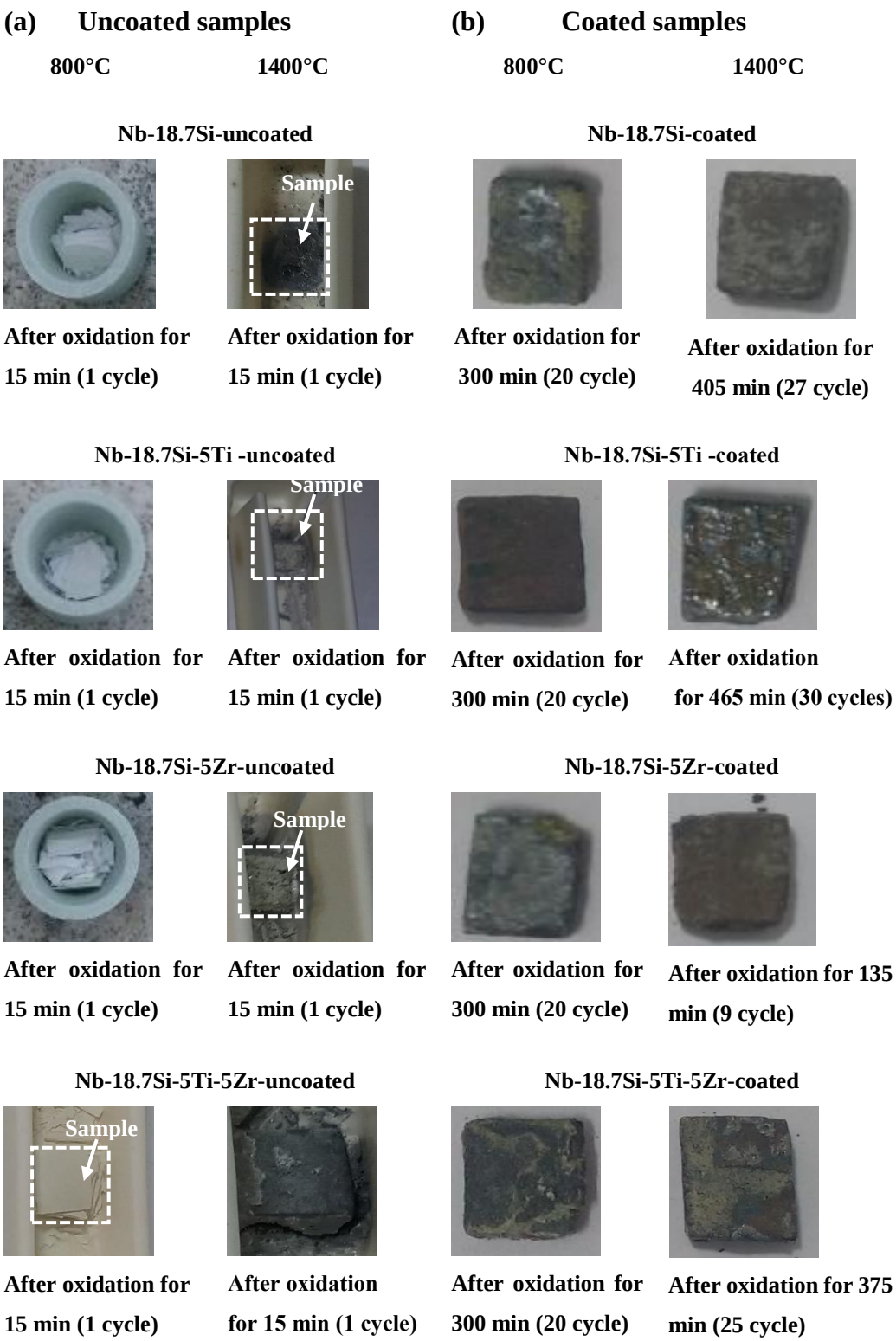

Fig. 6.1: Photographs of the (a) un-coated and (b) coated samples after oxidation at 800°C and 1400°C.

6.1.2 Microstructure of the coated alloys

6.1.2.1 Surface morphology

The surface morphology of the as coated samples is given in the **Fig. 6.2**. The surface is rough in appearance and contained micro-cracks. The phases are analyzed using XRD and is given in the **Fig. 6.3**. All the samples in as coated condition consist of $NbSi_2$ phase.

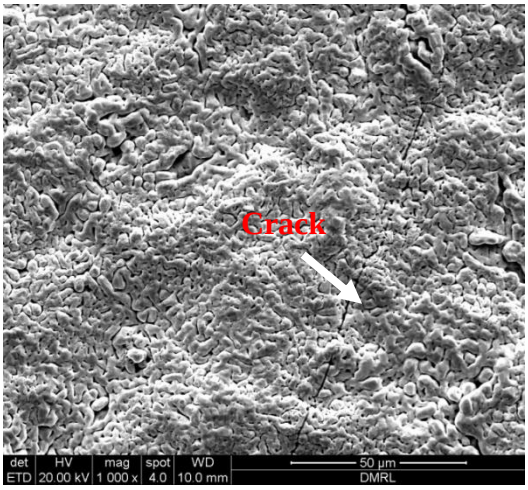

Fig. 6.2: Surface morphology of the coating prior to oxidation.

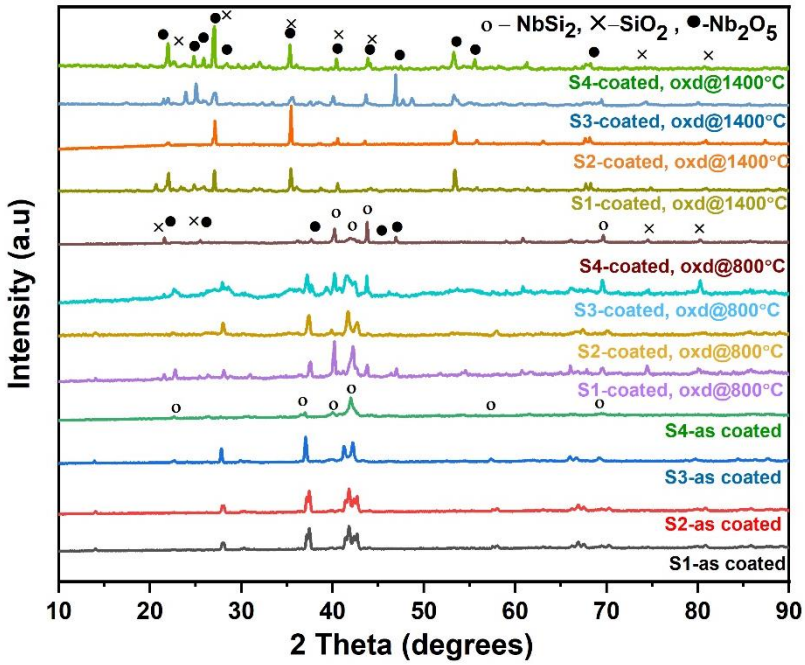

Fig. 6.3: X-ray diffractogram for the coated samples in the un-oxidized condition and after oxidation at 800°C and 1400°C for 300 and 405 min., respectively. S1, S2, S3 and S4 refer to the Nb-18.7Si, Nb-18.7Si-5Ti, Nb-18.7Si-5Zr and Nb-18.7Si-5Ti-5Zr alloys, respectively.

6.1.2.2 Cross section microstructure

The cross-section microstructure of the coating deposited on the various alloys is shown in **Fig. 6.4(a-d)**. For all the alloys, the coating exhibited similar microstructure and its thickness varied in the range of 250-300 µm. Several through-thickness cracks are observed in the coating cross-section and indicated with arrows (**Fig. 6.4**).

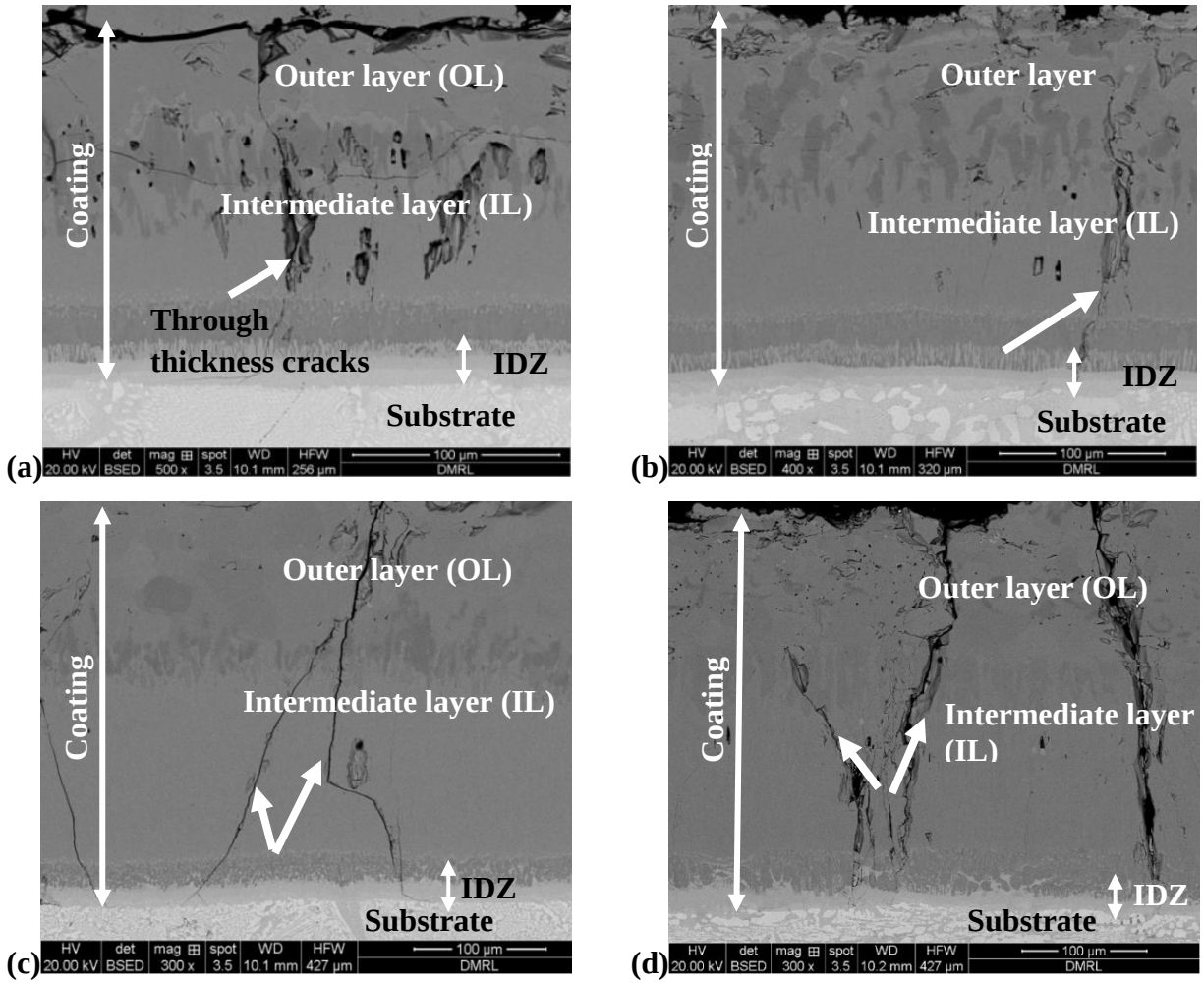

Fig. 6.4: Cross section microstructure of the coating formed on (a) Nb-18.7Si, (b) Nb-18.7Si-5Ti, (c) Nb-18.7Si-5Zr and (d) Nb-18.7Si-5Ti-5Zr alloys. Arrows indicate the through thickness cracks in the surface.

Based on the phase contrast in the back scattered electron micrographs (**Fig. 6.4**), the coating microstructure can be classified into three distinct regions: i.e., outer layer (OL), intermediate layer (IL), and inter diffusion zone (IDZ). The linear quantitative analysis, i.e., chemical composition, measured across the coating thickness is shown in **Fig. 6.5(a)**. The outer layer of the coating consists of 33 at.% Nb, 67 at.% Si and minor amounts of Fe and Cr (1-2 at.%). The atom ratio of 1:2 for Nb:Si indicated that the outer layer contained the $NbSi_2$ phase, which is also confirmed from the X-ray diffaction peaks corresponding to the unoxidized coated samples (**Fig. 6.3**). The intermediate layer contained lower amount of Nb, Si and higher content of Fe, Cr than that of the outer layer (**Fig. 6.5(a)**). The Nb and Si content in the intermediate layer is 23 and

45 at.%, respectively, whereas, Fe and Cr varied between 10-20 at.% and 10-25 at.%, respectively (**Fig. 6.5(a)**). The IDZ exhibited an increase in Nb and concomitant decrease in the Si, Fe and Cr content (**Fig. 6.5(a)**). Besides the relatively different compositions, the grain structure in each of the coating layers is also significantly different (**Fig. 6.4**).

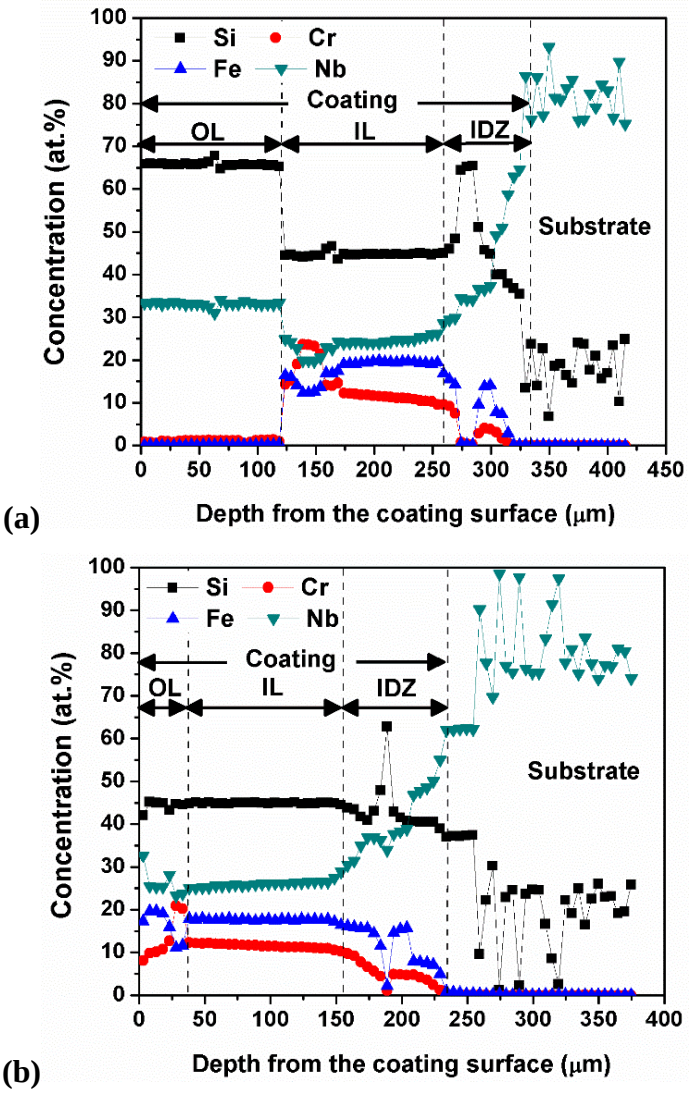

Fig. 6.5: EPMA-WDS concentration profile across the cross-section of the coated Nb-18.7Si alloy. (a) in the un-oxidized condition, and (b) after oxidation at 1400°C for 405 min. The legends OL, IL and IDZ denote the layers of the coating, i.e., outer layer, intermediate layer, interdiffusion zone, respectively.

The EBSD analyses confirmed that the outer layer of the coating is primarily constituted of the $NbSi_2$ phase and has an equiaxed grain structure, as typically shown in **Fig. 6.6**. On the other hand, the intermediate layer contained complex silicide phases of Nb, Fe and Cr, such as $Fe_3Nb_4Si_5$, $CrFe_3Nb_3Si_6$, $Fe_4Nb_4Si_7$, and exhibited a columnar grain structure (**Fig. 6.6(b)**). The IDZ, in turn has two distinct layers comprising of fine equiaxed $NbSi_2$ and Nb_5Si_3 phases, respectively (**Fig. 6.6**).

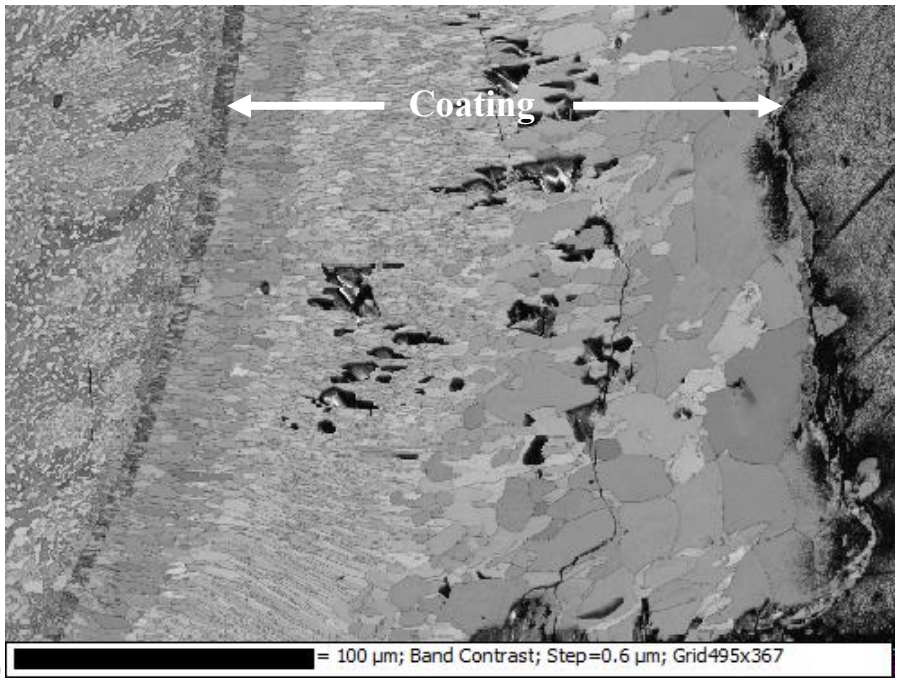

(a)

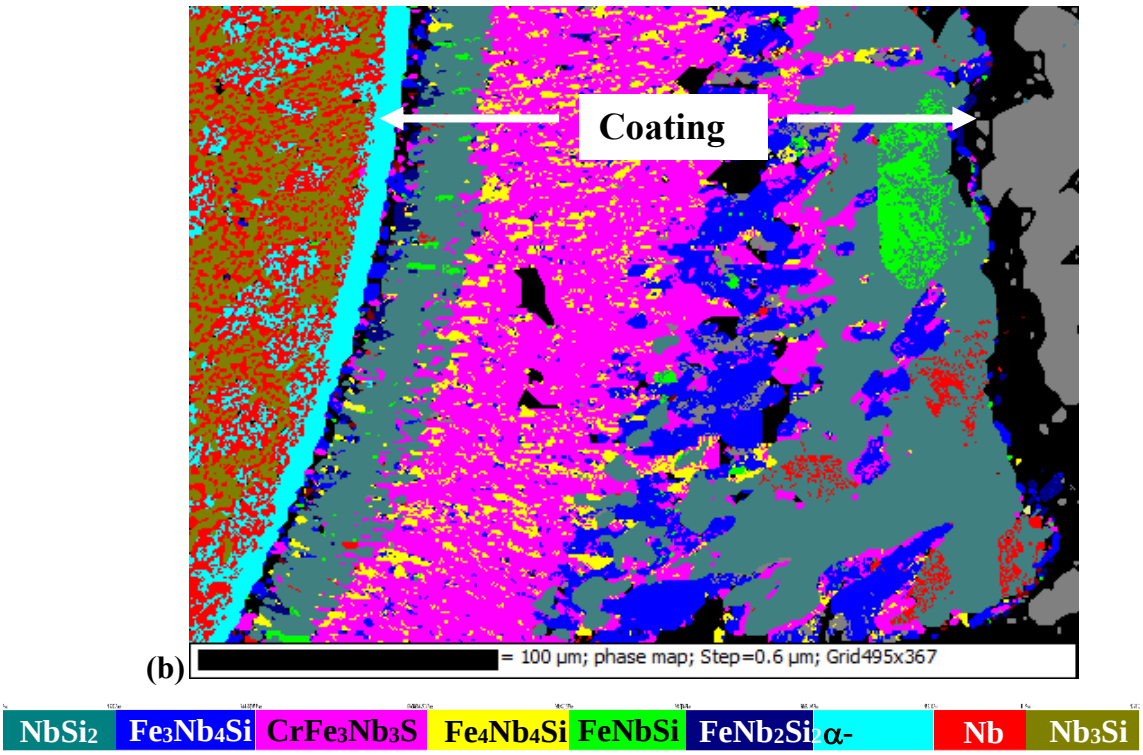

Fig. 6.6: (a) Image quality map and (b) EBSD phase map showing the phases constituting the cross-section of the coated Nb-18.7Si alloy prior to oxidation exposure.

6.1.3 Oxidation behavior of the coated alloys

As mentioned in the experimental procedure (Chapter-3), the samples are cyclically oxidized in air at 800, 1200 and 1400°C, and each cycle involves soaking of the samples at the oxidation test temperature for 15 min. followed by their cooling outside the furnace for 15 min. The typical temperature profile of the samples during one cycle of oxidation is shown in **Fig. 3.8**. The photography of the oxidation tested samples at different temperatures is given in **Fig. 6.1(b)**. Unlike that of the uncoated samples, all the coated samples exhibited weight gain and dimensional integrity at all temperatures (**Fig. 6.1(b)**). The weight change plots for the coated alloys showed three distinct regimes: (i) initial parabolic weight gain, (ii) subsequent steady weight gain, and (iii) rapid weight loss with further thermal exposure (**Fig. 6.7**). The value for the parabolic oxidation rate constant (k_p) is calculated using the weight change data over the regime corresponding to the initial parabolic weight gain, i.e., until the onset of the regime showing steady weight gain. At any given oxidation temperature, the k_p values are similar for all the coated alloys (**Table 6.1**). However, the k_p values increased by about an order of magnitude with the increase in oxidation

temperature from 800 to 1200°C (**Table 6.1**). With further increase in the oxidation temperature above 1200°C, the rate of increase in k_p is low, i.e., the k_p at 1400°C is about 4-5 times higher than that at 1200°C (**Table 6.1**). Whereas, for the Nb-18.7Si-5Ti-5Zr alloy the increase in the K_p value is low with increasing temperature from 800 to 1200°C, i.e., Kp at 1200°C is about 5 times higher than that at 800°C (**Table 6.1**). This is further increased by an order of magnitude at 1400°C. The maximum weight gain for the coated samples also increased with the increase in oxidation test temperature (**Fig. 6.7**). The oxidation life of the sample can be estimated as the duration over which the sample weight change remained positive. Except for the coated Nb-18.7Si-5Zr sample, which showed weight loss after 120 min. at 1400°C (due to sticking with the crucible) as compared to its longer oxidation life of 360 min. at 1200°C and 305 min. at 800°C, all the other coated samples registered an increase in the oxidation life. For instance, the oxidation life for the Nb-18.7Si sample is 305, 345 and 405min during oxidation at 800, 1200 and 1400°C, respectively, and the corresponding value for the Nb-18.7Si-5Ti sample is 240, 345 and 435 min. (**Fig. 6.7**). The corresponding values for Nb-18.7Si-5Ti-5Zr alloys is 350 min, 425 min and 375 min at 800°C, 1200°C and 1400°C.

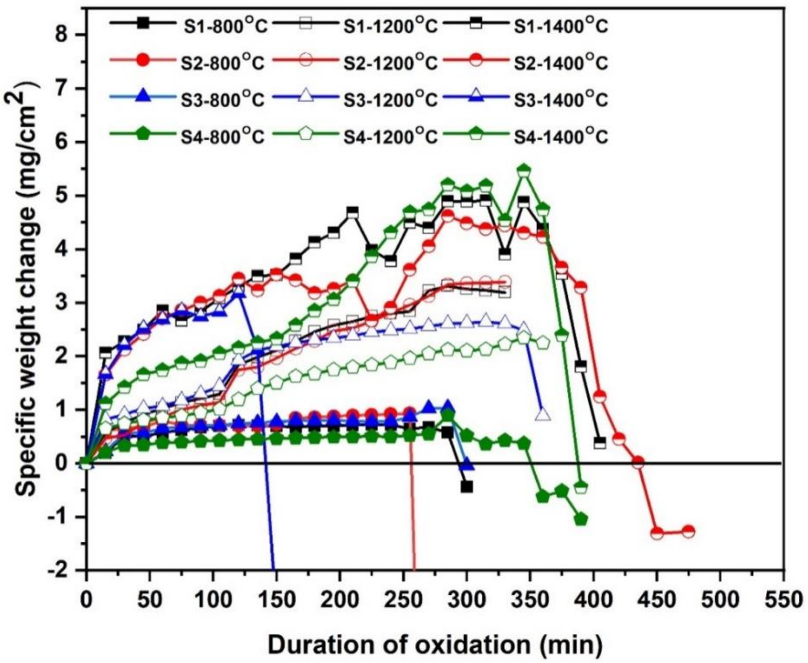

Fig. 6.7: Weight change plots for the coated alloys (S1: Nb-18.7Si, S2: Nb-18.7Si-5Ti, S3: Nb-18.7Si-5Zr and S4: Nb-18.7Si-5Ti-5Zr) during cyclic oxidation at 800, 1200 and 1400°C.

Table 6.1: K_p values ($mg^2.cm^{-4}.min^{-1}$) for the coated and oxidized samples at different temperatures.

Alloy composition	Temperature (°C)		
	800	**1200**	**1400**
Nb-18.7Si	4.63×10^{-3}	1.56×10^{-2}	7.40×10^{-2}
Nb-18.7Si-5Ti	3.68×10^{-3}	1.29×10^{-2}	8.91×10^{-2}
Nb-18.7Si-5Zr	4.98×10^{-3}	1.68×10^{-2}	7.17×10^{-2}
Nb-18.7Si-5Ti-5Zr	1.66×10^{-3}	8.18×10^{-3}	3.67×10^{-2}

6.1.4 Microstructure of the coating after oxidation

6.1.4.1 Surface morphology

The surface morphology of the samples after oxidation is shown in the **Figs. 6.8-6.12**. After oxidation at 800°C for 300 min., the surface consists of two distinct phases, i.e., the outer bright phase (region 1) and the inner dark phase (region 2), as indicated in **Fig. 6.8(a)**. Surface cracking and spallation of the outer bright oxide scale is detected, and the dark phase regions are visible mostly at the regions where the outer bright oxide scale has spalled off (**Fig. 6.8(a)**). A closer surface examination of the intact oxide revealed that the bright scale is dense and exhibited an elongated plate-like morphology (**Fig. 6.8(b)**). Based on the local EDS measurements, it is ascertained that the bright scale is primarily constituted of Nb-oxide along with silica and oxides of Cr and Fe (**Fig. 6.8(c)**). The dark regions, on the other hand, are relatively smooth in appearance (**Fig. 6.8(d)**) and contained silica along with oxides of Nb and minor amounts of Cr and Fe (**Fig. 6.8(e)**). The trace of the equiaxed grains of the $NbSi_2$ phase present in the outer layer of the coating is also evident in the backdrop of the dark regions (**Fig. 6.8(d)**). The surface features of the coated Nb-18.7Si-5Ti (**Fig. 6.8(f)**), Nb-18.7Si-5Zr (**Fig. 6.8(g)**) and Nb-18.7Si-5Ti-5Zr (**Fig. 6.8(h)**) samples after oxidation at 800°C are also similar to that explained above, i.e., the outer bright oxide scale is rich in Nb-oxide and exhibited elongated plate like morphology, whereas the inner nodular dark phase regions are rich in silica and has relatively smooth appearance. The XRD peaks

corresponding to the surface of all the oxidized coated samples indicated the presence of Nb_2O_5 (JCPDS NO: 74-0298) and SiO_2 (JCPDS NO: 85-0621) phases (**Fig. 6.3**). Since the surface oxide scale is relatively thin, the diffraction peaks from the underlying $NbSi_2$ phase of the coating is also detected in the XRD measurements of oxidized samples (**Fig. 6.3**).

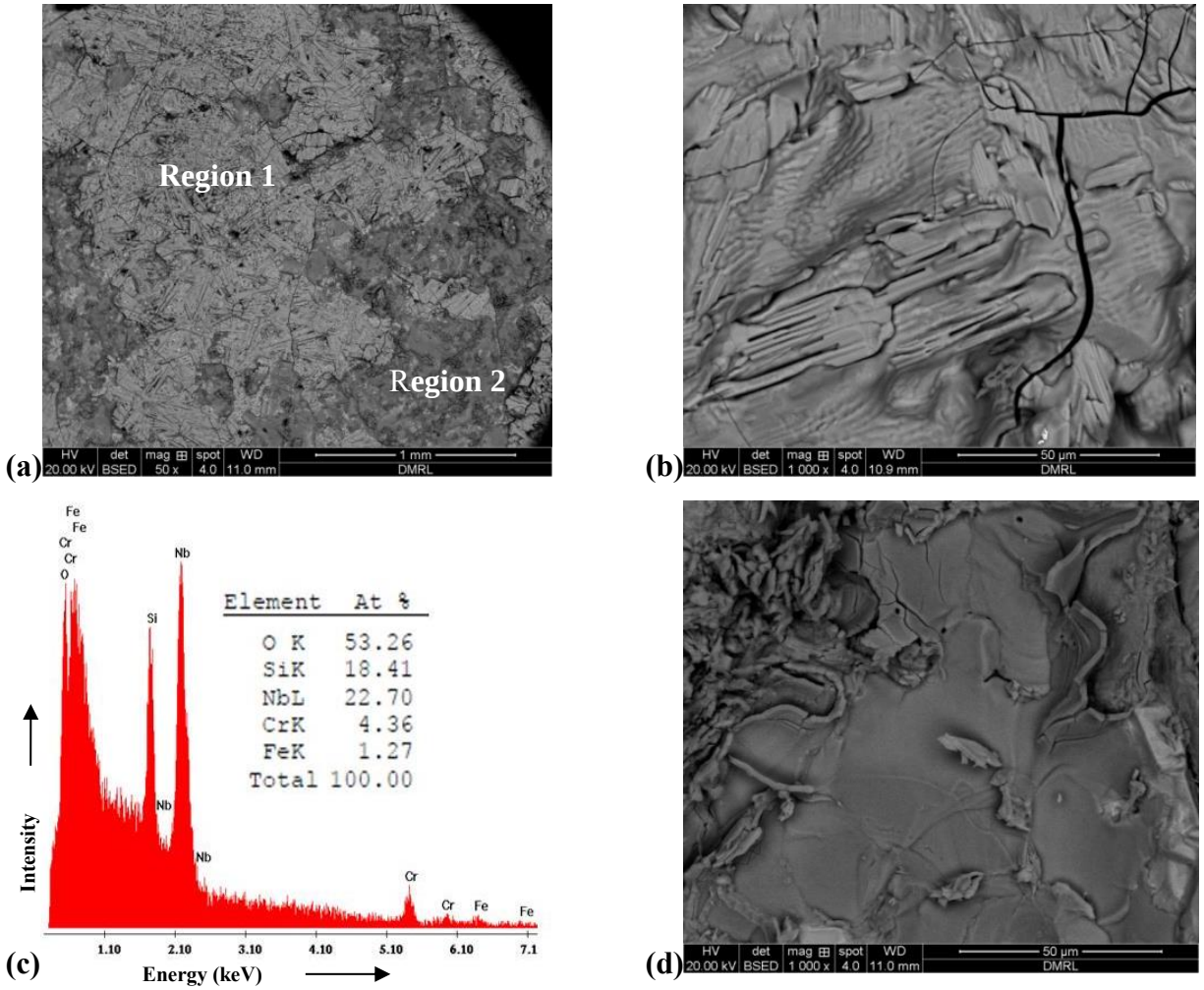

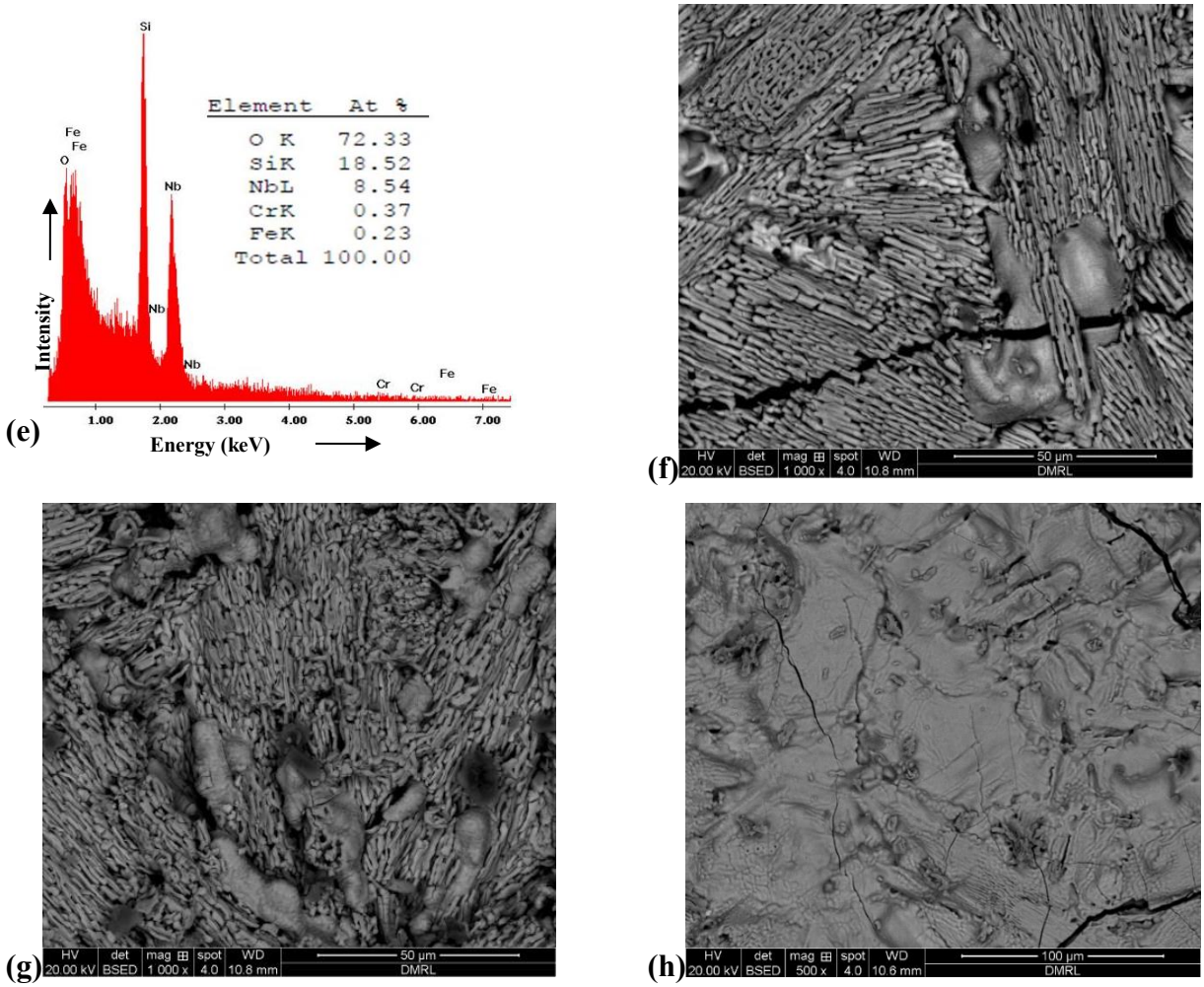

Fig. 6.8: Surface morphology of the coated and oxidized alloys at 800°C. (a) Nb-18.7Si after oxidation for 300 min., The magnified view and the corresponding EDS spectra of the regions marked 1 and 2 in (a) are shown in (b,c) and (d,e), respectively, (f) and (g) corresponds to the Nb-18.7Si-5Ti and Nb-18.7Si-5Zr samples after oxidation for 300 min., (h) Corresponds to Nb-18.7Si-5Ti-5Zr alloy after oxidation for 375 min.

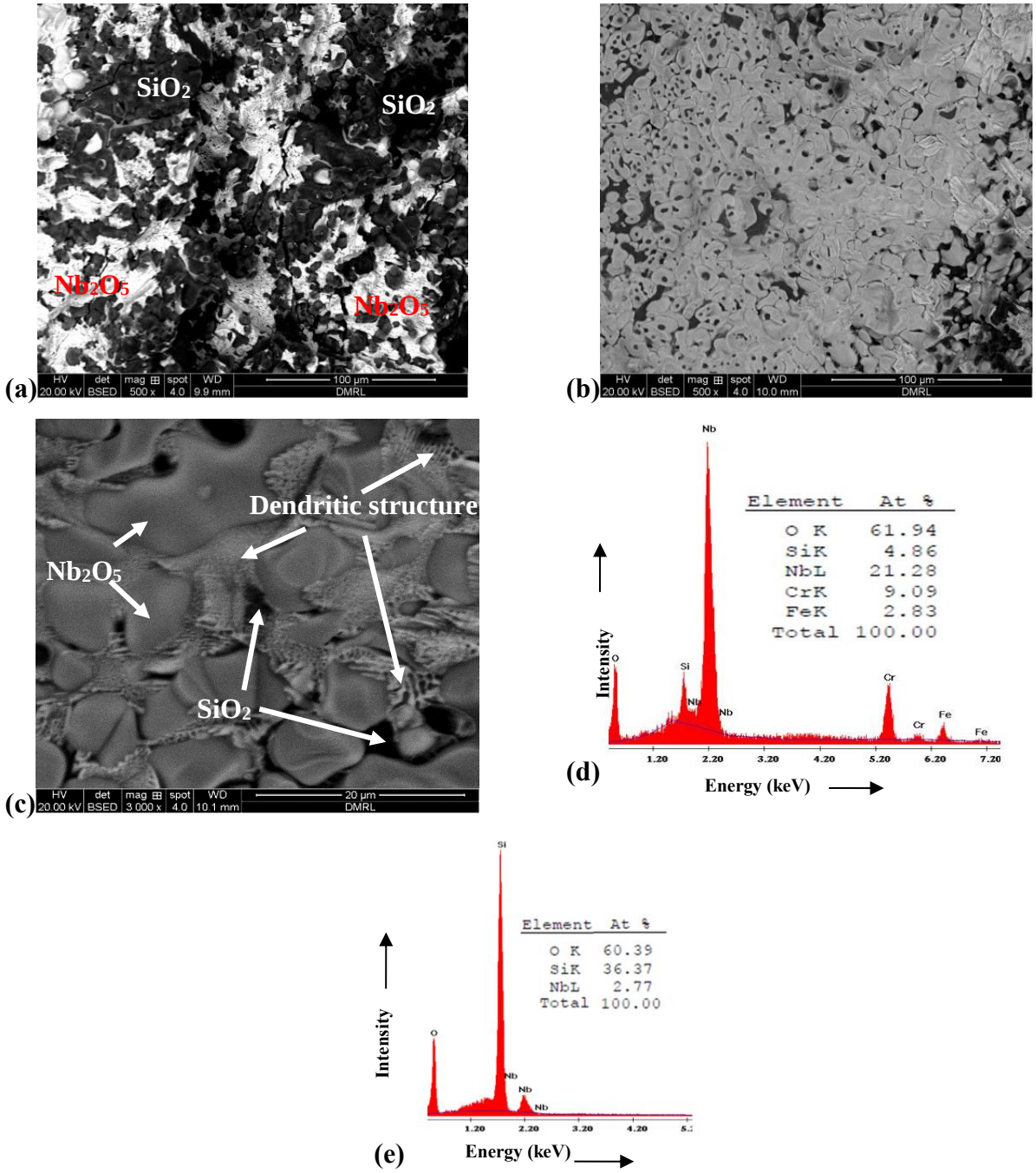

Fig. 6.9: Surface morphology of the coated Nb-18.7Si alloy oxidized at 1400°C for 405 min. The oxide scale on the coating surface comprised of the Nb_2O_5 (bright) and SiO_2 (dark) phases as typically shown in the low magnification image in (a), The high magnification images in (b) and (c) show the dense morphology and sintering of Nb_2O_5 oxides, respectively, The dendritic features formed after solidification of the eutectic liquid is also evident in (c), The corresponding EDS spectra for the bright and dark phases in (a) are shown in (d,e).

The oxide scale formed on the surface after oxidation at higher temperatures also exhibited a two-phase morphology and contained micro-cracks (**Fig. 6.9(a)**). However, the bright scale exhibited more of a disk-shaped morphology (**Fig. 6.9(b)**), which is unlike its plate-like elongated morphology observed at the lower oxidation temperature of 800°C (**Fig. 6.8(b)**). Besides, the bright regions are dense and a closer examination revealed the localized formation of a layer of silicate scale having dendritic morphology at the interparticle boundaries (**Fig. 6.9(c)**. The bright phase regions are predominantly rich in Nb-oxide (**Fig. 6.9(d)**). The dark phase is nodular (**Fig. 6.9(a)**) and primarily constituted of silica (**Fig. 6.9(e)**). The oxide scale formed on the coated Nb-18.7Si-5Ti sample after oxidation at 1400°C also exhibited the similar phase constitution (**Fig. 6.10**). A closer examination of the regions 1 and 2 in **Fig. 6.10(a)** indicated the presence of a fine dispersion of the bright Nb-oxide and dark silica phases (**Fig. 6.10(b)**) and the localized formation of dendrites (**Fig. 6.10(c)**), respectively. The oxide scale corresponding to the Nb-18.7Si-5Zr and Nb-18.7Si-5Ti-5Zr samples also shows the similar phase constitution, i.e., Nb_2O_5 and SiO_2 (**Fig. 6.11, 6.12**), and the localized formation of the dendritic structure at the Nb_2O_5 and SiO_2 phase boundaries (**Figs. 6.11(b, c), 6.12(b, c)**). Overall, the oxide scale in all the samples is constituted of the SiO_2 (JCPDS NO:85-0621) and Nb_2O_5 (JCPDS NO: 74-0298) phases, which is confirmed from the XRD measurements (**Fig. 6.3**).

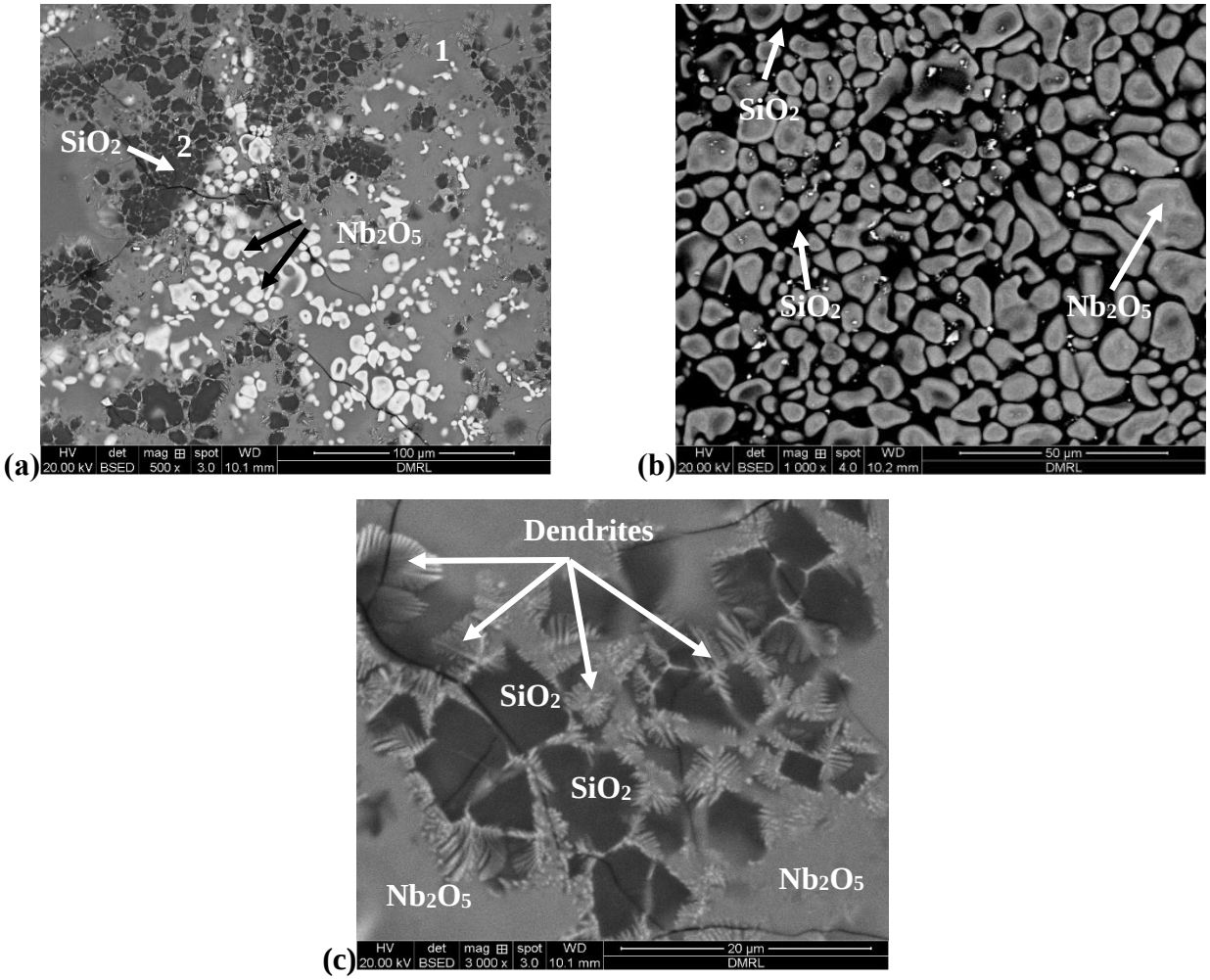

Fig. 6.10: Surface morphology of the coated Nb-18.7Si-5Ti alloy oxidized at 1400°C for 405 min. The oxide scale on the coating surface comprised the Nb_2O_5 (bright) and SiO_2 (dark) phases, as typically shown in the low magnification image in (a), The high magnification image in (b) corresponding to the region 1 in (a) shows the dense morphology and sintering of Nb_2O_5 oxides, (c) Magnified view of the region 2 in (a) shows the dendritic morphology formed after solidification of the eutectic liquid at the Nb_2O_5 and SiO_2 interphase boundaries.

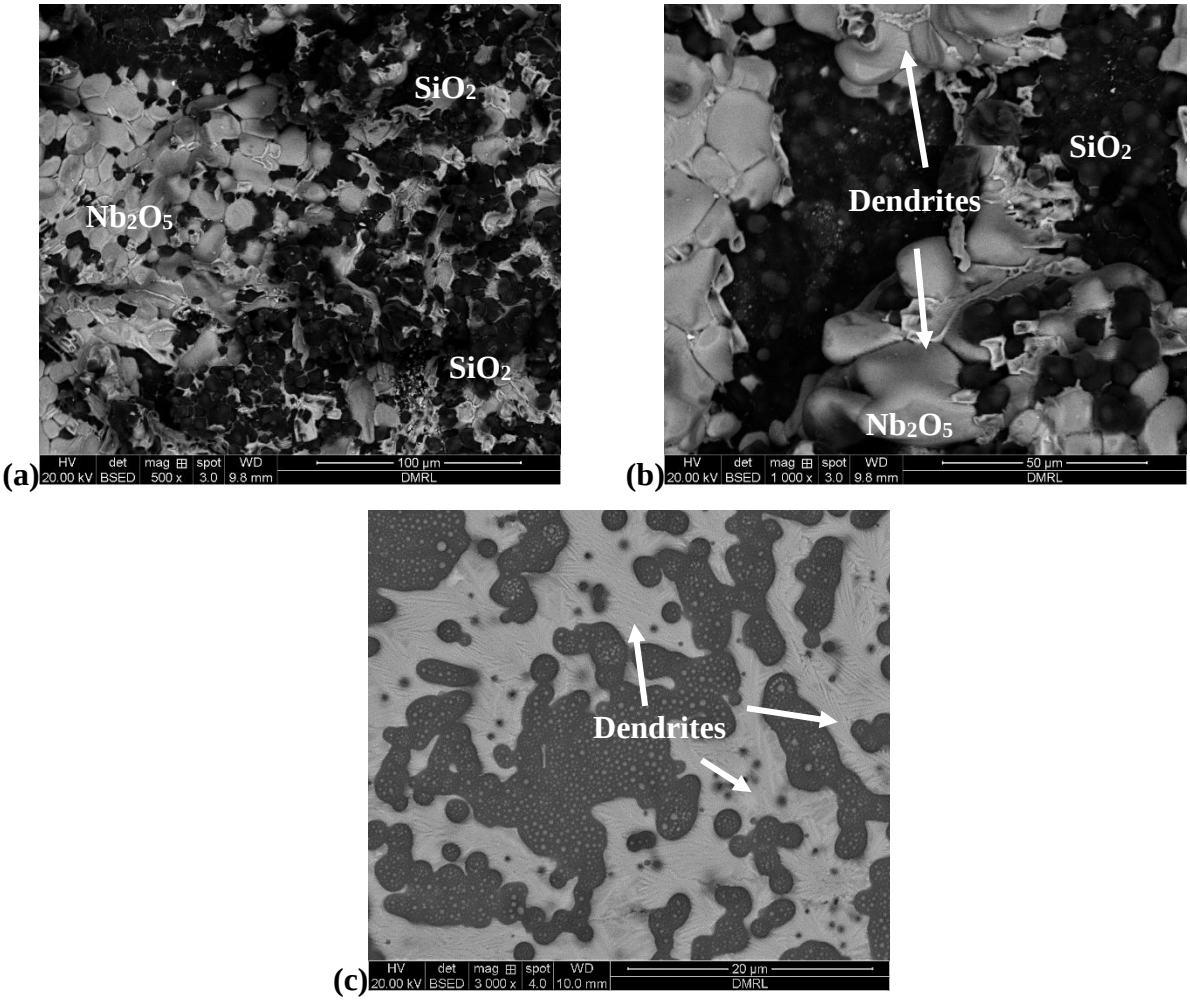

Fig. 6.11: Surface morphology of the coated Nb-18.7Si-5Zr alloy oxidized at 1400°C for 120 min. The oxide scale comprised the Nb_2O_5 (bright) and SiO_2 (dark) phases, as typically shown in (a,b), The high magnification image in (c) shows the dendritic morphology of the solidified eutectic formed by reaction of the Nb_2O_5 and SiO_2 phases at localized regions.

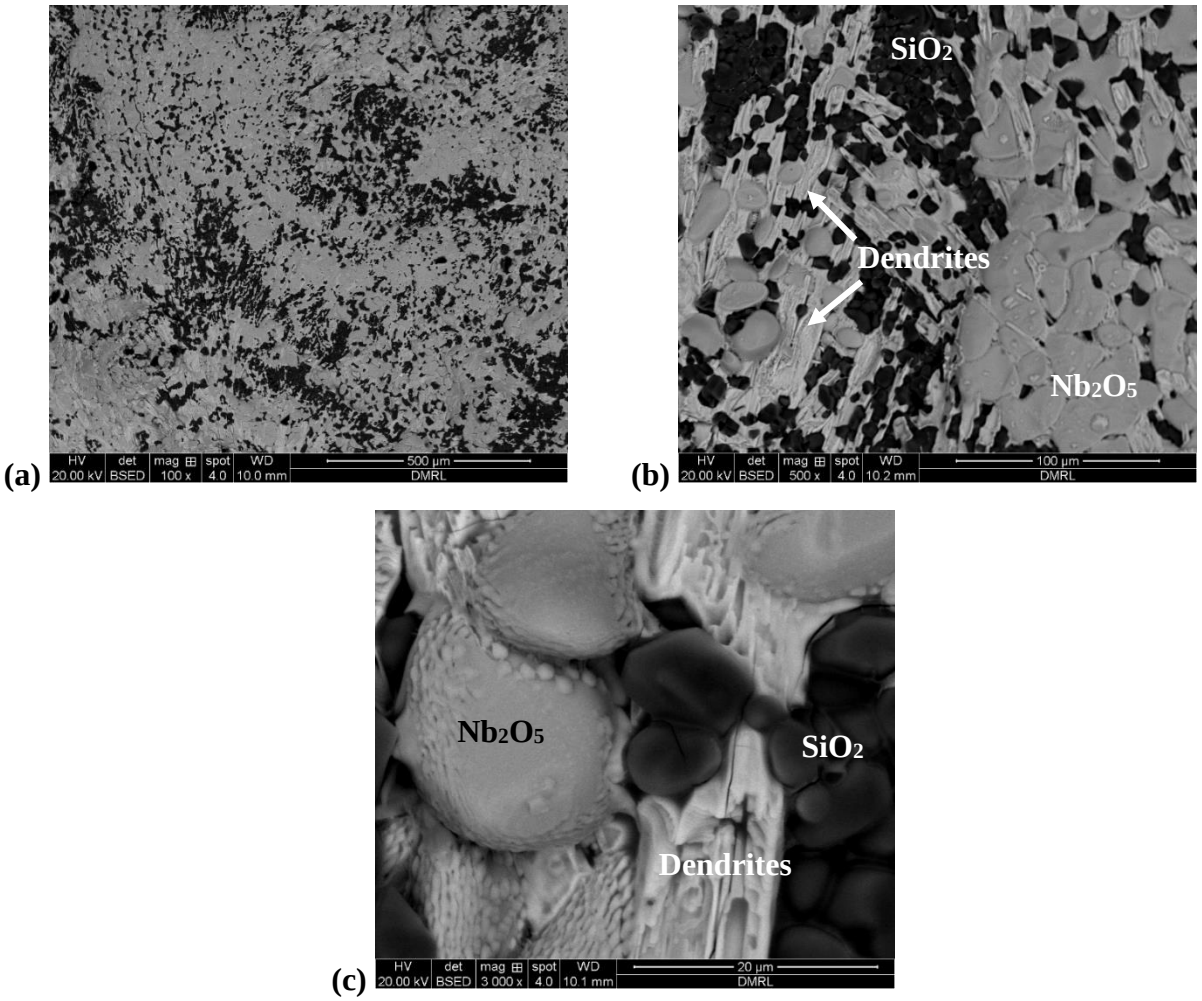

Fig. 6.12: Surface morphology of Nb-18.7Si-5Ti-5Zr oxidized at 1400°C for 375 min. (a) The oxide scale comprised the Nb_2O_5 (bright) and SiO_2 (dark) phases, (b,c) The high magnification image shows the dendritic morphology of the solidified eutectic formed by reaction of the Nb_2O_5 and SiO_2 phases at localized regions.

6.1.4.2 Cross section microstructure of the oxidation samples

The cross section microstructure of the coating after the oxidation test at 1400°C is shown in the below **Fig. 6.13**. The microstructure consisted of three layers: (1) outer layer (OL), (2) Intermediate layer (IL) and (c) Interdiffusion zone (IDZ) similar to the microstructure in as coated condition (**Fig. 6.4**). In addition, the microstructure consisted of a continuous layer of oxides as observed in the surface morphology (**Figs. 6.9-6.12**). The coating thickness decreased to 180-200 µm (**Fig. 6.13**). The linear composition profile across the thickness of the coating after oxidation is given in **Fig. 6.5(b)**. Except for decrease in the thickness of the outer $NbSi_2$ phase layer of the

coating, the composition of the intermediate layer and the IDZ (**Fig. 6.5(b)**) is similar to that of the as-deposited coating (**Fig. 6.5(a)**). The phases are analyzed in the EBSD is given in **Fig. 6.14**. The traces of equiaxed Nb and lower silicide Nb_5Si_3 phases in the outer layer of the coating (**Fig. 6.14**) is observed unlike the predominantly equiaxed $NbSi_2$ single-phase constitution of the outer layer in the un-oxidized coating (**Fig. 6.6**). The intermediate layer in the oxidized coating contained columnar grains of the complex silicide phases $Fe_3Nb_4Si_5$,$CrFe_3Nb_3Si_6$, and $Fe_4Nb_4Si_7$ (**Fig. 6.14**), which is similar to that of the as-deposited coating (**Fig. 6.6**). Likewise, the IDZ also has the two layers of fine equiaxed $NbSi_2$ and Nb_5Si_3phases (**Fig. 6.13**) as in the as-deposited coating (**Fig. 6.6**).

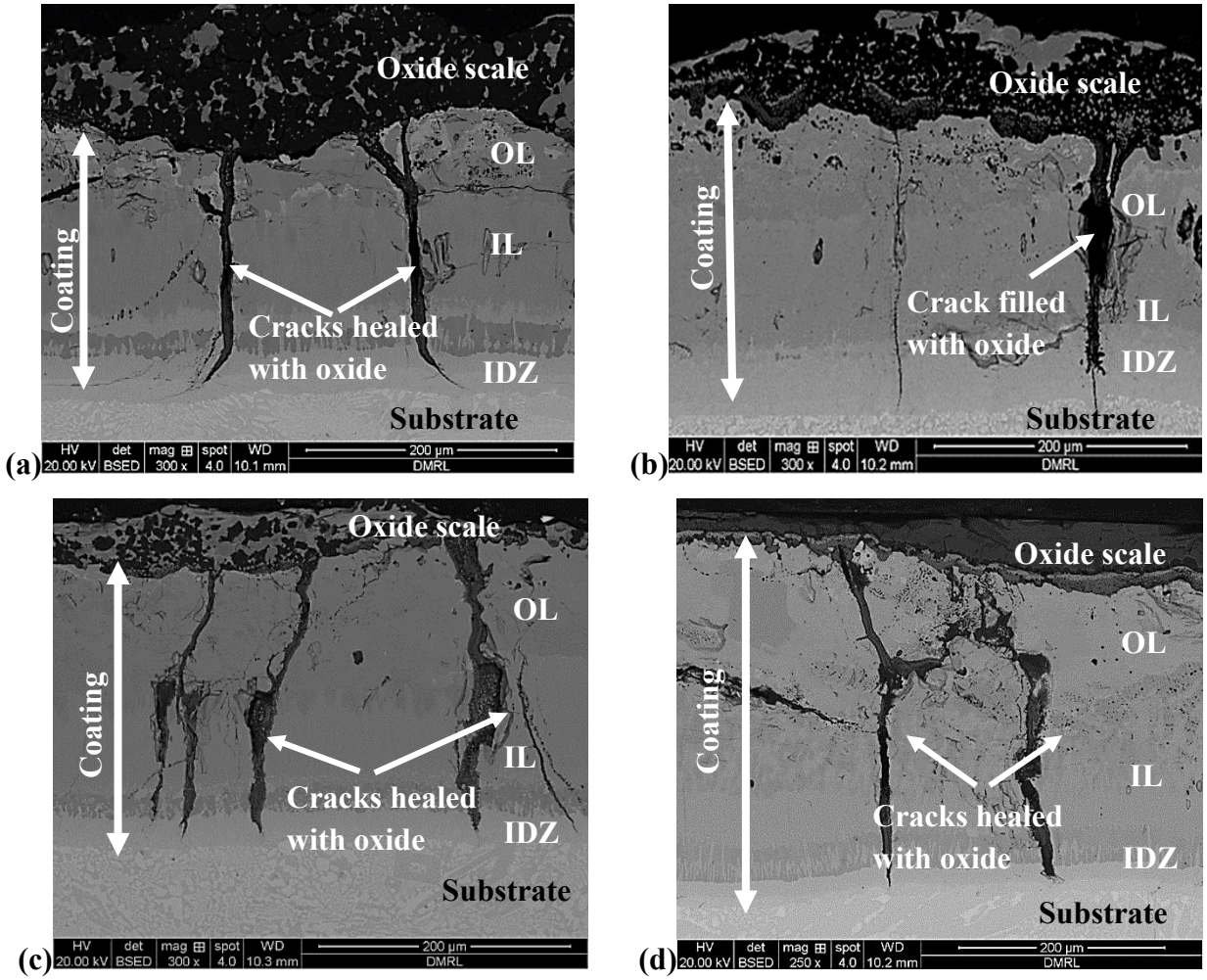

Fig. 6.13: Cross-section microstructures for the coated alloys after oxidation at 1400°C for 405 min. (a) Nb-18.7Si, (b) Nb-18.7Si-5Ti, (c) Nb-18.7Si-5Zr and (d) Nb-18.7Si-5Ti-5Zr.

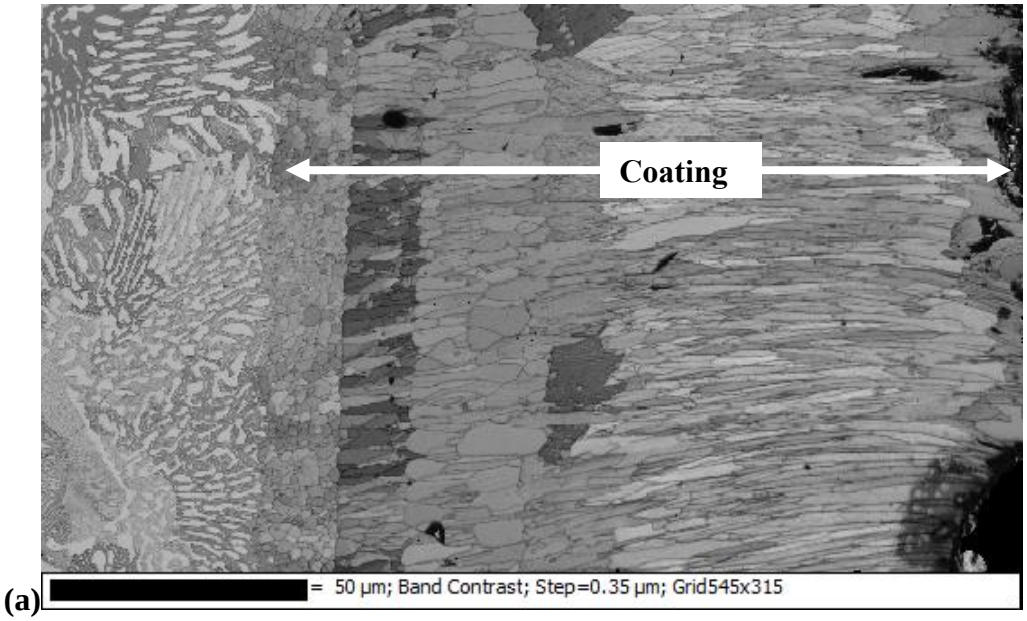

(a)

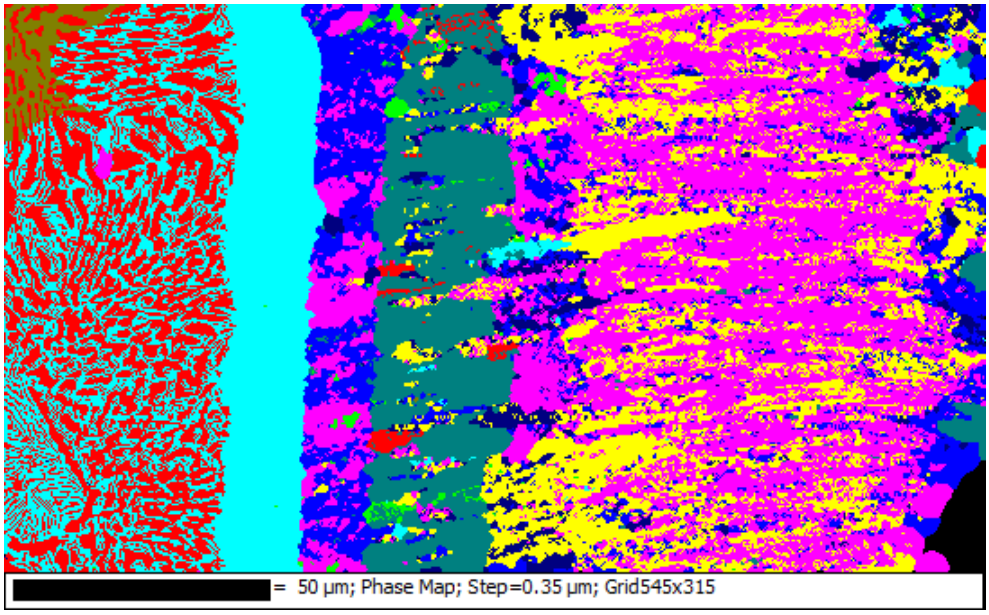

(b)

Fig. 6.14: (a) Image quality map and (b) EBSD phase map showing the phases constituting the cross-section of coated Nb-18.7Si alloy after oxidation at 1400°C for 405 min.

6.1.4.3 Phases constituting the oxide scale

The oxide layer formed on the coating surface is dense and had a multi-phase constitution across its thickness, as evident from the magnified image of the cross-section of the oxide scale (**Fig. 6.15**) The elemental X-ray maps indicated that the dark phase (region 1 in Fig. 6.15) is that of silica (SiO_2), whereas the bright phase (region 2 in **Fig. 6.15**) contained oxide of Nb (Nb_2O_5). The elemental maps also indicated that the bright phase (region 2 in **Fig. 6.15**) contained oxides of Fe and Cr along with oxide of Nb (**Fig. 6.15**). A careful examination of the oxide scale also indicated the formation of an innermost continuous thin layer of Cr-oxide (region 3 in **Fig. 6.15**). However, no complex oxides containing Nb, Fe and Cr are detected in the X-ray diffractogram (**Fig. 6.3**).

6.1.5 Substrate microstructure after oxidation

The substrate in all the coated alloys primarily exhibited a two-phase microstructure. For the Nb-18.7Si and the Nb-18.7Si-5Ti alloys, the bright and gray phases corresponded to the Nb solid solution (Nb_{ss}) and Nb_3Si, respectively, and their relative phase percentages are about 28.7 and 68.5%. Some minor amount of the α-Nb_5Si_3 phase (2.8%) is also present in both the above alloys, as evident from the EBSD phase map (**Fig. 6.16**). The α-Nb_5Si_3 phase is not expected in the as-cast Nb-18.7Si and Nb-18.7Si-5Ti alloys and however, it formed due to the eutectoid transformation of minor amounts of Nb_3Si phase during the coating formation heat treatment at 1400°C. The formation of the α-Nb_5Si_3 phase in the above alloys is consistent with the literature reports indicating that the eutectoid decomposition of the Nb_3Si phase is indeed promoted by diffusion heat treatments [*B.P. Bewlay et al., 2004, M.G. Mediratta, D.M. Dimiduk et al., 1991*]. The substrate in the coated Nb-18.7Si-5Zr alloy contained 56% of Nb_{ss} and 44% of α-Nb_5Si_3 phases and no Nb_3Si phase is detected (**Fig. 6.17**) similar to the cast microstructure.

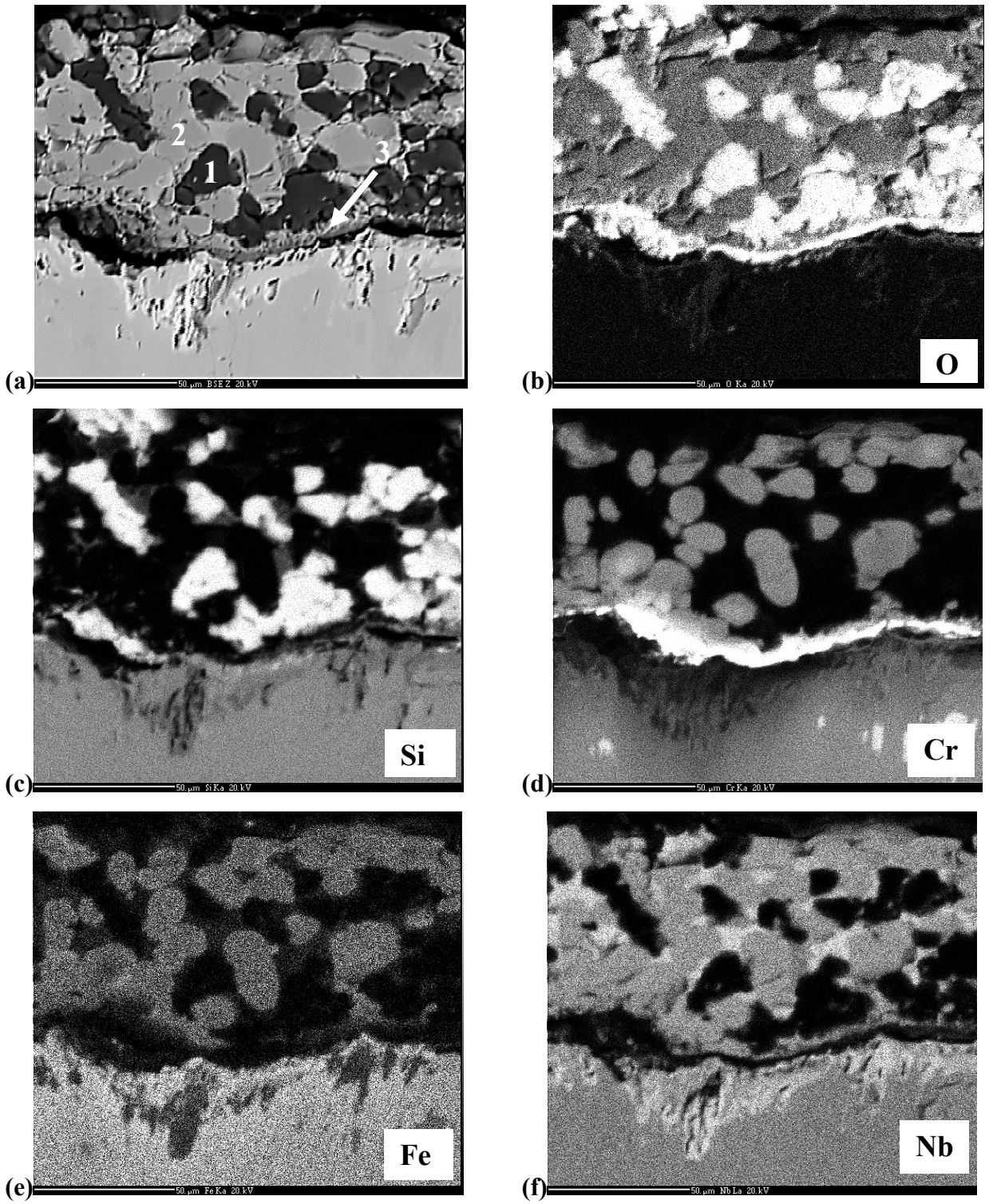

Fig. 6.15: (a) High magnification image of the typical multi-phase oxide scale and the corresponding X-ray dot maps showing the elemental distribution for (b) O, (c) Si, (d) Cr, (e) Fe and (f) Nb.

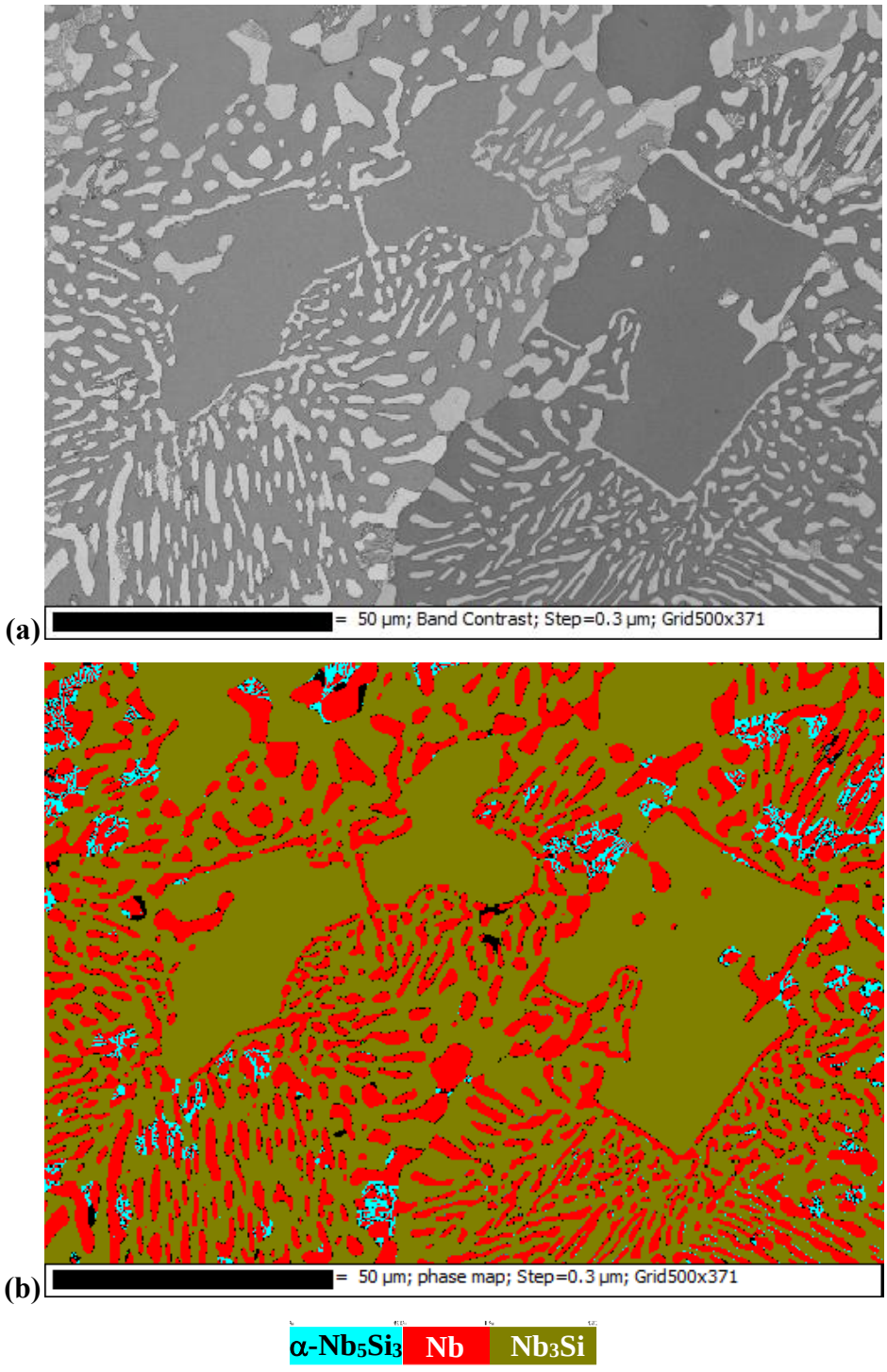

Fig. 6.16: (a) Image quality map and (b) EBSD phase map showing the phases in the substrate Nb-18.7Si alloy after oxidation at 1400°C for 405 min.

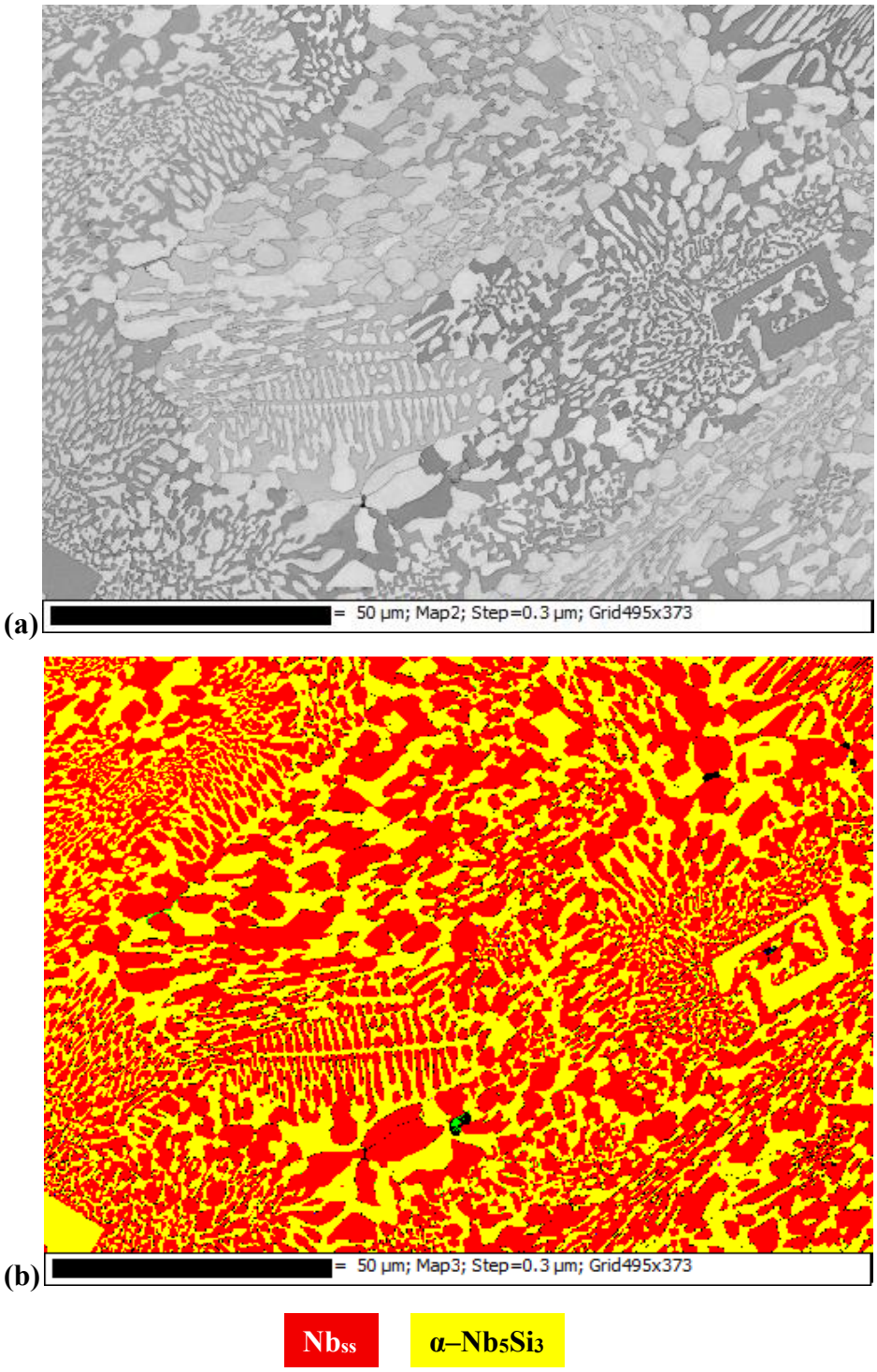

Fig. 6.17: (a) Image quality map and (b) EBSD phase map showing the phases in the substrate Nb–18.7Si–5Zr alloy after oxidation at 1400°C for 150 min.

6.2. Discussion

The loose oxide scale formation and dimensional degradation of the uncoated samples irrespective of containing Ti and /or Zr shows that the alloying did not improved the oxidation behaviour of the near eutectic Nb-Si alloy (**Fig. 6.1(a)**). Therefore, the coating is essential to control the non protective oxide formation thereby to improve the oxidation resistance.

The Fe-Cr modified silicide coating applied on all the samples is uniform and exhibited same phases with similar microstructure (**Figs. 6.3** and **6.4**). The thickness cracks observed in the coating cross section might have occurred due to the thermal stresses generated during cooling of the coating-substrate ensemble from the diffusion heat treatment temperature. The silicide coating experienced tensile residual stresses because of its higher CTE (7.3-11.7 µm.°C^{-1}) than that of the substrate alloys (7-9 µm.°C^{-1}) [*M.K. Kumawat, M.Z. Alam, A. Kumar et al., 2018 ,M.K. Kumawat, M.Z. Alam, D.K. Das et al., 2018*]. The coating being brittle is un-accommodative to the tensile thermal stresses and undergoes cracking. Such thermal stress induced cracks are typical of silicide coatings formed on Nb, W and Mo alloys [*M.Z. Alam et al., 2016, J. Otto et al., 2015, I.F. Su et al., 2015, Md.Z. Alam et al., 2011, C.M. Packer et al., 1988, S. Govindarajan et al., 1995*]. However, the cracks are confined to within the thickness of the coating and did not penetrate the substrate (**Fig. 6.4**).

6.2.1 Effect of oxidation on the coating microstructure

The coating microstructure before (**Figs. 6.4** and **6.6**) and after oxidation (**Figs. 6.13** and **6.14**) consisted of three layers, i.e., OL, IL and IDZ. The outer layer of the coating is primarily constituted of the $NbSi_2$ phase with equiaxed grain structure and the intermediate layer contained complex silicide phases of Nb, Fe and Cr, such as $Fe_3Nb_4Si_5$, $CrFe_3Nb_3Si_6$, $Fe_4Nb_4Si_7$, and exhibited a columnar grain structure (**Figs. 6.6(b), 6.14(b)**). The IDZ consisted of two distinct layers comprising of fine equiaxed $NbSi_2$ and Nb_5Si_3 phases, respectively. The above phase constitution and grain structure of the coating is consistent with that of the coating formed on the Nb-10 wt.% Hf alloy, C103 [*M.Z. Alam et al., 2016, M.K. Kumawat, M.Z. Alam, A. Kumar et al., 2018 ,M.K. Kumawat, M.Z. Alam, D.K. Das et al., 2018*].

During thermal exposure in air at high temperatures, the coating oxidized to form the continuous protective oxide layer, which is evident from the cross-section microstructures of the oxidized coated samples shown in **Fig. 6.13**. Apart from forming a protective layer on the surface, the oxide layer also healed the coating cracks which formed during repetitive thermal cycling due to the stresses arising from the difference in CTE between the coating and the substrate alloy [*M.Z. Alam et al., 2016, M.K. Kumawat, M.Z. Alam, A. Kumar et al., 2018*]. The outer layer of the coating comprising the equiaxed $NbSi_2$ phase is consumed towards formation of the oxide scale, as evident from **Fig. 6.13** and the typical EBSD map (**Fig. 6.14(a)**). The linear composition profile across the thickness of the coating after oxidation also indicated that except for decrease in the thickness of the outer $NbSi_2$ phase layer of the coating, the composition of the intermediate layer and the IDZ (**Fig. 6.5(b)**) is similar to that of the as-deposited coating (**Fig. 6.5(a)**). The traces of equiaxed Nb and lower silicide Nb_5Si_3 phases in the outer layer of the coating (**Figs. 6.14(a, b)**) formed by the loss of Si from the $NbSi_2$phase to form the silica scale, which was unlike the predominantly equiaxed $NbSi_2$ single-phase constitution of the outer layer in the un-oxidized coating (**Figs. 6.4, 6,6**). The similarity in phase constitution and composition of the intermediate and IDZ layers in the oxidized coating (**Figs. 6.5(b), 6.14(b)**) with that of the virgin coating (**Figs. 6.5(a)** and **6.6**) suggested that compositional changes caused by interdiffusion of elements across the coating-substrate ensemble is minimal during high temperature exposure.

6.2.2 Oxidation protection by coating and oxides formed from the coating during thermal exposure

The general trend of increase in the k_p values, weight gain, and oxidation life indicated that the coating is more protective against oxidation at higher temperatures (**Table 6.1, Fig. 6.7**). The resistance aganist oxidation is achieved by the formation of a protective oxide scale on the surface [*M.Z. Alam et al., 2016, M.K. Kumawat, M.Z. Alam, A. Kumar et al., 2018, M.M. Opeka et al., 2004, N.S. Jacobson et al., 1993*]. The parabolic oxidation kinetics suggested that the superficial oxide scale served as an effective barrier against the inward diffusion of oxygen from the ambient to the oxide-scale/coating interface, which thereby lowered the oxidation rate substantially [*M.Z. Alam et al., 2016, M.K. Kumawat, M.Z. Alam, A. Kumar et al., 2018, M.M. Opeka et al., 2004, N.S. Jacobson et al., 1993*]. The regime of steady weight gain is a manifestation of the lowering of the overall rate of weight gain in the samples, which ensued due to the competition between the

parabolic growth of the oxide scale and the volatilization loss of Si and Cr from the oxide scale in the form of SiO and CrO_3 vapors, as reported previously [*M.M. Opeka et al., 2004, N.S. Jacobson et al., 19393, P. Kofstad 1988, 1996*].The onset of weight loss in the coated samples, observed after approximately 300 min. of oxidation (**Fig. 6.7**), occured due to the cracking and spallation of the oxide scale under the influence of thermal stresses arising during the repititive heating and cooling oxidation test cycles, as evident from the surface morphology as shown in **Figs. 6.8-6.12**. It needs to be emphasized that despite the weight loss, there is neither catastrophic degradation nor any profuse scale formation in the oxidized coated samples. Rather, the coated samples appeared glossy and their dimensions remained intact over the entire duration of oxidation testing for 300-450 min., as shown in the **Fig. 6.1(b)**. Comparison of the surface morphologies indicated that the surface oxide scale is relatively more dense and compact at higher temperatures (**Figs. 6.9-6.12**), which can be ascribed to the sintering of the Nb-oxide scale [*P. Kofstad., 1988, 1996*]. The dendritic structure formation in the samples oxidized at higher temperatures is indicative of the formation of eutectic liquid during oxidation at 1400°C. The Nb_2O_5-SiO_2 phase diagram suggests the formation of eutectic liquid at 1448°C [*M. Ibrahim et al., 1962*]. However, the eutectic formation temperature can be potentially lowered by the presence of oxides of Fe and Cr. Since the coating contained additions of Fe and Cr, their respective oxides are also present in the oxide scale. Therefore, the localized formation of eutectic liquid at the boundaries between the Nb_2O_5 and SiO_2 phases is favored, which solidified as a dendritic structure upon cooling (**Fig. 6.9(c)**). Therefore, the interparticle boundaries in the bright regions are sealed with the eutectic liquid phase (**Fig. 6.10(c)**) and the amount of silica formation is relatively more at the higher oxidation temperature (**Figs. 6.9-6.12**) than that at the lower temperature (**Fig. 6.8**). Thereby, the glossy lustre of the surface is more prominent for the coated samples oxidized at higher temperatures.

The oxide layer consisted of niobia, Silica, Cr-oxide and no complex oxides containing Nb, Fe and Cr are detected in the X-ray diffractogram (**Fig. 6.15**). This suggested that Fe and Cr are present in solid solution in Nb_2O_5. Based on the free energy of formation ($-\Delta G_f^\circ$) values and the reported stability of oxides, it can be expected that oxidation of the Nb, Si, Cr and Fe containing phases in the coating results in the formation of the respective Nb_2O_5, SiO_2, Cr_2O_3 and Fe_2O_3 phases. The $-\Delta G_f^\circ$ over the temperature range of 800-1400°C for the above oxides are as follows: Nb_2O_5 (1175-1420 $kJ.mol^{-1}$), SiO_2 (610-712 $kJ.mol^{-1}$), Cr_2O_3 (692-843 $kJ.mol^{-1}$) and Fe_2O_3 (389-

537 kJ.mol^{-1}) [*NIST-JANAF, https://janaf.nist.gov/tables/Cr-index.html*]. The Nb_2O_5 is an ionic oxide containing positively charged anion vacancies in its crystal lattice [*O. Kubaschewski et al., 1960*], and the formation of substitutional solid solution is a possibility because the radius of Fe^{3+}(0.69 Å) [*https://www.webelements.com/iron/atom_sizes.html (Accessed on 13 Aug 2018)*] and Cr^{3+}(0.75 Å) [*https://www.webelements.com/chromium/atom_sizes.html (Accessed on 13 Aug 2018)*] ions is similar to that of Nb^{5+} ion (0.78 Å) [*https://www.webelements.com/niobium/atom_sizes.html (Accessed on 13 Aug 2018)*]. Besides their similar ionic radius, the Fe^{3+}, $Cr^{3+}$and Nb^{5+} ions exhibit octahedral coordination geometry, which favors the dissolution of Fe^{3+} and Cr^{3+} ions from the respective oxides in the Nb_2O_5 phase. On the other hand, the Si^{4+} ion in the cristobalite silica phase has significantly different ionic radius of 0.41 Å and exhibits tetrahedral coordination geometry [. *https://www.webelements.com/silicon/atom_sizes.html (Accessed on 13 Aug 2018)*]. Therefore, the formation of solid solution of silica in niobia is not feasible, and the distinct Nb_2O_5 and SiO_2 phases form in the oxide scale (**Fig. 6.15**).

The similarity in the k_p values for the coated Nb-18.7Si, Nb-18.7Si-5Ti, Nb-18.7Si-5Zr and Nb-18.7Si-5Ti-5Zr samples at the respective oxidation test temperatures indicated that the presence of Ti and Zr in the alloy did not have any effect on the oxidation characteristics of the coating (**Table 6.1**).

The beneficial effect of the coating in preventing oxidation and dimensional degradation of the samples can be ascribed to the formation of the protective multi-phase oxide scale which served as a barrier against the inward diffusion of oxygen and thereby reduced the overall oxidation of the substrate (**Fig. 6.3**). The activation energy (Q) associated with the cyclic oxidation in air of the coated samples is calclulated using the Arrhenius equation, i.e., $\ln k_p = A \exp(-Q/RT)$; where A, R and T denote the pre-exponential constant, universal gas constant, and oxidation test temperatures in K [*.P. Kofstad 1988, 1996, K. Chattopadhyay et al., 2008*]. The values of Q for all the coated alloys are similar in the range of 60-70 kJ.mol^{-1} (**Table 6.2**), and correspond to the energy required for the diffusion of oxygen through the multi-phase oxide scale during cyclic oxidation.

Table 6.2: Activation energy (Q) of the coated and oxidized samples.

Sample/Alloy	Nb-18.7Si	Nb-18.7Si-5Ti	Nb-18.7Si-5Zr	Nb-18.7Si-5Ti-5Zr
Q (kJ/mol)	62.1	70.0	60.0	65

The formation of silica is profuse above temperatures of 1000°C and sluggish at lower temperatures [*M.Z. Alam et al., 2016, M. M. Opeka et al., 2004, K. Kurokawa et al.,2006, M. Levy et al., 1974*]. This aspect is also evident from the comparison of surface morphologies which showed relatively high amount of silica formation at the higher temperature of 1400°C (**Fig. 6.10**) than that at the lower temperature of 800°C (**Fig. 6.9**). Concurrently, the formation of Nb-, Cr- and Fe-oxides is spontaneous at all temperatures, which is typically corroborated by the presence of the inner continuous layer of chromium-rich oxide just above the coating surface (region 3 in **Fig. 6.15**). The presence of Cr and Fe in the oxide layer (**Fig. 6.15(d, e)**) also suggested that during the exposure at high temperatures, the outward diffusion of Fe and Cr occurred from the intermediate layer of the coating to the outer layer, which is otherwise constituted predominantly of the single phase $NbSi_2$ in the un-oxidized coating (**Fig. 6.5**). Along with the Nb_2O_5 and SiO_2, the Fe- and Cr-oxides in the oxide scale also contributed to the oxidation resistance.

As alluded earlier, the weight loss occuring at the later stages of thermal cycling can be ascribed to the cracking and spallation of the protective oxide scale due to stresses generated during thermal cycling (**Fig. 6.7**). The Pilling Bedworth (PB) ratio for the Nb_2O_5 and SiO_2 is reported to be 2.69 and 2.15 respectively [*N.B. Pilling et al., 1923*]. Besides, the Nb_2O_5 scale is dense and is associated with high growth rate, which induces stresses in the oxide scale and its spallation [*K. Chattopadhyay et al., 2008, K. Kurokawa et al.,2006,M. Levy et al., 1974*]. On the other hand, the silica scale by virtue of its open network structure remains flexible in accommodating the stress in the oxide film without undergoing spallation at high temperatures [*M.Z. Alam et al., 2016, M. M. Opeka et al., 2004*]. However, at low temperatures below 1000°C, the rate of silica formation is low [*M.Z. Alam et al., 2016, M. M. Opeka et al., 2004*, *K. Kurokawa et al.,2006,M. Levy et al., 1974*]. Therefore, the dense outer oxide scale formed at the low temperature of 800°C, being predominantly constituted of the Nb_2O_5 phase (**Fig. 6.8**) underwent early cracking and spallation, which caused lowering of the oxidation life (**Fig. 6.7**). On the other hand, at higher oxidation temperatures above 1000°C, the oxide scale contained more of the compliant silica phase (**Figs.**

6.9-6.12), which contributed to the better retention and spallation resistance of the oxide scale, and hence improved the oxidation life of the coated samples (**Fig. 6.7**).

Despite the eventual spallation of the oxide scale, its reformation can be expected to continue until the entire coating thickness is consumed and exhausted. It is evident from **Fig. 6.11** that the coating remained intact and contributed to the formation of the oxide scale over the entire duration of the oxidation tests. The above aspect is also evident from the fact that despite the weight loss beyond about 300 min. of oxidation, there is no dimensional degradation in the coated samples (**Fig. 6.1(b)**). Besides, the coatings are compositionally compatible with the substrate alloys. Hence, no deleterious topologically close packed phases formed at the the coating-substrate interface during the high temperature oxidation exposure (**Fig. 6.11**). Therefore, the present study demonstrated that the Fe-Cr-modified silicide coating can provide significant oxidation resistance to the near-eutectic Nb-Si alloys and prevent their oxidation-induced dimensional degradation at high temperatures, which otherwise severly limits their high-temperature use irrespective of alloying with oxidation inhibitors such as Ti and Zr.

6.3 Summary

The cyclic oxidation behavior of uncoated and Fe-Cr-modified slurry silicide coated alloys are evaluated in air at 800°C, 1200°C and 1400°C. Summary of the current study is as following

1. All the uncoated alloys exhibited rapid oxidation and severe dimensional degradation, which is manifested by profuse scale formation from the very initial stages of oxidation exposure.
2. On the other hand, the Fe, Cr modified silicide coating imparted good oxidation resistance and prevented degradation in the alloys until 5-7 h even at the higher temperatures of 1400°C.
3. The protection against oxidation is ascribed to the protective multi-phase oxide scale, which formed on the coating surface as well as healed cracks.
4. The oxide scale served as a barrier against the inward diffusion of oxygen from the ambient and lowered the overall oxidation rate. The present Fe-Cr-modified silicide coating holds significance for the use of the near-eutectic Nb-Si alloys in strategic high-temperature applications involving oxidizing environments.

Chapter 7

Conclusions

&

Scope for future work

7.1 Conclusions

This chapter brings out the conclusions that emerge out of the thesis work. The microstructural aspects, room temperature mechanical properties and the high temperature oxidation response of the Nb-Si alloys, i.e., Nb-18.7Si, Nb-18.7Si-5Ti, Nb-18.7Si-5Zr and Nb-18.7Si-5Ti-5Zr is carried out. The microstructure and phase evolutions aspects are studied using SEM, EPMA, EBSD and TEM. The mechanical behaviour of the alloys at room temperature such is analysed, such as, hardness, elastic modulus, compression properties, and fracture toughness. Finally the deformation mechanisms in the alloys are proposed. Further, the oxidation behaviour of the Fe-Cr modified slurry silicide coated alloys in the temperature range of 800°C-1400°C is demonstrated. The following conclusions have been drawn from the studies:

1. The cast microstructure of Nb-18.7Si and Nb-18.7Si-5Ti alloys exhibited Nb_{ss} and Nb_3Si phases. Whereas, the Nb-18.7Si-5Zr and Nb-18.7Si-5Ti-5Zr alloys resulted in the formation of Nb_{ss} and α–Nb_5Si_3 phases.
2. The dissolved Si content in the Nb_{ss} phase played a dominant role on the hardness value which influenced with the alloying element present in the phase.
3. The Ti and Zr additions resulted in the solid solution strengthening and softening of the alloy, respectively. Solid solution strengthening of the Nb-18.7Si-5Ti-5Zr alloy depicts the dominant hardnening effect of the Ti.

4. Among the alloys, the Nb-18.7Si-5Ti-5Zr alloy exhibited maximum compressive strength (2236±81 MPa) along with the good fracture toughness (10.59±0.35 MPa.$m^{1/2}$) value.
5. Fracture in the alloys started with microcrack in the silicide phase and the Nb_{ss} phase acted as the barrier for the crack propagation by crack bridging, branching and deflection mechanisms and increased the crack path tortuousity.
6. High volume fraction and coarse Nb_{ss} phase increased the crack path tortuousity by crack bridging, branching and deflection mechanisms in the Nb-18.7Si-5Zr and Nb-18.7Si-5Ti-5Zr alloys and resulted with high fracture toughness. Further, decrease in the silicide phase fraction also contributed to the toughness enhancement.
7. The Fe, Cr modified silicide coating imparted good oxidation resistance and prevented degradation in the alloys until 5-7 h even at the higher temperatures of 1400°C.
8. The protection against oxidation can be ascribed to the protective multi-phase oxide scale, which formed on the coating surface as well as the crack healing.
9. The achievement of good combination of properties with stable microstructure without subjecting the Nb-Si alloys to any additional heat treatment process is the promising outcome of this work.

7.2 Scope for future work

In the current investigation, detailed effect of the Ti and Zr alloying additions on the microstructural behaviour, phase evolution, room temperature strength and fracture toughness properties of the cast Nb-18.7Si alloy was demonstrated. The deformation mechanisms in the alloys was proposed. Further, the high temperature oxidation behaviour of the Fe-Cr modified slurry silicide coated alloys in a temperature range of 800°C-1400°C was discussed. However, these alloys have the potential to replace the hot sections of the turbine engine that experience temperatures higher than 1200°C. Therefore, it is necessary to understand the high temperature mechanical behaviour of the alloys. Further, the high temperature encountered in the turbine engines with high velocities causes the oxide scales on the surface vulnerable to environmental and chemical attack.

The points listed below may be considered for future research in order to have better understanding of the Nb-Si alloys for turbine applications

1. High temperature strength, creep properties (1200°C) and detailed understanding of the deformation mechanisms in the Nb-18.7Si-5Zr and Nb-18.7Si-5Ti-5Zr alloys.
2. Microstructural changes and its stability in the alloys during heat treatment and its effect on mechanical properties of Nb-18.7Si-5Ti, Nb-18.7Si-5Zr and Nb-18.7Si-5Ti-5Zr alloys.
3. Study the synergic effect of Ti and Zr along with other alloying elements on microstructure evolution and mechanical properties of Nb-Si alloy.
4. Assessment of high temperature oxidation behaviour with Thermal barrier coatings.
5. Manufacturing of these alloys through directional solidification route and study the influence of processing route on the microstructure and mechanical properties.

References

1. ASTM E399–12 International, Standard Test Method for Linear–Elastic Plane-Strain Fracture Toughness of KIC Metallic Materials. ASTM International, West Conshohocken (PA), 2012.
2. B. Gleeson. Thermal barrier coatings for aeroengine applications. Journal of Propulsion and Power 22(2) (2006) 375-383.
3. B.P. Bewlay, M.R. Jackson, J.-C. Zhao, P.R. Subramanian, M.G. Mendiratta and J.J. Lewandowski. Ultra high-temperature nb-silicide-based composites. MRS Bulletin September (2003) 646–653.
4. B.P Bewlay, M.R. Jackson, J.C. Zhao, P.R. Subramanian. A Review of very high temperature nb-silicide based composites. Metallurgical and Matererials Transactions A 34 (2003) 2043–2052.
5. B.P. Bewlay, H.A. Lipsitt, M.R. Jackson, W.J. Reeder, J.A. Sutliff. Solidification processing of high temperature intermetallic eutectic-based alloys. Materials Science and Engineering A 192/193 (1995) 534–543.
6. B.P. Bewlay , Y. Yang, R.L. Casey, M.R. Jackson, Y.A. Chang. Experimental study of the liquid–solid phase equilibria at the metal-rich region of the Nb–Cr–Si system. Intermetallics 17 (2009) 120–127.
7. B.P. Bewlay, S.D. Sitzman, L.N. Brewer, and M.R. Jackson. Analyses of eutectoid phase transformations in nb–silicide in situ composites. Journal of Microscopy and Microanalysis 10 (2004) 470–480.
8. B.P. Bewlay, M.R. Jackson, W.J. Reeder and H.A. Lipsitt. Microstructures and properties of DS in-situ composites of Nb-Ti-Si alloys. Materials Research Society Symposium Proceedings 364 (1995) 943–948.
9. B.P. Bewlay, H.A. Lipsitt, W.J. Reeder, M.R. Jackson and J.A. Sutliff. in processing and fabrication of advanced materials for high temperature applications III. Eds. V.A. Ravi, T.S. Srivatsan and J.J. Moore (TMS Publications, Warrendale, PA, 1993) 547–565.

10. B.P. Bewlay, M.R. Jackson, and H.A. Lipsitt. The Balance of mechanical and environmental properties of a multielement niobium-niobium silicide-based insitu composites. Metallurgical and Materials transactions A 27 (1996) 3801–3808.
11. B.P. Bewlay, M.R. Jackson, R.R. Bishop. The Nb-Ti-Si ternary phase diagram: Determination of solid-state phase equilibria in Nb- and Ti- rich alloys. Journal of Phase Equilibria 19 (6) (1998) 577–586.
12. B.P. Bewlay, C.L. Briant, A.W, Davis, M.R. Jackson. The effect of volume fraction on the creep behaviour of nb-silicide based in-situ composites. Materials Research Society Symposium Proceedings 646 (2001) N2.7.1-N2.7.6.
13. B.A. Pint , J.R. Di Stefano, I.G. Wright. Oxidation resistance: One barrier to moving beyond Ni-base superalloys. Materials Science and Engineering A 415 (2006) 255–263.
14. C.L. Ma, J.G. Li, Y. Tan, R. Tanaka, S. Hanada. Microstructure and mechanical properties of Nb/Nb_5Si_3 in situcomposites in Nb–Mo–Si and Nb–W–Si systems. Materials Science and Engineering A 386 (2004) 375–383.
15. C.S. Tiwary, S. Kashyap, K. Chattopadhyay. Effect of Mg addition on microstructural, mechanical and environmental properties of Nb-Si eutectic composite. Materials science and Engineering A 560 (2013) 200–207.
16. C.M. Packer. Proceedings of the Workshop on the oxidation of high-temperature intermetallics. eds. T. Grobstein and J. Doychak (1988), p. 235.
17. D. Yonghua. Stability, elastic constants and thermodynamic properties of (α. β, γ) Nb_5Si_3 phases. Rare Metal Materials and Engineering 44 (1) (2015) 18–23.
18. D.L. Davidson, K.S. Chan and D.L. Anton. The effects on fracture toughness of ductile-phase composition and morphology in Nb-Cr-Ti and Nb-Si insitu composites. Metallurgical and Materials Transactions A 27 (1996) 3007–3017.
19. D. Farkas. Atomistic simulations of fracture in the B2 phase of the Nb–Ti–Al system. Materials Science and Engineering A 249 (1998) 249–258.
20. E. Guo, S. S. Singh, C. S. Kairaa, X. Meng, Y. Xu, L. Luo, M. Wang, N. Chawla. Mechanical properties of micro constituents in Nb-Si-Ti alloy by micropillar compression and nanoindentation. Materials Science and Engineering A 687 (2017) 99–106.

21. F. Wang, L. Luo, Y. Xu, X. Meng, L. Wang, B. Han, Y. Su, J. Guo, H. Fu. Effects of alloying on the microstructures and mechanical property of Nb-Mo-Si based in situ composites. Intermetallics 88 (2017) 6–13.
22. George E.Dieter, Mechanical Metallurgy, third Edition, Mc. Graw Hill Inc., (1986) 247-249.
23. I. Grammenos, P. Tsakiropoulos. Study of the role of Hf, Mo and W additions in the microstructure of Nb-20Si silicide based alloys. Intermetallics 19 (2011) 1612–1621.
24. I. Grammenos, P. Tsakiropoulos. Study of the role of Al, Cr and Ti additions in the microstructure of Nb–18Si–5Hf base alloys. Intermetallics 18 (2010) 242–253
25. I. Grammenos, P. Tsakiropoulos. Study of the role of Mo and Ta additions in the microstructure of Nb-18Si-5Hf silicide based alloy. Intermetallics 18 (2010) 1524–1530.
26. J.H. Perepezko, "The hotter engine, the better," Science 326 (2009) 1068–1069.
27. J. Wadsworth, T.G. Nieh, J.J. Stephens. Recent advances in aerospace refractory metal alloys. International Material Reviews 33 (1988) 131–50.
28. J.R. Zhou, J.B. Sha. Microstructural evolution and mechanical properties of an Nb-16Si in-situ composite with Fe additions prepared by arc-melting. Intermetallics 34 (2013) 1-9.
29. J. H. Kim, T. Tabaru, H. Hirai, A. Kitahara, Shuji Hanada. Tensile properties of a refractory metal base in situ composite consisting of an Nb solid solution and hexagonal Nb5Si3. Scripta Materialia 48 (2003) 1439–1444.
30. J. Geng, P. Tsakiropoulos, G. Shao. A study of the effects of Hf and Sn additions on the microstructure of Nb_{ss}/Nb_5Si_3 based in situ composites. Intermetallics 15(1) (2007) 69–76
31. J. Geng, P. Tsakiropoulos, G. Shao. The effects of Ti and Mo additions on the microstructure of Nb-silicide based in situ composites. Intermetallics 14 (2006) 227–235.
32. J. Geng, P. Tsakiropoulos, G. Shao. A thermo-gravimetric and microstructural study of the oxidation of Nbss/Nb5Si3-based in situ composites with Sn addition. Intermetallics 15 (2007) 270–281.
33. J. Geng , P. Tsakiropoulos. A study of the microstructures and oxidation of Nb-Si-Cr-Al-Mo in situ composites alloyed with Ti, Hf and Sn. Intermetallics 15 (2007) 382–395.
34. J. Geng, P. Tsakiropoulos, G. Shao. A thermo-gravimetric and microstructural study of the oxidation of Nb_{ss}/Nb_5Si_3-based *in situ* composites with Sn addition. Intermetallics 15(3) (2007) 270–281.

35. J. Nelson, M. Ghadyani, C. Utton and P. Tsakiropoulos. A Study of the effects of Al, Cr, Hf and Ti Additions on the microstructure and oxidation of Nb-24Ti-18Si silicide based alloys. Materials 11 (2018) 1579.
36. J. Zhao, C. Utton and P. Tsakiropoulos. On the microstructure and properties of Nb-12Ti-18Si-6Ta-2.5W-1Hf (at.%) silicide-based alloys with Ge and Sn additions. Materials 13 (2020) 1778.
37. J. D. Rigney and J. J. Lewandowski. Loading rate and test temperature effects on fracture of in situ niobium silicide-niobium composites. Metallurgical and Materials Transactions A 27 (1996) 3292–3306.
38. J. D. Rigney. Fracture of laminated and in-situ niobium silicide-niobium composites. Online proceedings library archive 434 (1996) 227–241.
39. J.T. Clenny, C.J. Rosa. Oxidation kinetics of niobium in the temperature range of 873–1083 K. Metallurgical Transactions A 11 (1980) 1383–1388.
40. J. Otto, L. Steffes, L. Su, M. Dana. Jackson and J.H. Perepezko. Mo–Si–B coating for improved oxidation resistance of niobium. Advanced Engineering Materials 17 (7) (2015) 1068–1075.
41. J.-C. Zhao and J. H. Westbrook. Guest Editors. Ultrahigh- temperature materials for jet engines. MRS bulletin SEPTEMBER (2003) 622–630.
42. K.S. Chan. Modelling creep behavior of niobium silicide in-situ composites. Materials Science and Engineering A 337 (2002) 59–66.
43. K.S. Chan. Alloying effects on fracture mechanisms in Nb-based intermetallic in-situ composites. Materials Science and Engineering A 329–331 (2002) 513–522.
44. K.S. Chan. Intermetallic composites toughened with ductile reinforcements. Intermetallic Matrix Composites. chapter 13 (2018) 359–407. http://dx.doi.org/10.1016/B978-0-85709-346-2.00013-3.
45. K.S. Chan and D.L. Davidson. Delineating brittle-phase embrittlement and ductile-phase toughening in Nb-based in-situ composites. Metallurgical and materials transactions A 32 (2001) 2717–2727.
46. K.S. Chan. Alloying effects on the fracture toughness of Nb-based silicides and laves phases. Materials science and engineering A 409 (2005) 257–269.

47. K. Chattopadhyay, G. Balachandran, R. Mitra, K.K. Ray. Effect of Mo on Microstructure and Mechanical behaviour of as cast Nbss-Nb5Si3 in situ composites. Intermetallics 14 (2006) 1452–1460.
48. K. Zelenitsas. T. Sakiropoulos. Study of the role of Al and Cr additions in the microstructure of Nb–Ti–Si in situ composites. Intermetallics 13 (10) (2005) 1079–1095.
49. K. Zelenitsas. T. Sakiropoulos. Study of the role of Ta and Cr additions in the microstructure of Nb–Ti–Si-Al in situ composites. Intermetallics 14 (2006) 639–659.
50. K. Chattopadhyay, R. Sinha, R. Mitra, K.K. Ray. Effect of Mo and Si on morphology and volume fraction of eutectic in Nb–Si–Mo alloys. Materials science and engineering A 456(1-2) (2007) 358–363.
51. K. Chattopadhyay, R. Mitra, and K.K. Ray**.** Nonisothermal and isothermal oxidation behavior of Nb-Si-Mo alloys. Metallurgical and Materials Transactions A 39 (2008) 577**–** 592.
52. K. S. Chan. Cyclic-oxidation resistance of niobium-base in situ composites: Modelling and experimentation. Oxidation of Metals 61(3/4) (2004) 165–194.
53. K. S. Chan and D. L. Davidson. Effect of Ti addition on cleavage fracture of Nb-Cr-Ti solid solution alloy. Metallurgical and. Materials Transactions A 30 (1999) 925–939.
54. K. Zelenitsas, P. Tsakiropoulos. Effect of Al, Cr and Ta additions on the oxidation behaviour of Nb-Ti-Si in situ composites at 800°C. Materials Science and Engineering A 416 (2006) 269–280.
55. K. Kurokawa, D. Goto, J. Kuchino, A. Yamauchi, T. Shibayama, H. Takahashi. Microstructures of SiO2 scales formed on MoSi2. Materials Science Forum 522–523 (2006) 595–602.
56. L. Zifu, P. Tsakiropoulos. Study of the effects of Ge addition on the microstructure Nb−18Si in situ composites. Intermetallics 18 (2010) 1072–1078.
57. L. Zifu, P. Tsakiropoulos. The microstructures of Nb–18Si–5Ge–5Al and Nb–24Ti–18Si–5Ge–5Al in situ composites. Journal of alloys and compounds 550 (2013) 553–560.
58. L. Zifu, P. Tsakiropoulos. Study of the effect of Ti and Ge in the microstructure of Nb-24Ti-18Si-5Ge in situ composite. Intermetallics 19 (2011) 1291–1297.

59. L. Su, L. Jia, K. Jiang, H. Zhang. The oxidation behaviour of high Cr and Al containing Nb-Si-Ti-Hf-Al-Cr alloys at 1200 and 1250°C. International Journal of Refractory Metals & Hard Materials 69 (2017) 131–137.
60. L. Su, O. Lu Steffes, H. Zhang, J.H. Perepezkp. An ultra-high temperature Mo-Si-B based coating for oxidation of Nbss/ Nb5Si3 composites. Applied Surface Science 337 (2015) 38–44.
61. L.X. Zhao, X.P. Guo, Y.Y. Jiang. Preparation and structural formation of oxidation-resistant silicide coatings on Nb-based alloy by pack cementation technique. Journal of nonferrous metals 17 (2007) 596–601.
62. M.E Schlesinger, H. Okamoto, A.B. Gokhale, R. Abbaschian. The Nb-Si (Niobium-Silicon) system. Journal of Phase Equilibria 14 (1993) 502–509.
63. M. Wu, Y. Wang, S. Li, L. Jiang, Y. Han. Effect of Si on microstructure and fracture toughness of directionally solidified Nb Silicide alloys. International Journal of Modern Physics B 24(15−16) (2010) 2964–2969.
64. M.G. Mediratta and D.M. Dimiduk. Phase relations and transformation kinetics in the high Nb region of the Nb-Si system. Scripta Metallurgica et Materialia 25 (1991) 237–242.
65. M.G. Mendiratta, J.J. Lewandowski and M. Dimiduk. Strength and ductile-phase toughening in the two-phase Nb/Nb_5Si_3 alloys. Metallurgical Transaction A 22 (1991) 1573–1583.
66. M.G. Mendiratta, D.M. Dimiduk. Strength and toughness of a Nb/Nb5Si3 composite. Metallurgical Transactions A 24 (1993) 501–504.
67. M. Sankar, G. Phanikumar, Vajinder Singh, V.V. Satya Prasad. Effect of Zr additions on microstructure evolution and phase formation of Nb−Si based ultrahigh temperature alloys. Intermetallic 101 (2018) 123–132.
68. M. Sankar, G. Phanikumar, V.V. Satya Prasad. Effect of Zr addition on the mechanical properties of Nb-Si based alloys. Materials Science and Engineering A 754 (2019) 224–231.
69. M. F. Ashby, F. J. Blunt, and M. Bannister. Flow characteristics of highly constrained metal wires. Acta Metallurgica 37(7) 1847–1857.
70. M. Bannister and M. F. Ashby. The deformation and fracture of constrained metal sheets. Acta Metallurgica et materialia 39(11) (1991) 2572–2582.

71. M. Z. Alam, A. Sambasiva Rao, D. K. Das. Microstructure and high temperature oxidation performance of silicide coating on Nb-based alloy C-103. Oxidation of Metals 73 (2010) 513–530.
72. M.D. Novak, C.G. Levi. Oxidation and volatilization of silicide coatings for refractory niobium alloys. Proceedings of IMECE 2007–42908.
73. M.Z. Alam, S. Sarin, M.K. Kumawat, D.K. Das. Microstructure and oxidation behaviour of Fe–Cr–silicide coating on a niobium alloy. Materials Science and Technology 32(18) (2016) 1826–1837.
74. M.K. Kumawat, M.Z. Alam, A. Kumar, K. Gopinath, S. Saha, V. Singh, V. Srinivas, DK. Das. Tensile behavior of a slurry Fe-Cr-Si coated Nb-alloy evaluated by gleeble testing. Surface Coatings Technology 39 (2018) 695–706.
75. M.K. Kumawat, M.Z. Alam, D.K. Das. Effect of cyclic oxidation on the tensile behavior of a Fe-Cr-Si coated Nb base alloy. Corrosion Science 131 (2018) 174–186.
76. Md. Z. Alam, S. Saha, B. Sarma, D.K. Das. Formation of WSi2 coating on tungsten and its short-term cyclic oxidation performance in air. International Journal of Refractory Metals and Hard Materials 29 (2011) 54–63.
77. M. M. Opeka, I. G. Talmy, J. A. Zaykoski. Oxidation-based materials selection for 2000°C hypersonic aero surfaces: Theoretical considerations and historical experience. Journal of Materials Science 39 (2004) 5887–5904.
78. M. Ibrahim and N.F.H. Bright. The binary system Nb2O5-SiO2. Journal of American. Ceramic Society 45(5) (1962) 221–222.
79. M. Levy, J.J. Falco, and R.B. Herring. Oxidation of Nb and coated Nb alloys. Jornal of Less-Common Metals 34 (1974) 321–343.
80. N. Sekido, Y. Kimura, S. Miura and Y. Mishima. Solidification process and mechanical behaviour of the Nb/Nb_5Si_3 two phase alloys in the Nb-Ti-Si System. Materials Transactions 45 (2004) 3264–71.
81. N. Sekido , Y. Kimura, S. Miura, F-G.Wei, Y. Mishima. Fracture toughness and high temperature strength of unidirectionally solidified Nb-Si binary and Nb-Ti-Si ternary alloys. Journal of Alloys and Compounds 425 (2006) 223–229.

82. N. Sekido, Y. Kimura, S. Miura, Y. Mishima. Microstructure development of unidirectionally solidified (Nb)/Nb3Si eutectic alloys. Materials Science and Engineering A 444 (2007) 51–57.
83. N. Sekido, Y. Kimura, F.G. Wei, S. Miura, Y. Mishima. Effect of lamellar spacing on the mechanical properties of (Nb)/(Nb,Ti)5Si3 two-phase Alloys. Journal of Japan Institute of Metals 64 (11) (2000) 1056–1061.
84. N. Vellios, P.Tsakiropoulos. The role of Sn and Ti additions in the microstructure of Nb-18Si base alloys. Intermetallics 15 (2007) 1518–1528.
85. N. Vellios, P.Tsakiropoulos. The role of Fe and Ti additions in the microstructure of Nb-18Si-5Cr base alloys. Intermetallics 15 (2007) 1529–1537.
86. N. Vellios, P.Tsakiropoulos. The role of Fe and Sn additions in the microstructure of Nb-18Si-5Sn base alloys. Intermetallics 18 (2010) 1729–1736.
87. N. Esparza, V. Rangel, A. Gutierrez, B. Arellano & S. K. Varma. A comparison of the effect of Cr and Al additions on the oxidation behaviour of alloys from the Nb–Cr–Si system. Materials at High Temperatures 33(2) (2016) 105–114.
88. N. S. Jacobson. Corrosion of silicon-based ceramics in combustion environments. Journal of American Ceramic Society 76(1) (1993) 3–28.
89. NIST-JANAF. Thermochemical Tables, https://janaf.nist.gov/tables/Cr-index.html (Accessed on 13 Aug 2018).
90. N.B. Pilling, R. E. Bedworth. The oxidation of metals at high temperatures. Journal of the Institute of Metals 29 (1923) 529–591.
91. O. Kubaschewski, B.E. Hopkins. Oxidation mechanisms of niobium, tantalum, molybdenum and tungsten. Journal of Less Common Metals 2 (1960) 172–80.
92. P. Tsakiropoulos. Alloys for application at ultra-high temperatures: Nb-silicide in situ Composites Challenges, breakthroughs and opportunities. Progress in materials science, (2020) https://doi.org/10.1016/j.pmatsci.2020.100714.
93. P.R. Subramanian, M.G. Mendiratta and D.M. Dimiduk. Microstructure and mechanical behavior of Nb-Ti base beta+silicide alloys. Materials resource symposium proceeding 322 (1994) 491–502.

94. P. Zheng, J.B. Sha, D.M. Liu, S.K. Gong, H.B. Xu. Effect of Hf on high-temperature strength and room-temperature ductility of Nb–15W–0.5Si–2B alloy. Materials Science and Engineering A (483–484) 2008 656–659.
95. P. Maji, R. Mitra, K.K. Ray. Effect of Cr on the evolution of microstructures in as-cast ternary niobium-silicide-based composites. Intermetallics 85 (2017) 34–47.
96. P. R. Subramanian, M. G. Mendiratta, D. M. Dimiduk and M. A. Stucke. Advanced intermetallic alloys-beyond gamma titanium aluminides. Material science and engineering A 239/240 (1997) 1–13.
97. P. Sudharshan Phani, W.C. Oliver. A critical assessment of the effect of indentation spacing on the measurement of hardness and modulus using instrumented indentation testing. Materials and Design 164 (2019) 107563.
98. P. Kofstad. High temperature corrosion. Elsevier Applied Science Publishers Ltd. (1988).
99. P. Kofstad. High temperature oxidation of metals. John Wiley & Sons, Inc. (1996).
100. R. M. Nekkanti and Dennis M. Dimiduk. Ductile-phase toughening in niobium-niobium silicide powder processed composites. Material Research Society Symposium Proceedings 194 (1990) 175–182.
101. R.T. Begley, J.H. Bechtold. Effect of alloying on the mechanical properties of niobium. Journal of less Common metals 3 (1961) 1–12.
102. R. J. Grylls, B. P. Bewlay, H. A. Lipsitt & H. L. Fraser. Characterization of silicide precipitates in Nb–Si and Nb–Ti–Si alloys. Philosophical Magazine A 81(8) (2001) 1967–1978.
103. S. J. Balsone, B. P. Bewlay, M. R. Jackson, P. R. Subramanian, J. C. Zhao, A. Chatterjee, T. M. Heffernan. Materials beyond, super alloys-exploiting: high-temperature composites. In Proceedings of the 2001 Intermetallics Symposium on Structural intermetallics, eds. K.J. Hemker, D.M.Dimiduk, H. Clemens. R. Darolia, H. Inui, J. M. Larsen, V.K. Sikka, M. Thomas and J.D. Whittenberger, 99-108. Warrendale, PA:TMS.
104. S. Drawin, D. Boivin, P. Petit. Microstructural Properties of Nb-Si Alloys Investigated using EBSD at Large and Small Scale. Metallurgical and Materials Transactions A 36 (2005) 497–505.

105. S. Miura, Y. Murasato, Y. Sekito, Y. Tsutsumi, K. Ohkubo, Y. Kimura, Y. Mishima, T. Mohri. Effect of microstructure on the high-temperature deformation behavior of Nb–Si alloys. Materials Science and Engineering A 510–511 (2009) 317–321.
106. S. Miura, M. Aoki, Y. Saeki, K. Ohkubo, Y. Mishima and T. Mohri. Effects of Zr on the eutectoid decomposition behavior of Nb_3Si into (Nb)/Nb5Si3. Metallurgical and materials transactions A 36 (2005) 489–496.
107. S. Qu, Y. Han, L. Song. Effects of alloying elements on phase stability in Nb-Si system intermetallics materials. Intermetallics 15 (2007) 810–813.
108. S. Zhang, X.P. Guo. Effects of Cr and Hf additions on the microstructure and properties of Nb silicide based ultrahigh temperature alloys. Materials Science and Engineering A 638 (2015) 121–131.
109. S. Shi , L. Zhu, H. Zhang , Z. Sun. Toughening of α-Nb_5Si_3 by Ti. Journal of Alloys and Compounds 689 (2016) 296–301.
110. S. Kashyap, C.S. Tiwary, K. Chattopadhyay. Microstructure and mechanical properties of oxidation resistant suction cast Nb–Si–Al alloy. Materials Science & Engineering A 559 (2013) 74–85.
111. S.M. Zhang, J.R. Zhou, J.B. Sha. Effect of Fe additions on microstructure and mechanical properties of a multi-component Nb-16Si-22Ti-2Hf-2Al-2Cr alloy at room and high temperatures. Intermetallics 57 (2015) 146–155.
112. S. Kashyap, C.S. Tiwary, K. Chattopadhyay. Effect of gallium on the microstructure and mechanical properties of Nb-Si eutectic alloy. Intermetallics 19 (2011) 1943–1952.
113. S. Mathieu, S. Knittel, P. Berthod, S. Mathieu, M. Vilasi. On the oxidation mechanism of niobium-base in situ composites. Corrosion Science 60 (2012) 181–192.
114. S. Knittel, S. Mathieu, L. Portebois, M. Vilasi. Effect of tin addition on Nb-Si-based in situ composites Part II: Oxidation behavior. Intermetallics 47 (2014) 43–52.
115. S. Knittel, S. Mathieu, M. Vilasi. Nb4Fe4Si7 coatings to protect niobium and niobium silicide composites against high temperature oxidation. Surface Coatings Technology 235 (2013) 144–154.
116. S. Knittel, S. Mathieu, L. Portebois, S. Drawin, M. Vilasi. Development of silicide coatings to ensure the protection of Nb and silicide composites against high temperature oxidation. Surface Coatings Technology 235 (2013) 401–406.

117. S.Y. Liu, S. Liu, D.J. Li, S. Wang, J.Guo and Y. Shen. Ab initio atomistic study on the oxidation mechanism of binary and ternary surfaces. The journal of chemical physics 142 (2015) 064705.
118. S. Priceman, L. Sama. Protective coatings for refractory metals formed by the fusion of silicon alloy slurries. Electrochemical Technology 6 (1968) 315–326.
119. S. Govindarajan, B. Mishra, D. L. Olson, J. J. Moore, and J. Disam. Synthesis of molybdenum disilicide on molybdenum substrates. Surface Coatings Technology 76–77 (1995) 7–13.
120. S. Zhang, X. Guo. Microstructural characteristics of Nb-Si based ultrahigh temperature alloys with B and Hf additions. Intermetallics 64 (2015) 51–58.
121. T. M. Pollock. Alloy design for aircraft engines. Natural materials 2016; 15:809-815.
122. T. M. Pollock, S. Tin. Nickel based super alloys for advanced turbine engines: chemistry, microstructure and properties. Journal of Propulsion and Power 22(2) (2006) 361–374.
123. T.B. Massalski, H. Okamoto, P.R. Subramanian, L. Kacprzak. Binary alloy phase diagrams. 2nd eddition. ASM International publishers (1990), vol. 3, p. 2767.
124. T. Thandorn, P. Tsakiropoulos. Study of the role of B addition on the microstructure of the Nb-24Ti-18Si-8B alloy. Intermetallics 18 (2010) 1033–1038.
125. W.Y. Kim, H Tanaka, S Hanada. Microstructure and high temperature strength at 1773 K of Nbss/Nb5Si3 composites alloyed with molybdenum. Intermetallics 10 (2002) 625–634.
126. W.Y. Kim, H. Tanaka, A. Kasama, S. Hanada. Microstructure and room temperature fracture toughness of Nbss/Nb_5Si_3 in situ composites. Intermetallics 9 (2001) 827–834.
127. W.Y. Kim, H. Tanaka, A. Kasama, R. Tanaka, S. Hanada. Microstructure and room temperature deformation of Nbss/Nb5Si3 in situ composites alloyed with Mo. Intermetallics 9 (2001) 521–527.
128. W. Wand, B.F. Yuan, C.G. Zhou. Formation and oxidation resistance of germanium modified silicide coating on Nb based in situ composites. Corrosion Science 80 (2014) 164–168.
129. W. Wang, C. Zhou. Characterization of microstructure and oxidation resistance of Y and Ge modified silicide coating on Nb-Si based alloy. Corrosion Science 110 (2016) 114–122.
130. William D. Callister. Materials science and engineering: An introduction. Seventh edition, John Wiley & Sons, Inc. (1940).

131. W.B. Pearson. Handbook of Lattice Spacings and Structures of Metals. New york, Pergamon Press Ltd (1967) Vol-2, 331-332.
132. W.C. Oliver, G.M. Pharr. An improved technique for determining hardness and elastic modulus using load and displacement sensing indentation experiments. Journal of materials research 7 (1992) 1564–1583.
133. W.C. Oliver, G.M. Pharr. Measurement of hardness and elastic modulus by instrumented indentation: advances in understanding and refinements to methodology. Journal of materials research 19 (2004) 3–20.
134. Y.X. Tian, J.T. Guo, L.Y. Sheng, G.M. Cheng, L.Z. Zhou, L.L. He, H.Q. Ye, Microstructures and mechanical properties of cast Nb–Ti–Si–Zr alloys. Intermetallics 16 (2008) 807–812.
135. Y. Qiao, X. Guo, Y. Zeng. Study of the effects of Zr addition on the microstructure and properties of Nb-Ti-Si based ultrahigh temperature alloys. Intermetallics 88 (2017) 19–27.
136. Y. Li, C. Ma, H. Zhang, S. Miura. Mechanical properties of directionally solidified Nb–Mo–Si-based alloys with aligned Nbss/Nb5Si3 lamellar structure. Materials Science and Engineering A 528 (2011) 5772–5777.
137. Y. Kang, S. Qu, J. Song, Q. Huang, Y. Han. Microstructure and mechanical properties of Nb–Ti–Si–Al–Hf–xCr–yV multi-element in situ composite. Materials Science and Engineering A 534 (2012) 323–328.
138. Y. Gu, L. Jia, B. Kong, H. Zhang, H. Zhang. Simultaneous improvement in fracture toughness and oxidation resistance of Nb-Si based alloys by vanadium addition. Materials Science and Engineering A 701 (2017) 149–157.
139. Y.X. Tian, J.T. Guo, L.Z. Zhou, G.M. Cheng, H.Q. Ye. Microstructure and room temperature fracture toughness of cast Nbss/silicides composites alloyed with Hf. Materials Letters 62 (2008) 2657–2660.
140. Y. Qiao, X. Guo. Formation of Cr-modified silicide coatings on a Ti–Nb–Si based ultrahigh-temperature alloy by pack cementation process. Applied Surface Science 256 (2010) 7462–7471.
141. Y. Qiao, M. Li, X. Guo. Development of silicide coatings over Nb-NbCr2 alloy and their oxidation behavior at 1250ºC. Surface Coatings Technology 258 (2014) 921–930.

142. Y. Sainan, J. Lina, S. Linfen, M. Limin, Z. Hu. The microstructure evolution of directionally solidified Nb-22Ti-14Si-4Cr-2Al-2Hf alloy during heat treatment. Intermetallics 38 (2013) 102–106.
143. Z. Li, L. M. Peng. Microstructural and mechanical characterization of Nb based in situ composites from Nb-Si-Ti ternary system. Acta Materialia 55 (2007) 6573–6585.
144. Z. Xu, C. Utton and P. Tsakiropoulos. A Study of the Effect of 5 at.% Sn on the microstructure and isothermal oxidation at 800 and 1200˚C of Nb-24Ti-18Si based alloys with Al and/or Cr additions. Materials 13 (2020) 245.
145. Z. Li and P. Tsakiropoulos. On the microstructures and hardness of the Nb-24Ti-18Si-5Al-5Cr-5Ge and Nb-24Ti-18Si-5Al-5Cr-5Ge-5Hf (at.%) silicide based alloys. Materials 12 (2019) 2655.

LIST OF PUBLICATIONS

Journal Papers

1. **Geethasree Kommineni, Brahma Raju Golla**, Zafir Alam, Rajdeep Sarkar, **V. V. Satya Prasad**. Structure-property correlation and deformation mechanisms in ductile phase (Nb_{ss}) toughened cast Nb-Si alloys. Journal of Alloys and Compounds (2021) 873, 159832. (**Impact factor: 5.316)**

2. **Kommineni Geethasree**, Zafir Alam, P. Sudharshan Phani, Rajdeep Sarkar, **V. V. Satya Prasad**, **Brahma Raju Golla**. Influence of Ti and Zr alloying elements on microstructure and micromechanical properties of near eutectic Nb-18.7Si alloy, Materials Characterization (2020) 171, 110723. (**SCI Impact Factor : 4.342**)

3. **K. Geethasree**, **V.V. Satya Prasad**, **G. Brahma Raju**, Md Zafir Alam. Cyclic oxidation behaviour of Fe-Cr modified slurry silicide coated Nb-18.7Si alloyed with Ti and Zr, Corrosion Science 148 (2019) 293-306. (**SCI Impact Factor : 7.205**)

Conferences/Proceedings

4. **K. Geethasree**, Md Zafir Alam, **G. Brahma Raju**, **V.V. Satya Prasad**, Microstructure and mechanical properties of uncoatedNb-18.7Si and Nb-18.7Si-5Ti alloys and their improved oxidation resistance after application of silicide coating, Materials Today Proceedings 15(1) (2019) 36-43.

Conferences Participated (Oral presentations)

1. On the title of **'Microstructure and mechanical properties of near eutectic Nb-18.7Si alloy with Ti and Zr additions'** in the **'International conference on Advances in Minerals, Metals, Materials, Manufacturing and Modelling (ICAM^5-2019)'** organized by NIT, Warangal.
2. On the title of **'Cyclic oxidation behaviour of uncoated and silicide coated Nb-18.7Si alloyed with Ti and Zr'** in the national conference on **'Frontiers in corrosion control of materials (FCCM-2018)'** organized by NIT, Warangal.